

M.Eng. Lei Zhang

**Microstructure-property Relationship
in Microalloyed High-strength Steel Welds**

BAM-Dissertationsreihe · Band 155
Berlin 2017

Die vorliegende Arbeit entstand an der Bundesanstalt für Materialforschung und -prüfung (BAM).

Impressum

**Microstructure-property Relationship
in Microalloyed High-strength Steel Welds**

2017

Herausgeber:
Bundesanstalt für Materialforschung und -prüfung (BAM)
Unter den Eichen 87
12205 Berlin
Telefon: +49 30 8104-0
Telefax: +49 30 8104-72222
E-Mail: info@bam.de
Internet: www.bam.de

Copyright© 2017 by
Bundesanstalt für Materialforschung und -prüfung (BAM)

Layout: BAM-Referat Z.8

ISSN 1613-4249

ISBN 978-3-9818270-4-0

Microstructure-property Relationship in Microalloyed High-strength Steel Welds

Dissertation

zur Erlangung des akademischen Grades

Doktoringenieur

(Dr.-Ing.)

von M.Eng. Lei Zhang

geb. am 22.10.1986 in Hubei

genehmigt durch die Fakultät für Maschinenbau
der Otto-von-Guericke-Universität Magdeburg

Gutachter:

Prof. Dr.-Ing. habil. Thomas Kannengießer

Prof. Dipl.-Ing. Dr.-techn. Peter Mayr

Promotionskolloquium am 29.Juli 2016

Zusammenfassung

Hochfeste Stähle sind bevorzugte Werkstoffe für die Herstellung von sicheren und zuverlässigen Strukturen in der Industrie. Dabei ist das Schmelzschweißen die Hauptverbindungstechnologie für diese Werkstoffgruppe. Während der Entwicklung der hochfesten niedriglegierten (engl. HSLA) Stähle wurden in der Vergangenheit unterschiedliche Legierungskonzepte mit fortgeschrittenen Herstellungstechniken kombiniert und umfassend untersucht. Jedoch befassten sich nur wenige Studien damit, wie die unterschiedliche Zusammensetzung der Legierungen die Eigenschaften der hochfesten Schweißverbindungen dieser Stähle beeinflussen, selbst im Fall begrenzter Gehalte von Mikrolegierungselementen. In der Schweißpraxis dieser hochfesten Stähle sind die Herausforderungen an die sich ausbildenden Mikrostruktur und den resultierenden mechanischen Eigenschaften von sehr großem Interesse. Diesbezüglich liegt der Hauptfokus des Interesses beim Einfluss der Mikrolegierungselemente auf die Phasenumwandlung sowie die resultierende Performance der Schweißverbindung selbst. Geringes Erweichen (Softening) der Wärmeeinflusszone (WEZ) sowie ein begrenztes Austenitkörner-Wachstum sind dabei erwünschte Eigenschaften der Schweißnaht, jedoch liegt das Hauptaugenmerk auf der Sicherstellung hervorragender Zähigkeits- und Zugeigenschaften. Zum Erreichen dieses Zieles werden Mikrolegierungselemente wie Ti, Nb oder V bewusst zu diesen modernen hochfesten Stählen zulegiert. Der Fokus der vorliegenden Arbeit ist das Verständnis, wie die mechanischen Eigenschaften der Verbindungen dieser HSLA-Stähle von Unterschieden in den jeweiligen Legierungskonzepten abhängen, die durch moderne Schweißprozesse gefügt werden.

Zunächst wurden dazu drei unterschiedlich mikrolegierte (Nb, Ti und Ti+V Zugabe) Stähle vom Typ S690QL untersucht. Lichtmikroskopische Untersuchungen bestätigten dabei, dass eine ähnliche Zusammensetzung aus angelassenem Bainit und Martensit in allen drei Grundwerkstoffen vorherrschte und unterschiedlich stark vergrößerte Ausscheidungen der Mikrolegierungselemente beobachtet wurden. Diese Ausscheidungen wurden weiterführend mittels thermodynamischer Softwareberechnung analysiert und durch Transmissions-Elektronen-Mikroskopie (TEM) identifiziert. Die Ergebnisse der mechanischen Werkstoffprüfung zeigten, dass alle drei Stähle oberhalb der nach Norm geforderten Zähigkeits- und Zugfestigkeitswerte lagen, jedoch Unterschiede im Dehnungsverhalten aufwiesen. Die drei Stähle wurden dann anschließend unter Verwendung des gleichen Schweißzusatzes geschweißt. Dabei wurde das abgeschmolzene Schweißgut durch die Mikrolegierungselemente aus dem Grundwerkstoff infolge der hohen Aufmischung beeinflusst. Die erhöhte Aufmischung bildet dabei ein wesentliches Merkmal der verwendeten modifizierten Sprühlichtbogentechnik. Als Ergebnis zeigte der Nb-mikrolegierte Stahl eine genügend hohe Aufnahme von Legierungselementen aus dem Grundwerkstoff in das Schweißgut, um dessen Mikrostruktur im Fall steigender Abkühlraten von nadeligem Ferrit hin zu Bainit zu verändern. Dieses wiederum reduzierte die Zähigkeitseigenschaften des Schweißgutes dieses Nb-legierten Stahls. Dieses Verhalten wurde in den beiden anderen Stählen nicht beobachtet.

Ein zweiter Hauptpunkt dieser Arbeit war die Ausbildung der Mikrostruktur in der Feinkorn- und Grobkorn-WEZ und deren Zähigkeitseigenschaften mit den sich verändernden Schweißparametern. Zu diesem Zweck wurden definierte Werkstoffzustände physikalisch simuliert, um die resultierende Mikrostruktur sowie das Austenitkorn-Wachstum zu charakterisieren. Die Mikrolegierungselemente bildeten dabei einen wesentlichen Faktor zur Begrenzung des Austenitkörner-Wachstums. Das Ausmaß der Austenit-Vergrößerung in der WEZ war dabei stark abhängig von der Art und dem Volumenanteil der unterschiedlichen Ausscheidungen infolge der unterschiedlichen Mikrolegierung. Von allen drei

Stählen zeigte die WEZ des Ti-legierten Grundwerkstoffes das geringste Kornwachstum als Folge des ausreichenden Umfangs von stabilen Ti-Ausscheidungen. Die Ausbildung von nadeligem Ferrit im Korn wurde dabei durch die Ti-Ausscheidungen unterstützt, da diese als bevorzugte Stellen der Nukleation des Ferrits dienten. Die Zähigkeit der WEZ erhöhte sich dabei infolge der Großwinkelgrenzen der feinen Ferrit-Platten. Aufgrund des kombinierten Effektes von Nb und Mo, welcher sich in der bevorzugten Ausbildung von unterem Bainit äußert, konnte die WEZ-Zähigkeit bei hohen Abkühlraten weiter verbessert werden. Im Fall eines größeren Wärmeeintrags bildete sich jedoch bevorzugt oberer Bainit, welcher wiederum die Zähigkeit reduzierte.

Der abschließende experimentelle Teil der Arbeit konzentrierte sich auf das Verständnis der Mechanismen, die in bestimmten Fällen zur Erweichung (oder Softening) der WEZ führen. Dieses Erweichen äußerte sich in den unterschiedlichen Zugeigenschaften der geschweißten Verbindungen der Stähle. Dabei war die Bruchlage entweder in der erweichten WEZ oder im Grundwerkstoff, abhängig von den Schweißparametern sowie der Art des geschweißten Stahls. Im Ti-legierten Stahl führte dabei ein erhöhter Wärmeeintrag zur Vergrößerung der Erweichungszone. Dieses führte zu einer signifikanten Abnahme der Härte und anschließend zum Versagen in dieser erweichten Zone im Zugversuch. Die Veränderung der Bruchlage hin zum Grundwerkstoff wurde durch die Begrenzung des Wärmeeintrags erreicht. Dieses Verhalten wurde nicht in den beiden anderen Stählen beobachtet. Dieses Verhalten zeigt, dass bereits kleine Unterschiede im Gehalt der Mikrolegierungselemente der Stähle zu großen Variationen in den Zugeigenschaften führten. Für alle drei Stähle, zeigten die Ti-enthaltenden Schweißverbindungen das am deutlichsten ausgeprägte Softening, gefolgt von den Ti+V-enthaltenden Schweißungen und schließlich den Nb-enthaltenden Schweißverbindungen. Das unterschiedliche Softening konnte dabei auf zwei Prozesse bezogen werden, die auch über zusätzliche Dilatometrie-Experimente gestützt wurden: die Phasenumwandlung und das Anlassverhalten. Im Ti-legiertem Stahl lag nach der Phasenumwandlung großformatiger Ferrit als Konsequenz der ursprünglich großen Austenitkörner vor. Dieses führte zu einer abgesenkten Härte dieses Stahls. Weiterhin resultierte die geringere Anlassbeständigkeit des Ti-legierten Stahls (gegenüber dem Nb-legierten Stahl) zu einem weiteren Softening der erweichten WEZ. Deswegen erwies sich diese Kombination aus Legierungszusammensetzung und Schweißwärmeeintrag als kritisch, gestützt durch die Experimente am gleichen S690QL Stahl.

Die vorliegende Arbeit hebt den wesentlichen Einfluss der Mikrolegierungselemente auf die Schweißmikrostrukturen und die mechanischen Eigenschaften der Schweißverbindungen hervor. Die Kenntnis dieser empfindlichen Balance zwischen Legierungskonzept des entsprechenden Stahls und geeigneten Schweißparametern ist als kritisch für das fertige Produkt anzusehen. Dazu stellt diese Arbeit spezifische Empfehlungen und Ergebnisse zur Verfügung, um die korrekte Schweißpraxis zu gewährleisten als auch für die Zusammensetzung mikrolegierter hochfester Stähle.

Abstract

High-strength steels are favoured materials in the industry for production of safe and sustainable structures. The main technology used for joining the components of such steel is fusion welding. Steel alloy design concepts combined with advanced processing technologies have been extensively investigated during the development of High-Strength Low-Alloy (HSLA) steels. However, very few studies have addressed the issue of how various alloy designs, even with limited microalloy addition, can influence the properties of high-strength steel welds. In high-strength steel welding practices, the challenges regarding microstructure evolution and the resulting mechanical properties variation, are of great interest. The main focus is the debate regarding the role of microalloy elements on phase transformation and weld performance. Limited Heat Affected Zone (HAZ) softening and limited austenite grain coarsening are significant design essentials, but the primary goal is to ensure excellent toughness and tensile properties in the steel weld. To achieve this purpose, microalloy elements such as Ti, Nb, or V were intentionally added to modern high-strength steels. The focus of this work was to understand the mechanical properties of HSLA steels resulting from differences in alloy design after joining by modern welding processes.

To begin, three microalloyed S690QL steels (Nb, Ti, and Ti+V addition) were investigated. Optical microscopy confirmed that similar mixtures of tempered bainite and martensite predominated the parent microstructure in the three steels, different types of coarse microalloy precipitates were also visible. These precipitates were analysed by using a thermodynamic-based software and then identified by Transmission Electron Microscopy (TEM). Results of mechanical testing revealed that all three steels performed above the standard toughness and tensile strength values, but with varied yielding phenomena. During the welding operation, each of the three steels was joined by using the same filler material. The fused weld metal was influenced by the high dilution of microalloyed elements in the base metal, this was significantly pronounced during the modified spray arc welding technique. As a result, the Nb-containing steel exhibited sufficient amounts of alloy pick-up to transition the microstructure in the weld metal from acicular ferrite to bainite as cooling rate was increased, leading to reduced toughness. This was not observed with the other two steels.

A second focus was made on the microstructure evolution and toughness properties of the coarse and fine grained HAZ as welding parameters changed. In order to characterise the microstructure and austenite grain growth behaviour, physical simulations were conducted. The microalloy precipitates were found to be a dominant factor restricting the austenite grain coarsening. The extent of austenite coarsening in the HAZ is closely related to the type and volume fraction of each microalloy precipitate. Among the three steels, the Ti-containing HAZ exhibited the smallest extent of grain growth due to the sufficient amount of stable Ti-rich precipitates. Microalloy addition also markedly influenced the subsequent phase transformation in the HAZ. The formation of intragranular acicular ferrite was promoted by Ti-rich precipitate, acting as favourable nucleation sites of ferrite. This structure enhanced the HAZ toughness owing to fine, high-angle boundaries of ferrite plates. The synergistic effect of Nb and Mo elements was beneficial to improve the HAZ toughness at fast cooling rates by promoting fine lower bainite formation. At high heat input, large upper bainite was formed which caused reduced toughness.

The final set of experimental work was concentrated on understanding the HAZ softening mechanisms that influenced variations in the tensile properties of the welded joints. The tensile failure in the softened HAZ or base material depended on the welding parameters and the type of steel being joined. In Ti-containing steel, increased heat input extended the softened zone width, which caused a significant decrease in hardness and then resulted in failure in this area. Therefore, limited heat input was used to shift failure position to base material. But this was not observed in the other two steels. Hence, small differences in microalloy addition exhibited large variation in tensile properties. Among the three steels, Ti-containing welds were found to have the most pronounced softening, followed by Ti+V-containing welds and finally Nb-containing welds. This varied softening phenomenon was related to two significant processes supported by the results of additional dilatometry simulation: phase transformation and tempering behaviour. In the Ti-containing steel, the phase transformation product ferrite was large-sized, as a consequence of initial large austenite grains. This led to the decreased corresponding hardness of the Ti-containing steel. Furthermore, lower tempering resistance in Ti-containing steel as compared to Nb-containing steel, resulted in additional softening effect in the softened HAZ. Therefore, steel alloy identification and heat input during welding were critical, proven by the experimentation within the same S690QL steel grade.

This work emphasised the influence of microalloy elements on weld microstructure and mechanical properties in welded joints. Knowledge of this delicate balance between steel alloy design and appropriate welding parameters is critical for the end product. Thus, this work provides specific recommendations and results to ensure proper welding practice and steel design of microalloyed high-strength steels.

Acknowledgements

I would like to express my overwhelming gratitude to my supervisor, Professor Thomas Kannengiesser, for all his support, guidance, advice and constant encouragement during my research and throughout my stay in Germany. I am very grateful to Professor Peter Mayr (Technical University of Chemnitz) for supporting this work and accepting to be my second supervisor. I would also like to thank Prof. Bernhard Karpuschewski (Otto von Guericke University Magdeburg) for being my committee chair together with the other committee members, Prof. Sven Juettner and Joerg Pieschel.

I earnestly acknowledge financial support from China Scholarship Centre for providing me the opportunity to pursue research in Germany. I also express my gratitude to Prof. Thomas Boellinghaus and Prof. Michael Rethmeier for giving me a chance to work at the Bundesanstalt für Materialforschung und –prüfung (BAM). I would like to extend further thanks to my colleagues who provided assistance and advice to me. To Andreas Pittner, Thomas Michael, Dirk Schroepfer, Stefan Brunow for the welding experiments; to Maria Marten, Lukas Stempin, Romeo Saliwan-Neumann, Gert Nolze, Michaela Buchheim, for helping with metallography and SEM work; to Prof. Axel Kranzmann, Rene Hesse, Ilona Doerfel, for helping with FIB and TEM work; to Ralf Haecker for assisting with mechanical testing; to Sebastian Recknagel for advice and guidance with chemical composition analysis; to Ping Xu for helping with X-ray work; to Daniel Stock and Frank Koehler for teaching me how to make a thermocouple and correctly measure the temperature; to Enrico Steppan for assisting with the partial dilatometry experiments; to Philipp Schempp, Carolin Kernchen, Thora Falkenreck, Tobias Mente, Eitan Dabah, Kaveh Momeni, Gunther Sproesser, Nicolas Haeberle and Cagtay Fabry for the many encouragements, discussions and nice working atmosphere in the office; to the secretaries Sandy Ney and Diana Griebisch for the support over the last few years; to Carola Hesse-Andres for arranging a lot of literature for me; and exceptional thanks to Michael Richter and everyone else in the workshop for machining support.

Additional thanks go to Alexander Nitsche, for assisting with dilatometry experiments and for providing invaluable discussion. I wish to express my sincere thanks to Prof. Fernando Cosme Rizzo Assuncao, at the National Institute of Technology Brazil, for the valuable discussion on thermodynamic calculation, and to Prof. Thorsten Halle, for providing access to the Thermo-Calc software. I am particularly indebted to Marion Behring and Prof. Rainer Stark, who gave me endless support during the first year work in TU Berlin. I am also unendingly grateful to the nice colleagues (if I did not mention them already) at BAM, TU Berlin and OVGU, who made my experience in Germany an exceptional and invaluable one.

I am extraordinarily grateful to Michael Rhode, for being always there in times of difficulties, for continuous support and for all of our helpful discussions. Particular thanks also go to Arne Kromm, Oded Sobol and Benjamin Steffens, for correcting my thesis and for giving good scientific advice and input for this thesis.

I will never forget all the beautiful moments I shared with my roommates, Lena Haselhorst and Janine Kalberlah, and other friends Bilge, Jenny, Dami, Lena and Ann. They are a constant source of emotional support, advice and amusement. I am also grateful to my Chinese friends Shanshan, Jiabi, Ji, Dan, Li, Hao and Shuying. Many thanks to them all for their love, support and companionship.

My special gratitude goes to Lena's and Sabine's families for treating me as a family member, for the wonderful Christmas and birthday celebrations we had together, and for believing in my potential and supporting me. My most heartfelt thanks go to my parents and my brother for their encouragement, love, trust, and for making me feel so close despite being so far. Of course, I am not forgetting the rest of my family, who supported me so much during all this time.

Lei Zhang

BAM, Berlin
July 2016

Contents

1	Introduction	1
2	Literature review	3
2.1	High-strength structural steels	3
2.1.1	Development of high-strength steels	3
2.1.2	Metallurgical approaches on QT steels	4
2.1.3	Standards, guidelines and products	7
2.1.4	Carbon equivalent with respect to weldability	13
2.2	Modern GMAW processes	16
2.3	Weld metallurgy	18
2.3.1	Background on weld microstructure	20
2.3.2	Compositional effects	31
2.4	Properties of the heat affected zone (HAZ)	36
2.4.1	Hydrogen-assisted cold cracking	36
2.4.2	Austenite grain growth	37
2.4.3	HAZ toughness	46
2.4.4	HAZ softening	49
3	Summary of literature and objectives	53
3.1	Summary of literature	53
3.2	Objectives of the present study	54
4	Experimental procedure	57
4.1	Base materials	57
4.2	Filler metal	57
4.3	Welding experiments	57
4.4	Principles of characterisation methods	59
4.4.1	Light optical microscopy	59
4.4.2	Scanning electron microscopy	59
4.4.3	Energy dispersive X-ray spectroscopy	61
4.4.4	Electron backscatter diffraction	62
4.4.5	Focused ion beam technique	62
4.4.6	Transmission electron microscopy	63
4.5	Mechanical testing	64
4.5.1	Hardness	64
4.5.2	Tensile test	64
4.5.3	Charpy impact test	65
4.6	Physical simulation of heat affected zone	65
4.6.1	Austenite grain growth simulation	65
4.6.2	Dilatometry	65
4.7	Thermodynamic prediction of phase stability	66
5	Microstructure characterisation and mechanical properties of base material	67
5.1	Microstructure of base materials	67

5.2	Microalloy carbonitrides	69
5.2.1	Prediction by thermodynamic calculation	69
5.2.2	Microalloy precipitates under optical microscopy	73
5.3	Mechanical properties	74
5.3.1	Tensile properties	74
5.3.2	Charpy V-notch toughness	75
5.4	Discussion	76
5.4.1	Microalloy precipitates	76
5.4.2	Relationship between microstructure and mechanical properties	77
5.5	Summary	78
6	Microstructure evolution and mechanical properties of weld metals	79
6.1	Hardness results	79
6.2	Microstructure characterisation	80
6.3	Toughness results of weld metals	84
6.4	Discussion	88
6.4.1	Effect of microstructure on toughness	88
6.4.2	Transition between acicular ferrite and bainite	88
6.5	Summary	90
7	Microstructure evolution and mechanical properties of CGHAZ and FGHAZ	91
7.1	Microstructure characterisation	91
7.2	EBSD analysis	94
7.3	Austenite grain growth simulation	98
7.3.1	Austenite grain growth behaviours	98
7.3.2	Microstructure of simulated HAZs	99
7.3.3	Hardness of simulated HAZs	103
7.4	Identification of microalloy precipitates by TEM	105
7.5	HAZ toughness results	108
7.6	Discussion	110
7.6.1	Effect of microalloy precipitates on austenite grain growth	110
7.6.2	Effect of microalloy addition on phase transformation	111
7.6.3	Effect of crystallographic orientation on fracture toughness	113
7.6.4	Effect of HAZ microstructure on toughness	113
7.7	Summary	115
8	Microstructure evolution and mechanical properties of softened HAZ	117
8.1	Tensile properties	117
8.2	HAZ softening in the welded joints	118
8.3	Dilatometry	121
8.3.1	Hardness of softened HAZs	122
8.3.2	Phase transformation analysis	122
8.3.3	Microstructure of the softened HAZs	127
8.4	Discussion	133
8.4.1	Effect of softening on tensile properties	133

8.4.2 Softening mechanisms	134
8.5 Summary	138
9 General conclusions and future works	141
9.1 Future works	143
References	145
List of Tables	158
List of Figures	161
Nomenclature	165

1 Introduction

To satisfy the needs of environmental-friendly and sustainable materials advancement, high-strength steels remain one of the preferred materials due to their relatively low cost, and versatility. The development of high-performance steels was encouraged by the need to have deeper understanding of the relationship between microstructural characteristics and mechanical properties [1, 2]. So far, many types of steels have been developed by varied alloy design and adjustable heat-treatment procedures. Using the sophisticated quenched and tempered (QT) technique, a minimum yield strength steel of 1300 MPa has been achieved. These excellent mechanical properties are the main goal of steel manufacturers. However, the significant implications of good steel weldability and thoroughly welded structures must be considered during production.

Concerning welding processes with respect to steels with strength above 1100 MPa, the requirements are very strict and the results can be problematic. European standard EN 10025 provides guidance with steels that have yield strength up to 960 MPa; some corresponding suggestions, specifications and rules on the welding procedures are offered as well [3]. Among these high-strength steels, the most utilised construction steel is currently a 690 MPa variety. It can be found in various applications such as bridges, automotive, pressure vessels, wind energy and other high-loaded components [4, 5].

Another key advancement that accompanied the development of high-strength steel is the very specialized alloy design; which respectively requires appropriate heat treatment processes. The very specific steel alloys have been designed to meet particular applications or desired material properties. The formulated steel has to satisfy all of the requirements specified in the corresponding standard. Apart from the common alloying elements, high-strength steels require the use of the microalloying concept, e.g. with Nb, Ti and V, as shown in this research.

The standards often provide a tolerant allowance on chemical composition for steels; normally the maximum value of alloying contents are important. Accordingly, individual steel manufacturers have to consider their own alloy resources, economical benefits, available production line and other factors when making any feasible alloy designs. Therefore, alternative alloying compositions have been proposed by steel manufacturers and have resulted in different steels with the same properties. Small compositional differences within the steel, with respect to microalloy content, have been shown to influence the weldability, in particular with modern welding technologies. If these weldability differences are apparent, it becomes necessary for the welding engineers to be aware of such a discrepancy and correspondingly change the welding operation to optimise the results.

Predicting HAZ properties in steels can be achieved by using carbon equivalent formulas, but this approach is still limited for use in modern high-strength steels because of the currently lower residual element levels. More importantly, the carbon equivalent formulas seldom incorporate microalloy elements (Nb, Ti or B) with weldability performance [6, 7]. Therefore, a standardized method to evaluate the weldability of modern microalloyed steels is necessary. This method would need to combine the necessary welding tests and assessments with the steel chemical composition and its fabrication process.

The present study compares the microstructure and mechanical properties of three microalloyed (Nb-, Ti- and Ti+V-containing) S690QL weldments; it provides a deep understanding of the influence of these microalloy elements on phase transformation and on the weld performance. This research will

deliver reference and guidelines to achieve thoroughly welded structures composed of modern steels with varied chemistries.

Thermodynamic and kinetic modelling have been important tools used in the development of new alloy designs. Thermo-Calc software was applied to predict the microalloy precipitation in different steels; by using this modelling process, the design of different phases can be studied and carbide and nitride quantities in the alloy can be evaluated. In the present study, the results from modelling were later confirmed by experimental analysis. Particular attention was given to the phenomenon of large quantity alloy pick-up by the weld metal from base metal due to the high dilution effect when using modern welding technology. Also of interest was the austenite grain growth behaviour in the HAZ and how it directly affects the subsequent phase transformation and toughness properties [8, 9]. In this phase transformation process, the role of microalloy elements in solid solution or in precipitate, and their influence on the HAZ toughness is of great interest due to potential negative effects that have been considered in literature [10–16]. The present research establishes how the microalloy elements influence the phase transformation and the final toughness properties under different welding conditions.

A better understanding of the mechanisms that govern the softening properties in quenched and tempered steel welds with different alloy additions is very important when considering structural integrity. Some contrary theories have been proposed to evaluate the softening phenomenon in different steel welds. It has been suggested that appropriate control of welding parameters can control the extent of softening [17, 18]. However, limited attention has been given to the chemistry and the grain structure of microalloyed high-strength steels.

The aim of this work was therefore to investigate the factors that influence toughness and tensile properties in S690QL microalloyed steel welds. The focus was on understanding how the three steels respond to different welding conditions dictated by modern welding technologies while maintaining the required mechanical properties. This included studying the varied microstructures and identifying the properties of the welded joints. The collection of research of the three steel alloys has provided the references and guidelines for welding engineers to carry out appropriate welding operations on these particular microalloyed high-strength steels.

2 Literature review

2.1 High-strength structural steels

2.1.1 Development of high-strength steels

Steels represent one of the most common metals used in today's world. The development of steel was and still is continuous in process due to the major role of this substance, with an annual consumption of more than a billion tonnes in improving the quality of our life [1, 2]. High-strength steels are gaining great interest of application due to the attractive economical advantages, reliable performance, environment-friendly and sustainability. By increasing the strength of a steel, the construction sector can be reduced. Less transportation and fabrication costs are required and therefore the environmental impacts are reduced due to less associated emissions. Long products life cycle and high recycling rate ensure steel as one of the most sustainable materials.

The progress in developing new steel grades is always encouraged in order to gain a diverse range of properties. Increase in yield strength can be approached by appropriate alloy design combined with process of toughening (hardening and tempering) or a thermomechanical treatment [1]. Many efforts have directed toward developing modern manufacturing technologies into high-strength steels production. Some typical production processes of structural steels are based on normalised, quenched and tempered (QT), and thermomechanical controlled processed (TMCP). By normalising procedure one can achieve moderate strength and toughness requirements only up to steel S460N. However, there is a continuous need for new advanced techniques to produce higher strength steels, thus QT and TMCP processes appeared. The historical evolution of steel grades available in Europe for rolled products is shown in Fig. 2.1 [1]. Historically, the rolled steel products enabled the introduction of higher grades at a fast rate over the last decades, which are promoted by QT and TMCP processes.

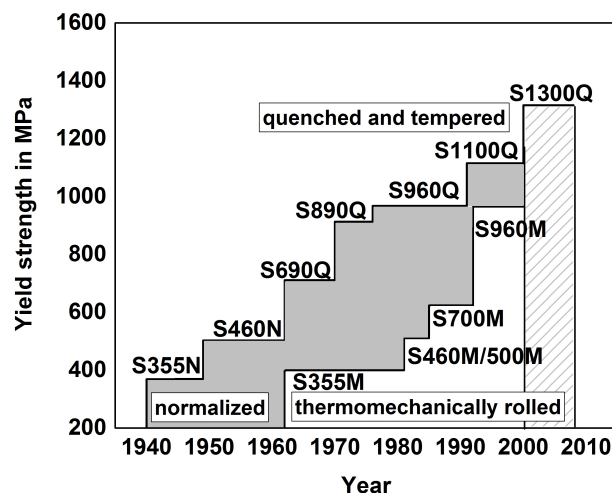


Fig. 2.1: Historical development of production processes for rolled steel products [1]

Compared with QT steels, the optimum level of mechanical properties in TMCP steels is achieved by an extremely fine grained microstructure with a sophisticated control on the rolling steps at particular temperature. The final strength dedicated by grain refinement allows to produce S460MC, S500MC, S700MC and S900MC steel grades. Even though TMCP steels contain reduced carbon and alloy contents, thinner plates will be more readily attainable than thicker plates with higher strengths, which restrains its production and application [19]. Contrary to TMCP steels with limited thickness, QT

steels can be available in thickness higher than 100 mm. For this reason, quenched and tempered process becomes the standard production route for very high-strength structural steels [4].

Recently, QT or quenched and self-tempered (QST) process can produce high-strength steels S690QL, S890QL, S960QL, S1100QL or even higher grade S1300QL. Steel S1100QL and S1300QL, as ultra high yield structural steel, are available on the market. This reveals the fact that industry has an ongoing requirement for stronger and lighter structural section. As illustrated in Fig. 2.2 [20], the overall costs when the structure is made of higher strength steels reduce greatly compared with conventional S355 steel. Also, it is expected that S1100QL and S1300QL could be the optimised as an alternative in the future for this purpose. But, it is still challenging to solve hydrogen-assisted cold cracking or matched filler metal problems for welding higher grade steels than S960QL [5].

Nowadays, European steel construction in various fields, such as bridges, automotive, pressure vessels, high buildings, wind energy, and other high-loaded components, mostly are utilised up to steel grade S690QL [4, 5]. Bridges for example, most of the steel bridges being designed formerly by S355 experiences a challenge to satisfy the need of high quality coupled with efficient cost. Therefore, the design with higher steel grades like S690 is widely applied in hybrid steel girders. Although the current price of high-strength steel is a little higher than that of S355, the evolution of S690 price owing to large market demand is predicted by Gogou [21] to show a decline since 2012. Thus, modern bridge design offers great potential for the use of high-strength steels. In addition, in application of car bodies, high-strength steels with yield limit of 600 MPa are often used for specific zones in order to achieve required strength and rigidity of car body coupled with reduced mass. Anyway, the structure that has to be considered for high-loaded support often take high-strength steels as one premium material to guarantee high safety and cost savings.

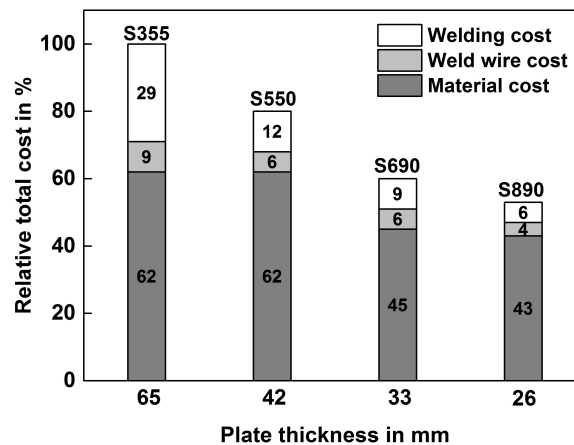


Fig. 2.2: Material and welding cost of higher strength steels relative to S355 [20]

2.1.2 Metallurgical approaches on QT steels

Alongside the development in manufacturing high-strength steels have come many principles involved in understanding the interaction between strength and toughness as influenced by steel chemistry, heat treatment and mechanical processing. As is well-known, when designing modern high steels, different strengthening mechanisms should be considered with the aim of desired yield strength. Several mechanisms are commonly applied to microalloyed steels that are solid solution strengthening, grain refinement, dispersion (or precipitation) strengthening and work hardening. All these mechanisms have the same potential to increase the applied stress required for the onset of plastic deformation [22].

The nature of solid solution strengthening is to increase the iron lattice resistance to deformation by different forms of interaction between solute atoms and dislocations [22]. C and N, as interstitial atoms in iron, induce some extent of lattice distortion, which inhibits the dislocation mobility. The presence of even a small amount of C up to 0.2 wt.-% has a great strengthening effect on ferritic iron, a fact known to smiths over 2500 year ago since iron heated in a charcoal fire can readily absorb carbon by solid-state diffusion [2]. But from a metallurgical standpoint carbon content must be kept low enough in steels to maintain adequate toughness and good weldability. In the absence of specific nitride-forming alloying elements, it is expected that most N will remain in solid solution. when strong nitride formers are present in the steel, some account has to be taken of the N removal by the nitride former [22]. Substitutional alloy (e.g. Mn, Ni, Cr, and Si) have much larger atoms and they contribute to substitutional solid solution strengthening. The strengthening coefficients (on a wt.-% basis) for the various solutes are shown as a function of the lattice dilation (again on a wt.-% basis) in Fig. 2.3.

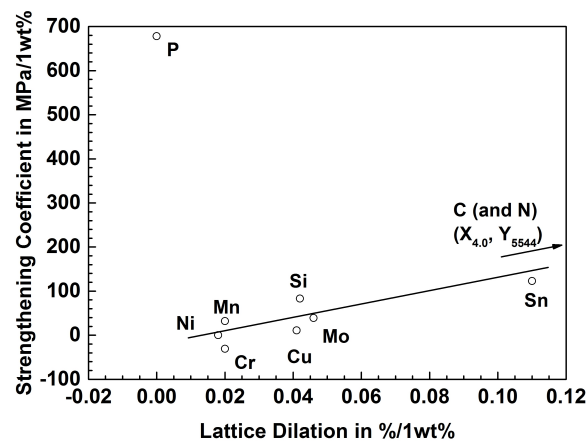


Fig. 2.3: Solid solute strengthening coefficients shown as a function of the lattice dilation due to the solute additions. Both strengthening and lattice dilation are expressed in terms of the weight percentage of solute [22]

Fig. 2.3 shows that different solutes have very different strengthening coefficients. These values appear to increase with increasing lattice dilation but the trend is dominated by interstitial carbon due to its larger dilation than that of other substitutional solute. There are two exceptional elements P and Cr in Fig. 2.3 which are out of the main trend but the reasons for this are not totally clear [22].

Another reason for alloying addition is their attributes on phase transformation and precipitates. It is known that most alloying elements move the time – temperature – transformation (TTT) curves to the right, with the consequence that they essentially increase steel hardenability and let martensite formation occur at slow cooling rate upon quenching. Moreover, the presence of alloying elements, particular the carbide former, also slow down the softening rate of martensite upon tempering through stabilising the transition carbide and martensite or by retarding the precipitation and coarsening of cementite [22]. The effects of individual alloying element on phase transformation and precipitation process are discussed in subsequent section.

The effect of adding special alloying elements is also reflected by the most important strengthening mechanism – grain refinement, which will not adversely influence ductility and toughness. The most effective method to achieve dramatic refinement is attributed to the addition of particular alloying elements combined with advanced mechanical treatment. It is believed that the best grain refining elements are very strong carbide and/or nitride formers, such as Nb, Ti, V, and Al. The reason is

that all these fine carbides or nitrides inhibit grain growth by the well-known Zener drag effect [22]. This effect is discussed in subsequent section. To understand the relationship between grain size and strength, Hall-Petch relation is proposed. This relation claims that the finer grain size, the higher the final yield stress. The generalised form of the Hall-Petch relationship can be expressed as:

$$\sigma_y = \sigma_0 + k_y d^{-1/2} = \sigma_i + \sum k_i \cdot c_i + k_y d^{-1/2} \quad (2.1)$$

The above overall strengthening is the final contribution from two parts: the solute strengthening σ_0 and the grain size strengthening $k_y d^{-1/2}$. σ_y is the yield stress, σ_i is the friction stress of iron, c_i is the concentration of the i component, k_i is the strengthening coefficient of the i solute, k_y is the strengthening coefficient for grain size and d is the grain diameter [22]. When dispersed second phase particles are present in microalloyed steels, the attention should be given to the precipitates strengthening on the additional increment in yield strength. By considering Ashby-Orowan equation, a more complete description of yield strength for microalloyed steel can be given by the expanded Hall-Petch relationship (equation 2.2):

$$\sigma_y = \sigma_0 + \sum k_i \cdot c_i + k_y d^{-1/2} + (10.8 f^{1/2} / X) (\ln(X / 6.125 \times 10^{-4})) \quad (2.2)$$

Where, X is the true three dimensional diameter. This diameter is not equal to the average diameter of the particles in the plane of intersection x ($X = (3/2)^{1/2} x$). f is the volume fraction of particles. Orowan has described that the dispersion hardening arises from looping of the dislocation between hard undeformable particles and the strengthening contribution is defined by the real particle diameter and the volume fraction [23]. The refinement in particle size and the increase in particle amount can enhance a significant increase in yield strength, as shown in Fig. 2.4.

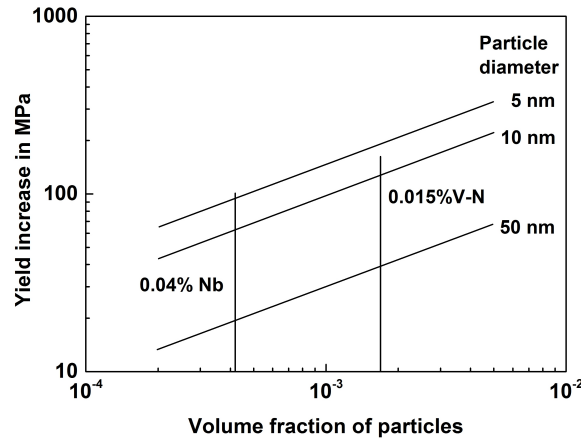


Fig. 2.4: The increase in yield strength of steels compared to the predictions of the Ashby-Orowan equation [22]

Fig. 2.4 shows that in Nb and V bearing steels with a given volume fraction the maximum strengthening contribution can reach up to 100 MP and 150 MP respectively when fine particles of 3 nm – 5 nm form under faster cooling process [22]. To reveal the influence of above different strengthening mechanisms on final strength, a quantitative assessment used for high-strength steels is given in Fig. 2.5 [20]. The overall strength is the balanced contribution from alloy addition coupled with thermomechanical production process. In general, the increase in strength above 460 MPa accompanies the evolution of microstructure in which the ferrite matrix changes and the pearlite formation is suppressed [20]. One method is to reduce the phase transformation temperature to a low value ($< 700^\circ\text{C}$). In this case,

the final microstructure is bainite or degenerated ferrite with increased dislocation density and refined grains. This phase transformation strengthening can be profoundly enhanced by addition of Mo and B.

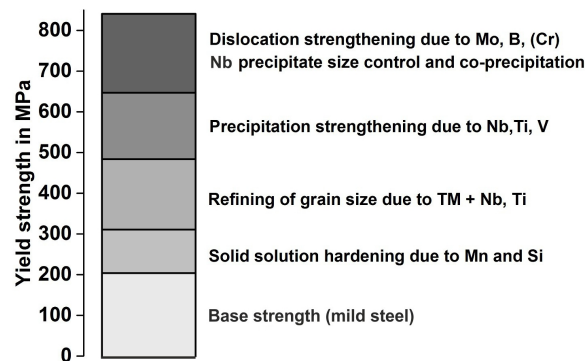


Fig. 2.5: Strengthening effects in HSLA steel [20]

Apart from the above mentioned metallurgical concepts for strengthening (Fig. 2.5), martensite structure resulted by quenching process increase the strength as well. By a separate heat treatment or directly after rolling, when an extreme high cooling rate is applied, the quenched condition across the whole section is obtained. To easily control the critical cooling speed during quenching, alloying of Mo, Cr and/or B are added because most alloying elements move the TTT curves to longer time. The tensile strength of martensite structure can range from 1200 MPa to 1600 MPa but it has a severe impact toughness. Subsequent tempering is essential in order to reduce internal stresses and improve toughness and processing behaviour. Such a quenching and tempering process (Fig. 2.6) contributes to a fine bainitic – martensitic structure with optimum strength, toughness and weldability [24].

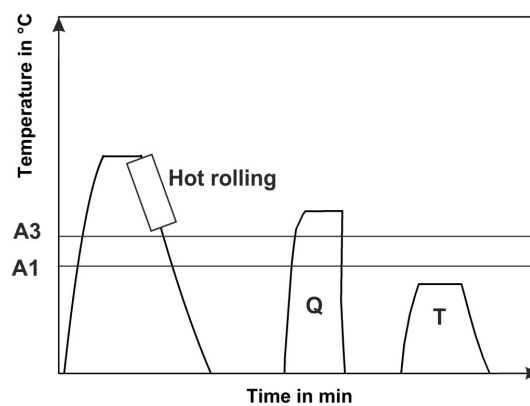


Fig. 2.6: Production process of QT high-strength steel [24]

Based on strengthening mechanisms mentioned above and existing fabrication techniques, grain refinement is getting part of the focus in the development of steels, mainly by using minimal alloying elements to achieve the desired strength level. Another part of the focus is given to decreasing impurities, which could cause lamellar or hot cracking. The next section describes the alloy design for the desired strength defined by standards or guidelines.

2.1.3 Standards, guidelines and products

Since 2004 the standard for hot-rolled steel products has been updated as EN 10025. It includes six parts and defines the chemical and mechanical properties of the most common structural steel grades. With respect to quenched and tempered steel, EN 10025 part 6 gives the standardised requirements

of the delivery condition for yield stress grades from 460 MPa up to 960 MPa [3]. Note that most constructional steelwork in Europe today is still limited to steel grades up to S690. Such quenched and tempered S690 steels also can be mechanically equivalent to other international standards, as shown in Table 2.1 [3, 25–27]. All these steel products shown in Table 2.1 are grouped based on the common mechanical properties and fabrication procedures, using the yield strength with a minimum value of 690 MPa as a guideline. The specific mechanical properties requirements in different standards are summarised in Table 2.2, however the actual steel products mostly exceed these minimum values.

Table 2.1: International standards for structural steels with a minimum yield strength 690 MPa [3, 25–27]

Standard	Description	Steel
EN 10025-6:2004	Hot rolled products of structural steel – Part 6: Technical delivery conditions for flat products of high yield strength structural steels in the quenched and tempered condition	S690QL
ASTM A514	High – yield – strength, quenched and tempered alloy steel plate, suitable for welding	Grade B
ISO 630-4:2012	Structural steels – Part 4: Technical delivery conditions for high – yield – strength quenched and tempered structural steel plates	S690
CSA G40.21	Structural quality steel – plates, sheet, floor plates, bars, and welded shapes	100QT
JIS G3128	High yield strength steel plates for welded structures	SHY 685
AS 3597	Structural and pressure vessel steel – quenched and tempered plates	Grade 700
CEN standard is from the European Committee for Standardisation ASTM standard is from the American society for Testing and Materials ISO standard is from the International Organisation for Standardisation CSA standard is from the Canadian Standards Association JIS standard is from the Japanese Standards Association AS standard is from the Standards Australia		

Table 2.2: Mechanical properties of structural steels with thickness of less than 50 mm [3, 25–27]

Standard	EN 10025-6:2004	ASTM A514	ISO 630-4:2012	CSA G40.21	JIS G3128
Steel	S690QL	Grade B	S690, quality E	100QT	SHY 685
R_e , MPa	690	690	690	700	685
R_m , MPa	770 to 940	760 to 895	770 to 940	760 to 895	780 to 930
A, min. %	14	16	14	18	see standard
Toughness min., J	27 (–40°C)	27(–45°C)	27(–40°C)	see standard	47(–20°C)

To fulfil the mechanical requirements, the standards also present the requirements on chemical composition; but normally the maximum values for alloying elements are very important. This permits a quite tolerant range of alloying selection [28], as shown in Table 2.3. Table 2.3 shows some European standards specifications on different high-strength steels. Different alloy designs are required for different strength levels in accordance to different fabrication processes, however, normally the maximum values are given in the standards.

Table 2.3: Some European standards specifications [3, 29, 30]

	EN 10025-6	EN10025-4	EN 10149-2
Grade considered	S960QL	S500M	S960MC
Thickness range	< 50 mm	< 16 mm	3 – 6 mm
Higher yield strength	960 MPa	500 MPa	960 MPa
Process of steel production	QT	TMCP or QST	TMCP
Selected alloying contents on ladle analysis (wt.-%) – maximum values			
Carbon equivalent	CEV < 0.82	CEV < 0.47	-
C %	0.20	0.16	0.12
Mn %	1.70	1.70	2.20
Cr %	1.50	0.30	-
Ni %	2.0	0.80	-
V %	0.12	0.12	0.20
Mechanical properties			
Minimum yield strength, MPa	960	500	960
Tensile strength, MPa	980 – 1150	580 – 760	980 – 1250
Minimum elongation, %	10	15	7

In the case of international standards for the same yield strength level of 690 MPa, different alloying ranges are set to meet comparable mechanical properties (Table 2.4). The CEN standard gives relatively large tolerance on alloying range. Normally the maximum values are very important and within this alloying range steel with a yield strength up to 960 MPa can be obtained. There is a good agreement between CEN and ISO standards since both require a high degree of consensus among the National Standards Bodies [31]. Note that CEN's P and S levels are more restrictive than other specification requirements. ASTM standard sets both minimum and maximum limit of alloy contents, indicating a narrow choice of alloying. Although there are some discrepancies in the alloying requirements between various standards, they essentially follow the same goal towards final mechanical properties with a minimum yield strength of 690 MPa. The principle of obtaining such a strength is based on allowing all the elements to enhance the strengthening during quenching and tempering processes.

Table 2.4: Chemical composition of the same strength steel according to different standards in wt.-% [3, 25, 26, 32]

Standard	EN 10025-6:2004	ASTM A514	ISO 630-4:2012	CSA G40.21
Element	S690QL	Grade B	S690	100QT
C	≤ 0.20	$0.12 \leq C \leq 0.21$	≤ 0.20	≤ 0.20
Mn	≤ 1.70	$0.70 \leq Mn \leq 1.00$	≤ 1.70	≤ 1.50
P	≤ 0.020	≤ 0.035	≤ 0.02	≤ 0.03
S	≤ 0.010	≤ 0.008	≤ 0.01	≤ 0.04
Si	≤ 0.80	$0.20 \leq Si \leq 0.35$	≤ 0.80	$0.15 \leq Si \leq 0.40$
Cr	≤ 1.50	$0.40 \leq Cr \leq 0.65$	≤ 1.5	-
Mo	≤ 0.70	$0.15 \leq Mo \leq 0.25$	≤ 0.7	-
V	≤ 0.12	$0.03 \leq V \leq 0.08$	≤ 0.12	-
Ti	≤ 0.05	$0.01 \leq Ti \leq 0.08$	≤ 0.05	-
B	≤ 0.0050	$0.0005 \leq B \leq 0.005$	≤ 0.005	$0.0005 \leq B \leq 0.005$
EN 10025-6:2004 / ISO 630-4:2012: Ni ≤ 2.0 , Nb ≤ 0.06 , Zr ≤ 0.15 , N ≤ 0.015 , Cu ≤ 0.50 , Al ≥ 0.015				

The information provided in the Table 2.4 is the most critical for steel manufacturers. The content and regulations in the standards are frequently subject to public consultation. Indeed, it is understandable to use a conservative upper limit on alloy content. Even in individual steel section, the composition

may vary with the thickness range and this can not be avoided especially in thick-plates. To reach the standard requirements, steel producers can achieve this easily by adapting advanced fabrication procedures and in the meanwhile keep the actual value of alloying much lower. Another important aspect to determine the final alloy design is the customer demands and economical profits from the steel product. Steel manufacturers can introduce different facilities or slight chemical variations to improve one specific property that the customers ask for [28]. A precondition is that all changes will not bring out additional costs on the benefits of steel industries. Therefore, to develop new grade high-strength steels, steel manufacturers have to deal with various processing routes in conjunction with chemistry variation. In the following, some examples are examined.

An example from the company Europipe shows that the development of X100 grades can represent the different production approaches of the same grade steel [33]. As shown in Fig. 2.7, three different approaches are generally possible with respect to different chemical compositions and cooling conditions. Table 2.5 and 2.6 list the chemical composition and mechanical properties for each approach.

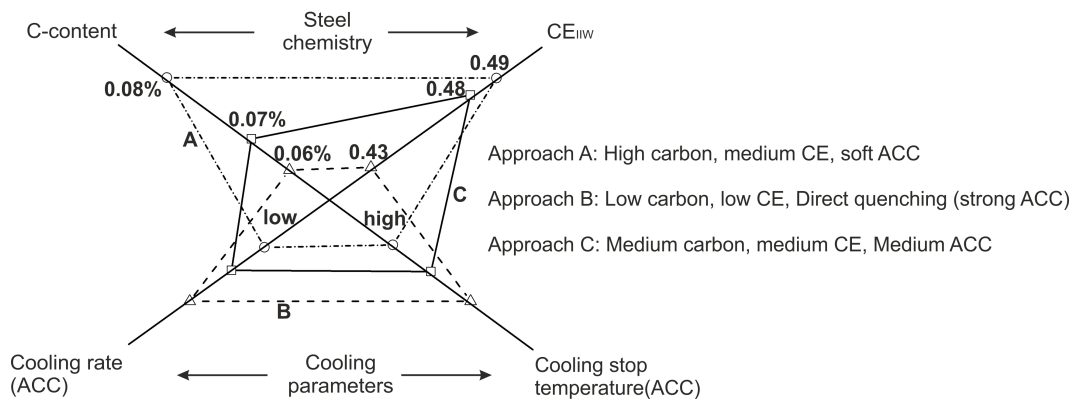


Fig. 2.7: Different approaches to achieve X100 by varying steel composition and cooling parameters [33]

Table 2.5: Chemical composition of X100 steels produced by different approaches [33]

Approach	C	Mn	Si	Mo	Ni	Cu	Nb	Ti	N	CE _{IIW}	P _{cm}
A	0.08	1.95	0.26	0.26	0.23	0.22	0.05	0.018	0.003	0.49	0.22
B	0.07	1.89	0.28	0.15	0.16	...	0.05	0.015	0.004	0.43	0.19
C	0.07	1.90	0.30	0.17	0.33	0.20	0.05	0.018	0.005	0.45	0.20
	0.06	1.90	0.35	0.28	0.25	...	0.05	0.018	0.004	0.45	0.19

Table 2.6: Mechanical properties of X100 steels produced by different approaches [33]

Approach	R _{p0.2} , MPa	R _m , MPa	Yield to tensile ratio	Elongation, %	CVN energy, J(20°C)
A	739	792	0.93	18.4	235
B	755	820	0.92	17.1	240
C	737	800	0.92	18	200
	752	816	0.92	18	270

Approach A involves comparatively high carbon and carbon equivalent (CE). This approach has the risk of crack and poor weldability. Approach B has low CE value and applies fast cooling rate in conjunction with low cooling stop temperatures to achieve martensite structure. In this approach, severe softening problem occurs in heat affected zone. Approach C, which uses optimised cooling conditions and medium carbon content, ensures excellent toughness as well as fully satisfactory weldability despite of not low CE value. Meanwhile, approach C becomes the mostly applied production procedure. The

comparison of these approaches shows that the range of properties achieved within a particular grade X100 can also vary significantly with process routes, particularly in the aspect of the weldability.

Similar case with respect to chemistry and processing variation can be found in high-strength steels from grade 355, 450 and 690, as shown in Table 2.7 [4]. All the alloying designs of different steel grades are considered acceptable for the purpose of reaching standards, because all steels have to satisfy the grade requirements primarily with regard to the minimum yield strength. It should be noted that the four 690 steels exhibit probably with varied weldability due to different CE values.

Table 2.7: Comparison of alloy designs on different steel grade 350, 450 and 690 (in wt.-%) [4]

Grade	C	Mn	Si	Ni	Cr	Mo	Cu	Al	V	R _{p0.2} MPa	CVN energy J	CE
355	0.20	1.35	0.30	-	-	-	-	0.02	-	360	70	0.43
450	0.11	1.49	0.30	0.52	0.11	-	-	0.03	-	480	300	0.40
690	0.15	0.90	0.33	1.28	0.49	0.45	0.2	0.073	0.03	700	74*	0.59
690a	0.14	1.20	0.29	0.04	0.31	0.21	0.04	0.100	-	-	139	0.45
690b	0.15	1.29	0.40	0.02	0.32	-	0.03	0.035	-	711	148	0.43
690c	0.14	1.15	0.31	0.06	0.30	0.17	0.01	0.038	0.01	760	177	0.43

Note: 690a contains Nb 0.03; 690b contains Ti 0.02; 690c contains Ti 0.011
* is at -60°C and the rest are at -40°C

When facing so many choices within a specified steel grades on the market, like the case of grade 690 steel (Table 2.7), the steel users and welding engineers cannot be aware of changes in composition or weldability between steels provided by different manufacturers. If such variations were realised by users, this would imply that some cautions should be exercised when considering the degree of weld overmatching or undermatching that occurs in final welded structure [28]. Hence, even if the standard includes the delivery condition of the steel, the subsequent welding operation (in the aspect of welding parameters and filler metal selection) has to be defined by the individual situation including the chemistry, process routes and final properties, in order to ensure a reliable welded structure.

Nowadays thanks to the current production facilities, metallurgist can combine their good knowledge of the underlying metallurgical interrelationships with adjustment of manufacturing procedures. This makes the increase in strength less of a challenge, since steel manufacturers have various solutions for the increased strength such as specific alloy designs. However, the real difficulty appears with respect to preservation of toughness and ductility accompanied with excellent weldability. This is always a key aspect to determine the final application of steels.

An explanation of the different alloy designs is the potential economic benefits during steel production. The steel alloy design is tailored to a particular application and is often considered on several economic reasons, which includes inter-balanced manufacturing cost, lifetime cost, maintenance cost, safety factor and initial raw materials cost. As mentioned previously, if the higher strength steels are applied, the subsequent manufacturing costs can be greatly reduced as well (Fig. 2.2), and finally a welded structure with long lifetime and high quality is generated. When speaking about raw materials, they generally consist of iron ore, coal, coke, steel scrap and various alloying elements. The raw materials cost is often determined by the global consumption, resources, the usage of up-to-date technologies and recycling. Nevertheless, over the past decade the significant acceleration in steel production growth has led to an increasing demand for raw materials. Fig. 2.8 shows the development of global crude

steel production since 1980. A significant increase in global crude steel started since 2000 and in 2014 the global value has reached up to 1.6 billion tones [34]. Note that there was an abrupt drop between 2008 and 2009. This is because at this time the global economic crisis has influenced the world steel industry and steel demand was reduced dramatically.

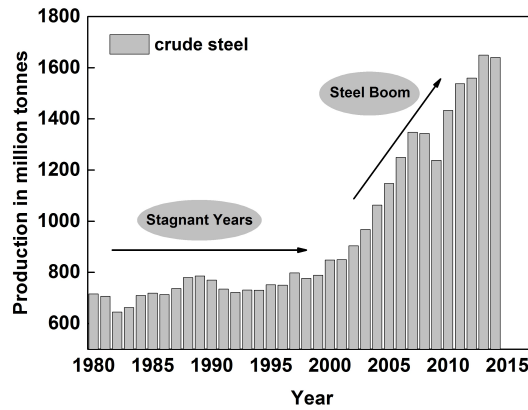


Fig. 2.8: Worldwide crude steel production (Data source: World Steel Association [34])

Indeed, the overall trend of recent steel production exhibits a sharp acceleration. As a consequence, the raw materials suppliers have to respond to the growth in demand by extensive mining, causing unexpected market imbalances and fluctuating materials prices. Two main materials used in steel production are iron ore and coking coal, which account for around 60 % of the costs in the hot-rolled coil steel industry [35]. Considering the price of iron ore, elevated price level reached the peak in 2011 due to the large steel market demand. An oversupply of iron ore in the market is happening in the recent years, causing a sharp price fall. On the other hand, other alloying elements that play major role in determining the properties of steel products also experience strongly fluctuated price evolution.

Apart from Mn and Si as the most often added elements in steels, Ni, Cr and Zn are also added to improve the corrosion resistance. Furthermore, microalloy elements (Nb, Ti, V, and B) are required to reach very high strength. Addition of alloying elements depends on their contribution to properties, as previously discussed (Fig. 2.5). Also, the cost of alloying elements has to be considered, which is based primarily on their abundance and cost of extraction, processing and purification [36]. Then, the relative cost and proportion of alloying elements influence the alloy design and overall cost of steel products. Fig. 2.9 shows the approximate cost of major alloying elements relative to iron [36].

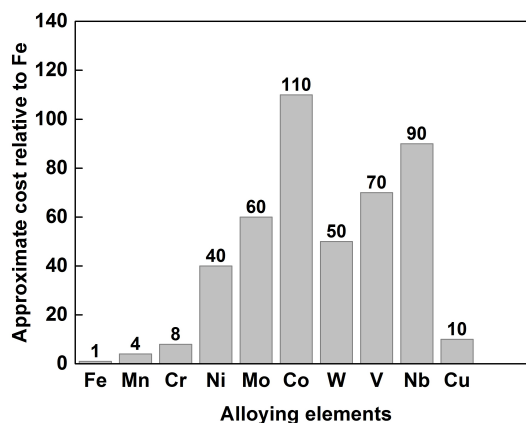


Fig. 2.9: Approximate cost of major alloying elements relative to iron [36]

Most of the alloying elements are much more expensive compared with the price of iron, as shown in Fig. 2.9. This is one reason for a limited amount of alloy addition in steel, with regard to economic grounds and expected properties. A noteworthy fact is the modern trend towards the use of microalloy elements that are associated with a reduced cost and the need of improved mechanical properties [37]. The historical price evolution of some alloys over the last years is shown in Fig. 2.10 [38]. It is evident that during the economic crisis the price of most alloying elements went through a strong fluctuation, where Mo, Ni, V and Cr experienced a significant decrease in the early of 2009. Correspondingly, the volatility of the price of alloy additions has led to different approaches to steel design.

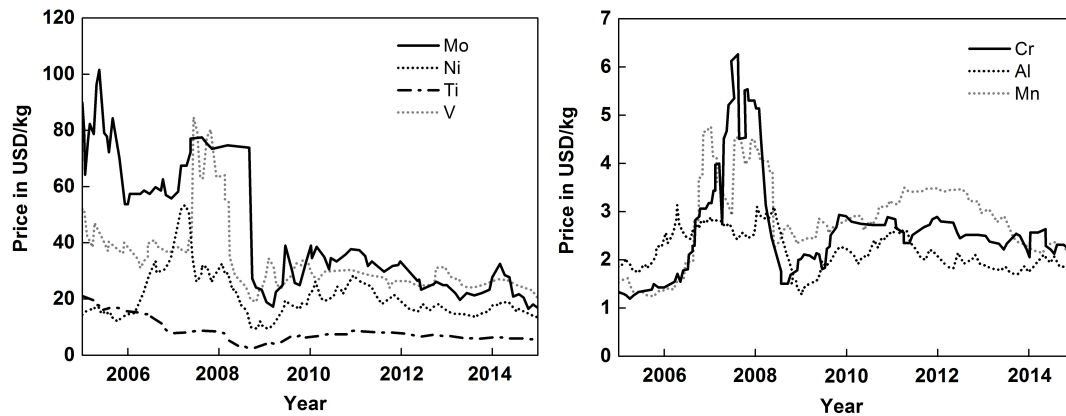


Fig. 2.10: Price of alloying elements since 2005 (Data source: InfoMine.com) [38]

Even though there is certain flexibility in alloy design, the principal goal is to apply the most cost-effective choice for individual steel producer. Additionally, such a design also depends on other factors such as market demands, available production line, and anticipated service qualities. Therefore, the price variation directly impacts the steel alloying design. In fact, in the same grade steels made by different producers, the content of alloy and microalloy elements can vary within a certain range but the steels have to ensure mechanical properties reaching required values by standards (Table 2.7). Furthermore, the impact of alloy cost factor is important for assessing the varied weldability in the application of steels with the same strength grades.

Considering quenched and tempered high-strength steels, S690QL grade is designed for the use as a structural components. Welding strategy is essential and should be developed in a way produces reliable welds with minimal and predictable changes in the mechanical properties. So far limited literature has shown whether the varied alloy design, particularly in microalloy elements, results in great discrepancy of welded properties after modern welding procedures. Therefore, this work is focused on three microalloyed S690QL steels and evaluates their discrepancy on weld microstructure and properties as a result of advanced modified spray arc welding.

2.1.4 Carbon equivalent with respect to weldability

Most of the high-strength steel applications involve welding fabrication. Welded joints in service are required to have mechanical properties with a purpose of matching those of the base materials. For this matter, steel weldability is employed to indicate the ease with which sound weldments can be obtained using normal welding procedures. Good weldability indicates that a steel can be more preferably welded without weld defects but with satisfactory mechanical properties and reliable service condition. To evaluate whether a steel is suitable for welding or not, one has to consider several aspects regarding the steel itself, filler metal, welding method used and the properties of the weldments [39]. The first

concern focuses on the given steel in terms of hardenability and risk of cracking. One of the most acceptable method to assess the cold cracking susceptibility is to correlate the hardness in the HAZ with the carbon equivalent (CE). The original hardenability equation suggested by Dearden and O'Neill around 1940 [40] and was further modified by International Institute of welding (IIW). The CE_{IIW} has been commonly used as a weldability index (equation 2.3), where the relative influence of the important elements on hardness is weighted against the influence of carbon (in wt.-%):

$$CE = CE_{IIW} = C + \frac{Mn}{6} + \frac{Cr + Mo + V}{5} + \frac{Ni + Cu}{15} \quad (2.3)$$

It can be easily concluded from this formula that as the carbon content decreases, the carbon equivalent decreases and the steel presents excellent weldability due to less susceptibility to cold cracking. This formula can be quite useful for predicting the hardenability in C-Mn steels. A maximum hardness of 350 HV10 is suggested in the HAZ, according to the observation from Dearden and O'Neil. Another well-known carbon equivalent is the Ito and Bessyo parameter cracking measurement P_{cm} formula (equation 2.4), applicable for high-strength pearlite reduced steels produced by thermo-mechanically controlled rolled process [41].

$$P_{cm} = C + \frac{Si}{30} + \frac{Mn + Cu + Cr}{20} + \frac{Ni}{60} + \frac{Mo}{15} + \frac{V}{10} + 5B \quad (2.4)$$

Another important carbon equivalent formula CET (equation 2.5) deals with quenched and tempered steels and is specified in the EN recommendations for welding of metallic materials – part 2 arc welding of ferritic steels.

$$CET = C + \frac{Mn + Mo}{10} + \frac{Cr + Cu}{20} + \frac{Ni}{40} \quad (2.5)$$

This formula is valid for steels having carbon content in the range of 0.05 wt.-% to 0.32 wt.-%, and it specifies the maximum limits for all the major and microalloy elements. Table 2.8 shows the comparison between alloying contents range of different CE formulae, according to CEN ISO/TR 17844 [42].

Table 2.8: Specified alloy contents ranges applied to different carbon equivalents [42]

Element \ Formula	CE _{IIW}	CET	P _{cm}
	0.30 ≤ CE ≤ 0.70	0.20 ≤ CE ≤ 0.50	-
C	0.05 ≤ C ≤ 0.25	0.05 ≤ C ≤ 0.30	NS
Si	≤ 0.8	≤ 0.8	NS
Mn	≤ 1.7	0.5 ≤ C ≤ 1.9	NS
Cr	≤ 0.9	≤ 1.5	NS
Cu	≤ 1.0	≤ 0.7	NS
Ni	≤ 2.5	≤ 2.5	NS
Mo	≤ 0.75	≤ 0.75	NS
V	≤ 0.20	≤ 0.18	NS
Nb	NS	≤ 0.06	NS
B	NA	≤ 0.005	NS

NS = Not specified , NA = Not applicable

Many other formulae others were developed by researchers with different boundary conditions, such as carbon contents, welding condition and steel production process [43]. Table 2.9 shows some of these formulas, which differ from each other by the weightage given to different alloying elements.

Table 2.9: Carbon equivalents calculation from different researchers

Group	Formula (values in wt.-%)	References
A	$CE_{IIW} = C + \frac{Mn}{6} + \frac{Cr+Mo+V}{5} + \frac{Ni+Cu}{15}$	[40]
	$CE_{WES} = C + \frac{Mn}{6} + \frac{Si}{24} + \frac{Ni}{40} + \frac{Cr}{5} + \frac{Mo}{4} + \frac{V}{14}$	[44]
B	$CE = C + \frac{Mn}{10} + \frac{Si}{24} + \frac{Ni+Cu}{40} + \frac{Cr}{5} + \frac{Mo}{4} + \frac{V}{10}$	[45]
	$CET = C + \frac{Mn}{10} + \frac{Cu}{20} + \frac{Ni}{40} + \frac{Cr}{20} + \frac{Mo}{10}$	[46]
C	$P_{cm} = C + \frac{Mn}{20} + \frac{Si}{30} + \frac{Cu}{20} + \frac{Ni}{60} + \frac{Cr}{20} + \frac{Mo}{15} + \frac{V}{10} + 5B$	[41]
	$CE_{Düren} = C + \frac{Mn}{16} + \frac{Si}{25} + \frac{Cu}{16} + \frac{Ni}{60} + \frac{Cr}{20} + \frac{Mo}{40} + \frac{V}{15}$	[47]
	$CE_{Graville} = C + \frac{Mn}{16} + \frac{Si}{50} + \frac{Ni}{23} + \frac{Cr}{7} + \frac{Mo}{5} + \frac{Nb}{9}$	[48]
D	$CEN = C + A(C) \times \left\{ \frac{Si}{24} + \frac{Mn}{6} + \frac{Cu}{15} + \frac{Ni}{20} + \frac{Cr+Mo+Nb+V}{5} + 5B \right\}$ $A(C) = 0.75 + 0.25 \times \tanh [20(C - 0.12)]$	[49]
Group A: medium-carbon (> 0.16) steel, not for low-alloy steel Group B: medium- to low-carbon or low-alloy steels, stronger effect of carbon than Group A Group C: low-carbon and low-alloy steels including HSLA steels Group D: range of carbon and alloy content, special factor for carbon		

It should be noted that most of the above equations can be applied with limited validity in terms of chemical composition and welding process. However, one common point revealed by these equations is that the most effective way to enhance steel weldability is to reduce the carbon volume because the corresponding low carbon equivalent is in general beneficial. As discussed previously, carbon has a great strengthening effect and then a decreased carbon content could result in reduced strength. Such a loss of strength can be compensated by increasing the alloying elements concentrations. Finally, a low CE level for a high-strength steel can be reached, mainly by appropriate alloying design combined by improved thermomechanical production process.

The purpose of using CE formula is to restrict the steel chemistry and to gain excellent weldability. Low CE values (< 0.4) are suggested to ensure that the HAZ hardness being limited to 350 HV (accepted as critical value for avoiding cold cracking). Nevertheless, recent studies on modern steels indicated that there is still a risk of cracking even with a lower HAZ hardness level and low CE value. Hart and Harrison [50] studied the effect of five elements (C, Mn, Ni, Mo and V) in C-Mn steels on the risk of HAZ hydrogen cracking and hardenability. In this study, the newly established equations related cooling time to the critical hardness as a function of composition. The critical hardness values were found to decrease with reduced C content and vary in the range of 250 HV – 450 HV. Similar results shown in other studies also indicated that hardness limitation to the conventional 350 HV as a maximum value might not be applicable to all low CE steels with respect to prevent cracking. In addition, there is an agreement that a maximum hardness is not an adequate index to evaluate the risk of cracking. In this case, the microstructure susceptibility to cold cracking should also be considered [51, 52].

In view of above, the use of CE formula can reveal the contributions from some alloying elements (Mn, Mo, Ni and Cr) to steel weldability. However, there is still one difficulty involved prediction of weldability and metallurgical response when elements such as B, Nb, and Ti are contained in modern steels [6, 7]. Additionally, other factors have to be considered in modern steels' weldability, such as austenite grain size and austenisation temperature. These factors are seldom compared to the dominant effect of the whole chemistry in conventional steels. The idea of grain size control in modern steel production is achieved mostly by addition of microalloy elements and the use of TMCP process [7]. These two methods intend to decrease the steel hardenability for a given chemical composition. However, such kind of effects aren't taken into account in most CE formulae. Yurioka [49] attempted to consider the

contribution of Nb to steel weldability, but the solutions to a broad class of steels still have not been found with high degree of confidence in the CE formulae. Based on the CE formulae from Yurioka, an overestimation on hardness might be resulted by the addition of Ti to the steel [49, 53]. Except the absent consideration of microalloy elements, utilising the conventional CE formulae can bring to a disagreement or overestimation of the real weldability. The CE formulae are based on experiments and developed over time, therefore, they are based on steels with different residual elements levels. With respect to modern high-strength steels, the impurities were significantly reduced over time (Table 2.10 [54]). Thus, the concept of CE formulae to assess the hardenability and weldability for modern steels seems to be quite limited. However, there is a continuous need for qualifying weld procedure when taking into account the development of new steels and welding techniques.

Table 2.10: Impact of development of metallurgical processes on the levels of impurities in steel [54]

Element, ppm	Metallurgical processes in the years		
	1950/1960	1980/1990	1990/2010 ^b
Sulphur	100 – 300	50 – 80	60
Phosphorus	150 – 300	80 – 140	6
Hydrogen	4 – 6	3 – 5	-
Nitrogen	80 – 150	< 60	-
Oxygen	60 – 80	< 12 ^a	-
Note: ^a a technology made it possible to obtain the oxygen content at the amount < 12 ppm; however in practice, the oxygen content in steels was higher.			
^b the manufacturers do not indicate the content of hydrogen, nitrogen and oxygen.			

When using the existing carbon equivalent relationship to characterise the weldability, it is unlikely to obtain all the information about HAZ properties. Since the carbon equivalent for evaluating the weldability can not always provide reliable information about mechanical properties of the HAZ (neither the hardness nor the toughness), specific tests have to be conducted in each steel in order to determine its properties. This is essential for modern high-strength steels having addition of microalloy elements (Nb, Ti, V). These compositional factors are not considered in the carbon equivalent index but they play a significant role in the metallurgical aspects and toughness property of the HAZ. Consequently, additional work has to be carried out in order to understand the influence of microalloy elements on the HAZ properties.

The steel customers might not recognise the slight differences in alloy designs of modern high-strength steels in the market, particularly the microalloy concentration. Considering steels with different microalloy elements, it is understandable that the first step is to try to link weldability to carbon equivalent. This approach can demonstrate the weldability in some cases. In this case, varied weldability can be resulted from even small difference in microalloy. Hence, to understand the weldability of a given modern steel, attention should be given to the compositional factors, in particular the microalloy elements. Moreover, further research on the effect of microalloy elements on weldability is needed in order to provide useful guidelines for modern steel weldments to utilise their benefits in service.

2.2 Modern GMAW processes

Gas metal arc welding (GMAW) is one of the most often applied welding processes in practice. This is due to its attractive advantages, such as adjustable penetration profiles, smooth bead, low spatter, and high productivity [55]. During welding process, there is an electric arc existing between the electrode and work piece, which melts filler metal into molten pool. In order to protect the melted

weld metal, appropriate shielding gas is often used. This atmosphere consists of an inert or mixed gas. Different welding parameters (such as welding current, wire size, arc length (voltage), power supply characteristics and shielding gas) can contribute to different drop transfer modes [55,56]. One common classification of arc types is given by the American Welding Society (AWS): short arc, globular arc and spray arc. However, recently a further detailed classification has been proposed [56]. Fig. 2.11 demonstrates the main characteristics (current and voltage) of different transfer modes [55,57]. In short arc (also named as short circuiting mode), metal transfer happens when an electrical short circuit is established, when the molten metal at the end of electrode contacts the molten weld pool. Globular transfer indicates the presence of large metal drops. These drops move toward the weld pool by gravity. In spray arc process, relatively small droplets are detached at a high-frequency from the electrode and projected by electromagnetic forces towards the weld pool. Spray arc is characterised by a non-short-circuiting and spray-like material transfer.

Short arc welding operates at low welding voltage and low current, which is particularly used for out-of-position and root passes welding due to its low heat inputs. The disadvantages of short arc welding are excessive spatter and low deposition rates. As the welding current and voltage are increased above the maximum value recommended for short arc welding, the metal transfer will begin to appear in a globular shape with a diameter larger than the wire. By further increasing the welding current and voltage, the type of arc changes to a projected spray arc transfer. This spray arc can yield high deposition rates of weld metal with very little spatter, good fusion and no clean-up. Almost all materials can be welded using this mode, although it is limited to flat and horizontal welding positions.

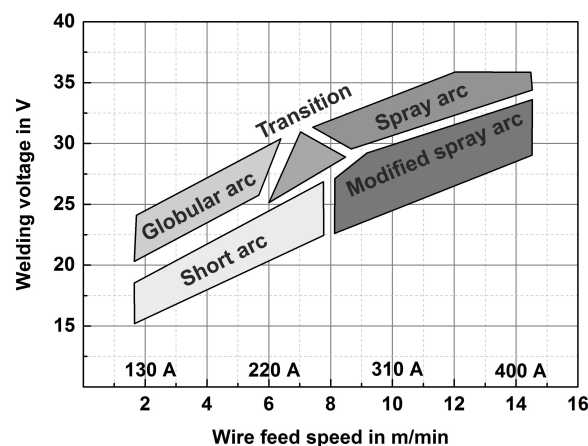


Fig. 2.11: Arc types and main properties [55,57]

Despite the advantages of conventional spray arc, odd arc stabilities and disordered metal transfer restrict its application. The development of shortening arc (a reduction in voltage) is expected. But due to the technical problems it was proved impossible to obtain arc reduction before as longer-lasting short-circuits and increased spatter formation happened in the process. Fortunately, due to inverter technology with highly dynamic actual value regulation, the "forced" arc with lower voltage was achieved. In addition, this rapid regulation control process also made it possible to weld joints with restricted openings and fillets [58,59]. In comparison to the standard spray arc welding, the modified spray arc benefits the advantages of deeper penetration due to high plasma pressure arc, easier handling in manual welding (with directional stable arc) and no undercuts owing to the very short arc. Moreover, the high welding speed and low welding voltage (welding parameters are presented in Table 2.11 [58]) contribute to increasing efficiency, excellent seam quality with narrow HAZ and few distortion.

Table 2.11: Comparison of welding parameters between modified and standard spray arc welding [58]

Modified spray arc welding		Standard spray arc welding
12.5	Wire feeding speed, m/min	12.5
320	Welding current, A	285
29.8	Welding voltage, V	31.5
Shielding gas in both cases: mixed gas (Argon with 10% CO ₂)		

Base on the above characteristics, the users benefit from applying modified spray arc welding by reducing considerable preparation work and overall weld costs. Fig. 2.12 shows an example of welding plates with 20 mm thickness and 1000 mm length by standard and modified spray arc process. For standard spray arc welding, the joint geometry is designed with 60° groove and there is a needs of 8 layers welding. In comparison, by modified spray arc welding, the groove angle is reduced to 40° and the corresponding welding needs only 5 layers. Consequently, applying modified spray arc welding can contribute to a cost saving of 37% in filler wire consumption, 56% in gas consumption and 56% in total saving. Therefore, based on the above mentioned advantages, modified spray arc welding becomes one of the most attractive advanced welding technologies [58].

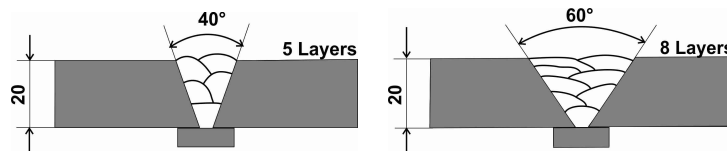


Fig. 2.12: Comparison of joint design for modified (left) and standard (right) spray arc welding [58]

2.3 Weld metallurgy

In general upon the welding process, not only fresh solidified weld metal is deposited between the connected parts but also the heat affected zone (HAZ) is altered by different local thermal cycles. In the HAZ, several regions can be further classified according to the peak temperature, T_p . A single pass weld can be divided into seven different regions. Each region is characterised by specific microstructure and properties [2, 51]. Fig. 2.13 shows the influence of welding process on the weld metallurgy in comparison to the equilibrium Fe – C phase diagram.

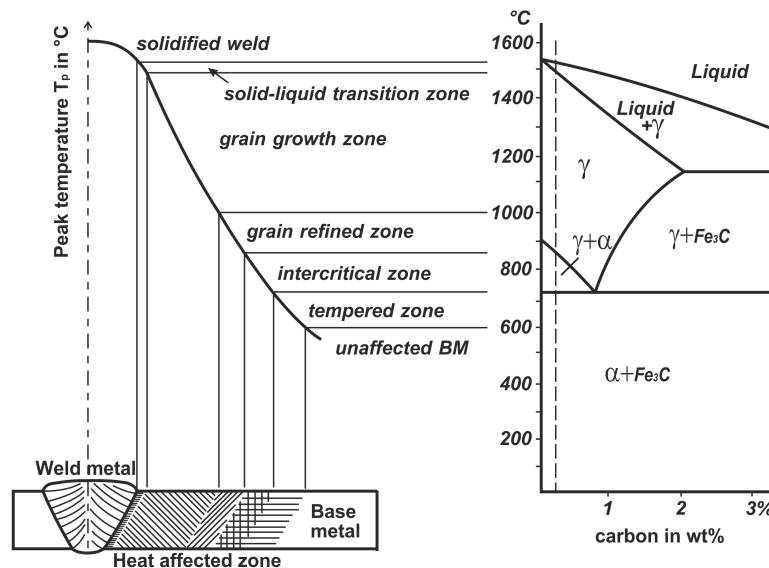


Fig. 2.13: Schematic of the sub-zone in the HAZ and relation to the equilibrium Fe – C phase diagram [51]

1. Solidified weld

This region is a mixture of the deposited weld metal and melted base materials. The dilution ratio from base materials strongly depends on the applied welding process. The final structure in the weld metal (WM) consists of long thin austenite grains, nucleated from the grains from parent steels and newly formed transformation products, among which acicular ferrite is always the most desirable one. The reason is discussed in the following.

2. The solid/liquid transition zone

This is a very narrow layer that is subjected to a very high temperature close to the melting temperature of parent steel. The fusion boundary or fusion line in some cases is located in this region.

3. Coarse grained heat affected zone (CGHAZ)

This region is adjacent to the fusion boundary and suffers from thermal cycle with high T_p (greater than 1200°C). This significantly exceeds the A_{c3} temperature (A_{c3} is the temperature at which austenite formation is completed upon heating). Hence, the steel at such elevated temperature is totally austenitic and can experience fast grain growth due to dissolution of stable carbides and nitrides. The resulted coarse grain structure is known as the coarse grained austenite zone. The final microstructure in this region is determined by many factors (e.g. austenite grain size, cooling rate and steel hardenability or CE values). This region generally transforms into a ferritic structure for lower CE steels. low-temperature transformation products such as martensite or bainite can be obtained with higher CE steels. Since coarsened austenite grains and brittle structure probably occurs, this region is likely to be the weakest zone of the welded joint, especially with respect to toughness. The present study focuses on this important topic of the HAZ properties.

4. Fine grained heat affected zone (FGHAZ)

As T_p only minimally exceeds the A_{c3} temperature, no significant austenite grain coarsening occurs in this region. Therefore, it is called as the fine grained HAZ. Moreover, the carbide and nitride may not be completely dissolved during thermal cycle. During cooling, the refined austenite transforms into fine grained ferrite and this generally brings to improved properties.

5. Intercritical heat affected zone

The intercritical HAZ region is defined by T_p range between the A_{c1} (A_{c1} is the onset temperature of austenitisation) and A_{c3} temperature, resulting in partial austenitisation on heating. During transformation, if austenite has a relatively higher concentration of C, Mn or other alloying elements than their concentration in the base material, it can further transform to ferrite, bainite or high carbon martensite and this depends on the cooling rate. The part that does not transform into austenite becomes tempered during thermal cycle.

6. Subcritical heat affected zone

The subcritical HAZ region, occurs furthest from the fusion line in the weld. In this case, T_p is well below the A_{c1} temperature but greater than 600°C . No austenitisation occurs, but at this temperature carbon diffusion is easier and partial coarsening of carbides may occur. This is also called as tempered zone [51].

7. Unaffected parent material

When T_p is less than 600°C , the heat affected zone ends and the material maintains its original state

without any changes in the microstructure [51].

To summarise, the resultant microstructure at each region is not only governed by the T_p (as defined in different regions) but also controlled by the heating rate, cooling rate, dwell time and the final post-weld heat treatment. The microstructure in general contains austenite grain growth behaviour, phase transformation and tempering behaviour. When welding microalloyed steels, it is of a great importance to control the austenite grain growth. By controlling the grain growth, the further phase transformation behaviour and the final mechanical properties can be monitored. The austenite grain growth is strongly influenced by the pinning effect from microalloy precipitates. However, subjected to the weld thermal cycle, precipitates tend to dissolve, coarsen or re-precipitate, changing their capability to restrict grain growth. The detailed discussions on grain growth and phase transformation is done in the subsequent sections.

2.3.1 Background on weld microstructure

Acicular ferrite

The first research that described the improved toughness properties from acicular ferrite came in the late 1970s with the discovery that TiN precipitates activate the formation of acicular ferrite [60, 61]. Since then, extensive researches have been conducted on the nucleation and growth of acicular ferrite with respect to inclusions, weld chemistry, cooling processes and its influence on weld strength and toughness [62–65]. Fusion welding with remelting and resolidification of steels and filler metal leads to complex physical processes in the weld metal, resulting in microstructure that is different from the base material. Therefore, it is essential to understand and control the physical processes during welding in order to achieve the desirable microstructure in the final weld. A schematic representation of the reaction sequences that occur in low-alloy steel weld metal is shown in Fig. 2.14 [66].

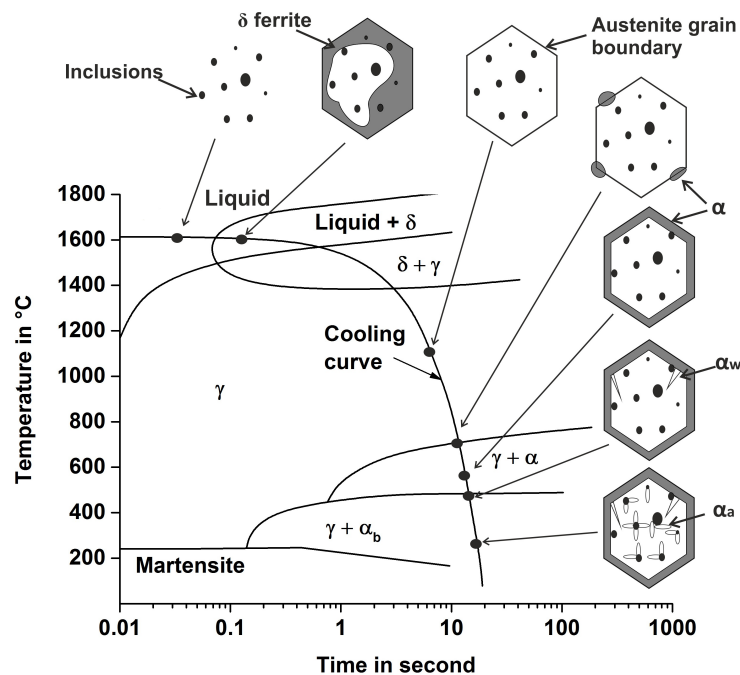


Fig. 2.14: Schematic of the phase transformation sequences that occur in the weld metal during cooling [66]

At temperature greater than 1600°C, the dissolved gases and alloying elements react to form complex oxide or nitride inclusions from liquid weld due to their thermodynamic stability at high temperature.

As the liquid weld metal cools, δ -ferrite (bcc structure) starts to form that further transforms into γ -austenite (fcc structure). Once the temperature is low enough for the formation of bcc phase, austenite begins to decompose. The allotriomorphic ferrite (α) which is the first product forms at prior austenite grain boundaries and eventually covers the overall boundaries. Widmanstaetten ferrite (α_w) is the next phase to nucleate at the α/γ interfaces. This phase grows into the inside of untransformed austenite. As a further drop in temperature, acicular ferrite (α_a) would nucleate on inclusions within the austenite. If there is no potent inclusions, bainitic ferrite (α_b) might substitute acicular ferrite. Further temperature decrease to room temperature can let the remaining austenite transform completely or partially into martensite.

Among the above microstructure, acicular ferrite is mostly desired due to its combination of excellent strength and toughness. In many research works, the topic concerning the competition between acicular ferrite and bainite formation is of particular interest [64, 65]. Indeed, bainite or acicular ferrite can be gained under the same temperature range in the same steel. In addition, the transformation mechanisms of acicular ferrite and bainite are similar. The most significant distinction between these two phases from a metallurgical aspects is that the nucleation of acicular ferrite requires potent inclusions acting as nuclei but bainite nucleates along the grain boundaries. The typical weld microstructure that is containing acicular ferrite and bainite is shown in Fig. 2.15. The characteristics of acicular ferrite morphology is often called as a "basket – weave structure" and this interlocked nature is shown in Fig. 2.15 (b). The formation of acicular ferrite can be activated by sympathetic nucleation on a pre-existing ferrite plate, thus resulting in a chaotic arrangement of ferrite plates that do not grow in sheaves (as the case in bainite) [64]. Such a chaotic structure with the characteristics of high angle misoriented plates can give rise to improved toughness in weld metals [67, 68]. A schematic illustration of a propagation path for a cleavage crack in acicular ferrite in comparison with other microstructure is shown in Fig. 2.16.

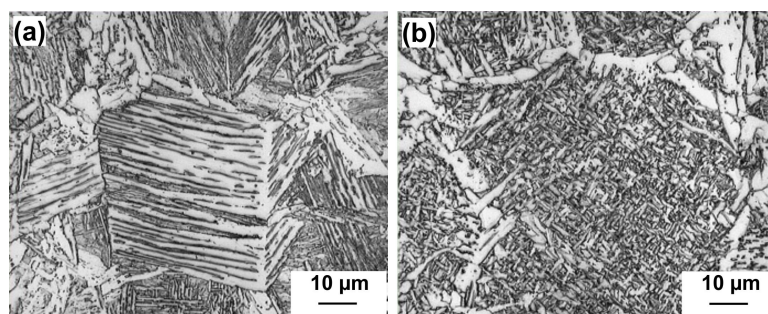


Fig. 2.15: Optical micrograph of samples mainly containing (a) bainitic ferrite and (b) acicular ferrite [66]

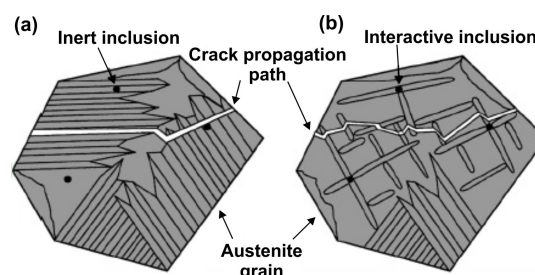


Fig. 2.16: Schematic of different crack propagation paths for (a) ferrite with side plates and (b) acicular ferrite [69]

It demonstrates that parallel ferrite plates (from Widmanstatten ferrite or upper bainite) are easy propagation paths for the crack (Fig. 2.16(a)). This is related to the low angle boundaries between

bainite packets. In contrast, acicular ferrite plates have a high angle boundary which efficiently impedes the crack growth. Such excellent toughness properties are attributed to the nature of acicular ferrite transformation. Hence, acicular ferrite becomes one desired structure in welds due to its excellent properties. The mechanism of acicular ferrite formation is expected to be well understood because it is closely linked to the control of weld microstructure and the design of filler metal. So far, the formation of acicular ferrite is still not fully understood. It has been proposed that the acicular ferrite transformation exhibits with the incomplete reaction phenomenon, an important characteristics of bainite [70]. The transformation stops when the carbon concentration in the residual austenite reaches to a critical value. This suggests that acicular ferrite grows supersaturate with carbon. The excess carbon is shortly afterwards segregated into the surrounding austenite.

Previous studies demonstrated that acicular ferrite exhibits with either the Nishiyama – Wasserman (NW) or Kurdjumov – Sachs (KS) orientation relationship with the parent austenite [67, 68]. An invariant plane strain with a large shear component exist upon the transformation into acicular ferrite and a surface relief phenomena can be observed [70]. Similar to bainite, the ferrite plates are formed by a displacive transformation mechanism. No substitutional partition occurs but interstitial elements like carbon partition can occur during transformation [71]. Due to the similarities to bainite, acicular ferrite is sometimes considered to be intragranularly nucleated bainite [70]. Some authors even call it as intragranularly nucleated Widmanstaetten ferrite but the low angle boundaries of Widmanstaetten ferrite make it significantly distinguishable from the high angle boundaries of acicular ferrite [72]. The Widmanstaetten ferrite also bears some strong similarities to bainite in some cases, leading some researchers to insist that there should not be a distinction between the two phases [73]. In contrast, it is believed that the two shows a similar appearance but with different transformation mechanisms [70, 74].

The key characteristic of acicular ferrite nucleation is the intragranular nucleation on inclusions [75]. Several mechanisms (Fig. 2.17 [65]) have been proposed to interpret the nucleation behaviour promoted by inclusions [69, 72, 76–84]. The first mechanism (Fig. 2.17 (a)) indicates that the inclusions act as inert surfaces leading to a reduction of the activation energy to promote the ferrite nucleation. The second mechanism (Fig. 2.17 (b)) demonstrates that inclusions having a good lattice coherency with the ferrite which therefore assist with the ferrite nucleation. The third one (Fig. 2.17 (c)) suggests that the solute depletion near the inclusions causes a local increase in the driving force for ferrite to nucleate. The fourth mechanism (Fig. 2.17 (d)) considers different thermal expansion coefficients of inclusions and austenite. The thermal strains can develop near the inclusion/austenite interface and further reduce the activation energy for the formation of a ferrite nucleus.

With the availability of the sophisticated imaging and characterisation techniques, the proof for the formation of acicular ferrite was often described [85, 86]. One remarkable study is from Zhang et al. [86] by a laser scanning confocal microscopy to observe in-situ the formation of acicular ferrite. The potent and inactive inclusions with respect to the nucleation centre were quantitatively determined and distinguished. Based on TEM investigations, Lee et al. [81] found that there was no one-to-one correlation between the inclusions and the acicular ferrite with respect to the auto-catalytic nucleation characteristic. The crystallographic misorientation results, obtained by electron backscattered diffraction technique, showed that the high angle boundaries between the ferrite plates, confirming that the formation of secondary ferrite occurs through sympathetic nucleation [67, 68]. Hence, the role of inclusions to stimulate acicular ferrite nucleation is critical for understanding the ferrite formation

mechanisms. More specifically, several characteristics of inclusions should be considered: composition, heterogeneity of the inclusions (surface and bulk composition), size distribution and volume fraction [66].

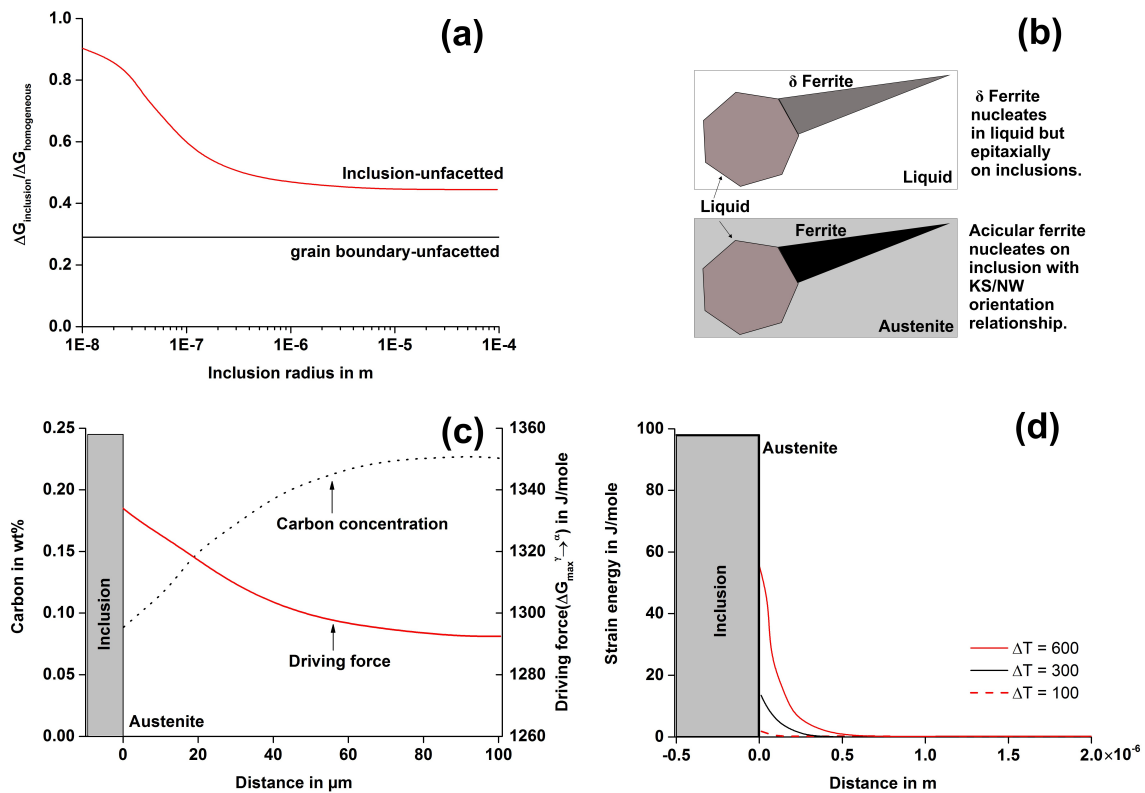


Fig. 2.17: Schematic illustration of different mechanisms for nucleation of acicular ferrite on inclusions [65]

The influence of inclusions on stimulating nucleation process is related to the thermal strains, lattice mismatch and the presence of a Mn-depleted zone near MnS inclusions [77, 87]. Different thermal strains can lead to high or low barrier to ferrite nucleation, as proposed by Grong and others [62, 84]. It is suggested that the mismatch strain between inclusions and ferrite/austenite should be low enough for ferrite to nucleate. For this, the simple crystallographic planes of ferrite and inclusion should be parallel and they have a simple crystallographic orientation relationships. Mills and others [76, 88] calculated the minimum mean planar disregistry between various inclusions and ferrite and the misfit values are shown in Table 2.12.

Table 2.12: Misfit values between different inclusions and ferrite [76, 88]

Inclusions	Crystal structure	Lattice mismatch, %
VN	Cubic	1.3
MnO · Al ₂ O ₃	Cubic	1.8
CuS	Cubic	2.8
TiO	Cubic	3.0
γ -Al ₂ O ₃	Cubic	3.2
TiN	Cubic	3.8
BN	Hexagonal	6.5
MnS	Cubic	8.8
TiO ₂	Tetragonal	8.8
α -Al ₂ O ₃	Hexagonal	16.0
Ti ₂ O ₃	Hexagonal	26.8
Ti ₂ O	Hexagonal	29.3

The phases γ - Al_2O_3 , $\text{MnO} \cdot \text{Al}_2\text{O}_3$, TiO , TiN and VN have been most widely accepted as effective nucleant for acicular ferrite in weld metals [89]. This demonstrates that some inclusions become nucleant due to their low misfit orientation relationship with the ferrite. The phase MnS and BN do not have very good lattice coherency with ferrite and are regarded as ineffective in promoting acicular ferrite. This is also the case with Ti_2O_3 and TiO . The Ti-containing oxides can be particularly good nucleation agents when other de-oxidants or alloying elements (Mn , Si or Cu) are contained in the matrix [76, 82, 83].

When TiO or TiN are present on the surface of inclusions, this can also decrease the free energy barrier for ferrite to nucleate. Apart from TiO/TiN that are commonly observed at the surface layer, the MnS was also frequently found to newly precipitate near titanium oxides. MnS precipitation in general occurs in the solute-enriched interdendritic region of the solidification microstructure. If using a diffusion theory to describe its formation process, a Mn-depleted zone will form in close vicinity of inclusion, where the tendency of ferrite to nucleate will be encouraged. Fig. 2.18, taken from the work of Yamamoto et al. [90], illustrates the mechanism in a structure containing acicular ferrite.

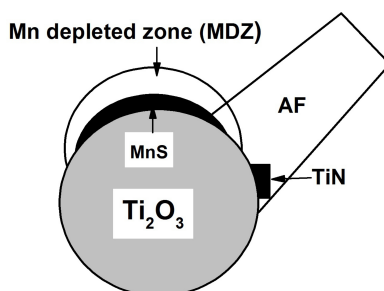


Fig. 2.18: Schematic illustration of a Mn-depletion zone [90]

There are many evidences to suggest that the Mn-depleted zone near a MnS inclusion is related to the nucleation of intragranular ferrite. Mabuchi et al. [91] have directly proved the depletion of Mn at the interface of $\text{MnS}/\text{ferrite}$ matrix. They attributed the Mn depleted zone to the nucleation of ferrite. Another evidence has been given by Byun and others [82, 83], who demonstrated such Mn depletion zone around the interface between Ti_2O_3 and the matrix. In some cases, there was no direct observation of any Mn variation in composition surrounding inclusions [72, 81]. It should be noted that there are cases where instead of Mn, the local depletion of C close to the inclusion/austenite interfaces may also facilitate ferrite nucleation [92]. In general, MnS alone is regarded as ineffective nucleant for acicular ferrite. Nevertheless, if it is combined with $\text{V}(\text{C},\text{N})$ or Ti-rich inclusions developing coherent interfaces with ferrite, acicular ferrite formation can take place [93].

Based on the above evidences and discussion on acicular ferrite nucleation, Babu [65] pointed out that there are still many open questions and controversial points that need further experimental work. He proposed that local depletion of carbon and/or manganese in conjunction with thermal strains appears to be the most plausible mechanisms for displacive nucleation. Additionally, the composition heterogeneity of inclusions in welds should be considered when building up a new model to interpret the nucleation mechanisms.

Nucleation assisted by the presence of inclusions is also experimentally demonstrated to be influenced by inclusion size distribution and volume fraction. One explanation to correlate inclusions size to ferrite nucleation is the inert substrate model suggested by Ricks et al. [72], in which it has been emphasised

that the energy barrier to heterogeneous nucleation at inclusions decreases significantly with an increase in inclusion diameters up to $1\ \mu\text{m}$. This also indicates that a larger inclusion is energetically more preferable nucleation site than a smaller one, as shown in Fig. 2.17 (a). The quantitative analysis from Lee et al. through extensive TEM studies has well proved the classical theory and the agreeable relationship between the probability of ferrite nucleation and inclusion size (Fig. 2.19 [81]). Other authors suggested that the most effective inclusions are in a size range of $0.4\ \mu\text{m} - 0.6\ \mu\text{m}$ over a wide range of cooling times [94].

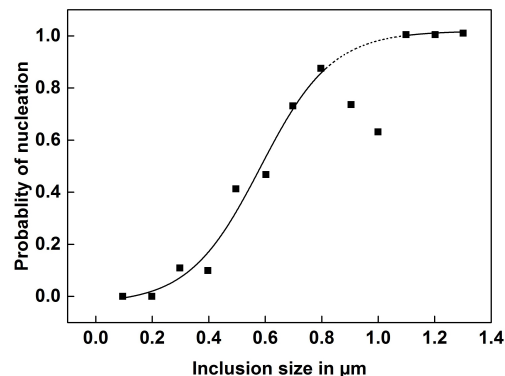


Fig. 2.19: Effect of inclusion size on the probability of ferrite nucleation [81]

Another influencing factor for the amount of acicular ferrite is the number of inclusions. It is stated by Kim et al. [95] that acicular ferrite was in proportion with the number of inclusions with size less than $2\ \mu\text{m}$. It was also observed that the total number of acicular ferrite plates can be one order of magnitude higher than the number of inclusion nucleants but this can be attributed to multiple nucleation of ferrite on inclusions and sympathetic nucleation nature of acicular ferrite [94]. Additionally, in order to ensure that sufficient oxides are formed in weld metal, a balanced concentration of oxygen and oxide formers was suggested [76, 96].

During weld microstructure evolution, several other factors besides inclusions, are recognised to influence the formation of acicular ferrite, which include austenite grain size, cooling rate, and the hardenability. Large austenite grain size with reduced $\gamma - \gamma$ grain boundary area per unit volume favours the formation of acicular ferrite at the expense of bainite since bainite nucleates at the austenite grain boundaries. The cooling rate can be more specifically defined by the $t_{8/5}$ time, under which austenite transforms to ferrite. It is well known that fast cooling rate prefers the formation of low-temperature transformation products such as martensite rather than acicular ferrite [66]. The optimum cooling rate for acicular ferrite formation closely depends on the chemical composition of the weld [97].

With respect to hardenability or solute alloy in welds, Byun et al. has evaluated the contribution of Mn and pointed out that Mn can suppress ferrite nucleation at grain boundaries and encourage acicular ferrite formation even its concentration larger than 2 wt.-% [98]. It is suggested that the segregation of Mn to austenite grain boundaries reduces the driving force for bainite nucleation and at the same time the Si is believed to enhance Mn segregation [99]. Similar segregation phenomena of B at grain boundaries is also assumed to retard bainite nucleation and promote acicular ferrite [100]. Additionally, Bhadeshia [70] has concluded that the steel hardenability is low enough to ensure that the austenite grain surfaces are completely covered by uniform layers of allotriomorphic ferrite, allowing intragranular acicular ferrite formation. Ohkita et al. and Evans [101, 102] summarised the effect of alloying elements on the microstructure evolution, especially on acicular ferrite formation, and on the resultant weld

performances. The individual effect from compositional chemistry is discussed in the following section. Overall, with the aim to gain a desirable microstructure, filler metal has to be selected not only on the basis of matching the physical properties of the base metal but also on considering the effect of the alloying elements on phase transformation.

It is known that bainite is the most competitive phase with acicular ferrite upon austenite transformation process, due to their strong similarities. It is also clear that acicular ferrite is in some cases preferable than bainite. For this purpose, three methods are often applied to switch the microstructure between bainite and acicular ferrite, as schematically demonstrated in Fig. 2.20 [65]. The first way is to control the austenite grain size, where coarse austenite grain with reduced boundary areas will suppress bainite transformation and intragranular nucleation on inclusions dominates (Fig. 2.20 (a)). The second way depends on the formation of thin layer of allotriomorphic ferrite covering the austenite grain boundaries (Fig. 2.20 (b)). The allotriomorphic ferrite/austenite interface cannot develop into bainite because the adjacent austenite is enriched with C and the corresponding bainite start temperature reduces drastically. The third way indicates the incorporation of potent inclusions within the austenite grain (Fig. 2.20 (c)). The presence of effective inclusions acting as nucleant plays a critical role in the possibility of acicular ferrite to form. Without inclusions or with ineffective inclusions within the austenite grains, bainite formation will occur. Recently, researchers [65] have attempted to develop an integrated model to describe the competition between acicular ferrite and bainite reaction but further experimental work is needed to provide reliable data. Acicular ferrite is one desired structure, not only in weld metal but also in the HAZ. In the HAZ, non-metallic inclusions are proved to play an important role in controlling grain growth and microstructure evolution. This is discussed in the subsequent section.

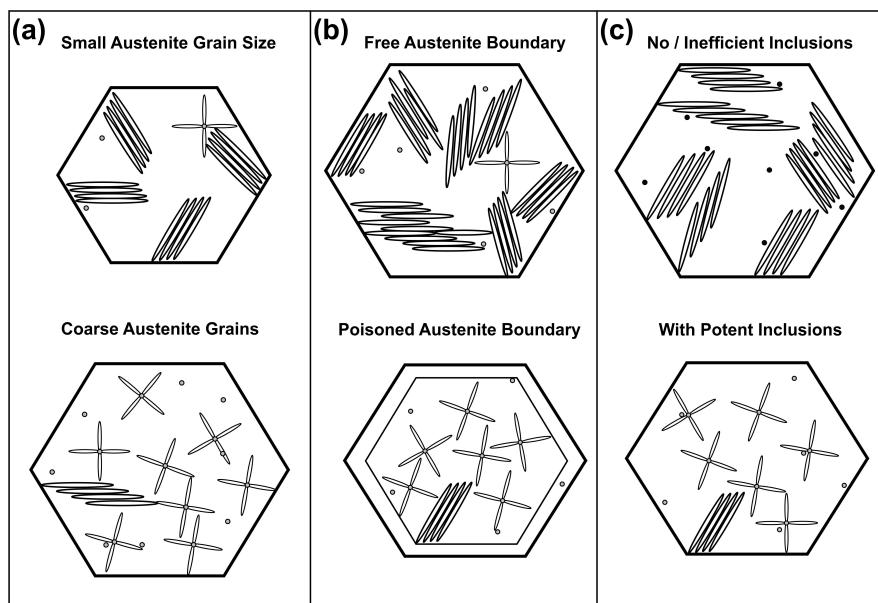


Fig. 2.20: Schematic illustration of different mechanisms by which bainite formation can be suppressed to form AF: (a) austenite grain size, (b) poisoned austenite grain boundary, (c) presence of potent inclusions [65]

Bainite

Bainite is described as one of the most discussed structure. It has drawn great interests of metallurgists and engineers to investigate the mechanism of bainite formation and its application in the development

of new generation steels [103]. It should be highlighted that bainite has been used in order to describe a huge variety of product morphology. This has sometimes blurred the exclusive characteristics of bainite [104]. Over time, the definition of bainite became a major challenge for researchers because the definition is used in order to link the structure to a specific mechanism. There are still controversies on the bainite transformation mechanisms in terms of two opposite theories, diffusionless transformation and diffusion-driven transformation. They are claimed by evidences from researchers [73, 105], however it is still unclear which one is more convincing. In some cases these contradictory observations are present at the same time [106].

The most accepted theory of bainite transformation process is illustrated in Fig. 2.21 [107]. It manifests that bainite has two distinguishable forms: upper bainite and lower bainite. In the beginning, researchers claimed that bainite forms in the similar manner like martensite but with partitioning of interstitial carbon element upon nucleation process [70]. At relatively high temperature, the excess carbon soon enters the surrounding residual austenite and then further precipitates from the supersaturated austenite, forming the inter-plate carbide between ferrite subunits. These are the typical characteristics of upper bainite microstructure. The ferrite subunits can be either plate or lath morphology. If they share matching crystallographic orientation, they are defined as bainitic sheaves. When a fine distribution of carbides form inside the subunit before the carbon evacuation is finished, the lower bainite is obtained.

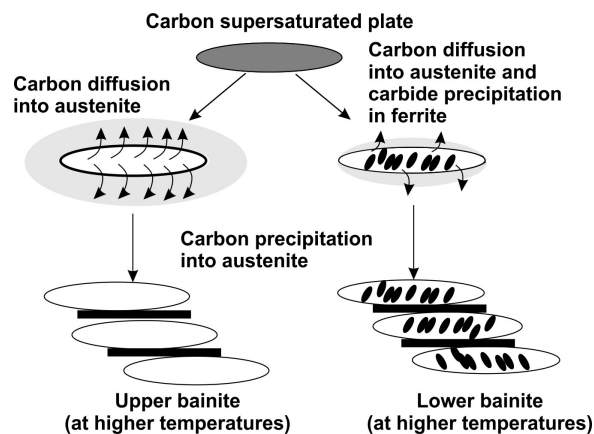


Fig. 2.21: Schematic illustration of the bainite formation in steels [107]

From experimental observation it is revealed that carbides in lower bainite nucleates and grows within supersaturated ferrite in a process identical to the tempering of martensite, with a single crystallographic variant within a given ferrite plate [74]. In Si-rich steels or under very fast cooling process, the precipitation of carbides upon bainite transformation can be suppressed, since Si can strongly retard the precipitation of cementite. The carbon that is rejected from the bainitic ferrite enriches the surrounding austenite, resulting in a complete or partial austenite down to room temperature. The resulted microstructure consists of bainitic ferrite and austenite or M – A constituent [70]. The influence of carbide forming elements (Cr, Mo, W and V) is to slow down the bainite growth since they are believed to anchor carbon atoms.

Evidence that supports displacive theory is provided with respect to surface relief, plastic relaxation and carbon partitioning [108–110]. Some researchers argue that bainite nucleates and grows through a reconstructive mechanism by a crystallographic approach [73]. Based on this theory a precise kinetic model for calculating the overall transformation has been developed [111]. Both the displacive and diffusionless theory of bainite transformation are accepted since they are applied on practical alloy

design by providing quantitative prediction of the amount and chemical composition of the reaction products [112]. One representative example is the design of carbide-free bainite structure and its further contribution to the invention of TRIP-assisted steels, which exhibits excellent properties due to a mixed bainite – austenite – allotriomorphic ferrite microstructure [113].

Zajac [114] pointed out one new classification from the perspective of ferrite morphology and the type and distribution of second phases. He divided bainite into three main groups: a) granular ferrite composed of irregular ferrite with second phase between ferrite grains ; b) upper bainite with lath-like ferrite and second phases on lath boundaries; c) lower bainite with lath-like or plate-like ferrite and carbides within the ferrite (Fig. 2.22). Further degenerated upper bainite is defined when M – A constituent is contained in upper bainite instead of carbides. The degenerated lower bainite is discovered in lower bainitic microstructure in which intra-lath M – A replaces cementite. Here, it should be noted that the visible granular ferrite gives an appearance of coarse plates but these are sheaves of bainitic ferrite with very thin regions of austenite between the subunits [70]. Furthermore, this classification system has its drawbacks. By considering the ferrite morphologies, it is impossible to differentiate the nature of granular ferrite, especially when polygonal ferrite or massive type of ferrite exist in the microstructure.

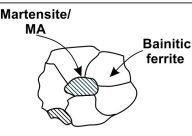
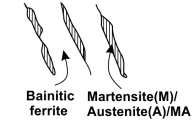
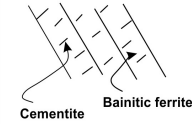
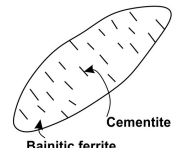
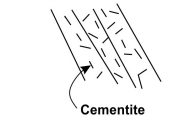
Bainite	Morphology	Bainite description
Granular bainite	Irregular ferrite with M/A.	
Cementite-free lath-like upper bainite	Lath-like ferrite with M/A on lath boundaries.	
Lath-like lower bainite	Lath-like ferrite with cementite inside the ferrite laths	
Plate-like lower bainite	Plate-like ferrite with cementite inside the ferrite plates	
Lath-martensite	Tempered lath martensite	

Fig. 2.22: Bainite classification according to Zajac [114]

As a consequence of different microstructure characteristics (such as bainitic ferrite morphology, carbide distribution and carbide composition), bainite show varied toughness and strength properties. Lower bainite has a higher toughness than upper bainite due to much finer carbides within bainitic ferrite. Large cementite is generally brittle and easily cracks under the influence of the stresses created by dislocation pile-ups. Once the crack occurs in upper bainite, it propagates fast into the ferrite under appropriate conditions of stress and temperature, leading to cleavage fracture. Based on the relationship between carbides and toughness, it is believed that the carbide size controls the fracture behaviour of bainitic steels. In addition, the bainite packet size is demonstrated to be another microstructural factor

that is controlling the cleavage resistance (when laths in a bainite sheaves are nearly with the same orientation, the sheaves are also called as packets as similar to those of lath martensite) [70].

M – A constituent is another significant structure that can influence the toughness and fracture behaviour. Its presence is closely related to the incomplete austenite to bainite phase transformation phenomenon. In general it appears with elongated or massive shape between bainitic laths as well as at the prior austenite grain boundaries in CGHAZ or intercritical CGHAZ. It is stated that carbon and other alloying elements (Nb, V, Al) enhance the formation of M – A constituent. Moreover, the same assistance effect will happen by the segregation of Mn, Ni and solidification and C, N and B during phase transformation [115]. The property of M – A constituent that it causes crack initiation or cleavage fracture was postulated but the mechanism is not fully understood yet. Evidence shows that M – A constituent assists the propagation of cleavage fracture due to the observation that a cleavage fracture favourably propagate along the interface between M – A constituent and matrix [116]. It was reported that toughness decreased monotonically with increasing the amount of M – A island [117]. However, such special structure of martensite and austenite was advantageous to the properties, as reported in [115, 118]. Based on the controversial opinions on the influence of M – A constituent to steel properties, different mechanisms are proposed to understand the role of M – A constituent [116]. It should be noted that the stress concentration between M – A constituent and matrix is believed to be critical and this strongly depends on different steel types. Therefore, several factors such as shape, size or composition of M – A constituent as well as the matrix structure have to be considered when discussing the influence of M – A constituent on toughness [115].

Martensite

If austenite is quenched very fast to low temperature, a displacive transformation occurs with a new phase formation called martensite. Martensite has a body-centred cubic (bcc) or body-centred tetragonal structure (bct). Martensite transformation is believed to take place without diffusion of carbon or other alloying elements. As a result, it is supersaturated with carbon and the carbon concentration is the same as the parent austenite. The substitutional solute elements that are kinetically immobile cannot segregate to form any alloy carbides. The main effect of solute elements is to influence the driving force for martensite transformation that occurs in a similar way to bainite transformation.

Lath martensite forms in low and medium carbon steels. The martensite units consist of small laths that are in parallel groups and have the same crystallographic orientation. These parallel groups can be further referred as block and a group of parallel or nearly parallel laths is termed as packet. It is suggested that the block and packet size are key parameters to influence the strength property of lath martensite in low carbon steels [119].

Martensite can be often obtained in high-strength steel welds with relatively low heat input. It is known that high hardness from martensite is not favourable in some cases since it can make the welded joints susceptible to cold cracking. Thus, in order to prevent cold cracking, preheating treatment is sometimes suggested to slow down the cooling rate or heat input should be well adjusted to avoid too fast cooling. In any case, attentions should be given to the presence and volume fraction of martensite in the HAZ, which is closely related to the welding parameters and also directly influenced by steel chemistry and martensite start temperature M_s .

M_s has been often reported to be related to chemical composition for carbon and low alloy steels. Several thermodynamic and empirical equations have been proposed to reveal such a relationship [120–123]. However, most equations are not sufficiently general due to their limited boundary conditions. Moreover, some can not provide accurate prediction for modern microalloyed steels, where the effect of austenite grain size and microalloy elements must be considered. Recently, austenite grain size is recognised to become one important factor to influence M_s temperature [124, 125]. Lee and Park [125] insisted that austenite grain refinement decreased the M_s temperature but in their work the mechanism of such a role of austenite grain size was not interpreted. Capdevila et al. [124] have looked deeply into the influence of austenite grain size upon martensite transformation and given a clear explanation to the mechanisms. Although the influence of microalloyed elements such as V and Nb were discussed in their work, another important microalloy element Ti was not considered. Hence, there is a clear need for further investigation into the influence of Ti, Nb and V on austenite grain growth and martensite transformation.

When a steel has a microstructure of fully as-quenched martensite, it can display extremely high-strength but have unacceptable residual stresses and poor toughness. In order to improve the toughness and ductility of such a structure, the steel is generally tempered at a high temperature. As a result, high strength as well as excellent toughness can be achieved if temper embrittlement can be avoided. Previous researches indicated that after tempering, mixture of lower bainite and martensite can outperform the individual phases [126]. The mixed structure is tougher than either martensite or bainite, moreover, the strength can exceed that of the martensite alone (Fig. 2.23). With the up-to-date technology, modern quenched and tempered process can generate advanced steels with especially high tensile strength over 1200 MPa, such as S1300QL and S1100QL steels.

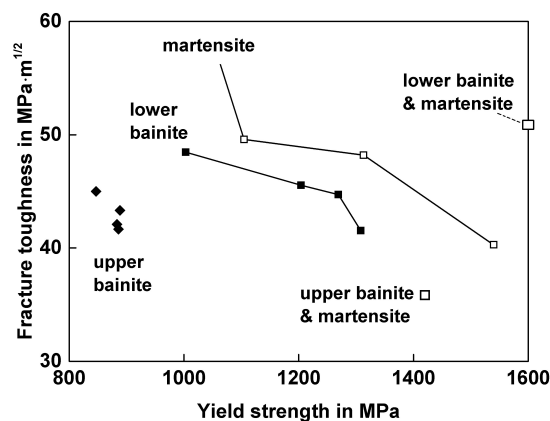


Fig. 2.23: Plot of toughness vs. strength for a variety of microstructure in ultra high-strength steels [70]

Metallurgists have done many works on the understanding and optimising martensite tempering process. It is known that carbon partitioning to surrounding austenite or carbide precipitation from ferrite occur upon bainite formation. As a result, the bainitic microstructure shows less sensitivity to tempering than martensite [2]. Additionally, the decrease in strength on tempering bainite is smaller because unlike martensite there is hardly any carbon in solid solution. In general, the martensite tempering process begins with the rejection of excess carbon to precipitate carbides but no partitioning of substitutional solute takes place [2, 127]. A series of overlapped stages are agreed to explain the tempering process in plain carbon steel [2]: in the first stage (up to 250°C) precipitation of ϵ – carbide starts; in the second stage, between 200°C and 300°C, retained austenite decomposes to form α – ferrite and cementite; and in the last stage, above 200°C the replacement of ϵ – carbide by cementite occurs,

and it further coarsens and spheroidises followed by recovery or recrystallisation of martensite above 600°C. Compared with the plain carbon steel, the alloy steels experience more complex tempering process of martensite. As mentioned previously, Si can retard cementite precipitation since it enters into the ϵ – carbide structure and considerably delay ϵ – carbide further transformation into cementite. Other alloying elements, such as Cr, Mo, and W can also restrain the coarsening of cementite in the range 400°C – 700°C by entering into the cementite structure or by segregating at the carbide – ferrite interface [2].

Another significant effect of alloying elements is the secondary hardening process where the relatively coarse cementite is substituted by a much finer alloy carbide dispersion. Such alloy carbides, in general created by carbide forming elements (e.g. Cr, Mo, W, and V), form at an elevated temperature 500°C – 600°C due to sufficient diffusion of metallic atoms at this temperature. On the other hand, non-carbide forming elements (e.g. Ni, Co, and Si) do not cause secondary hardening. Indeed, alloy carbides precipitation and its influence on property of tempering martensite have been extensively studied. Grange et al. [128] presented a systematic study to the effect of different alloying elements on the hardness of tempered martensite. It was demonstrated that for strong carbide former, the tempering temperature for greatest hardness increase was 472°C for Cr, 592°C for Mo and 649°C for V.

The addition of microalloy elements have a significant influence on retarding hardness loss during tempering. Kwun et al. [129] observed the secondary hardening from the niobium carbides in tempered martensite microstructure with 0.034% Nb and 0.08% C. Robertson [130] has drawn attention to the differences in ranking the tempering resistance ability of microalloy elements in quenched and tempered steels with a yield strength of 690 MPa. It was believed that V and Nb displayed the greatest temper resistance with the indicator from hardness reduction results. The reason for this was that the V and remaining Nb segregated to or precipitated on dislocations during tempering and therefore delayed softening of the quenched steel.

Based on the above understanding of tempering reactions, the steel producers can properly adjust the production process and alloy design in order to approach desired microstructure and mechanical properties [131]. For welding process, it is essential to consider the martensite tempering because in some cases it may lead to HAZ softening phenomenon and deteriorate the integrity of welded structure. The softening caused by tempering is reported to depend on the steel composition and the precipitation behaviour during welding. An addition of Cr and Mn in dual-phase steel assisted the softening resistance since very fine cementite and less decomposed martensite were formed [132]. It is also suggested that HAZ softening for creep-resistant steel that occurred at around 900°C was probably due to the lack of Nb and V precipitates coherent with the matrix [12]. Furthermore, high heat input with corresponding long time over subcritical temperature, facilitates the tempering reaction as well. Some works were done to characterise the effect of different high-strength steels and processing parameters on HAZ softening [132, 133]. However, very limited studies are done to compare the tempering behaviour of modern microalloyed high-strength steels having different microalloy addition.

2.3.2 Compositional effects

A well-considered steel design of alloying elements combined with appropriate production process is always conducted to exploit their metallurgical effects in approaching the required properties of steels. Different metallurgical aspects, such as solute effect, precipitates formation, austenite grain growth,

and phase transformation, are still significant topics for microalloyed high-strength steels. Hence, a comprehensive understanding of compositional effects is critical.

In general, the alloying elements can be regrouped in terms of macro (e.g. Mn, Si, Ni, Mo, Cr) and microalloy (e.g. B, Al, V, Ti, Nb), relative to the typical weight being added. So-called microalloy elements is typically less than 0.1 % by weight. A further classification is possible according to the role of suppressing or promoting either the fcc or bcc phase. Alloying elements can be divided into austenite stabilisers (e.g. Ni, C, Mn, Cu and N) or ferrite stabilisers (e.g. Si, Cr, Al, W, Mo, V and Nb).

Based on the various roles during phase transformation, the combined alloy addition makes it possible that a precise control of transformation process can be approached. It should be pointed out that in the weld metal the alloy composition is the summary from base steel and filler metal, which strongly depends on the dilution effect of welding process, particularly in the case of microalloyed steels [134]. Although microalloy element is present in a small amount, its presence in solid solution form or in precipitation plays remarkable influence on austenite grain growth, microstructure and mechanical properties of welded joints. The following section highlights the influence of the common alloying elements on phase transformation and properties of microalloyed high-strength steel weldments.

C

Carbon is the most important element deliberately added to steel and weld metal. It influences not only the overall strength and toughness but also the phase transformation during cooling. Carbon often remains in solid solution or partially forms fine carbides, which could contribute to strong strengthening effect. However, excess addition of carbon is avoided because of its harmful effect on the steel weldability, as mentioned in previous section. When high carbon level austenite transforms into martensite in the HAZ, this kind of martensite has low toughness and as well low resistance for hydrogen assisted cold cracking. In general, carbon interacts with alloying elements to form complex carbides. Since these alloying elements possess different affinity to carbon, their corresponding carbides have different stabilities in ferrite or austenite. Moreover, the various nature of carbides can influence the austenitisation temperature during heating or phase transformation kinetics during cooling.

Mn

Mn, acting as a solid solution strengthener, is the most common alloy added in steels due to its comparatively low cost. It can also lower the austenite – ferrite transformation temperature. Another benefit from Mn is to reduce solidification cracking risk, while it ties up the sulphur to form manganese sulphides. As a result, this reduces the chances of low melting point iron sulphides which can promote hot cracking. Mn can also serves as a deoxidant in weld metal or generally precipitates as manganese sulphide on other oxide inclusions (e.g. Ti, Al, Si oxides) [97]. The negative problem from alloy with Mn is that it tends to segregate which leads to non-uniform hardness or microstructure [135]. Therefore, the content of Mn is in general adjusted to prevent serious solidification segregation.

The effect of Mn on weld metal microstructure and properties is well documented. Mn can replace the coarse primary ferrite in as-deposited and coarse grained reheated zones by fine acicular ferrite formation in preference to by ferrite with second phase [102]. But it is noteworthy that the rate of acicular ferrite volume increase with Mn content was not linear and the critical value was 1.4 %, according to Evans [102]. As discussed in previous section, a Mn-depleted zone around MnS inclusions can effectively facilitate the nucleation of acicular ferrite. Therefore, with respect to gain sufficient

acicular ferrite accompanied with excellent toughness, adequate Mn addition as well as other alloying elements is extremely necessary for filler metal and steel design.

Si

Si can considerably increase the hardenability of steel by solid solution and it has strong deoxidising capability. The oxide inclusion of Si can activate the formation of acicular ferrite in weld metal. Si has been proposed to influence the deoxidising process in combination with Mn by Mn/Si ratio [136,137]. One significant effect from Si is to inhibit the precipitation of cementite and for this reason it is commonly used to control the tempering of martensite in high-strength steels. Meanwhile, Si can assist in the formation of carbide-free bainitic microstructure by suppressing carbide precipitation, which is applied to create steel with very strong bainite [112].

Ni

Ni is an austenite stabiliser element like Mn. An addition of Ni increases the hardenability and lowers the austenite decomposition temperature. But the potent strengthening effect of Ni is much less than that of Mn, Cr or Mo. Evans [102] showed that both Mn and Ni can change the weld metal microstructure in a similar way, which indicated that both can enhance the formation of acicular ferrite at the expense of grain boundary ferrite and ferrite side plates. Moreover, Ni could also increase the ration aspect of acicular ferrite.

The level of Ni in general plays a positive influence on both strength and toughness. Kim et al. [138] claimed that an increase in Ni content contributed to a remarkably high impact toughness due to the formation of auto-tempered martensite at a low temperature. However, there are some investigation revealing that the positive role of Ni on toughness should be conditional with the concentration of other alloying elements. Evans [102] concluded that at low Mn content (< 1.0 wt.-%), increased Ni level led to continuous increase in acicular ferrite volume but at higher Mn content, acicular ferrite was replaced by ferrite with second phase aligned. Zhang and Farrar [139] stated that an optimum toughness was achieved when a combination of 0.6 wt.-% – 1.4 wt.-% Mn and 1.0 wt.-% – 3.7 wt.-% Ni was used and the concentration beyond this range can result in martensite formation and a reduced toughness. Keehan [140] also confirmed that there was a great amount of martensite formed when the combination of Ni and Mn was not properly balanced. As a result, the strength was increased by solid solution hardening from Ni but the toughness was reduced by the presence of martensite and coarse grained coalesced bainite.

Mo

Mo is a potent hardenability element and can cause a substantial increase in strength. Mo has also a great carbon affinity to form fine alloy carbides, causing precipitation hardening in ferrite. Additionally, in the presence of Mo coupled with other strong carbide forming elements such as Cr and W, cementite could be replaced by the fine alloy carbides. Mo facilitates the formation of M_2C type carbide. This type carbide becomes unstable at sufficiently high temperature, transforming to M_6C type carbide by reaction with iron at 750°C or could be dissolved before austenite formation [141]. It is very common in some microalloyed steels to add Mo combined with Nb to achieve beneficial synergistic effect. Because Mo can assist Nb in retarding recrystallisation and optimise the precipitation hardening effect of Nb. Moreover, both elements can enhance the tempering resistance behaviour in the steel [142].

Another major influence of Mo on transformation appears to effectively promote bainite formation

instead of acicular ferrite. This can have a negative effect on toughness, which is closely associated with Mn or Ti contents and cooling rate [63, 142, 143]. Evans [102] pointed out that an addition of 0.25% Mo promoted acicular ferrite at 1% Mn concentration and optimised Charpy toughness, but above 0.5% Mo ferrite with second phase substituted acicular ferrite.

Cr

Cr can not only enhance the steel hardenability but also cause precipitation of alloy carbide, which greatly improve the creep resistance during subsequent heat treatment. It can form $Cr_{23}C_6$ carbide and in some cases Cr_7C_3 during annealing, which depends on its content in steels. These carbides in general are dissolved during austenitisation at temperature above 900°C and must be completely dissolved above 1100°C. During cooling and phase transformation process, an increase in Cr up to 1% in weld metal caused a decrease of allotriomorphic ferrite and contributed to large amount of acicular ferrite formation. Above this level the microstructure becomes bainitic, resulting in decreased toughness in the weld metal [102].

Al

Al is a highly efficient de-oxidiser and nitride former. Al can encourage strong grain refinement. Aluminium oxides are the most common inclusion in the weld metal. The effect of Al content (Al/O mass ratio) on acicular ferrite formation has been systematically analysed in low carbon steel weld metals by Takada et al. [96]. The main conclusion is that acicular ferrite can be encouraged with low and medium aluminium content (Al/O mass ratio of 0.28 and 0.79) due to a TiO layer on the surface of inclusions. At high Al content (Al/O mass ratio of 1.63) no acicular ferrite formed. Additionally, it is often suggested that the optimum microstructural development can be approached by a balance between Al and Ti since inclusion surface layer contains Ti-rich phase that can more efficiently stimulate the nucleation of acicular ferrite [76].

Nb

Nb is well known to be a strong carbide and nitride former, which can meanwhile be effective to increase the strength by precipitation hardening and grain refinement. Nb has intermediate solubility (higher than V but lower than Ti) and can form precipitates in austenite or ferrite. The presence of fine niobium nitride not only remarkably limits the grain growth but also favours precipitate strengthening [22, 144].

As a consequence of solute Nb, it enhances the hardenability of austenite [145]. Moreover, another typical characteristic of Nb is that it shows strong retardation on recovery and recrystallisation progress [146]. A comparison of the solute retardation effect reveals that Nb exhibits the strongest retarding effect, V has the weakest and Ti the intermediate. Such an advantage is taken of certain Nb addition in TMCP steels. With respect to the dilution effect from welding, the addition of Nb results in somewhat pick-up in the weld metal. The introduction of Nb into weld metal has to be taken into account when considering the transformation behaviour, particularly during welding with very high dilution [147]. In the literature such Nb pick-up is reported to be detrimental since an increase as little as 0.01% Nb was found to induce upper bainite structure in submerged arc weld deposits [148]. There is still a debate among researchers about the influence of Nb on phase formation. It is necessary to evaluate the influence of Nb on phase transformation based on several aspects from the overall hardenability, Nb content and cooling rate [149].

In solid solute, Nb is often reported to segregate to grain boundaries, because it is proposed that due

to large misfit of Nb atom in the iron lattice, austenite grain boundaries become preferable location of Nb atom where it interacts with the carbon. The consequence of such interaction is suggested to be either the decrease of local driving force for ferrite formation or slower diffusion of carbon from ferrite nuclei. Both results are expected to slow down the ferrite nucleation [145].

Ti

Ti is an efficient de-oxidiser and has comparatively higher affinity to nitrogen and carbon, compared to Nb. Ti is always encouraged to be added in filler metal due to its assistance on acicular ferrite nucleation, as discussed in the previous section. Evans [102] has compared the mechanical properties of single alloyed weld metal with and without Ti addition. The results showed that the addition of Ti in general remarkably improves the toughness and as well restrained the negative effect of Mo and Mn on deteriorating toughness. Beidokhti et al. [150] demonstrated that the best combination of weld metal microstructure and impact properties was obtained in the range of 0.02% – 0.05% Ti. He also studied the combined effect of Ti and Mn on acicular ferrite formation, the high toughness was obtained in two groups of compositions, i.e. 1.92% Mn – 0.02% Ti and 1.40% Mn – 0.08% Ti [151].

Ti reacts with nitrogen to form TiN, which can be obtained as coarse inclusion (ranging from 0.5 μm – 12 μm in side length) when present firstly in liquid steel, or as fine precipitate (ranging from a predicted 10 nm – 500 nm) when precipitating during solidification. The high stability of TiN precipitate in austenite is the principal reason for the addition of Ti, which acts as one preferred grain refining agent at high temperature during steel production (above 1450°C). Notably, coarse precipitate of TiN is often ineffective in pinning grain boundaries and may decrease the steel toughness by initiating cracks [14,15]. Fine particles of TiN are effective to pin the movement of grain boundary and therefore a certain dispersion of fine TiN is always expected. However, there are some processing difficulties in approaching optimum ratio of Ti and N in the steel [152] and further discussion on this is shown in the next section. Another important feature of Ti-rich nitride is that their complex inclusions ($\text{Ti}_2\text{O}_3+\text{TiN}$, $\text{TiN}+\text{MnS}$) can facilitate intragranular ferrite nucleation and show a Baker – Nutting orientation relationship with the ferrite grains [153].

V

V is also known as a strong carbide and nitride former. The addition of V provides a strong and easy controllable precipitation strengthening in steels [154]. The main reason for this is the relatively large solubility product of vanadium carbonitrides resulting in a lower solution temperature and a larger capacity to dissolve them at an elevated temperature (around 1050°C). One significant effect of V is that its carbide formation can replace cementite and maintain as fine dispersion up to A_{c1} temperature. Zajac [154] claimed that the extent of such precipitation strengthening depended on the free amount of carbon and nitrogen, of which nitrogen showed more reliable effect by some 6 MPa increase in strength for every 0.001% N. V can also contribute to the formation of intragranular nucleated ferrite and thus assist in grain refinement, although the exact mechanism is still not clear [155,156]. Recent work from He and Edmonds [156] considered the effect of composition and heat treatment on microstructure with a comprehensive study on the inclusion. They observed no significant evidence that inclusion-assisted-nucleation was solely the determining factor in producing acicular ferrite.

V is not a deliberate addition to the weld metal, although it is a common microalloy element in high-strength steels. By using modern welding process, V can often be picked up in the weld metal from the base material due to the high dilution. V can increase the amount of acicular ferrite and refine

its structure when V level increase from 0 ppm – 800 ppm with 40 ppm Ti and 1% – 1.7% Mn addition in weld metal [102]. Also, the corresponding strength increases over this range without any large drop in toughness. However in a stress-relieved condition, V is particularly detrimental for toughness, even in a small amount of 200 ppm, due to the formation of embrittled carbide [102]. Therefore, up to 200 ppm of V is an acceptable value within weld metal if the structure goes through unavoidable stress relieving. Here, it should be noted that the coexistence of other microalloy element, such as Ti and Nb, will make the physical metallurgical process more complicated, which needs to be studied.

2.4 Properties of the heat affected zone (HAZ)

2.4.1 Hydrogen-assisted cold cracking

One of the major problems that can occur during welding high-strength steels is cold cracking in the HAZ or weld metal. It is well known that cold cracking is in general promoted by three main inter-related factors: sufficient hydrogen concentration; local residual stress/strain and susceptible microstructure [5]. Based on the contribution of these factors to the formation of cold cracking, several standards and specifications are proposed to provide predictive monograms in addition to equations and algorithms that are targeted at preheating treatment, inter-pass temperature and post-heating conditions to avoid cold cracking [42]. Although all these methods attempt to give general guidelines for the engineer, the results gained by these methods can vary from one method to another. Therefore, applicable welding process should be determined individually for steels by practical experiments experience to avoid cold cracking. The most common procedure to prevent cold cracking is preheating in order to slow down the cooling rate. A low cooling rate gives sufficient time for hydrogen to effuse from the weldments and helps to prevent the formation of hard or susceptible microstructure. Hence, in order to find an appropriate preheating temperature, several aspects should be considered, such as steel chemistry or carbon equivalent, plate thickness, assessment of hydrogen content involved during welding process, and heat input.

One of the diagrams that represents the relationship between all these parameters and preheating temperature T_0 is shown in Fig. 2.24 [42]. This figure shows two S690QL steels with different alloying designs (Table 2.13) that have reached the same strength level. Such an alloying difference results in various preheating temperatures [42]. This phenomenon indicates that an appropriate preheating temperature should be directed for individual steel with validation by practical experiments, not only based on the same welding process or strength level.

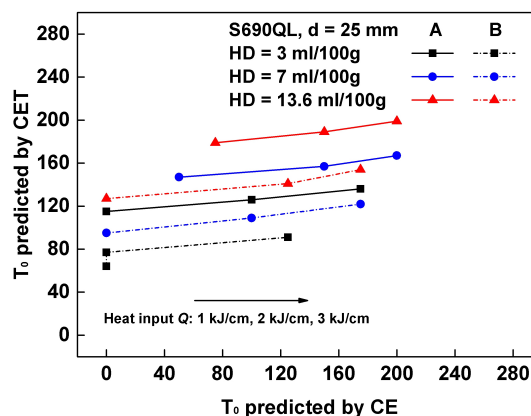


Fig. 2.24: Preheating temperature T_0 predicted by carbon equivalent CE and CET methods

Table 2.13: Chemical composition and carbon equivalent values of two S690QL steels

S690QL	C	Si	Mn	Cr	Cu	Mo	Nb	Ni	Ti	V	CE	CET
A	0.16	0.26	1.50	0.70	0.01	0.46	-	0.80	-	-	0.70	0.41
B	0.17	0.65	0.90	0.85	0.02	0.45	0.020	0.03	0.020	0.003	0.58	0.35

In order to slow down the cooling rate, apart from preheating treatment, increased heat input or controllable welding speed are also often suggested. In practical welding, engineers often use the $t_{8/5}$ time to transpose one set of welding condition (preheating temperature and heat input) to another one (changes in thickness and preheating temperature) [28]. Therefore, steel manufacturers generally recommend a specified $t_{8/5}$ time range for their products. The S690QL steel is one example, it is suggested that the appropriate $t_{8/5}$ should be between 5 s – 20 s, which also depends on welding methods. Indeed, there is standardised method to calculate the $t_{8/5}$ time from a given welding parameter and certain joint geometry [46]. Therefore an applicable working range can be obtained. Fig. 2.25 compares the working ranges for welding several structural steels [157]. The lower limit of welding condition is set to avoid cold cracking, whereas the upper limit is set to ensure excellent tensile and toughness properties. S690QL steel, with narrow applicable parameter windows, permits more restrictive welding conditions than the other two steels S355J2 and S500M.

The susceptibility of a steel to cold cracking in the HAZ or weld metal is also closely related to weld metallurgy involving hard microstructure with high hardness. As discussed in previous section, the CE value could be one indirect index for hardness prediction in some cases but for steels having microalloy addition it cannot make a reliable prediction on HAZ properties. The metallurgical effect from microalloy, such as the presence of microalloy precipitates, upper bainite, and the M – A constituent, should require additional consideration with respect to HAZ properties.

The residual stress, as another important factor influencing the cold cracking, is experimentally verified to be reduced by using the low transformation temperature welding consumable. The mechanism for approaching this is that the residual compressive stress is induced by martensitic transformation expansion of weld metal near the ambient temperature and meanwhile the fatigue strength can be improved [158]. Recently, this concept has been successfully applied to weld high-strength steels and other alloys with the aim of preventing cold cracking [159, 160].

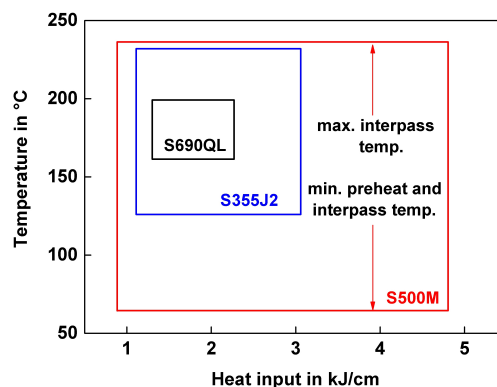


Fig. 2.25: Typical working ranges of steels (S355J2, 80 mm; S500M, 50 mm; S690QL, 30 mm) [157]

2.4.2 Austenite grain growth

As cold cracking most commonly occurs in the CGHAZ, this region is the most vulnerable point of the HAZ. As discussed in the previous sections, cold cracking can result from the formation of an

embrittled structure. Such structure is directly influenced by the presence of coarsened austenite grains. A large austenite grain often facilitates the formation of unfavourable microstructural constituents that are susceptible to cold cracking. It meanwhile results in coarse-sized transformation product, leading to a loss in strength and toughness. One solution for this problem is to introduce fine stable particles that can restrict the austenite grain growth. Grain refining elements (Nb, Ti, V and Al) are often added for this purpose. The particle characteristics (such as thermal stability, the coarsening and dissolution behaviour) are known to be significant in controlling the austenite grain growth during welding process.

Over the years plenty of research work was conducted on the isothermal austenite grain growth process and the controlling factors. However, in the industrial field, the austenite grain growth occurs mostly under non-isothermal process. One typical situation is the case in the HAZ that experiences a non-isothermal condition of the weld thermal cycle. In the grain growth stage, the larger grains grow at the expense of the smaller ones. The driving force for this is the reduction of total grain boundary surface energy of the system. It is demonstrated that, in classical austenite grain growth tests, the grain grows above the so-called grain coarsening temperature. Impurities can reduce the rate of grain growth but the most significant factor is the presence of stable precipitates [51]. Fig. 2.26 shows a general overview about the effect from microalloy elements on the grain coarsening temperature of the austenite. Specific grain coarsening temperatures depend on the microalloy content, the nitrogen content and the effect of thermal cycle [22]. The nitrogen content should be considered in most cases, due to the pronounced stability of microalloy nitrides compared with their respective carbides. From a kinetic standpoint, the boundary pinning effect is expected to be most pronounced during rapid heating due to an associated increase in the required extent of particle super heating prior to the dissolution process [161]. This was also been proven by Banerjee et al. [141] who compared the influence of heating rates (from $10^{\circ}\text{C} \cdot \text{s}^{-1}$ to $1000^{\circ}\text{C} \cdot \text{s}^{-1}$) on the non-isothermal austenite grain growth behaviour. In contrast, a slow cooling rate, that accompanies with long time available for particles dissolution, can cause remarkable austenite coarsening.

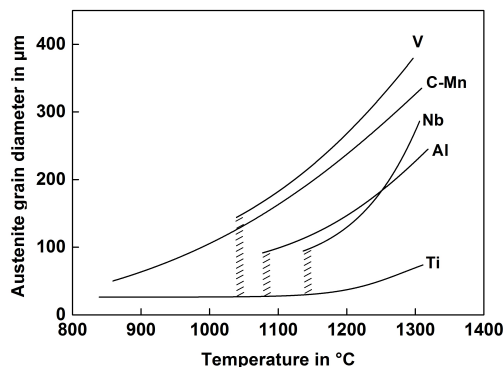


Fig. 2.26: The general effects of microalloy additions on the grain coarsening temperature of austenite [22]

Another factor that is influencing the grain boundary mobility is the peak temperature T_p in the HAZ (depending on the distance from the fusion line). Elevated peak temperature, high above the dissolution temperature of precipitates, can accelerate complete particle dissolution and therefore reduce pinning effect. As a result, fast austenite grain growth is achieved [141, 161]. Hence, in the case of weld, austenite grain growth in the HAZ depends on the steel composition, peak temperature reached and the cooling rate or dwell time above the grain coarsening temperature.

Despite the complex non-isothermal nature of the welding process, some efforts were made to study

the austenite grain development in the HAZ by experimental, physical simulation or theoretical approaches [9, 141, 161–165]. One problem to conduct precise measurement in the HAZ is the presence of extremely narrow and inhomogeneous sub-zones. The solution for this problem is a physical simulation, which allows generation of almost homogeneous microstructure that can represent one local sub-zone of the HAZ. This method becomes a common method to investigate the HAZ properties. Several weld simulators, such as GleebleTM, SmitweldTM, dilatometer etc., are most often used.

Ashby and Easterling [162, 163] were the first to develop a model to predict the HAZ microstructure and hardness, based on elementary kinetic models for grain growth and carbide dissolution. Their approach was based on assuming diffusion controlled transformation process. The idea comes from the integration of the grain growth equation over weld cycle. It is described by the following kinetic equation:

$$D^{1/n} - D_0^{1/n} = K_1 \int_{t_1}^{t_2} \exp(-Q_{app}/RT(t)) dt \quad (2.6)$$

Where D is the mean grain diameter, D_0 is the initial grain diameter, n is the time exponent, K_1 is a kinetic constant and Q_{app} is the apparent activation energy for grain boundary motion. t_1 and t_2 are the time range. The other symbols have their usual meaning. For most metals and alloys the time exponent varies typically in the range of 0.1 to 0.4 due to the solute or impurity drag effect [166, 167]. Only in the metals of ultra-high purity and at high annealing temperatures the time exponent approaches the ideal value of 0.5 [167]. This corresponds to the limiting case where the grain boundary migration rate is proportional to the driving pressure γ/D (γ denotes the grain boundary surface free energy and D is the instantaneous grain size). Alselsen et al. [161] concluded that HAZ grain boundary migration rate was approaching this upper theoretical limit ($n = 0.5$) owing to the high driving force involved for Nb containing steels. This value was also agreed by other researchers [9, 141, 165] later on.

Andersen and Grong [168] proposed an extensive analytical model for grain growth in metals with growing or dissolving precipitates. They applied an overall differential grain growth equation which can be integrated in temperature – time space to give the mean grain size for fixed starting conditions. Shome et al. [165] proposed a modified model compared with Anderson's method, which applied to the Nb-containing HSLA-100 welds. They introduced the net kinetic strength for grain growth along with an appropriate kinetic constant pertaining to the precipitate free austenite regime within a single thermal cycle. Moon et al. [169] developed a model which incorporated the Zener pinning effects of precipitates in a Ti-microalloyed steel. It was based on a general isothermal grain growth model considering the particle pinning effect. This model combined the additivity rule to predict the grain growth during continuous weld thermal cycle. In his work, only one type of precipitate is considered, but in the case of multi-precipitates steel it will be more challenging to deal with the austenite grain growth [9, 141].

The detailed generic grain growth model is discussed in the following part. It is known that the grain growth inhibition can be approached by introducing second phase particles (the Zener drag effect) [22]. The Zener effect shows that if a grain boundary intersects a particle, a small area of grain boundary disappears. When the boundary intersects the particle diametrically, the maximum pinning force acting by a particle on the grain boundary is given by

$$p = \pi r \gamma \quad (2.7)$$

Where r is the radius of particle and γ is the surface energy of the boundary. To consider an array of randomly dispersed particles in steels, the pinning force per unit volume of the grain boundary, P_z , is expressed by

$$P_z = p \cdot \frac{3f}{4\pi r^3} \cdot 2r = 3f\gamma/2r \quad (2.8)$$

Where f is the volume fraction of particles and r is the mean particle radius. More recently, many researchers have modified this relationship to be more realistic with consideration of the different particle shape. The pinning force is then defined by

$$P_z = c_4 \frac{\gamma \cdot f}{r} \quad (2.9)$$

Where c_4 is a dimensionless Zener coefficient. Moreover, this modified pinning force relationship, according to Rios ($c_4 = 12$) [170], was accepted for use in modelling of grain growth by Maalekian and Banerjee [9, 141]. In their work, multiple particles present in the system and the summarised pinning parameter can be described by

$$P_p = 12\gamma \sum_i \frac{f_i}{r_i} \quad (2.10)$$

Where the index i represents all present precipitate classes.

The driving pressure for grain growth is given by

$$P_d = c_3 \frac{\gamma}{D} \quad (2.11)$$

Here D is the mean volumetric grain diameter, γ is the grain boundary energy and c_3 is a dimensionless geometric constant. The net driving pressure on the boundary can be derived from $\Delta P = P_d - P_z$. In response the grain boundary moves with a growth rate dD/dt that is related to the effective driving pressure and the time exponent by the following relationship [167]:

$$\frac{dD}{dt} = M(\Delta P)^{(1/n-1)} \quad (2.12)$$

Where the constant M is the effective mobility of boundaries and can be given by

$$M = M_0 \exp\left(-\frac{Q_{app}}{RT}\right) \quad (2.13)$$

Combining equation 2.8 - 2.13, the differential equation for grain growth in the presence of particles can be obtained:

$$\frac{dD}{dt} = M_0 \exp\left(-\frac{Q_{app}}{RT}\right) \cdot \left(\frac{1}{D} - \frac{1}{k r}\right)^{(1/n-1)} \quad (2.14)$$

Here k equals to the ratio between c_3 and c_4 and represents the pinning efficiency of the precipitates. M_0 is the pre-exponential mobility factor, Q_{app} is the apparent activation energy of the grain boundary mobility. In general, the activation energy Q_{app} coupled with n can be numerically evaluated and estimated by isothermal grain growth experiments [161]. Uhm et al. determined Q_{app} by a multiple regression analysis method from several Nb-bearing steels [171]. From equation 2.14, it can also be concluded that fine particles with a high volume fraction are more effective in inhibiting the grain growth.

The isothermal grain growth model given in equation 2.14 is based on the modified Zener equation. Indeed, several limitations are not involved in the original Zener equation, such as the effect from initial grain size distribution on the driving pressure, the particles distribution, different geometries of particle-grain boundary interaction and so on. The modified Zener equation can be utilised to establish a non-isothermal grain growth model combined with additivity rule, which is able to predict austenite grain growth with a fair degree of accuracy [141].

When applying the grain growth – precipitation models to the welded HAZs, Mishra and Debroy [164] emphasised the special features of the grain growth in welding type non-isothermal process. These features involve significant spatial gradient of grain size and 'thermal pinning' of growth owing to steep spatial temperature gradients. Most available models that focus only on austenite growth in post-processing specimens do not well demonstrate quantitatively these features of the welding process. Recently, Maalekian et al. [9] have applied laser ultrasonics to directly measure austenite grain growth during continuous heating. This technique allows in-situ observation on the evolution of grain structure. Unfortunately, this method did not consider the above-mentioned special features of the welded HAZ. Therefore, further efforts are needed to deepen the understanding of austenite growth during welding.

In order to gain a better understanding of the austenite grain growth, it is also important to know the behaviour of microalloy precipitates during welding. From the above proposed models on non-isothermal grain growth, it can be easily concluded that the grain growth in the HAZ occurs predominantly at temperature above the solubility limits of the particles. On this basis, it is essential to consider the solubility and stability of precipitates. More specifically, the efficiency for grain refinement is directly correlated with the particle coarsening, dissolution or reprecipitation behaviour during weld thermal cycle. The detailed discussion on particles will be made in the following section.

Solubility of microalloy precipitates

The presence of fine precipitate is related to two aspects of microalloyed steels that involve strengthening effect and grain growth inhibition. These two effects are desired from metallurgical and mechanical standpoints. Thus a detailed knowledge of the stability and precipitation behaviour is required. In terms of evaluation of the stability of microalloy carbides or nitrides, thermodynamic or chemical methods are used for assessing solubility behaviour of different microalloy precipitates in the austenite and the ferrite. The solubility behaviour depends on the temperature and the steel composition [22]. The widely accepted definition of solubility product is expressed by the following relationship:

$$\log k_s = A_1 - \frac{A_2}{T}, (k_s = (M)^m(C)^n) \quad (2.15)$$

Where the terms M and C represents the molar fraction of microalloy and interstitial elements respectively. At very low concentration encountered in microalloyed steels, the weight percentage can be used. k_s is the equilibrium constant, referring to as the solubility products. For a given steel, the A_1 and A_2 are constants and T is the thermodynamic temperature (K).

Table 2.14 summarises some representative solubility products assessed by different methods. In some cases the variations in stoichiometry have been found in some compounds (e.g. NbC_x), where a fraction of the carbon/nitrogen lattice sites is zero. The exact composition of microalloy carbonitrides with regard to stoichiometry is still an area of dispute. It is known that carbon and nitrogen can substitute each other in the lattice if both elements are presented in the steel. Using the equations from Table 2.14, the equilibrium dissolution temperature can also be calculated and often used as

a reference to predict the stability of a certain precipitate. The literature shows that the predicted dissolution temperature for niobium carbonitrides is in the range between 1050°C and around 1200°C (similar to that of AlN), while for TiN it can reach above 1400°C; for vanadium carbonitrides it is limited to 1050°C. Indeed, the actual dissolution temperature of the precipitate, when subjected to weld thermal cycle, is approximately 30°C – 50°C higher than this equilibrium solubility data due to the non-isothermal cycle [163].

Table 2.14: Solubility products of precipitates defined based on equation 2.15 [172] [173]

Compound	Constants (A_1, A_2)
NbC	(-0.63, 2500); (4.37, 9290); (3.7, 9100); (3.04, 7290); (3.3, 7900)
Nb(CN), $k_s = (Nb)(C + N)$	(1.54, 5860)
Nb(CN), $k_s = (Nb)(C + \frac{12}{14} N)$	(2.26, 6770)
Nb(CN), $K = (Nb)(C)^{0.83}(N)^{0.14}$	(4.46, 9800)
NbC _{0.87} , $k_s = (Nb)(C)^{0.87}$	(3.18, 7700)
NbC _{0.87}	(3.11, 7520)
Nb(CN), $k_s = (Nb)(C)^{0.24}(N)^{0.65}$	(4.09, 10400)
NbN	(4.04, 10230); (3.79, 10150)
TiC	(2.75, 7000)
TiN	(5.40, 15790); (2.0, 20790); (6.75, 19740); (0.322, 8000); (3.82, 15020)
VC _{0.75} , $k_s = (V)(C)^{0.75}$	(5.36, 8000); (4.45, 6560); (4.24, 7050)
VN	(2.27, 7070); (3.46, 8330); (3.46+0.12(Mn), 8330)
AlN	(1.03, 6770); (4.56, 12310); (0.725, 6180); (1.8, 7750); (1.48, 7500)

Fig. 2.27 shows the comparison between solubility products of different microalloy carbides and nitrides in austenite and ferrite [22]. The microalloy nitrides are generally more stable compared with their respective carbides. Vanadium carbide and nitride are the most soluble products compared with other groups. It should be emphasised that TiN has a significantly higher stability in austenite and even in liquid than other microalloy carbides and nitrides. Although TiN is considered as effective grain growth inhibitor by virtue of its high dissolution temperature, several precautionary actions should be taken during steel production to obtain the desired TiN number density and size distribution in the final steel product. Otherwise, large particles can form and play a negative effect on the steel and its weldment toughness [14, 15].

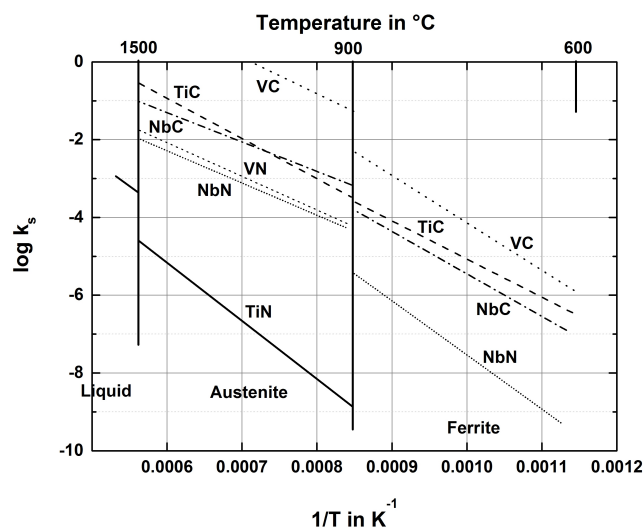


Fig. 2.27: Comparison of the solubility products of microalloy carbides and nitrides [22]

The individual solubility of microalloy carbonitrides shown in Fig. 2.27 also provides valuable indications to microalloy addition for specific requirements, such as austenite grain refinement or precipitates strengthening effect in the ferrite. In practical application, mutual presence of microalloy carbonitrides commonly occurs for multiple purposes by the simultaneous addition of two or more microalloy elements. Moreover, the coexistence of carbon and nitrogen is difficult to be avoided as well. Therefore, it is essential to consider the complex precipitate solubility behaviour in multi-microalloyed steels.

The extensive mutual solubility between microalloy carbides and nitrides stems from the fact that they have the same cubic structure and similar lattice parameters. Each carbonitride has cubic crystal structure with lattice parameter intermediate between that of nitride and that of carbide, depending on the carbon/nitrogen ratio. In modern single or multi-microalloyed steels, two or more solutes often form interstitial compound in the form MC_xN_{1-x} or $M'_yM''_{(1-y)}C_xN_{1-x}$ [22, 174]. Here, special attention should be drawn to the aluminium nitrides. In spite of its hexagonal structure, it can also form a mutually exclusive compound and is thermodynamically stable at lower temperature. However AlN formation is generally sluggish in austenite and in the end AlN formed are relatively coarse.

Two or more mutually exclusive precipitates are formed after fast heat treatment in steelmaking, as reported in Nb-V-N, Nb-V-Al or Ti-V-Al steels [174–176]. In non-equilibrium conditions, the formation of complex mutually soluble carbonitride may follow the concept of core and shell that can be illustrated by one example in Fe-Ti-Nb-C-N steel, where titanium nitride formed as core particle and niobium carbide act as shell component [22, 177]. It is also described that particle chemistry and their morphology are controlled by the processing conditions as well as the overall steel composition [178].

In modern multi-microalloyed steels, in most cases, the interpretation of the precipitation behaviour is much more difficult due to the involvement of complex precipitates. Subsequently, the formation of more complex precipitates can take place during welding process. The results are assured to be totally different from ideal equilibrium situation products. Therefore, it is a great interest to understand this evolution process of microalloy precipitates and the final weld performance.

The steel is exposed to an elevated temperature above the dissolution temperature of precipitates during weld thermal cycle. Particles dissolution, reprecipitation or the Ostwald ripening process can occur in the HAZ [174, 176, 179]. The particles can dissolve to a certain extent, depending on the peak temperature and dwell time, with a consequent matrix enrichment of solute elements. The most possible dissolved precipitates (e.g. AlN, VN, Nb(C,N) and V(C,N)) are those with lower dissolution temperature, comparatively with the experienced peak temperature [175, 176]. Reprecipitation could occur in some cases, such as at much higher heat input, otherwise this is suppressed, leading to some solute supersaturation in the HAZ [179]. It is also proposed that if more stable precipitates are forming, the independent reprecipitation of these dissolved particles may not happen due to the limited time. The complexity in this process occurs when the solute elements are attracted to the undissolved stable particles forming complex precipitates in the final weld [176]. In most simulation models, the particle dissolution and coarsening behaviour are the two main aspects considered. These aspects are discussed in the following part.

Particles dissolution

If a local region in the HAZ undergoes thermal cycle with a peak temperature higher than the equilibrium dissolution temperature of precipitate, the dissolution of precipitate can potentially happen.

Since precipitate possesses a composition different from that of the matrix, such a dissolution process is in general controlled by diffusion. Several models have been developed to provide quantitative information about the extent of particle dissolution. The original invariant size approximation model was described by Whelan, which considered a spherical particle embedded in an infinite matrix. This model was further modified by Agren [180] and can be expressed by:

$$r^2 = r_0^2 - 2(dc/dx)_r D_m t \quad (2.16)$$

where r_0 is the initial particle radius, D_m is the solute diffusivity in the bulk, and $(dc/dx)_r$ is the dimensionless supersaturation value that can be replaced by the expression: C_i/C_p . C_i is the concentration of solute in the matrix/particle interface and C_p is the concentration of solute in the particle. Andersen and Grong [168] have further applied this model to continuous heating and cooling process by numerical integration of the cycle time in equation 2.16 over the thermal cycle:

$$r^2 = r_0^2 - 2 \int_{t_1}^{t_2} (dc/dx)_r D_m dt \quad (2.17)$$

The corresponding volume fraction f of precipitates can be given by:

$$f = f_0 \left(1 - \frac{2}{r_0^2} \int_{t_1}^{t_2} (dc/dx)_r D_m dt \right)^{3/2} \quad (2.18)$$

where f_0 is the initial volume fraction of the precipitates. The lower and upper integration limits refer to the time of the thermal cycle in the austenite region, during this time the influence of particle dissolution is considered to occur. By using such a modified model, the simulation results was proved to have a good agreement with the experimental results [8].

Particles coarsening

When some quite stable particles exist in the HAZ, they can undergo the Ostwald ripening process. This process is defined as the selective growth of the larger particles at the expense of other smaller ones. The driving force for such a process is provided by the minimisation of the interfacial energy between matrix and precipitates. The control mechanism is the bulk diffusion of the solute through the matrix due to the local solubility at the particle – matrix interface. This equation correlates with the particle size described by Gibbs-Thomson equation [22]. The kinetic of particle size change was further developed by Lifshitz, Slyozov and Wagner and the equation is shown by:

$$r^3 - r_0^3 = \frac{8\gamma f C_m D_m}{9RT} t \quad (2.19)$$

where r is the particle radius, γ is the interfacial energy between matrix and particle, f is the molar volume of the particle, C_m is the solute concentration in matrix, D_m is the diffusivity of the solute atoms, t is the ageing time and T is the ageing temperature. Such theory has been further applied by Ion et al. [163] to the continuous heating and cooling that is involved in the welding process. They modified equation 2.19 into a more general form:

$$r^3 - r_0^3 = \frac{K_2}{T} \exp\left(-\frac{Q_s}{RT}\right) t \quad (2.20)$$

where K_2 is a kinetic constant and Q_s is the activation energy for the coarsening process. By integrating this equation over the thermal cycle, the particle coarsening in the HAZ then gives the following equation:

$$r^3 - r_0^3 = K_2 \int_{t_1}^{t_2} \frac{1}{T} \exp\left(-\frac{Q_s}{RT}\right) dt \quad (2.21)$$

Equation 2.21 should be applied only in the cases where the peak temperature in the HAZ is well below the equilibrium dissolution temperature of precipitate. One typical application of this equation is the prediction of the extent of TiN particles coarsening during weld thermal cycles [163].

Previous suggested models regarding the precipitates dissolution and coarsening generally require extensive and time consuming TEM work to obtain reliable data on the initial particle size and volume fraction. Thermodynamic calculations enables a new approach to estimate the initial distribution of precipitates in the as-received steels and analyse their dissolution behaviour during thermal cycle with less experimental efforts [9]. This approach then need much less demand of TEM work and less time. Hence, this computer-assisted methodology is becoming a promising tool however still great efforts are needed in order to validate this approach in different steel chemistries based on practical experimental work for the comparison with the theoretical work.

As indicated by the previous suggested models, the significant factors for controlling austenite grain growth retardation are the volume fraction, particle size, distribution and the stability of the precipitates. Knowing this information can makes it predictable and adjustable for the steel chemistry design to achieve fine grain structure. In addition, an appropriate welding procedure is suggested when considering the behaviour of microalloy precipitates in the austenite grain growth and subsequent phase transformation.

Quantifying precipitation

As discussed in the previous section, quantifying the precipitate size and the volume fraction is significant because both influence the grain boundary pinning effect and the strengthening effect. Since the microalloy precipitates presented in steels are frequently quite fine, the quantification work becomes extensive, time consuming, and tedious. The most often used method is an analysis of thin foils or extraction replicas by TEM.

Fig. 2.28 (a) shows the ellipsoidal particle morphologies. The particles are typical for those observed in the Ti- and Ti+V-steels [172]. After weld thermal cycling with T_p of 1350°C and $t_{8/5}$ of 100 s, the particles have more angular and well defined, cuboidal morphologies (Fig. 2.28 (b)).

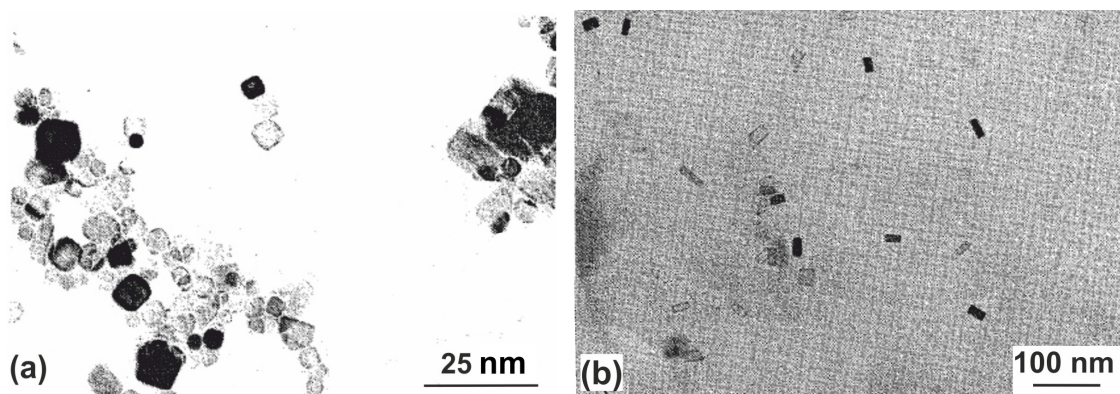


Fig. 2.28: TEM micrographs showing the particle morphology in the base metal (a) and welded sample (b) [172]

Fig. 2.29 compares the TiN particle size distribution in the as-received steel and after weld thermal cycle [163]. The mean particle diameter is anticipated to increase after welding. Although the size distribution of individual foil or replica is easily done, the volume fraction of precipitates in the whole specimen is much more challenging to be precisely determined. This is due to the low efficiency of replica extraction of small particles, a wide distribution of particle size and a low volume fraction

of precipitates in one macro-specimen. In order to gain reliable precipitate information, extensive TEM work is generally required. However, this experimental analysis can also yield data that can be inaccurate, particularly for much finer particles. In this case, it is suggested that combined TEM with atom probe field ion microscopy can image particles with an average diameter of 1 nm. This is below the resolution limit of the TEM [181]. However, due to its poor statistics of particle distribution in a small FIM specimen, this technique was not widely used.

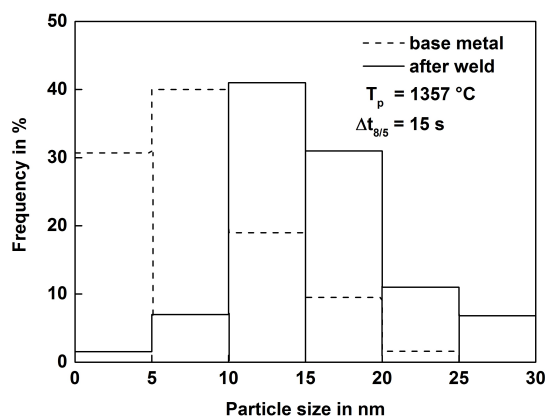


Fig. 2.29: Particle size distribution in as-received steel (dash line) and after weld thermal cycle (solid line) [163]

Other alternatives are developed to quantify the precipitate size and distribution, such as electrolytical extraction technique and thermodynamic calculation. The electrolytical extraction technique employs a selective dissolution process, which is based on the mechanism that the precipitate is nobler than the matrix in the electrolyte during polarisation. If various types of precipitates are extracted from the matrix, they can further be separated from the solution by centrifuging. Further, they are identified using TEM and XRD analysis without the interference from the matrix. The quantification of microalloy concentrations in solution and precipitate form is analysed through inductively coupled plasma mass spectrometry (ICP – MS). Such a method can offer more representative quantitative information of the steel strip than only microscopy methods. It has been successfully applied in microalloyed pipeline steels (X70, X80, and X100) [182]. Beyond this, the prediction of precipitate volume fraction by using MatCalc or Thermo-Calc software shows reasonable agreement with experimental observations [9, 183]. Although one significant advantage of simulation is the less demand of extensive TEM or other experimental work, it is still fairly hard to know the accurate information of complex precipitates in multi-microalloyed steel. Hence, experimental work is always needed to validate the calculation results.

2.4.3 HAZ toughness

Toughness is defined as the capability of a material to absorb energy during fracture. It is often measured using notched bar impact tests, of which the most common is the Charpy test [70]. HAZ toughness is one critical property to determine the integrity of a welded component because it indicates the HAZ resistance to cracking. As previously mentioned, the CGHAZ region close to the fusion boundary is likely to be the most susceptible to cracking and thus HAZ toughness is often of great interest and importance.

When assessing the HAZ toughness from the perspective of microstructure and measurements, two experimental approaches are usually used. They involve analysis being conducted either on specimens containing thermally simulated HAZ or on specimens machined directly from welded joints [184]. The first method with thermal simulation may not accurately reproduce the HAZ microstructure but it

can provide valuable and comparable information of the welded HAZ. One fact should be noted that austenite grain can grow more rapidly in the simulated HAZ compared with welded HAZ, due to a small temperature gradient. As a result, this can bring about a marginal difference in the subsequent phase transformation behaviour between the simulated and welded HAZs. Considering this difference, the prediction and assessment of HAZ toughness can be more realistic and acceptable if thermal cycle simulation techniques (such as dilatometer, GleebleTM, SmitweldTM, and other induction or conduction equipment) are employed.

According to Mitchell et al. [11], five main factors influencing the HAZ toughness of microalloyed steel should be considered: a) the solubility of microalloy elements, interactions between them and the effect of welding conditions on the extent of approach to equilibrium, b) the size of any precipitates present and their coarsening rate during welding, c) the resultant HAZ austenite grain size, d) the effect of microalloy addition on phase transformation, e) precipitation hardening within the HAZ. All these factors interact to determine the final HAZ toughness.

Although in a practical welding case an equilibrium condition is rarely approached, the equilibrium solubility of microalloy carbides and nitrides shown in Fig. 2.27 can be taken as a reference to assess their behaviour during welding. From Fig. 2.27, it is known that most microalloy carbides and nitrides would be in solution in the CGHAZ, where the peak temperature can reach above 1450°C, except the least soluble particles TiN. TiN has low solubility and keeps stable even at high temperature. It can offer strong pinning effect on grain growth but TiN particles in some cases undergo coarsening that can reduce such an effect. Therefore, effective control of austenite grain growth requires a large volume fraction of very fine precipitate that can provide optimised pinning effect. From the literature that if limiting the Ti/N ratio close to 2, the optimum pinning effect from precipitates can be obtained, as shown in Fig. 2.30 [185]. Meanwhile, the Ti/N ratio slight above the stoichiometric also ensures limited austenite grain growth [186].

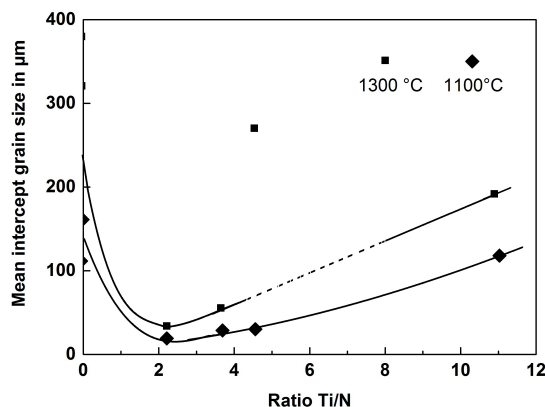


Fig. 2.30: Austenite grain size influenced by ratio of Ti/N at 1100°C, 1300°C for 10 min [185]

In a multi-microalloyed steel that has not only Ti as microalloy addition, the extent of microalloy precipitates coarsening is higher than the case in the Ti single microalloyed steel. Moreover, the coexistence of other strong nitride formers (Al, V, Nb) in general tends to decrease the stability of TiN particle [176]. In the case of Nb treated steel, Nb and V show less effective pinning potential on restricting austenite grain growth than Ti. However, Nb and V can contribute to precipitation strengthening by increasing the hardness/strength and enhance resistance to HAZ softening [130, 154].

Another major concern on HAZ toughness is the tendency of TiN to become offending particles and potent cleavage initiator. Fairchild et al. [14] carried out an investigation on the mechanism of brittle fracture in a microalloyed steel containing TiN inclusions. It was proposed that within the plastic zone at a notch or crack tip, the strong TiN inclusion – matrix bond allowed matrix stresses to be transferred to TiN. Once a TiN cleaved, this continuous interface permitted the TiN crack to transfer from the inclusion, across the interface, and into the surrounding ferrite matrix. This work implied that coarse TiN that generated from a casting schedule with a long dwell time at high temperature could play a deleterious effect on toughness. Zhang et al. [15] claimed that HAZ toughness depended on a complex interaction of matrix microstructure, grain size, alloy composition, carbide precipitates and the presence of large TiN particles. It was also observed that the generation of a fine grained matrix microstructure can mitigate the deleterious effects of large TiN particles. Du [187] correlated the influence of TiN particle with average ferrite grain size. It was concluded that within ferrite grain size in the range $9.5 \mu\text{m} - 27.3 \mu\text{m}$ coarse TiN particles were observed to cause initiation sites for cleavage fracture in heat treated samples. But with an average size of $5.0 \mu\text{m}$ no TiN initiated cleavage was observed.

The work of Echeverria and Rodriguez-Ibabe [16] supported the possibility of avoiding brittle fracture initiation from TiN by varying the matrix microstructure, for example AF instead of bainite. Detailed SEM examination of fracture surfaces shows two possible roles of TiN particles (Fig. 2.31 [14, 16]). But, the interpretation of this observation remained open in their study. To conclude the above observations, the coarse TiN particle is not always the origin of fracture. This strongly relies on the matrix microstructure, grain size and TiN particle size.

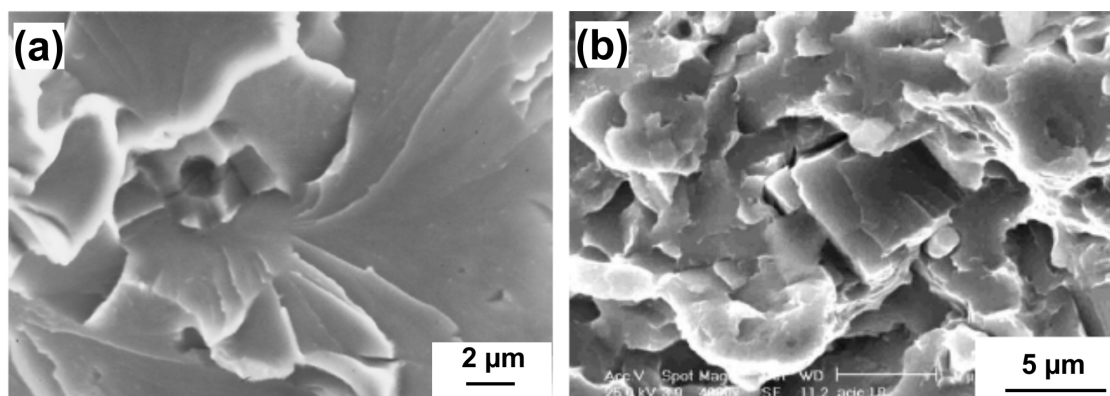


Fig. 2.31: SEM fractographs of TiN at initiation site (a) and TiN particle not as initiator (b) [14, 16]

The effect of Nb, V and Ti on phase transformation start temperature and transformation rates is always of great importance and interest in improving the HAZ properties. It is shown that an addition of Nb can depress the transformation start temperature, while V showed little effect on it. Additionally, Nb-containing steels tend to generate a more classical upper bainitic structure, while V treated steels tend to create structure similar to the intragranular ferrite observed in the weld metal. Therefore, the improvement toughness of V treated HAZ is thought to result from such favourable microstructure, which occurs conditionally related to heat input and prefers to form under relatively low heat input. This is because that the suppression of M – A constituent can diminish under high heat input, causing reduced toughness. In Ti containing HAZs, the transformation start temperature can increase with the presence of intragranular ferrite as transformation product [11]. The positive effect of TiN on intragranular ferrite formation has been already discussed in the previous section.

There are several controversial ideas with regard to Nb contribution to microstructural evolution and corresponding properties in the HAZ [6, 115, 188, 189]. On the one hand, it is discussed that coarse grain size, bainite or M – A constituent are the major reason of low toughness in Nb treated steels and HAZ [10, 190]. Hattingh and Pienaar [188] pointed out the adverse influence of Nb on HAZ toughness at high C level (0.19%) and high heat input but Nb addition could also play a beneficial effect on toughness, depending on the C level and cooling rate. The work from Li et al. [190] showed that the addition of 0.03% Nb produced worse intercritical CGHAZ toughness than C-Mn-V and C-Mn steels as the result of large size and area fraction of M – A phases. However, in the view of Yang et al. [189], Nb had a strong retardation effect on the austenite transformation to pearlite and the addition of Nb was advantageously characterised by the appearance of the interlocking structure formation. Anyway, the properties of Nb-containing welds appear to be very sensitive to the control of heat input and the microstructure composition. Another HAZ feature of Nb-containing steels is the limited softening phenomenon due to the presence of multiple particles consisting of Nb, Mo and C, which contribute to low-temperature transformation products and precipitation hardening in the HAZ [11–13].

As described above, the topic about the effect of microalloy elements on HAZ toughness is always of great research interest. However, no comparison data of HAZ toughness is available in different microalloyed high-strength steel welds. As modern steels actually have quite different steel designs due to updated production process, it is essential to investigate the behaviour of microalloy addition in modern high-strength steels when welded by advanced welding technologies.

2.4.4 HAZ softening

HAZ softening is a subject of particular concern with respect to consideration of tensile properties of welded joints. This issue arose in the late 1980s during welding of steels having lean low carbon microalloyed chemistry or steels produced by accelerated cooling (AC) and direct quenching process [17]. It is observed that steel softening mostly occurs in the HAZ. This softened region is characterised by a hardness drop accompanied with microstructure change or precipitation effect. Since then, it is known that the presence of a softened zone in welded structure becomes a weak link. It could probably limit the design strength or toughness to a lower value. The effect of softening HAZ was extensively investigated in terms of transversal tensile strength, fatigue resistance, fracture toughness, and other properties of welds [17, 18, 191].

In terms of tensile behaviour, some characteristics of HAZ softening are critical to determine the tensile properties, such as strength mismatch, heat input, geometry, and relative thickness which is the ratio of soft zone width related to sample thickness [192, 193]. The value of relative thickness, acting as one index of strength loss, is suggested to be limited. However, a general agreement on the maximum value is not reached, which is reported to vary between 0.25 and 1 [18, 194]. Also, if the thickness or width of the tensile specimen is large enough, relative to the softening zone width, the strength of a weld joint can increase up to that of base metal because of constraints of plastic deformation on the softened HAZ [192, 195]. Pisarski and Dolby [17] assessed the importance of HAZ softening in a 550 MPa QT steel welded with mismatched weld metal. CTOD fracture toughness tests showed that the transition temperature of HAZ for overmatched weld was 60°C higher than the equivalent HAZ for undermatched weld. In the case of armour steels, an excellent ballistic performance is closely related to the softening extent in the HAZ and therefore a high energy density welding process is often suggested to alleviate this problem [191, 196]. In view of pipeline steel development (e.g. X120), Koo

et al. [197] reported that hardness softening less than 15 % (and more preferably less than 10 % of the base metal) was critical to design against an unacceptably soft HAZ.

In addition to the above understanding of the resultant properties change with the existence of HAZ softening, it is equally essential to gain deep understanding of the softening mechanism. The following factors are often discussed: manufacturing process (QT or TMCP), heat input and pre/post heat treatment, steel chemistry, and filler metal. Both TMCP and QT steel welds are prone to HAZ softening but QT steels can exert much wider softening zone compared with TMCP steels as shown in Fig. 2.32 [18]. To interpret the softening phenomena illustrated in Fig. 2.32, metallurgical aspects, mainly including phase transformation and precipitation effects, should be considered. According to the peak temperature during the weld thermal cycle, two softening reactions are often defined: tempering softening below A_{c1} temperature and transformation softening above A_{c1} , which further corresponds to the subcritical, intercritical ($A_{c1} - A_{c3}$) zone and part of FGHAZ.

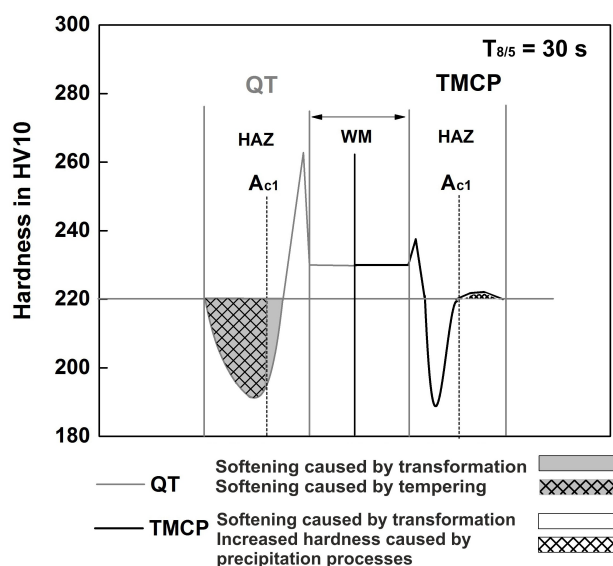


Fig. 2.32: Vickers hardness profile of welded joints from QT steel and TMCP steel [18]

Upon a tempering, the rejection of carbon from the supersaturated martensite occurs in the initial microstructure, and then carbide coarsening, spheroidisation, or recrystallisation of grains can also occur. As with a martensite/bainite mixture in a QT steel, all above mentioned carbide reactions can take place if tempering happens at an elevated temperature for a certain time. Likewise, for armour steels and advanced high-strength steels, it is common to encounter HAZ softening [133, 191, 196]. If a steel is subject to weld thermal cycle with T_p above A_{c1} , partial austenitisation occurs and austenite further decomposes into soft phase microstructure, e.g. ferrite or bainite. This also accelerates the HAZ softening behaviour. Fig. 2.32 also illustrates the contribution from the above two reactions to the final HAZ softening. It is evident that hardness drop for a QT weld comes only to a small extent from phase transformation reaction, while it depends to a large extent on tempering process. Similarly, in microalloyed TMCP welds, phase transformation produces soft microstructure with coarser grain size, resulting in remarkable softening. However, compared with QT steel, TMCP steel exhibits increased hardness rather than tempering softening when it is exposed to temperature below A_{c1} , due to a precipitation hardening effect.

HAZ softening can develop to certain extent but is strongly dependant on welding process and steel chemistry. Regarding various welding processes, it is imperative to keep heat input as low as possible in any welding process, to avoid excessive softening. Low heat input welding process increased the resistance to softening, where SMAW (shielded metal arc welding) was superior to GTAW and GMAW because the width of soft zone increased linearly with increasing heat input and cooling time, as reported by Mohandas et al. [198]. Mauer et al. [199] compared the effect of HAZ softening on tensile behaviour in 700 MPa TMCP steels welded by EBW (Electron beam welding) and GMAW. In their observation, the fracture in the GMAW welds occurred in the softened HAZ, while in EBW joints with low heat input the failure was located in base metal rather than in softened HAZ. Additionally, the work from Hochhauser et al. [18] related the softening characteristics to the variations of GMAW welding parameters. The results showed that reasonable softening under appropriate welding variables did not impair acceptable mechanical properties of the joint but excessive HAZ softening should be avoided. Thus, the referenced work suggests low heat input as significant precaution for welding high-strength QT steels in order to avoid excessive softening.

A deep understanding the metallurgical behaviour, illustrated in Fig. 2.32, has to be correlated with steel chemistry. The resistance to softening can be increased by the addition of carbide forming elements (e.g. Cr, Cu, Mo, B, Nb, V or Ti), which can provide precipitation hardening and increase the hardenability [13,18,198]. Without these alloying elements, a plain carbon steel can soften severely after tempering under high temperature, largely due to the rapid coarsening of cementite [200]. Therefore, to avoid excessive softening, it was common for pipeline steels to have B, Ti, Nb, and V elements in order to enhance the hardenability and tempering resistance. Kojima et al. [12] attributed the HAZ softening of high Cr ferritic steel to the lack of fine Nb and V carbonitrides coherent with the matrix. Increased C and Nb contents from HSLA80 to HSLA100 facilitated to resist excessive softening [201]. In addition, for Cu-precipitation-strengthened steel, a local softening occurred during fusion welding. This was because that the Cu-rich precipitates were dissolved and the re-precipitation on cooling was too less to fully recover the lost strength [183]. In the case of HAZ softening behaviour of DP steels, it was known that softening resistance increased with the addition of Cr and Mo [133]. Additionally, similar effect from Mn and Cr elements was also observed by other researchers [132]. In fact, the effect of alloy design on HAZ softening resistance is indirectly revealed by its influence on phase transformation process as well as precipitation behaviour. The overall effect of alloying is due to a combination of precipitation hardening in conjunction with the development of transformation product.

To reveal the influence of phase transformation on HAZ softening, Bang and Kim [195] estimated the extent of HAZ softening by using an established microstructural evolution model and a rule of mixtures (martensite, bainite and ferrite/pearlite). Also, Hanhold et al. [191] attributed the softening behaviour of armour steels to the formation of allotriomorphic ferrite. In the case of ultra-fine grained steel, softening can be explained by the coarsened grains and a high volume fraction of ferrite and M – A constituent [202].

The tempering of martensite is another key factor to determine the softening extent. A detailed substructure change of martensite phase is illustrated in Fig. 2.33, which is from DP steel with moderate CE subjected to non-isothermal tempering. The fine interlath plate-like cementite coupled with partial recovery of lath contributes to softening behaviour [132]. Likewise, major changes in hardness and strength can occur due to bainite tempering when the microstructure coarsens or the

onset of recrystallisation starts where equiaxed grains of ferrite replace the bainite plates [70]. Thus, it is notable that the suppression of carbide growth can be one effective approach to resist softening. In addition, the hardenability should be acceptably high thus facilitating bainite formation instead of coarse ferrite in the microstructure.

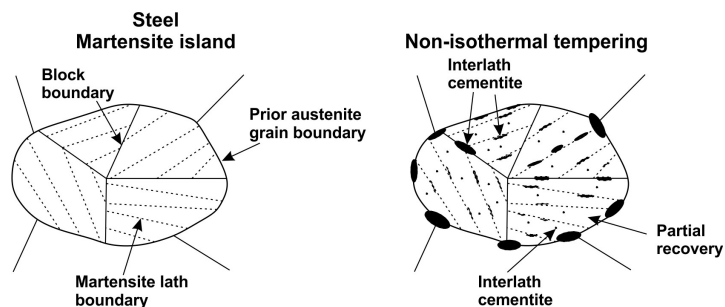


Fig. 2.33: Schematic illustration showing substructure changes of martensite phase in DP steel subjected to non-isothermal tempering [132]

Despite the fact that HAZ softening has been often investigated in TMCP steel, DP steel or armour steel, a more comprehensive analysis and comparison work is required on the influence of different microalloy elements. Knowledge of controlling the HAZ softening is critical for the integrity of modern microalloyed high-strength steel weldments.

3 Summary of literature and objectives

3.1 Summary of literature

The recent development of high-strength steels shows that scientific researches concerning advanced steel are still progressing rapidly. Application experiments, particularly in welding area, are required to understand how steel components can be fabricated efficiently to obtain optimum tailor-made properties. Some standards, specification and suggestion have been established for the instruction to weld high-strength steels. However, one problem pointed out by Dainelli and Maltrud [28], has to be seriously taken into account. The steel users and welding engineers cannot be aware of the varied chemistries and the resultant different weldability between steels offered by different producers. When welding steels having the same strength level, some problems, such as HAZ hardening, softening and reduced HAZ toughness, cannot be fully predictable by the often used carbon equivalent or other conventional methods [42]. Therefore, a particular focus of welding modern high-strength steels is on the chemical composition with regards to approaching an optimised welding control and a sound welded structure.

Regarding welding technology, advanced welding processes with high productivity have been developed to satisfy the demands of efficient manufacturing [58]. Such a modified spray arc welding was first introduced in 2005. Due to its attractive benefits, it becomes one of the most preferable welding processes in various fields. However, it is still unclear if this new technology will bring about new questions and challenges to weld modern high-strength steels. Thus, several important issues (tensile properties, HAZ toughness and softening) will be focused in the present study.

The above summarised state of the art describes advantages and challenges of microalloy addition in steels. Also, this gives an overall understanding of its influence on weld microstructure and mechanical properties. It is beneficial to control the austenite grain growth through adding grain refining elements. This can be achieved by well-adjusted welding procedure. Several factors, including alloy design, microalloy element type, and welding parameters, are known to influence phase transformation and final mechanical properties of the weld joints. Nevertheless, the exact effect of each factor and their interaction during welding of modern high-strength steels by advanced technology remains unclear. Based on the literature review, the most important issues that have not been addressed sufficiently so far are:

1. Due to specific characteristics of modified spray arc welding, deep penetration and high dilution effects gives rise to much alloy pick-up from base materials in final weld metal. Although some authors [148] pointed out that such alloy pick-up, particularly the Nb elements, can lead to microstructural changes in weld metal, one comparison work between different microalloy pick-ups on influencing weld metal transformation and toughness is not identified in the literature, especially in the case of microalloyed high-strength steels.
2. Regarding the influence of microalloy addition on HAZ toughness, it is of great interest to investigate their effect on restricting austenite grain growth behaviour and the subsequent phase transformation. Previous studies claimed that Ti addition has stronger pinning effect on austenite grain coarsening compared to Nb and V addition. However, in terms of the Ti/N ratio or the optimum Ti content, there are still controversial discussions [22, 185]. Moreover, few work was done to compare their influences on the HAZ toughness of microalloyed high-strength steels.

3. It is significant to understand the role of microalloy during phase transformation. Nb and V appear to affect the austenite decomposition conditionally depending on the applied heat input. The exact reason for the reduced toughness of Nb-containing HAZ is not completely understood from the metallurgical standpoint of view [6, 115, 188, 189]. Although some factors such as coarse grain, M-A constituent, upper bainite or other second phases are pointed out to play a certain role on influencing the toughness and fracture behaviour, further investigation is still necessary.
4. With respect to Ti addition on influencing HAZ toughness, two aspects are considered to be important, involving phase transformation and TiN coarsening behaviour. It is known that the beneficial effect of TiN on assisting the formation of intragranular acicular ferrite, however, coarse particle of TiN could probably act as crack initiator, resulting in brittle fracture and reduced HAZ toughness [14, 15]. Echeverria and Rodriguez-Ibabe [16] observed the negative effect of TiN strongly depended on the matrix microstructure. Such controversial opinions towards the role of TiN particle have to be further clarified.
5. HAZ softening phenomenon, regarded as one of the most concerning issues for component safety, has been often studied for welding TMCP, DP, or amour steels in order to control the softening extent and understand the influence of softening on tensile properties. It is suggested in the literature that strong carbide forming elements contribute to increased resistance to softening [18, 132, 183]. However, no comparable data for considering the roles of microalloy addition on softening extent was available. In addition, the role of microalloy elements on influencing softening mechanisms is seldom investigated.
6. A deep understanding of metallurgical evolution in microalloyed high-strength steel welds is essential when expecting balanced properties between HAZ toughness and softening. This also offers useful implications for the application of advanced modern welding technology. The comparison work on the role of different microalloy additions on weld performance provides a significant and valuable reference for steel users, engineers as well as steel manufacturers.

3.2 Objectives of the present study

This thesis aims, on the one hand, to give reasonable explanation on the previously discussed issues based on the experimental or simulated results. On the other hand, this thesis provides specific recommendations to steel manufacturers and users as well as weld engineers. More precisely, optimised welding parameters are suggested for welding different microalloyed steels having a comparable strength class. Hence, the objectives of the present research are:

1. Welding of high-strength steels with different sets of welding parameters and analysis of the microstructure evolution, tensile properties and toughness of the welded joints
2. Prediction of the precipitate characteristics (composition, dissolution temperature and volume fraction) in the base metal using thermodynamic software Thermo-Calc
3. Characterisation of microstructure and precipitate evolution occurring under different cooling rates
4. Comparison of the austenite grain growth behaviours and microstructural changes in the HAZs

simulated by induction equipment

5. Analysis of different microalloy concepts on phase transformation in weld metal (considering the alloy pick-up effect) and welded HAZs
6. Evaluation of the difference in mechanical properties arising from varied welding parameters and correlation between this difference and steel alloy composition, austenite grain size and microstructure changes
7. Assessment of HAZ softening behaviour, including hardness and microstructure, on the tensile properties and investigation of the HAZ softening mechanisms by dilatometry with a special purpose to understand the role of microalloy addition
8. Suggestions for welding modern microalloyed high-strength steels by advanced new technology in order to ensure weld joints with satisfied strength and toughness

4 Experimental procedure

4.1 Base materials

The materials investigated in the present study involve Nb-, Ti- and Ti+V-microalloyed S690QL steels from different steel manufacturers. Such a quenched and tempered steel today is widely used in steel construction (bridges, buildings or hydraulic steelwork) [4, 5]. The chemical composition of the three base materials and the corresponding standard requirements are shown in Table 4.1.

Table 4.1: Chemical composition and carbon equivalent value of the investigated steels

Steel	Chemical composition, wt.-%												
	C	Mn	Si	Cu	Cr	Ni	Al	Mo	Ti	Nb	V	N	CET
A	0.14	1.20	0.29	0.04	0.31	0.04	0.100	0.21	...	0.03	...	0.006	0.30
B	0.15	1.29	0.40	0.03	0.32	0.02	0.035	...	0.02	0.010	0.30
C	0.14	1.15	0.31	0.01	0.30	0.06	0.038	0.17	0.011	0.005	0.01	0.0064	0.29
EN	0.22	1.80	0.86	0.55	1.60	2.1	≥ 0.01	0.74	0.07	0.07	0.14	0.016	-

The three steels comply the requirements of chemical composition specified in the EN 10025-6 standard [3]. Steel A contains Nb and Mo, which increase the hardenability and promote bainite and carbide formation. It contains relatively high amount of Al that is often added to achieve a grain refinement and faster transformation. In contrast, steel B does not contain Mo. Its alloy design leads to relatively low hardenability. However, addition of Ti can restrain austenite grain growth. Steel C uses the combined effect from Ti and V, which provide grain refinement and precipitation strengthening. The three as-received steel plates have a thickness of 6 mm (steel A), 6.5 mm (steel B) and 8 mm (steel C). Measured mechanical properties are presented in Table 4.2. The three steels satisfy the mechanical requirements specified in the standard.

Table 4.2: Mechanical properties of the investigated steels

Steel	Mechanical properties				
	R _{p0.2} , MPa	R _{eH}	R _m , MPa	A, %	CVN energy, J (-40°C)
A	-	748	792	16	108 / 139
B	711	-	775	15	120 / 148
C	760	-	820	21	147 / 177
EN	690	-	770 – 940	14	27 / 30

4.2 Filler metal

The scope of this work comprises the investigation on butt welds from three microalloyed S690QL steels using identical filler metal. A welding wire (∅1.2 mm) with a yield strength of around 720 MPa was selected to achieve a matched weld metal. The classification is G Mn4Ni1.5CrMo according to EN12534 standard. The chemical composition of welding wire is presented in Table 4.3.

Table 4.3: Chemical composition of filler metal, wt.-%

C	Mn	Si	Cu	Cr	Ni	Al	Mo	Ti	Zr	V	P	S
0.09	1.71	0.59	0.02	0.22	1.49	0.008	0.49	0.045	0.006	0.004	0.005	0.011

4.3 Welding experiments

The direction of this work follows the industry requirement and development, which attempts to apply modern welding technology for high-strength steels. In the present study, automated welding system

was employed to fulfill the specific welding tasks. Also, a specific geometry design is done to approach a desirable productivity and low cost. All experimental work was carried out at Bundesanstalt für Materialforschung und –prüfung (BAM). A large amount of preliminary welding was performed in order to understand the influence of welding variables on weld geometry [203]. The present study is to investigate the metallurgical aspects and mechanical properties of weldments under different welding conditions. For this purpose, the welding parameters are selected from the preliminary work results.

All steel plates were welded using semiautomated gas metal arc welding (GMAW) system. Modified spray arc technique was applied to conduct V-groove single-pass butt welds (opening angle 30°) with a shielding gas of 82% Ar and 18% CO_2 . No preheating or post heating treatment was done. The welded plates were subjected to radiographic tests for detecting internal imperfections, according to DIN EN 17636-1:2013 standard [204]. After radiographic examination, welded plates without defects or with acceptable defects were selected to make further microstructural analysis and mechanical testing. Fig. 4.1 illustrates the geometry of welded plate and locations of mechanical specimens.

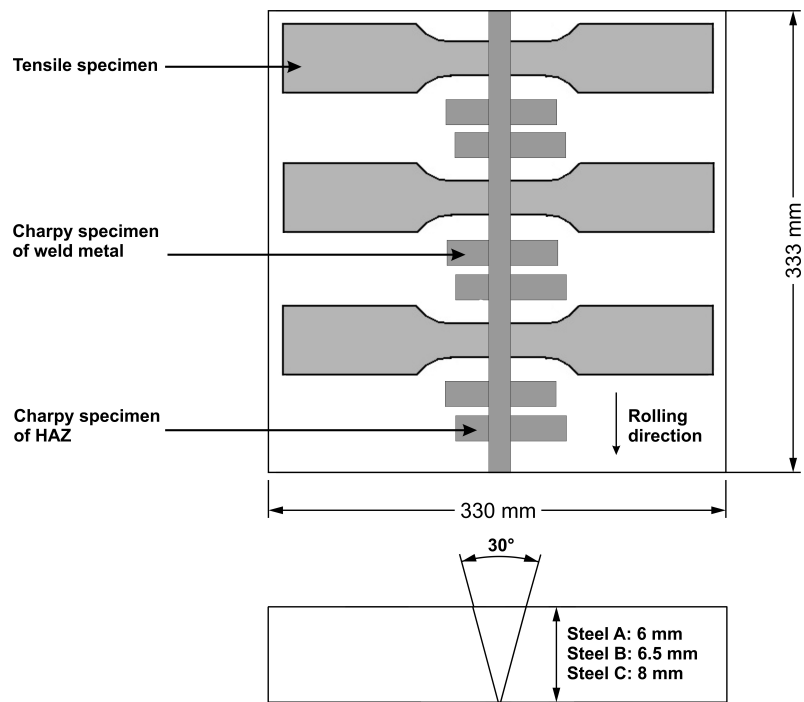


Fig. 4.1: Schematic of welded plates and specimen positions for mechanical tests

During welding, thermocouple was inserted into each weld pool to record the thermal cycle. The measured $t_{8/5}$ time of thermal cycle represents the cooling rate. The dilution factor can be calculated from measuring geometric cross sectional areas of the deposited filler metal and dissolved base material (Fig. 4.2). An assessment of the dilution is essential because the weld metal property is determined by the final microstructure, which is influenced by the chemical composition and cooling rate [102, 148].

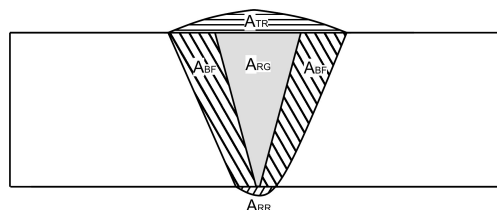


Fig. 4.2: Schematic view of different parts of cross section considered in a graphical measurement

The total weld deposit (A_{WD}) constitutes part of top reinforcement (area of this part is A_{TR}), part of root reinforcement (A_{RR}), part of base metal fusion (A_{BF}), part of weld root gap (A_{RG}). The calculation of dilution percentage (P_{DL}) is presented as follows:

$$P_{DL} = \frac{A_{BF}}{A_{WD}} \times 100\% \quad (4.1)$$

In the present study, a matrix of experiments was intentionally designed to obtain three cooling rates: slow, medium and fast. The welding parameters applied for each weld depended on the thickness of steel plate. Accordingly, different welding parameters were used for the three steels in order to approach the same level of cooling rate. The welding parameters, cooling rate and dilution factor are shown in Table 4.4.

Table 4.4: Welding Parameters, cooling rate and dilution for each weld

Weld	Welding speed, cm/min	Current, A	Voltage, V	Heat input, kJ/cm	Dilution, %	Cooling time $t_{8/5}$, s
A1	40	283.9	28.9	12.31	46.7	20.4
A2	50	291.7	29.3	10.26	49.6	15.3
A3	60	293	29.3	8.58	50	11.4
B1	80	379.8	34.5	9.83	55.1	17.3
B2	70	350.8	32.1	9.65	54.4	15.0
B3	80	328.1	31.2	7.68	51.1	11.2
C1	46	340.0	28.6	12.68	51.4	18.0
C2	55	340.0	28.6	10.61	48.7	15.0
C3	67	342.0	28.7	8.79	46.9	11.2

4.4 Principles of characterisation methods

4.4.1 Light optical microscopy

To characterise the microstructure, grain boundaries or to highlight specific structure features and phases, all the metallographic specimens were ground, mechanically polished and etched with different etchants. The 2 % Nital solution is commonly used to reveal ferrite grain boundaries in low carbon steels. The applied etching time is around 10 s – 15 s. When the specimens were prepared for scanning electron microscopy, the etching time can be extended to 20 s. The optical microscopy was done on a Reicher-Jung Polyvar MET microscopy with Leica DFC 290 camera. ImagePro Plus imaging and Imagic IMS software were used for image analysis.

The purpose to reveal the austenite grain boundaries was achieved by etching with an aqueous solution of picric acid with 80 mg CuCl_2 and 60 ml Agepon as the surface active reagent at 75°C – 80°C for 15 s. Afterwards, slight polishing and repeated etching for two or three times were sometimes required to obtain clear grain boundary. The austenite grain size measurement was determined through linear intercept method in accordance to DIN EN ISO 643 [205].

4.4.2 Scanning electron microscopy

Etched cross-section welds or simulated HAZ samples were observed using a LEO 1530 VP Gemini scanning electron microscopy. A SEM image can provide various structure information, which depends on the detector and the detected signal types.

A SEM contains an electron source at the top of a main chamber. The specimen is placed under the optical system. The primary electrons are extracted from a field emission source (Schottky type in the present study) and accelerated with an energy up to 30 keV. An interaction between the primary electrons and the specimen produces a variety of inelastic or elastic collisions, where some interactions lead to distinct emission signals such as X-ray. Each signal generates from a specific interaction volume within the specimen and can be collected by detector, which can be used to analyse the properties of the specimen. Hence, to adjust different signals should consider the source accelerating voltage, source diameter, and information about the specimen such as microstructure, composition, and crystal structure.

When the accelerated electrons penetrate the surface and initiate a number of elastic and inelastic interactions with the specimen. These interactions generate a range of signals including partly the backscattered electrons (BSE), low energy secondary electrons (SE), characteristic photons (X-rays and Auger electrons). The energy spectrum of emitted electrons is classified into three main groups: (a) elastically scattered electrons with energy similar to primary electrons (E_0), (b) multiply scattered electrons with energies in the range of 50 eV to E_0 , and (c) low-energy electrons (i.e. < 50 eV) [206]. A backscattered electron is defined as one which has experienced a single or multiple scattering and emits with energy higher than 50 eV. While a secondary electron possesses low energy (< 50 eV).

Fig. 4.3 illustrates the interaction volume of different emission signals within a specimen [206, 207]. Secondary electrons, with comparatively low energies, are released from surface and carry high resolution topographic information but no composition information. Due to this characteristic, the secondary electrons signal is by far the most widely utilized signal for resolving the surface structure down to the resolution of 1.5 nm for field emission SEM. Backscattered electrons have higher energy and large emission region. When the electron-sample interaction occurs even deeper, much less electrons are detected but characteristic X-rays that are generated from the whole interaction volume are emitted and can provide more quantitative elemental information. The BSE carry qualitative information about the composition and can indicate on the existence of lighter atoms regions and heavier atoms regions.

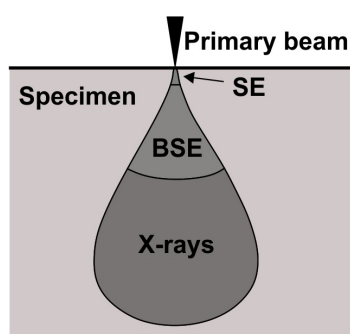


Fig. 4.3: Schematic illustration of the interaction volumes and the emitted signals [206, 207]

Backscattered electrons image can provide a qualitative information about the composition. It shows different contrasts between the phases in one sample despite a uniform topology. This is resulted by the number of backscattered electrons which are governed by the atomic number (Z contrast) of the components. The "bright" region in the image correlates with higher Z than the "dark" region [206].

The LEO 1530 VP Gemini SEM is equipped with a quadrant backscatter detector. With this detector it can offer a quick method to distinguish inclusions or precipitates in the weld metal and base materials.

In the QBSD mode, the SEM is operated at an accelerated voltage of 15 kV or 20 kV with a working distance varying from 8 mm to 10 mm.

Fig. 4.4 shows a representative image of different precipitates acquired in the QBSD mode. The Z contrast in a backscatter electron image reveals a distribution of Ti-rich precipitates (Fig. 4.4 (a)). Likewise, inclusions in weld metal also appear as dark particles against the ferritic matrix, whereas the Nb-rich precipitates appear as bright particles (Fig. 4.4 (b)). Additionally, point analysis by EDX, provides chemical composition and further allows the identification of Ti-rich, Nb-rich carbonitrides or other oxides.

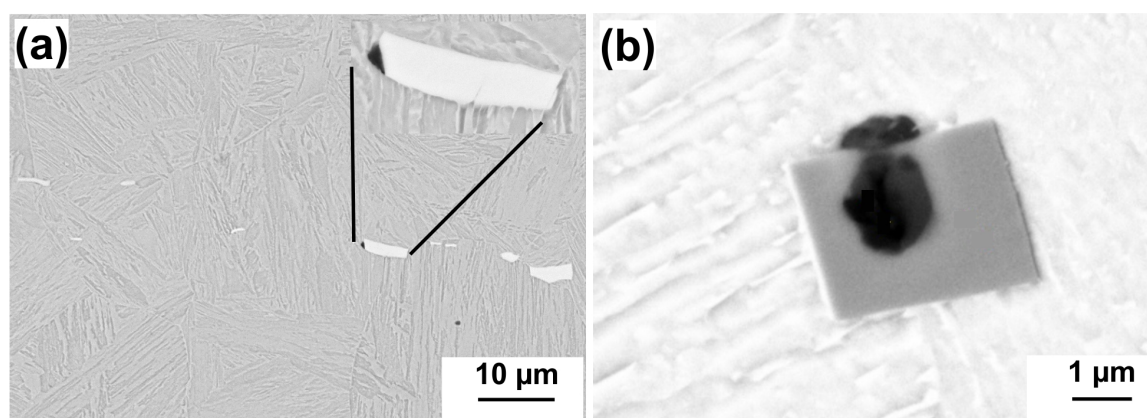


Fig. 4.4: Images of (a) Nb-rich and (b) Ti-rich particles in the QBSD mode

The LEO 1530 VP Gemini SEM is equipped with two detectors for secondary electrons: a high efficiency in-lens detector and a conventional secondary electron detector (Everhart-Thornley (ET)). The secondary electrons can be further classified to the SE1 and SE2 types electrons with different energies. The SE1 electrons are generated by the primary electron beam as it hits the surface of specimen. They can be detected efficiently by in-lens detector even at low voltages and small working distances. The SE1 electrons can escape close to the surface, resulting in high resolution images with surface information. The SE2 are generated by high energy backscattered electrons and escape deeper from the bulk, leading to obtain somewhat lower resolution image than SE1 electrons.

In the present work, the in-lens secondary electron detector was applied for observation on nano-scale precipitates or other small phases in much higher magnification. Working parameters for different detectors were adjusted according to specific purposes. In SE2 mode, the accelerating voltage was 15 kV and the large working distance increases the depth of field, whereas low distance contributed to higher resolution. Around 10 mm and 5 mm were used in the present study. In SE1 mode, SEM operated with a voltage of 15 kV and working distance of 6 mm. All fracture surfaces of Charpy specimens were analysed using a Tescan VEGA3 scanning electron microscopy, which is equipped only with a secondary electron detector. The operation voltage was at 20 kV and working distance varied from 18 mm to 45 mm.

4.4.3 Energy dispersive X-ray spectroscopy

In SEM, the interaction of the incident beam with the sample generates characteristic X-rays. The formation of the characteristic X-rays is the result of the collision between the energetic incident beam and the electrons from the inner shell of the atom. This collision is leaving a vacancy in the shell. As an excited electron returns to the ground state filling the inner shell hole, it yields X-rays that

are characteristic to the elements in which the electron transition occurs. Such kind of characteristic X-rays allow the elements in the sample to be identified in a qualitative or quantitative manner [206]. In the SEM, the spectrum consists of the characteristic peaks and this can be analysed by energy dispersive X-ray spectrometry (EDS). A Bruker XFlash 5030 EDX unit was used in conjunction with the LEO 1530 VP Gemini SEM. The spectra were analysed using Esprit 1.9 software. The Tescan VEGA3 SEM was equipped with an Oxford X-Max^N EDX unit. The spectra were analysed using AZtec software. Spot and area analysis was conducted to identify the inclusions or chemical composition of a defined area.

4.4.4 Electron backscatter diffraction

Electron backscatter diffraction (EBSD) is one SEM based technique that provides quantitative microstructural information about the crystallographic nature of materials. One stationary electron beam strikes a flat, highly polished sample tilted at 70° from horizontal. A carefully calibrated camera captures the patterns of high energy diffracted electrons. These patterns show the characteristics of the crystal structure and orientation of the sample. The analysis of these patterns is used to reveal structural information (such as grain boundary character, grain size, grain orientation, texture and phase identity). To create one mapping database especially across a polycrystalline sample, the beam moves from pixel to pixel in a grid and at each point the orientation of individual pixel are recorded using electron backscattered patterns. Such mapping data can be further evaluated to investigate the phase transformation, grain size and fracture mechanism in steels or other metals on a microscopic scale [208]. In the case of the present ferritic weld, electron backscattering diffraction is applied to characterise different types of weld structure.

4.4.5 Focused ion beam technique

Focused ion beam (FIB) machining is a technique for TEM foil sample fabrication. It uses a focused Gallium ion beam to scan the sample surface in a similar way as a SEM utilizes electrons. Since the ions strike the sample surface with elastic ion-atom collisions the result is a removal of the surface atoms. The interaction of ions with the material also generates secondary ions and secondary electrons, which can be collected to form an image. FIB technique provides several advantages over conventional electro-polishing methods for TEM observation [209]. FIB milling allows making TEM samples extremely thin (< 200 nm) with large, uniform and relatively contamination free surface. In the present work, the FEI dual beam system was used, by which a high accuracy was achieved. This system is based on the in-situ SEM high resolution imaging and precise manipulation.

In the present work, the Quanta 3D FEG was used to prepare TEM foil sample. The beam acceleration voltage was 20 kV and current range was from 60 nA to 0.5 nA. The TEM foil sample was precisely cut out of the bulk dilatometer specimens. Selected area of interest was containing the grain boundary. The area to be thinned was selected from the secondary electron image. The thinning process was performed several times and the final thickness of TEM foil sample was reduced to less than 150 nm. Fig. 4.5 (a) shows the TEM samples preparation using FIB in-situ lift-out process. Fig. 4.5 (b) shows the thin foil welded to TEM grid for final milling, where the ferrite plates with different orientation can be seen from the different contrast.

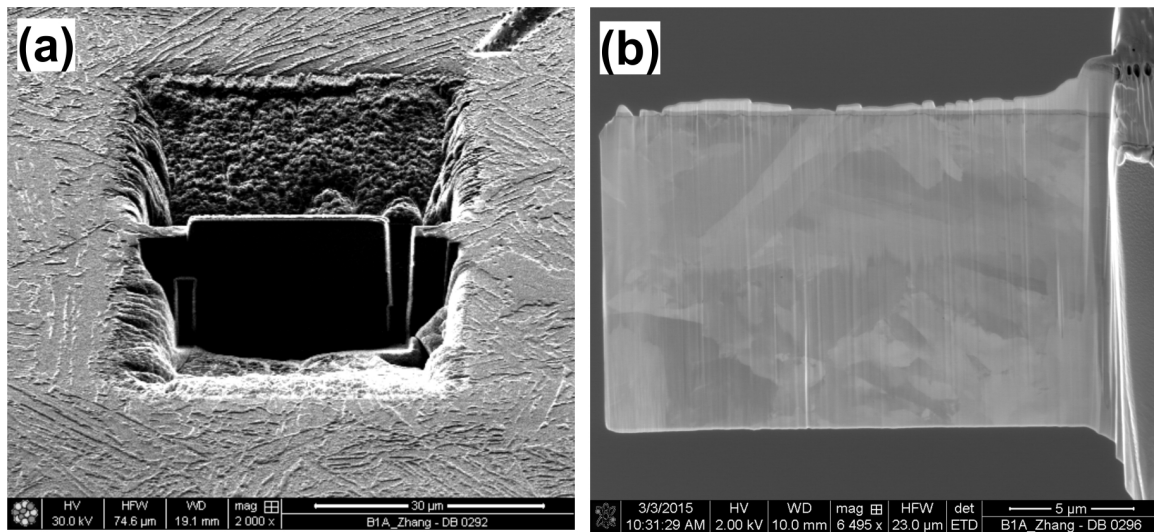


Fig. 4.5: TEM sample preparation using FIB imaging in secondary ion (a) and secondary electron (b) mode

4.4.6 Transmission electron microscopy

Transmission electron microscopy (TEM) was performed using JEOL JEM 2200FS field emission transmission electron microscopy operating at 200 kV acceleration voltage. The two important methods used in the present study are scanning transmission electron microscopy (STEM) and high-resolution TEM (HRTEM). In STEM, two types of detectors are used: bright-field (BF) detector and high-angle annular dark-field (HAADF) detector. BF-detector is centred on the optical axis and its BF image shows the intensity of low angle elastic and inelastic scattering of the incident beam with the atoms of the sample. HAADF-detector is ring-shaped. The HAADF image consists of the electrons scattered in higher angles, which have interaction close to the nucleus of the atoms within the sample [209]. Therefore, HAADF image contains chemical information with atomic resolution and high contrast (Z contrast imaging) when structural heterogeneities occurs due to heavy and light elements. This advantage makes the HAADF technique to be particularly suited for studying precipitates in steels and alloys.

The first step is to rapidly highlight the location of nano-scale precipitates in the present steel by using HAADF detector and to record the Z-contrast image. Then the chemical analysis of precipitates is carried out by EDX. This energy dispersive X-ray spectroscopy is very useful in mapping out elemental spatial distribution and identifying precipitates and correlating those to the rest of the results. In comparison to energy filtered TEM (EFTEM), EDX has a relatively poor resolution, because sometimes carbon and nitrogen occur in very small precipitates that cannot be revealed in elements mapping process. FETEM works by combing both imaging and spectroscopy, which is often used to image a few selected spectral features. When electrons undergo inelastic scattering during interaction with the sample, they will lose a certain amount of energy. Such specific energy loss can be characteristic for the atoms that are contained in the sample. By choosing an energy band one can transmit only the electrons which have lost a specified amount of energy. The energy-filtered image is formed based on these electrons [209]. Therefore, EFTEM allows to generate high resolution spatial maps (< 1 nm) of the element of interest across the sample [210]. There are several example of EFTEM in steels such as grain boundary characterisation and different nano precipitates analysis (TiN, VN, and other different MX phases) [211, 212]. In the present case, Ti, C and N elements were mapped by selection

of suitable energy windows, in order to fast identify the elemental distributions within precipitates. Another type of spectroscopy is by studying the electron energy loss. This process is known as electron energy loss spectroscopy (EELS) that has been also applied to determine the chemical composition of nano-scaled precipitates. The EELS spectra allows us to obtain a satisfactory detailed information about composition at investigated areas [213]. In the present TEM work, EELS and EDX data have been compared to confirm the composition of precipitates. The precipitate/matrix interface structure was analysed by HRTEM and nano-beam diffraction (NBD). The HRTEM images of the precipitates were taken in very thin regions of foil and then evaluated by means of fast Fourier transformation (FFT). Such nano-diffraction provides crystallographic information on near atomic scale and allows local structure, orientation and defects to be determined in the investigated area.

4.5 Mechanical testing

4.5.1 Hardness

Vickers macro hardness measurements were completed on flat cross-section samples. A standard Vickers pyramid indentation load of 10 kgf was used. The full load was normally applied for 15 s. Tests of welded joints were performed according to DIN EN ISO 9015-1:2011 [214]. One representative measurement is shown in Fig. 4.6. Hardness values of simulated HAZ specimens were averaged from at least five single indentations. For hardness mapping of welded joints, Vickers indentation with a load of 0.1 kgf (HV0.1) was performed every 0.1 mm using fully-automated UCI (Ultrasonic contact impedance) hardness scanner UT 200. Hardness scanning on a cross-section of welded joints can show the hardness distribution in the weld metal, HAZ and base metal.



Fig. 4.6: Hardness measurement on a cross-section sample

4.5.2 Tensile test

Tensile tests of base materials and welded joints were performed at room temperature. Static tensile tests were carried out with a constant strain rate of 0.05 mm/s according to DIN EN ISO 6892-1: 2009 [215]. Standard tensile specimens were fabricated according to DIN EN ISO 4136: 2013 [216]. The weld reinforcement was machined away so that the weld was flush with the exterior of the base material. The specimen geometry and images are shown in Fig. 4.7.

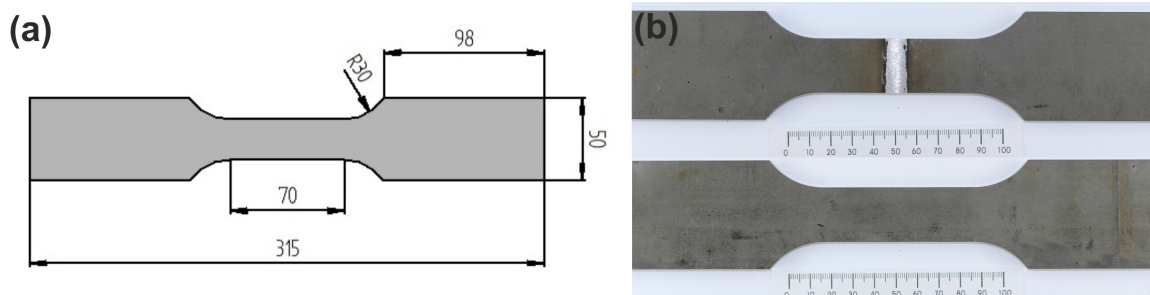


Fig. 4.7: Geometry (in mm) (a) and image (b) of the tensile specimen

4.5.3 Charpy impact test

The Charpy V-notch impact tests were performed at -40°C according to standard DIN EN ISO 148-1: 2011 using a 300 J Wolpert impact test machine [217]. To evaluate the Charpy toughness of different microstructure, at least three specimens from weld metals and HAZs were obtained from the start-point, middle and end part of welds and then machined into the size of 5 mm x 10 mm x 55 mm according to DIN EN ISO 9016:2011 [218], as illustrated in Fig. 4.8.

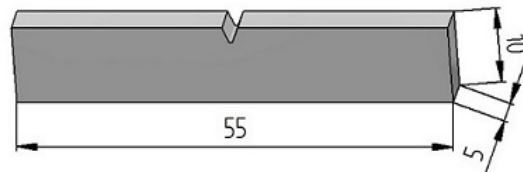


Fig. 4.8: Geometry of the Charpy V-notch specimen, in mm

4.6 Physical simulation of heat affected zone

4.6.1 Austenite grain growth simulation

There are four regions that are included in the HAZ: (1) the CGHAZ region; (2) the FGHAZ region; (3) the intercritical HAZ region; (4) the subcritical HAZ region, as shown in Fig. 2.13. These regions are defined by the peak temperature of thermal cycle which the steel underwent during welding process. Above A_{c3} temperature, the austenitisation can take place and austenite grains start to grow. In the present study, four peak temperatures were chosen to investigate the austenite grain growth behaviour. Two temperatures of 1300°C and 1200°C were selected to simulate the CGHAZ and two temperatures of 1100°C and 1000°C were representative of the FGHAZ.

The samples were machined to 6 mm x 8 mm x 13 mm (steel A, B) and 8 mm x 8 mm x 10 mm (steel C). A type S-thermocouple was spot-welded onto the middle of sample for temperature record during simulated thermal cycle. Such a thermal cycle was controlled by an induction heating and nitrogen quench-gas spray system. The heating rate was around 80 K/s and cooling rate was controlled to achieve $t_{8/5}$ time of around 15 s. The holding time at peak temperature was around 1 s. In simulated specimens, prior austenite grain size measurement, hardness and microstructure analysis have been carried out.

4.6.2 Dilatometry

Cylindrical dilatometry samples with diameter of 4 mm and length of 10 mm were taken transverse to the rolling direction. A Baehr DIL – 805A\D dilatometer was used to impose various heat treatment schedules, during which the temperature and expansion data were recorded. Since phase changes and precipitation or dissolution of different carbides can induce a change in the lattice parameter of iron, these changes can further induce a macroscopic volume changes in the sample. So these changes can be precisely recorded by the dilatometer.

Inside the dilatometer vacuum chamber, the specimen is placed between two quartz tubes holders. A type S thermocouples is spot-welded on the middle of the samples in order to record the programmed temperature cycle. There is one induction coil surrounding the specimen that has also an inner coil for controlled inert gas cooling. During the heating and cooling process, the dimensional changes can

be recorded through a high-sensitivity linear transducer. In the present study, the thermal cycle of simulated HAZ was almost equivalent to thermal cycles in the as-welded HAZs through choosing a distributed Newton type of cooling law.

In order to simulate the different critical regions of the HAZ, it is first necessary to identify the critical transformation temperatures, the A_{c1} and A_{c3} temperature. This data was then used to formulate an experimental matrix of simulated HAZ samples that can represent different HAZ regions. Six experimental groups were characterised by a peak temperature from 700°C to 900°C (step of 40°C). An identical heating rate as well as cooling rate of $t_{8/5}$ 15 s was applied. This cooling process was controlled by quenching the samples at defined peak temperature with an inert gas jet. The simulated thermal cycle curve is shown in Fig. 4.9 (a). The post-processing and analysis on data of phase transformation is illustrated in Fig. 4.9 (b).

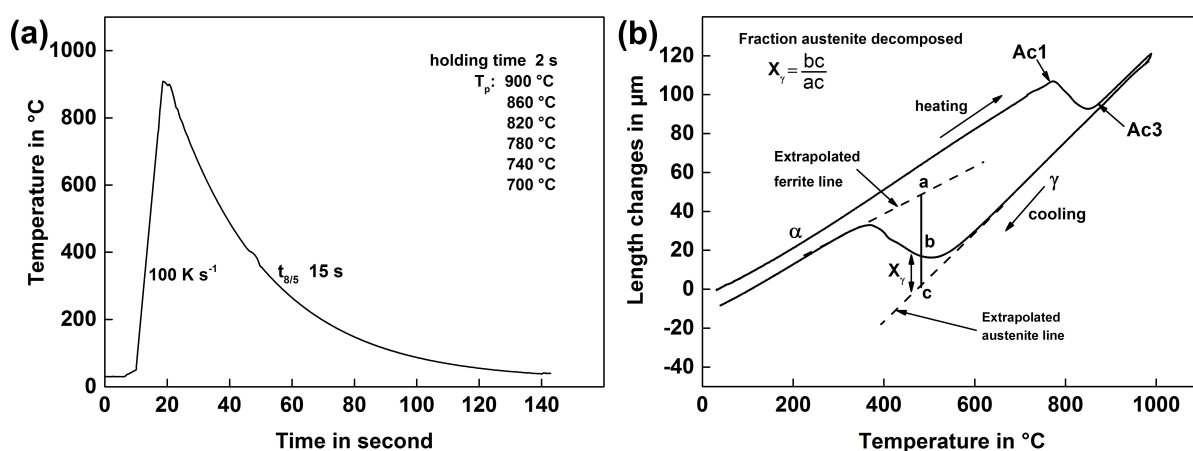


Fig. 4.9: Thermal cycle (a) used in dilatometry experiment and the analysis on dilatation curve (b)

An additional, very fast cooling rate with maximum gas flow speed was applied on some samples. This allowed an observation of ferrite nucleation and growth during phase transformation as the microstructure can be immediately frozen by sudden cooling. Therefore, for Ti-microalloyed steel B, in order to reveal the complex ferrite transformation, samples were heated up to 980°C and then cooled down to 560°C or 570°C, at which the phase transformation just started and very limited amount of ferrite was formed. Immediately at this temperature, fast quenching gas jet was directly applied to the specimens. As a result, martensite transformation started and then the microstructure remained newly-formed ferrite in the surroundings of martensite matrix. The analysis on dilatation data and the direct microstructural observation can reveal the characteristics of ferrite nucleation and growth (e.g. temperature, morphology, position).

4.7 Thermodynamic prediction of phase stability

Thermo-Calc software can be used to predict the equilibrium phase balance, precipitate formation temperatures, transformation temperatures and the phase compositions [219]. For the present work the database TCFE6 was used for the phase diagram calculation and prediction of different microalloy precipitates such as TiN, Nb(C,N), and V-rich carbonitrides. The input data contains most of chemical composition, as shown in Table 4.1. Phase fraction of different carbonitrides as a function of temperature are derived from stepped equilibrium calculation in a temperature range of 500°C to 1600°C. The thermodynamics calculation can provide information about the stability, volume fraction and composition of microalloy precipitates in the three steels.

5 Microstructure characterisation and mechanical properties of base material

This chapter presents the metallurgical and mechanical characterisation for the three investigated steels. As the three steels differ greatly in chemical composition despite their similar strength, it is essential to characterise their as-received state prior to welding. Various characterisation methods, such as light microscopy and high resolution SEM combined with EDX, are applied to observe the microstructure. Thermodynamic calculation with Thermo-Calc software is carried out to confirm the experimental observations of microalloy precipitates. The major differences in the microstructure between the three steels are discussed. As a consequence of these differences, the potential impacts on subsequent welded joints may differ among the three steel.

5.1 Microstructure of base materials

Optical micrographs of the three steels in as-received condition are shown in Fig. 5.1. All steels exhibit a bainite – martensite microstructure under optical microscopy. Coloured precipitates (most are in orange or bright gold) are sometimes found aligned in the rolling direction.

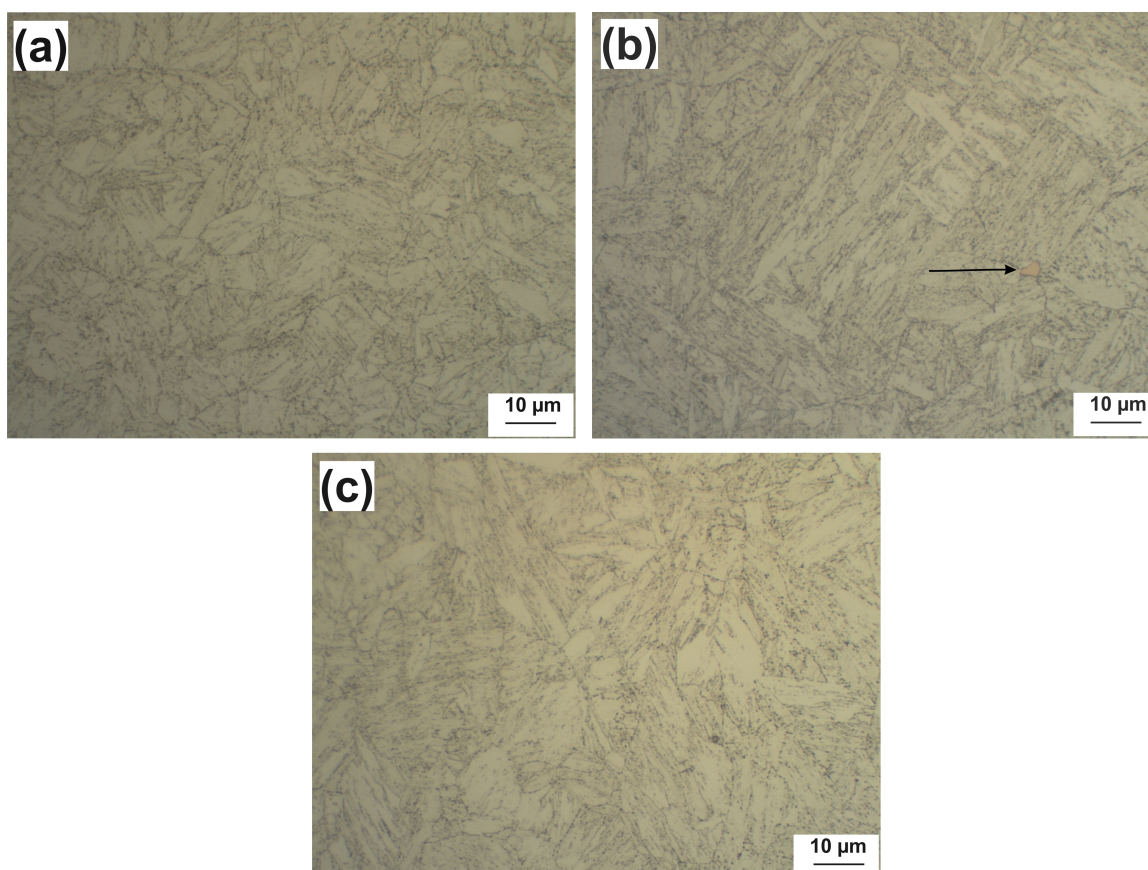


Fig. 5.1: Optical micrographs of steel A (a), steel B (b) and steel C (c)

In microstructural perspective, there is no great difference between the three steels. The hardness for three steels is almost at the same level, around $270 \text{ HV}_{10} \pm 5 \text{ HV}_{10}$. But the prior austenite grain size of the three steels are $8.6 \mu\text{m} \pm 0.1 \mu\text{m}$, $21.3 \mu\text{m} \pm 4.7 \mu\text{m}$ and $9.7 \mu\text{m} \pm 1.2 \mu\text{m}$, respectively. Different sized austenite grain combined with different chemical compositions can influence the phase

transformation in the HAZs and the mechanical properties, which is in details discussed in the chapter of HAZs. Also, SEM micrographs are used to more accurately delineate the micro-constituents. A representative precipitate distribution is shown in Fig. 5.2.

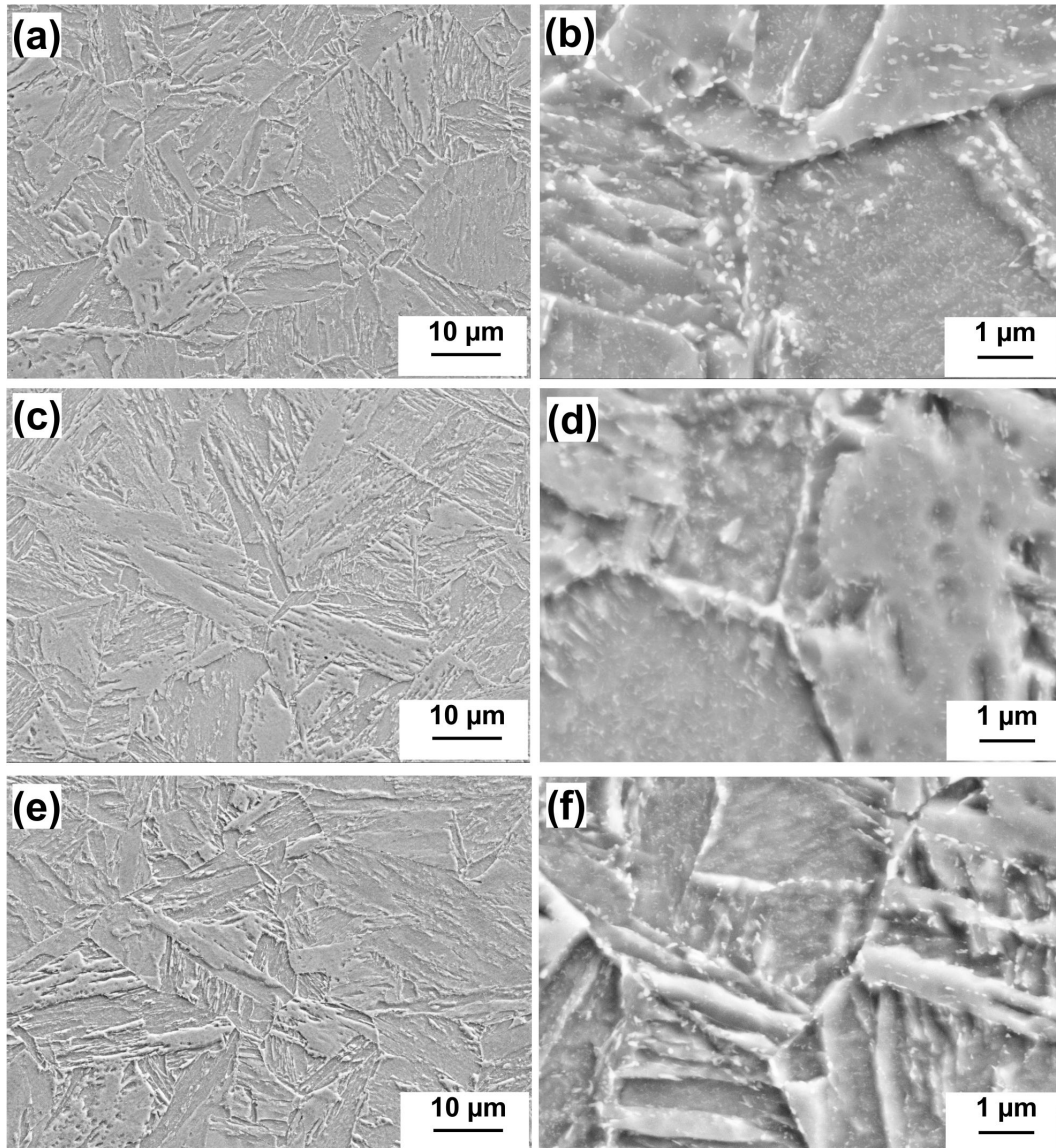


Fig. 5.2: SEM images of steel A (a, b), steel B (c, d), and steel C (e, f)

Magnified view of bainite and tempered martensite is clearly detected. Meanwhile, different types of precipitate distributions are observed in as-received base plate. Prior austenite grain boundaries were populated by a mixture of very coarse white or bright precipitates. At lath boundaries coarse precipitates were formed. Some intra-lath needle finer precipitates are observed in the martensite and bainite. Although this phase could not be identified by SEM, it is assumed from literature that they are probably carbides (e.g. M_3C) that are typical of lower bainite and tempered martensite [132]. Also, it could be expected that dispersions of nano-scale Ti, Nb, or V-rich carbonitrides coupled with other alloy precipitates exist in steels. This point has to be confirmed by thermodynamic calculation and experimental results.

5.2 Microalloy carbonitrides

5.2.1 Prediction by thermodynamic calculation

The quantitative TEM for the three steels was not performed in this study, due to limited time. However, many efforts have been made to identify the type of microalloy precipitates present in steels by thermodynamic simulation and direct or indirect experimental works. Microalloy precipitation under equilibrium condition has been predicted by Thermo-Calc calculation. This thermodynamic calculation approach can provide the information about the stability and the total volume fraction of microalloy precipitates in steels.

Equilibrium phase diagrams within a temperature range of interest from 500°C and 1600°C have been calculated for the three steels, as shown in Fig. 5.3. The three steels have a similar solidus temperature around 1500°C. On further cooling, austenite starts to form on the expense of delta ferrite. At below A_{e4} temperature (the onset of delta ferrite formation) the steels are fully austenitic. Table 5.1 lists the detailed phase transformation temperature under equilibrium condition. Further inspection of phase transformation from high to low temperature provides the precipitation information of different microalloy precipitates.

Table 5.1: Calculated equilibrium phase transformation temperatures using Thermo-Calc

Steel	A_{e1} , °C	A_{e3} , °C	A_{e4} , °C
A	710	842	1482
B	701	829	1484
C	704	842	1483

In the steel A, at around 1190°C AlN firstly precipitates in austenite followed by precipitation of Nb(C,N) around 1140°C (Fig. 5.3 (a)). Due to the mutual solubility of different niobium precipitates NbC and NbN, Nb(C,N) is frequently found in steels. But the atomic ratio between substitutional solute atom (Nb) and interstitial atoms (C,N) is estimated to be non-stoichiometric because of vacancies in the interstitial sites of the Nb(C,N) crystal lattice, as shown in Fig. 5.4. In addition, Nb(C,N) start with the metal lattice filled with Nb and the non-metal lattice with about 0.65 of C and 0.35 of N. When diffusion occurs inside carbonitrides under slow cooling, it would get richer in C and at very low temperatures, Cr would probably enter it.

Fig. 5.3 (b) shows the phase diagram predicted for the Ti-containing steel. The precipitation of Ti(C,N) takes place much earlier, when it is at the end of solidification, around 1486°C. The precipitate starts with the metal lattice filled with Ti and the non-metal lattice with almost only N (Fig. 5.5). Only if there was diffusion inside, under quite slow cooling, the carbonitrides would get some enrichment in C, especially when AlN starts getting some Al from the matrix. Many researchers have observed that a binary compound, TiN, without mixing of other solute species, can be often obtained in Ti-containing steels and such TiN particle show little dissolution in the HAZ except close to fusion line [169, 174]. AlN precipitate also forms but the onset temperature decreases to a relatively low temperature of around 1080°C.

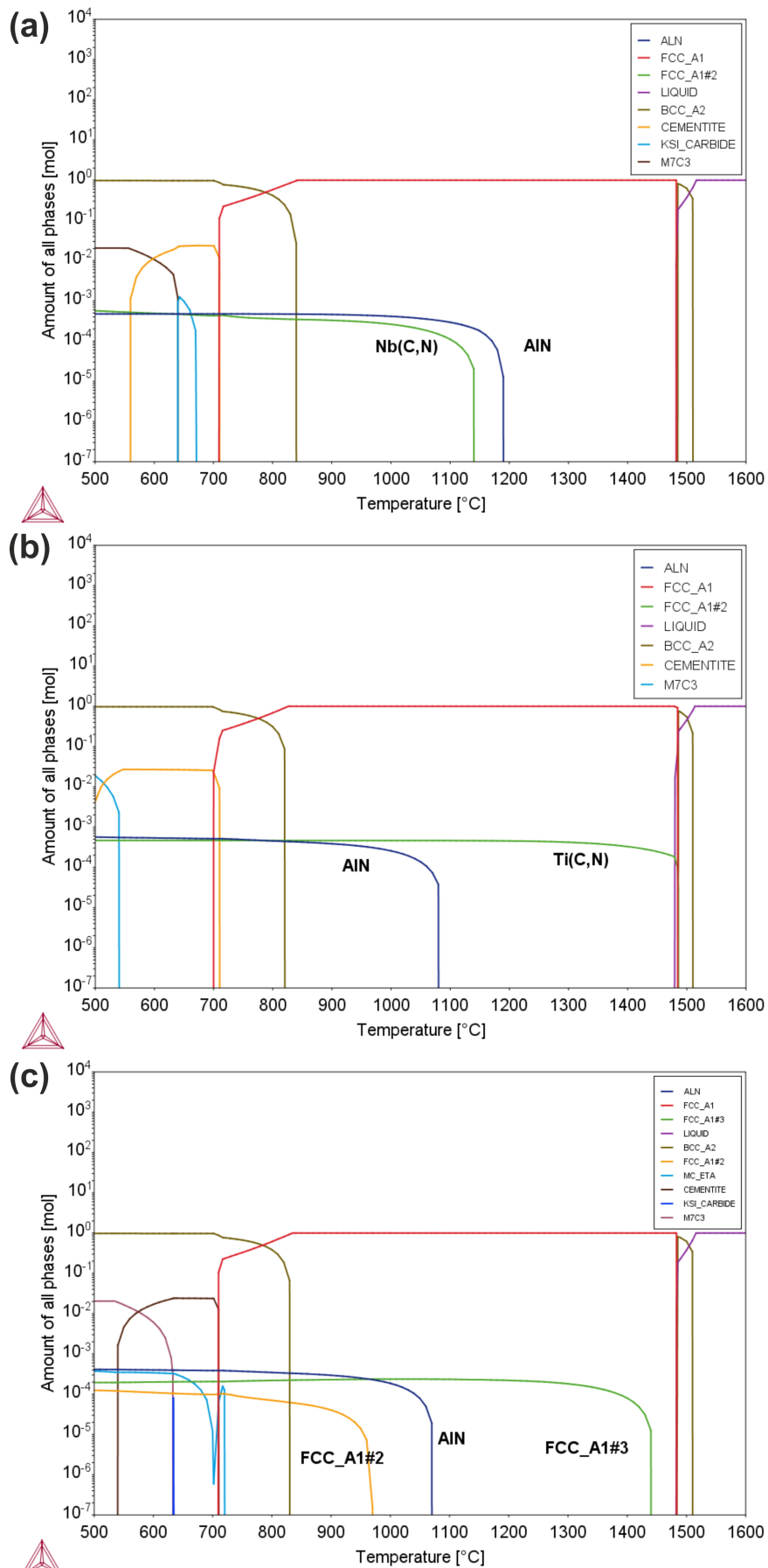


Fig. 5.3: Phase diagrams calculated for steel A (a), steel B (b) and steel C (c)

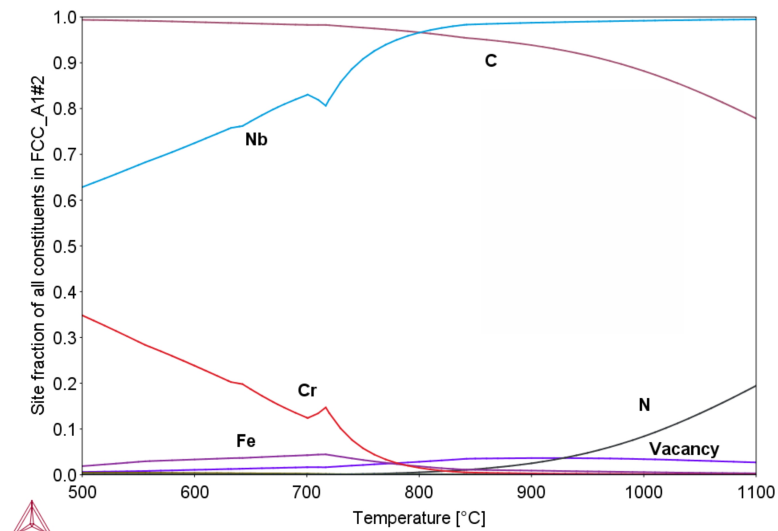


Fig. 5.4: Nb(C,N) composition as functions of temperature

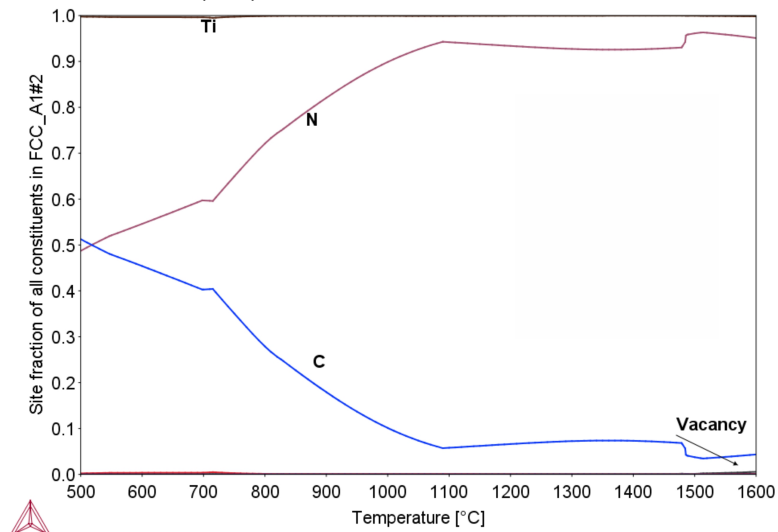


Fig. 5.5: Ti(C,N) composition as functions of temperature

The types of precipitates that form in the Ti+V-containing steel were predicted to be complex due to the multi-microalloy addition. In that case, more than one type of microalloy precipitate exist (Fig. 5.3 (c)). The literature [176] indicates that complex microalloy carbonitrides can form in multi-microalloyed steels, where competitive formation and extended solubility among these precipitates would happen. There are two types of microalloy precipitates in the Ti+V-containing steel. The FCC_A1# 3 Ti(C,N) is much closer to TiN (Fig. 5.6 (a)). The FCC_A1# 2 Nb(C,N) contains a few Ti and V but small amount of Nb dominates (Fig. 5.6 (b)). Ti(C,N) starts to precipitate at higher temperature of 1452°C, followed by AlN precipitation at around 1067°C. In the last, Nb(C,N) precipitates at 967°C.

As to be noted, some low temperature carbides (e.g. cementite, KSI carbide, MC_Eta carbide or M_7C_3) in this calculation need to be further verified. KSI carbides are cementite that probably contains some amount of Mo. Although M_7C_3 is stable, it takes longer tempering time to form at lower temperature since it needs greater partitioning of substitutional elements. Thermodynamic calculation indicates that M_7C_3 become stable below 560°C in the Nb-containing steel.

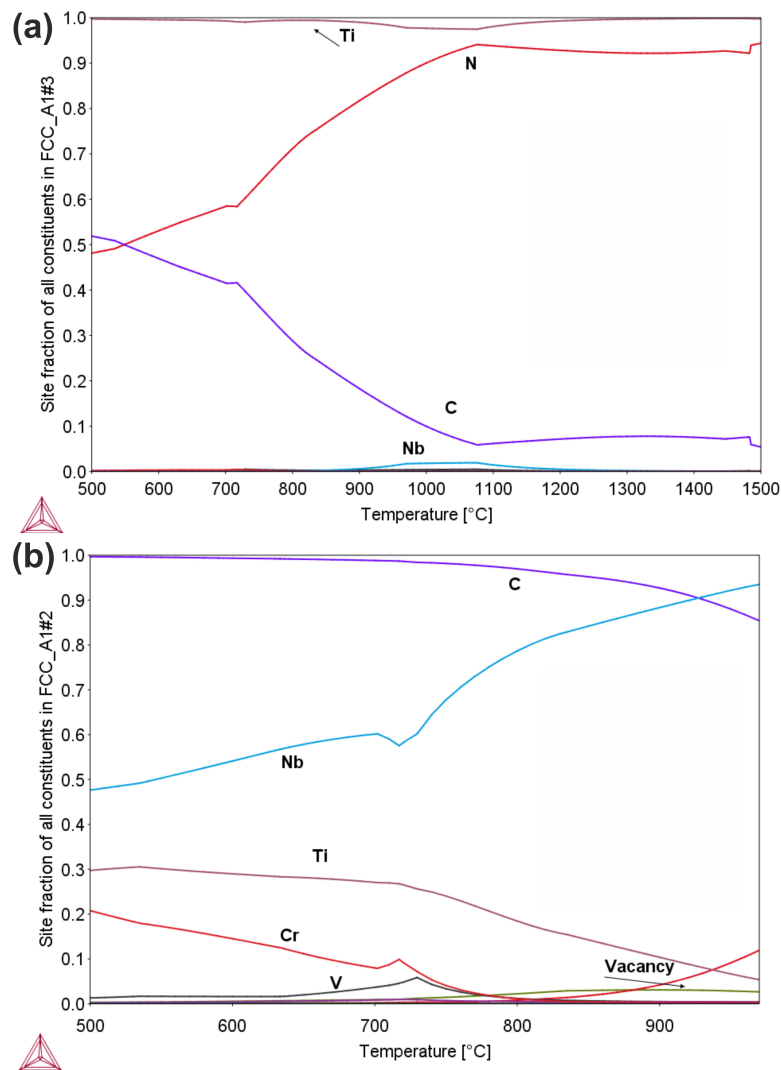


Fig. 5.6: $Ti(C,N)$ and complex $Nb,Ti,V(C,N)$ composition as functions of temperature

In the phase diagrams, the temperature at which the amount of precipitate is "zero" represents the dissolution temperature (T_{diss}). This temperature also indicates the thermal stability of precipitates. Table 5.2 shows the dissolution temperatures of precipitates and their final volume fractions.

Table 5.2: Calculated T_{diss} , °C and volume fraction f of microalloy precipitates in the three steels

Particles	AIN	Nb(C,N)	Ti(C,N)	Nb,Ti,V(C,N)
Steel A	1190, 4.17×10^{-4}	1140, 4.86×10^{-4}
Steel B	1080, 5.0×10^{-4}	...	1486, 3.84×10^{-4}	...
Steel C	1067, 3.5×10^{-4}	...	1452, 1.7×10^{-4}	967, 1.08×10^{-4}

Fig. 5.7 shows the volume fraction of different precipitates as functions of temperature. The volume fraction of precipitates increases as the temperature decreases. For austenite grain growth in the HAZ, the complex microalloy precipitate could probably cause pinning effect. In particular, the relatively stable precipitates $Ti(C,N)$, $Nb(C,N)$ and AIN should be considered with respect to the precipitates evolution.

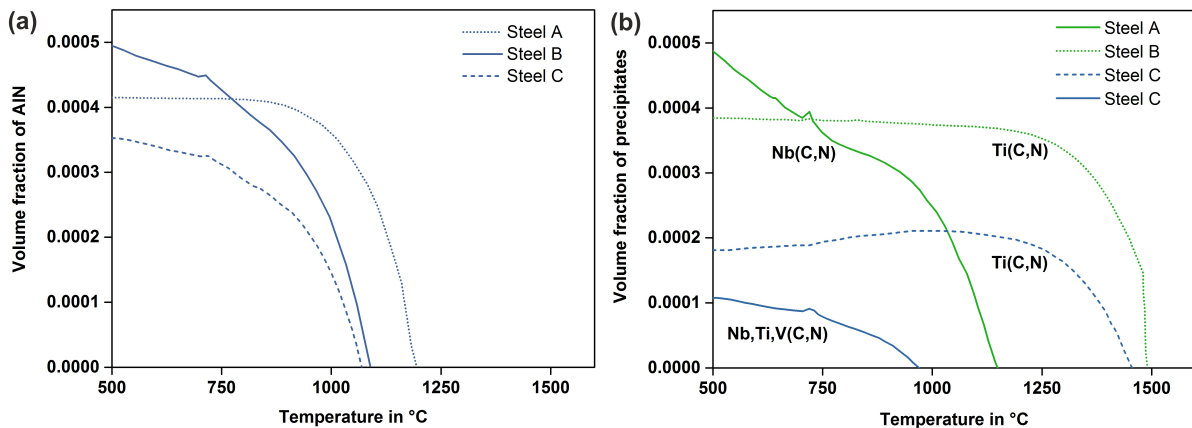


Fig. 5.7: Volume fraction of AlN (a) and microalloy precipitates (b) as functions of temperature

5.2.2 Microalloy precipitates under optical microscopy

To confirm the thermodynamic calculation result, the presence of microalloy precipitates was checked under optical microscopy. Fig. 5.8 shows several large precipitates in samples longitudinally sectioned to rolling direction. It is observed in non-etched Nb-containing steel (Fig. 5.8 (a)) that precipitates appear bright-gold in colour. Some precipitates in orange colour are found in Ti and Ti+V-containing steels (Fig. 5.8 (b, c)). Meanwhile, these precipitates are not always shaped as perfect cubes and some may have corners or edges. The Ti-rich inclusions appear in groups along band-like segregation area. This is consistent with TiN forming in or being swept into the solute enriched interdendritic liquid during solidification, resulting in an inhomogeneous spatial distribution.

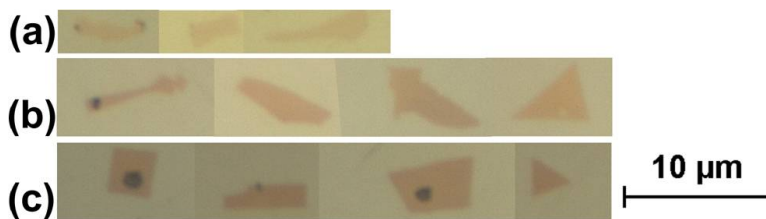


Fig. 5.8: Optical micrographs of coarse precipitates in steel A (a), steel B (b) and steel C (c)

The EDX spectrum identifies the coloured precipitates close to Nb-rich carbides or Ti-rich nitrides (Fig. 5.9 (a) and (b)). Some mixed inclusions with dark spots within the coloured precipitates can be clearly observed. These dark spots were reported as slag particle nucleus which probably contains oxides, sulphides or other complex phase from Mg, Al, S, O and Ca elements [14]. Due to different coefficients of thermal expansion compared with TiN, the presence of slag particle can be regarded as large internal defect in the TiN particle, probably causing microcracking inside TiN particles under heavy stress [187]. Fig. 5.9 (c) reveals one example of complex precipitate in Ti+V-containing steel. One TiN inclusion nucleates on a slag particle that is rich in magnesium oxide.

The observation of microalloy carbonitrides in the three steels is in good agreement with the previous results of the thermodynamic calculation. This confirms that coarse microalloy precipitates are formed which have compositions similar to NbC or TiN. In the following part, Ti(C,N) precipitate in a nano-scaled size is identified by TEM analysis.

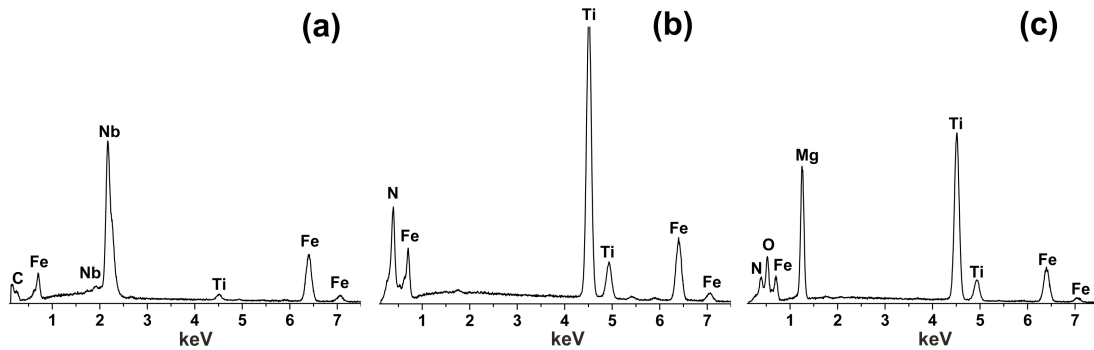


Fig. 5.9: EDX spectra of precipitate in steel A (a), steel B (b) and steel C (c)

5.3 Mechanical properties

5.3.1 Tensile properties

The tensile test results are summarised in Table 5.3. Ultimate tensile strengths levels of the three steels range from 775 MPa to 792 MPa, which satisfies the standard requirements. The fine grain size, microalloy precipitate and initial dislocation density are expected to influence the tensile behaviour, as also suggested by literature [220–223]. Consideration of austenite grain size and microalloy precipitates content, in light of the Hall-Petch relationship (equation 2.2) also implies relatively higher strength from Ti+V and Nb-containing steels. The stress-strain curves for the three steels are plotted in Fig. 5.10.

Table 5.3: Summary of the mechanical properties of the three steels

Properties	Steel A	Steel B	Steel C
Ultimate tensile strength (R_m), MPa	792	775	820
0.2% proof strength ($R_{p0.2}$), MPa	–	711	760
Upper or lower yield strength (R_{eH} , R_{eL}), MPa	748, 742	–	–
Fracture Elongation (A), %	16	15	21
Reduction of area (Z), %	42	43	–
Charpy impact energy (-40°C), J	108 / 139	120 / 148	147 / 177

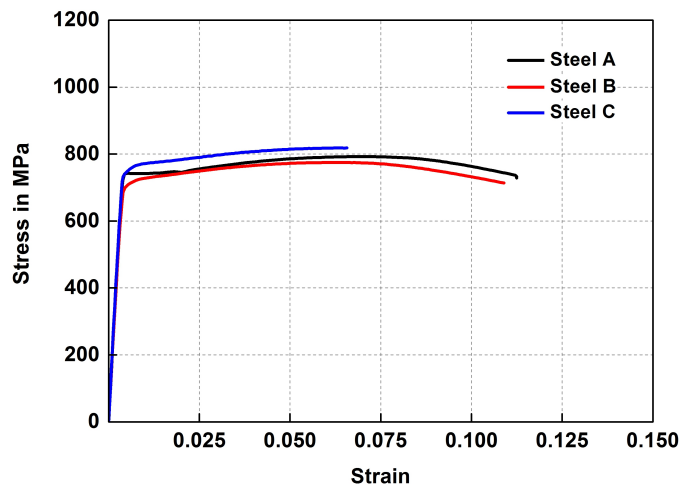


Fig. 5.10: Strain-stress curves of steel A (a), steel B (b) and steel C (c)

One interesting feature is that yielding phenomenon differs remarkably between the three steels. Nb microalloyed steel A show discontinuous yielding behaviour, with the presence of a clearly defined

upper and lower yield point (R_{eH} and R_{eL}) and followed by work-hardening; whereas for Ti-containing steel B and Ti+V-containing steel C, a continuous yielding behaviour is observed. Ti+V-containing steel has a relatively higher tensile strength than the other steels. In order to elucidate the cause of different yield phenomena in stress-strain curves, a detailed discussion of microstructure characteristics is done in the next part.

5.3.2 Charpy V-notch toughness

Fig. 5.11 shows the images of Charpy specimens from the three steels in longitudinal and transverse orientation. All specimens show a light-absorptive surface and dull appearance under optical microscopy, indicating that ductile fracture dominates. One distinguishing feature is observed on the fracture surfaces for the Ti-containing steel that is the presence of delaminations. Similarly, the Ti+V-containing steel shows some tendency to form delaminations. However, the Nb-containing steel shows no tendency of sharp delaminations formation in both longitudinal and transverse orientation.

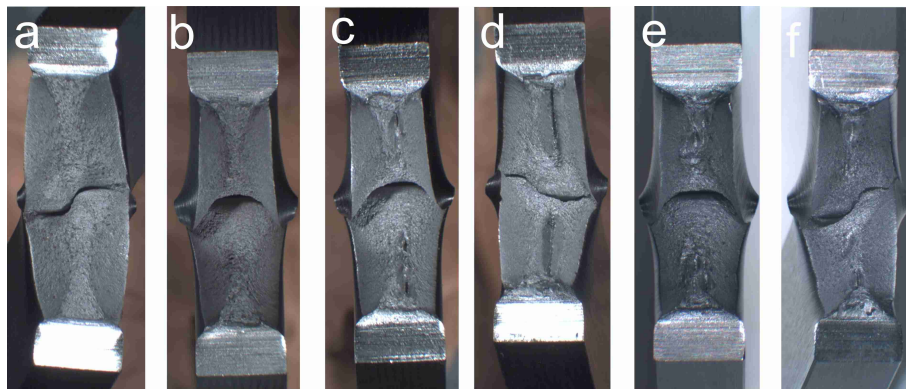


Fig. 5.11: Charpy specimens of steel A (a, b), steel B (c, d), steel C (e, f). a, c and e are longitudinally orientated and b, d, f are transversely orientated

Delaminations were further observed by SEM, as shown in Fig. 5.12. The fracture surface during delaminations crack propagation is composed of brittle transgranular cleavage fracture (Fig. 5.12 (a)). Due to relatively large austenite grain, the crack tends to preferentially propagate through coarse grain regions. Fig. 5.12 (b) shows the head of a delaminations crack, which is near the notch of the Charpy specimen. Ti-rich nitrides or complex Ti nitride-containing inclusions are observed to have initiated voids. An example of this is shown in Fig. 5.13.

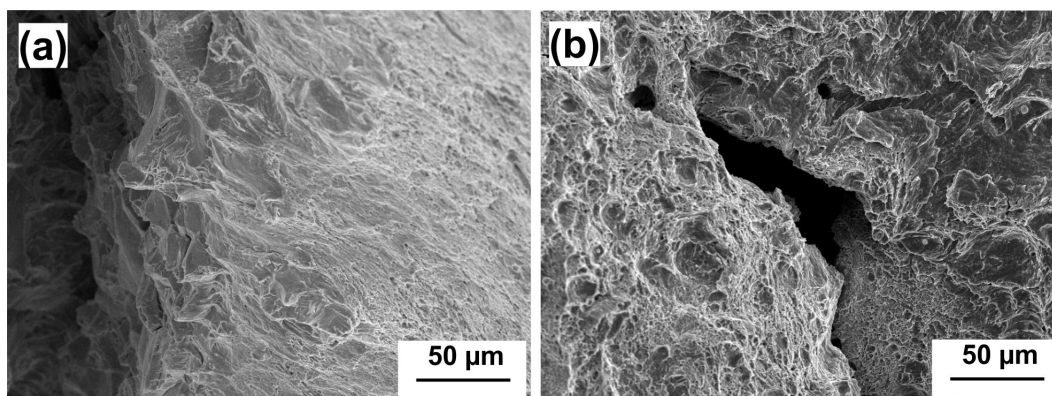


Fig. 5.12: SEM images of delaminations crack propagation (a) and the head of delaminations crack (b) in steel B

In the ductile voids, there are TiN or complex TiN containing other sulphides/oxides. Due to a relatively poor bond exist between TiN and the nucleus involving the slag particles (similar to the particles in Fig. 5.8 with dark spot), the TiN are well debonded to the nucleus and separated into several pieces during Charpy tests, as shown in Fig.5.13 (a). But the nucleus was lost during fracture.

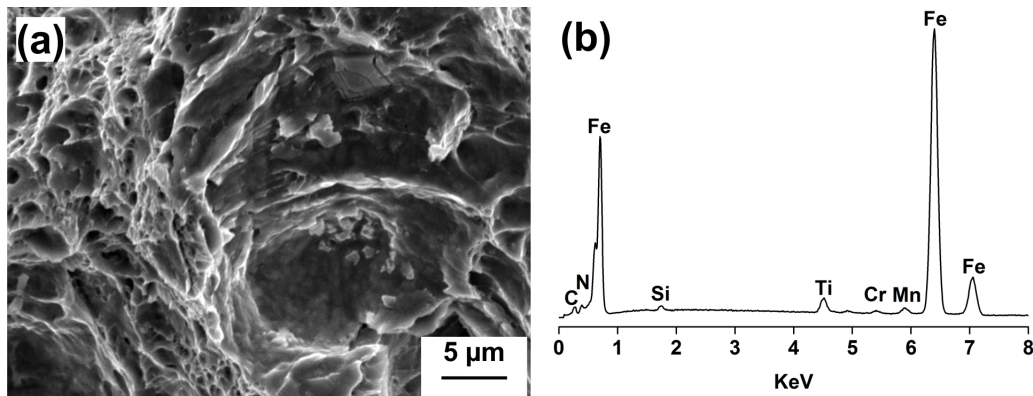


Fig. 5.13: TiN in ductile voids (a) and the corresponding EDX spectrum (b)

5.4 Discussion

5.4.1 Microalloy precipitates

By high resolution SEM, nano-scale precipitates were revealed along the grain boundary or within bainite and martensite. However, such fine precipitates are not possible to detect by EDS method coupled with SEM. So more precise technique is required for their identification. It has been pointed out that equilibrium thermodynamics can be used to make reasonable predictions of particle composition [172]. Thermodynamic analysis of equilibrium phases predicts different types of microalloy precipitates in three steels as a consequence of different alloying concepts.

Apart from AlN precipitate, single or multi microalloy precipitates can be formed in the three steels and they have varied volume fractions. Among all these precipitates, Ti(C,N) are supposed to be most stable even above 1400°C. But the other microalloy precipitates can also resist to dissolve up to relatively high temperature (Table 5.2). Consequently, the calculated volume fraction and dissolution temperature show a key indicator of precipitate stability. The stability of precipitate strongly influences the austenite grain growth in the HAZ during welding process. Therefore, the thermodynamic calculation results can provide useful information of the precipitate characteristics (e.g. type, dissolution temperature, volume fraction, etc.). However, in the practical steel production that often experiences fast cooling procedures, most precipitation occurs under a continuous cooling condition within a wide range of temperatures. In this non-equilibrium case, precipitates normally grow and distribute non-uniformly and inhomogeneously. Hence, it is accepted that the calculated precipitate characteristics can not completely agree with the actual situation in steel and these characteristics can change during welding.

Under optical microscopy, the presence of large-sized microalloy precipitates are observed and this provide experimental support for the results of the Thermo-Calc calculation. In the case of very fine precipitate, a detailed TEM study should be done further in order to confirm the theoretical calculation. One representative TEM study was performed to characterise the Ti(C,N) precipitates and the results are presented in the subsequent section. Although the precipitates in longitudinal direction appear large, the potency from them to become offending particles or act as potent cleavage initiators, is

still unknown. This is because cleavage resistance in the HAZ is associated with several combined factors (austenite grain size, ferrite/bainite packet size, matrix microstructure, martensite island and precipitates) [14, 16, 224]. But if large-sized Ti-rich particles are still formed in the HAZ after thermal cycle, especially in the case of bainite as the matrix microstructure, they may be problematic from the toughness point of view. This implies that appropriate welding parameter or cooling rate should be considered, in order to obtain desired matrix microstructure and meanwhile avoid the negative influence of large-sized particle on toughness.

5.4.2 Relationship between microstructure and mechanical properties

In the as-received quenched and tempered condition, the three steels consist of a bainite and martensite microstructure and have a similar level of hardness. High resolution images revealed that very fine dispersed precipitates are formed. These precipitates are expected to be generated by carbides formers (e.g. Cr, Mo) or even strong carbides formers (e.g. Nb, Ti, and V). The secondary-hardening reaction and secondary dispersion effect from these fine precipitates, also provide additional strengthening effect in the three steels.

Despite of the differences in microalloy precipitates, another appreciable structure difference is the larger austenite grain size in Ti-containing steel, compared with the other steels. Such a difference in austenite size can result in varied mechanical properties and transformation products during weld thermal cycle. Considering the different features of yielding phenomena, the stress-strain curves of the three steels have similar characteristics to the different type curves described by Yu [223]. The phenomenon that stress-strain curve shows Lueders strain occurs in Nb microalloyed steel. This has been also reported by Vervynckt [221] and Reskovic [222]. It was proposed that the tensile properties, particularly the deformation behaviour, depend strongly on Nb content and Nb-rich precipitates. This is because the presence of Lueders bands is related to the pinning of dislocations on the dissolved interstitial atoms (e.g. C and N in b.c.c. steels) which form the so-called Cottrell locking mechanisms [225]. Additionally, the kinetics of strain ageing and density of dislocation are also recognised to influence the yield phenomenon [220]. Recently, the appearance of a yield point in polycrystalline metals is linked to grain refinement [223, 226]. The yielding peak or Lueders deformation is not a result of the existence of interstitial atoms but arise from the lack of mobile dislocations due to the increased density of dislocation sink area provided by grain boundaries. Also, accumulation of dislocations on the series of Nb-rich precipitates postpones the beginning of plastic deformation [222]. These can explain the observation of long Lueders elongation and delayed strain hardening in Nb-containing steel.

The strain-stress curve of Ti-containing steel B represents a conventional behaviour with continuous hardening. The reason for this is probably the relatively coarse grains compared with Nb steel. This phenomenon has been reported to be similar to materials owning coarse grain size [223, 226]. Ti+V-containing steel C has also large amount of strength contribution from grain refinement like steel A and enjoys increased tensile strength with normal continuous hardening behaviour.

The formation of delaminations required a higher percentage of the total energy to fracture. In the literature, this was proven to be related to the texture, elongated MnS inclusions, microstructural banding, carbides on grain boundaries and elongated grains [227]. Steels containing coarse TiN inclusions, particularly in coarse grained steels, was reported to observe the delaminations on fracture surfaces during Charpy test [227]. The presence of delaminations in the Ti-containing steel is in good

agreement with the literature data. This probably be ascribed to the large austenite grain size in combination with coarse complex inclusions involving MnS, MgO, and TiN. As shown in Table 5.3, a higher percentage of the fracture energy is required for delaminations formation in the transversely orientated specimens compared with the longitudinally oriented specimens. Moreover, delaminations in steel B do not cause a lower toughness values compared with the other two steels. This indicated as delamination toughening from literature [227, 228]. Results in Table 5.3 show that transverse Charpy specimens have always better toughness than longitudinal specimens. This result is in good agreement with reported results in [227].

5.5 Summary

A variety of characterisation techniques were used to study the three steels microalloyed with Nb, Ti or Ti+V. The observation regarding microstructure under light microscopy reveal that the three steels have tempered bainite and martensite as matrix structure. Their hardness is at the same level around 273 HV10. SEM observations show that the nano-scale precipitates are present along the grain boundaries or within bainitic ferrite. On that account, it is not possible to identify these precipitates using X-ray methods combined with SEM. Thermodynamic calculation with Thermo-Calc suggests that different microalloy precipitates are present and meanwhile cementite and other carbides can also appear in the three steels.

Experimental evidence indicates that a proportion of coarse microalloy precipitates (Ti-rich nitrides, Nb-rich carbonitrides) form during the steel solidification process. This provides strong evidence in support of the thermodynamic calculation results. Furthermore, the quantitative assessment of different types of precipitates in steels can be reliably used. So austenite grain growth behaviour during welding can be well interpreted.

The tensile strength and Charpy toughness of the three steels satisfy the requirements of standards. A difference in yielding characteristics of strain-stress curves is observed. Nb-containing steel has discontinuous yielding, whereas the other two have continuous yielding. The reason for this difference remains unclear, although the varied prior austenite grain size is a reasonable explanation in the present case. Anyway, the differences observed in base materials imply the resultant discrepancy between their welds. The next chapters detail the results of different regions of the welded joints.

6 Microstructure evolution and mechanical properties of weld metals

In the new solidified weld metal, it consists mainly of the deposited weld metal and partially diluted parent steels. These two parts combine to determine the final chemistry of the weld metal. This chapter describes experiments performed on different weld metals with the purpose of better understanding their Charpy impact toughness behaviour. This part represents the investigation of the weld microstructure evolution under different cooling conditions. The results provide explanations of the microstructural changes that fit the observation with particular focus on the varied weld chemistry responses to high dilution.

6.1 Hardness results

In an attempt to characterise the weld microstructure heterogeneity, hardness mapping across the entire weld was performed on a cross section of different welds, as displayed in Fig. 6.1. Each hardness map provides a visual indication of the hardness distribution in various regions of the welded joint with specific welding parameters. The hardness in the three types of welds shows different variation as a function of heat input.

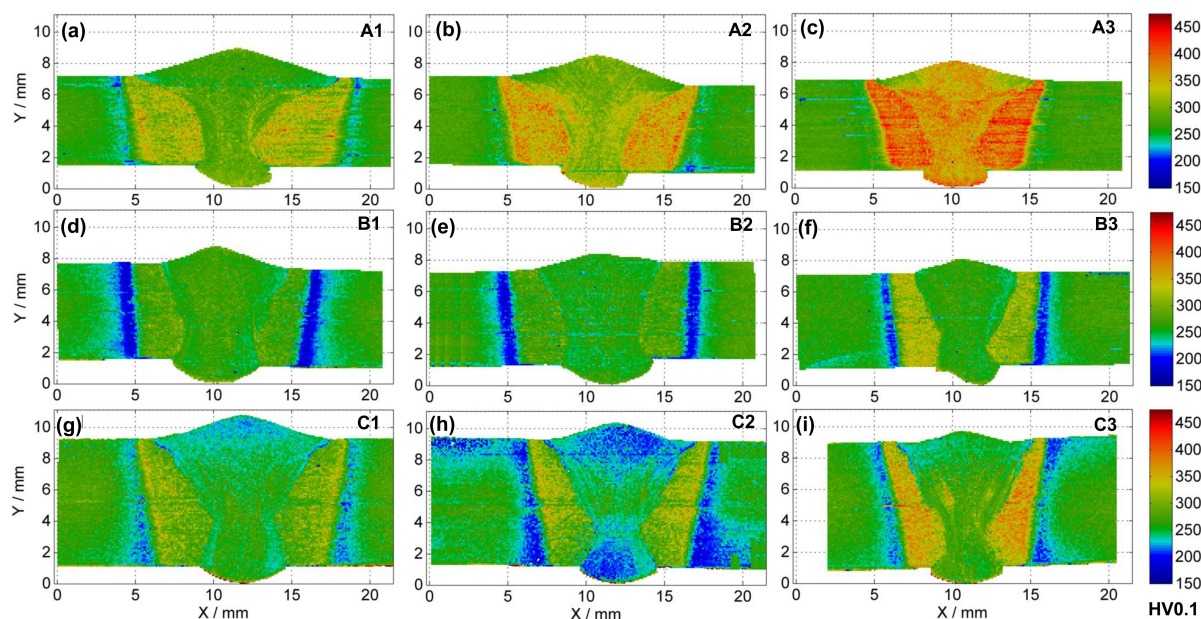


Fig. 6.1: UCI hardness maps of weld A1 – A3 (a – c), B1 – B3 (d – f) and C1 – C3 (g – i)

Observation of hardness variation in the Nb-containing steel reveals that weld A (Fig. 6.1 (a) – (c)), in particular its weld metal and CGHAZ, exhibits mostly sensitive to the changes in heat input or cooling rate. Its hardness increases continually to the largest extent as cooling rate increases. However, in the case of Ti-containing steel B (Fig. 6.1 (d) – (f)) and Ti+V-containing steel C (Fig. 6.1 (g) – (i)), the weld metal hardness values almost keep at a constant level even under fast cooling. Additionally, the tendency of CGHAZ hardness increase with decreasing heat input also occurs in the two steels but the degree of increase differs remarkably. Another significant feature is that a distinct blue band, corresponding to hardness drop, is sometimes visible in the HAZ but far away from the fusion line. This is commonly referred to as the softening zone. Note that the three welds have varied softening phenomena that will be discussed in details in the last chapter.

Apart from hardness assessment by the micro hardness tester, the detailed Vickers hardness (HV10) profiles across the welds are shown in Fig. 6.2 and Fig. 6.3 (a). All hardness curves agree well with the mapping results, presenting the varied hardness changes as a function of heat input and weld chemistry. The detailed HV10 hardness increase or decrease can be read directly from the measured points. Apparently, the lowest value in each curve suggests the hardness drop in the softened HAZ.

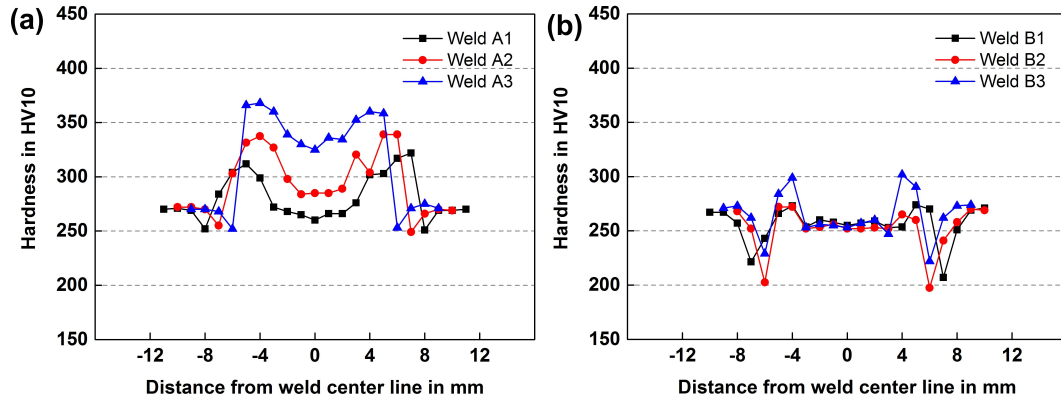


Fig. 6.2: Hardness profiles of weld A (a) and B (b) under different cooling rates

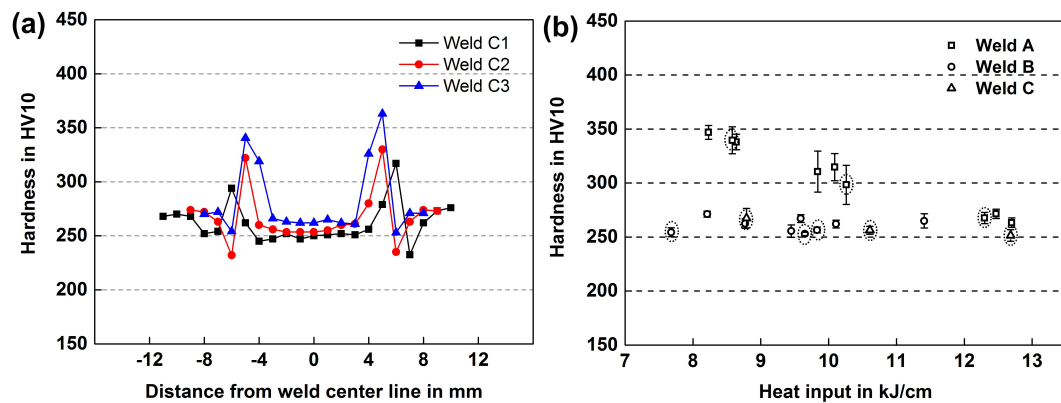


Fig. 6.3: Hardness profiles of weld C (a) and comparison of average hardness from all weld metals (b)

Fig. 6.3 (b) shows the comparison results of the average hardness in weld metal as a function of heat input. Further microstructure analysis is done in the welds highlighted by dashed circles. Each hardness value is the average of several hardness measurements within weld metal. It is evident that weld metal A exhibits distinguishable hardness variation as a function of cooling rate. At low heat input the average hardness increases remarkably, which reaches up to approximately 350 HV10. Such trends can be expected when a hard structure forms in the weld metal A. By contrast, no significant differences are found in weld metal B and C at all cooling rates, indicating that the two welds are not sensitive to all cooling conditions in the present case. The hardness values keep at a constant level of around 250 HV10. This result reflects that predominant microstructure could remain similar even under different cooling rates. In addition, the feature of scatter band indicates that weld metals B and C obtain more homogeneous microstructure than weld metal A irrespective of under fast or slow cooling.

6.2 Microstructure characterisation

Fig. 6.4 shows the microstructure evolution in the weld metal A as a function of cooling rate. Under slow cooling, predominantly interlocked AF is visible in weld A1 (Fig. 6.4 (a)). Large round inclusions are sometimes observed as well. As heat input drops to medium level, this characteristic microstructure

is still dominant in the centre of weld A2 (Fig. 6.4 (b)), but a tendency to form more elongated ferrite with a large aspect ratio is clearly shown. Under fast cooling (weld A3), the microstructure differs remarkably from AF, having a bainitic-martensitic structure (Fig. 6.4 (c)). Fine AF plates are observed to form intragranularly on fine granular inclusions in weld A1 and A2 (Fig. 6.5).

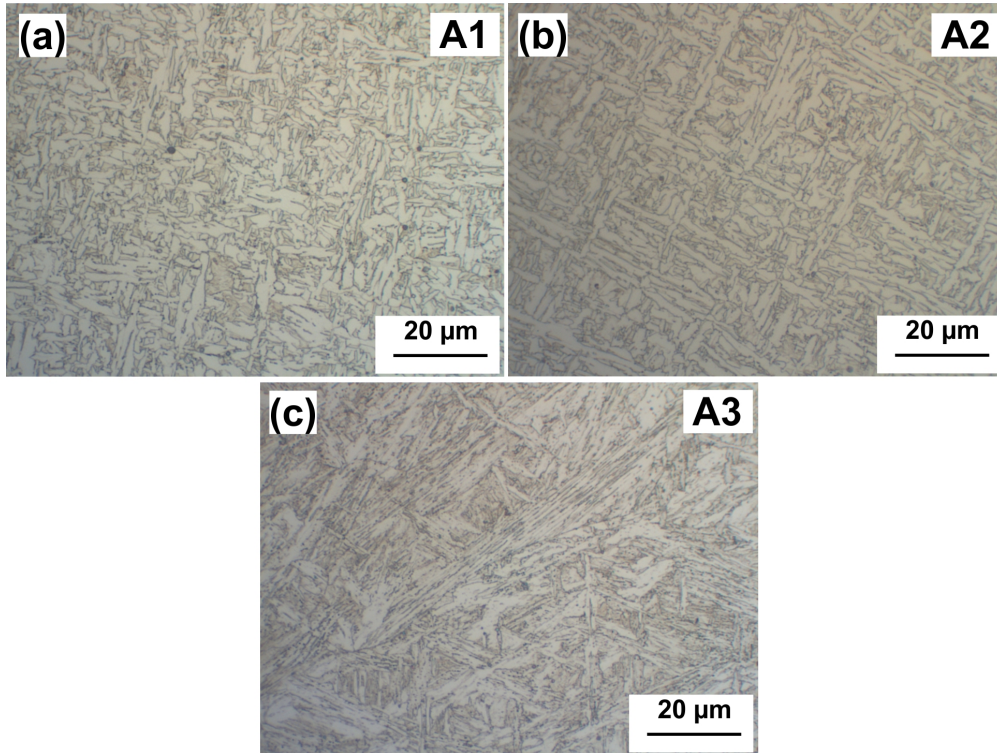


Fig. 6.4: Optical micrographs of weld metal A1 (a), A2 (b) and A3 (c) [147]

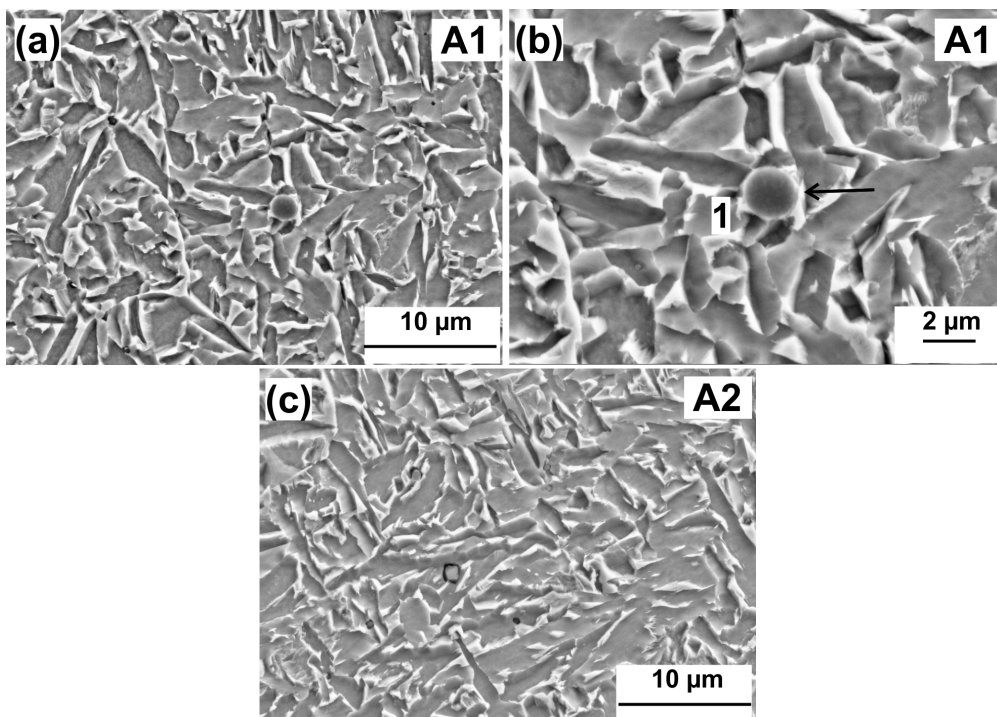


Fig. 6.5: SEM images of weld metal A1 (a, b) and A2 in weld centre (c) [147]

The SEM micrographs (Fig. 6.6) show that the predominant microstructure in the weld A3 is bainite. Some round inclusions are found between parallel bainitic ferrite plates but they are not effective to promote AF nucleation (indicated by arrows in Fig. 6.6 (b) – (d)). A high concentration of fine needle-shaped carbides are observed within bainitic ferrite. Due to such specific carbide characteristics, bainite has generally higher hardness value relative to AF. Hence, in weld A3, the hardness increases substantially due to a large fraction of bainite. This observation in weld A implies that the main microstructure is sensitive to variations of heat input or cooling rates, causing remarkable hardness changes of weld metals.

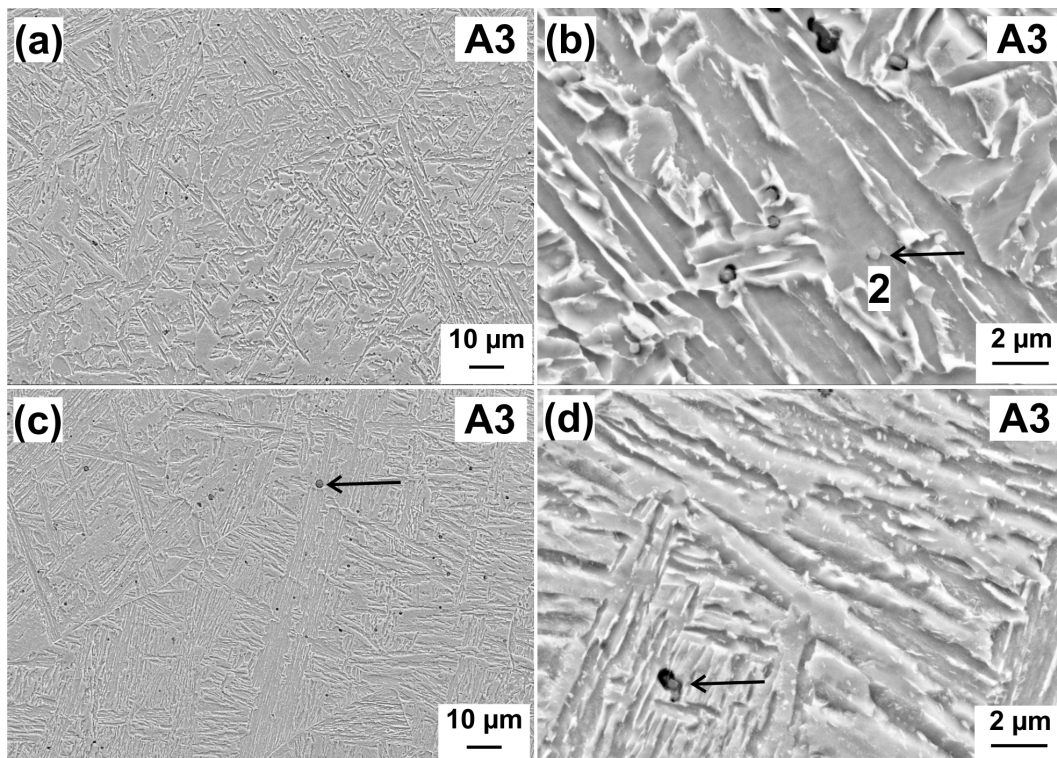


Fig. 6.6: SEM images of weld metal A3 in weld centre (a, b) and near FZ (c, d) [147]

Extensive EDX analysis was performed in order to make a qualitative analysis on the inclusions. Two representative results of inclusions are shown in Fig. 6.7, which are within different matrix structures (arrowed in Fig. 6.5 (b) and Fig. 6.6 (c)). The results show that both inclusions are rich in Al, Ti, Mn, Si, O, and S. Although they are formed within different matrix structures, they could have a marginal difference in composition. This is actually expected due to the similar composition in all weld metals A.

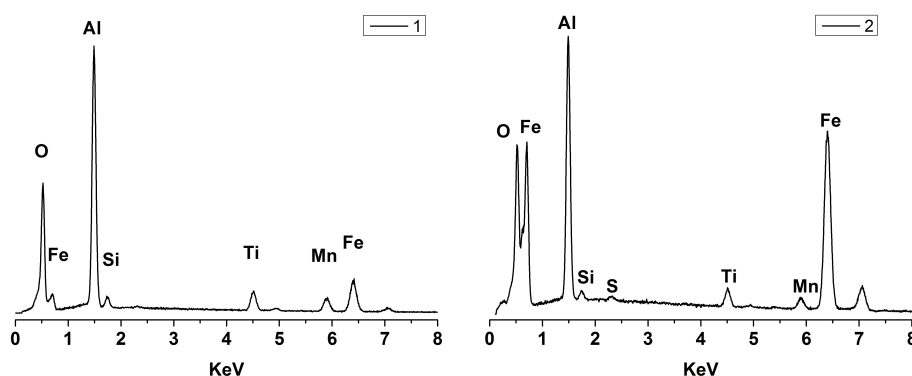


Fig. 6.7: EDX spectra of inclusions in weld metal A1 (Fig.6.5 (b)) and A3 (Fig.6.6 (b))

Weld metal B shows no remarkable microstructural change under varied cooling rates and it has acicular ferrite as the main structure (Fig. 6.8). Correspondingly, the weld metals B have the same level of hardness (Fig. 6.2). Fig. 6.9 shows that acicular ferrite is still preferred even under fast cooling.

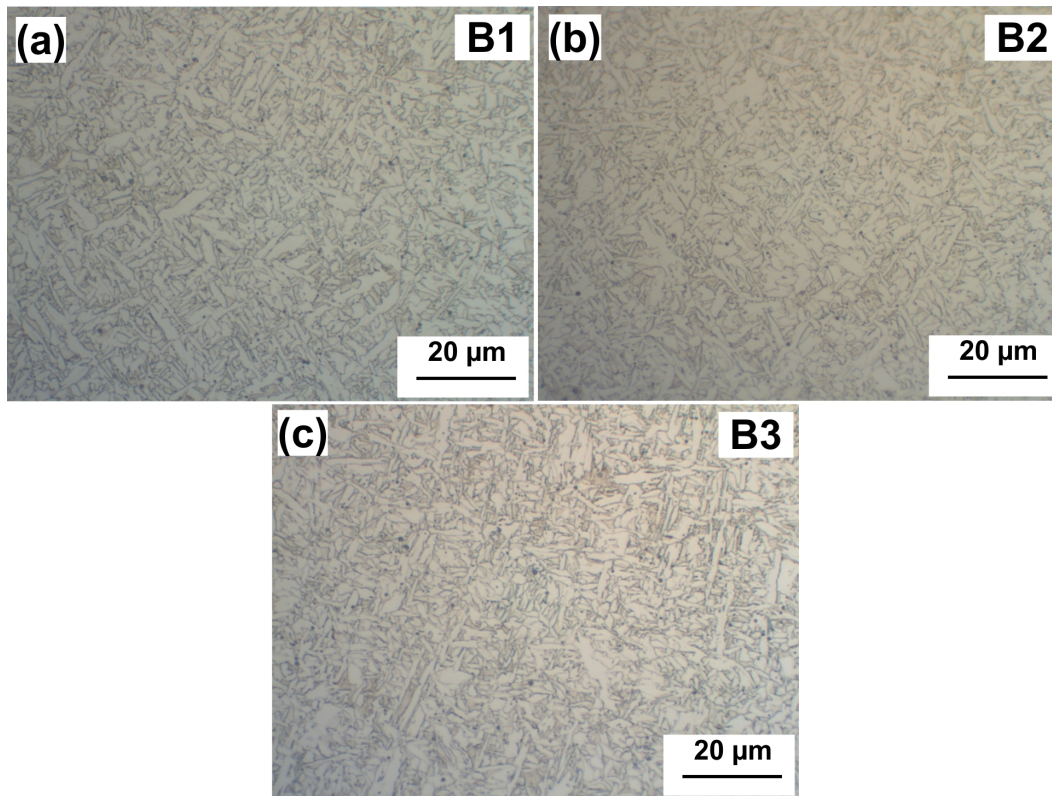


Fig. 6.8: Optical micrographs of weld metal B1 (a), B2 (b) and B3 (c) [147]

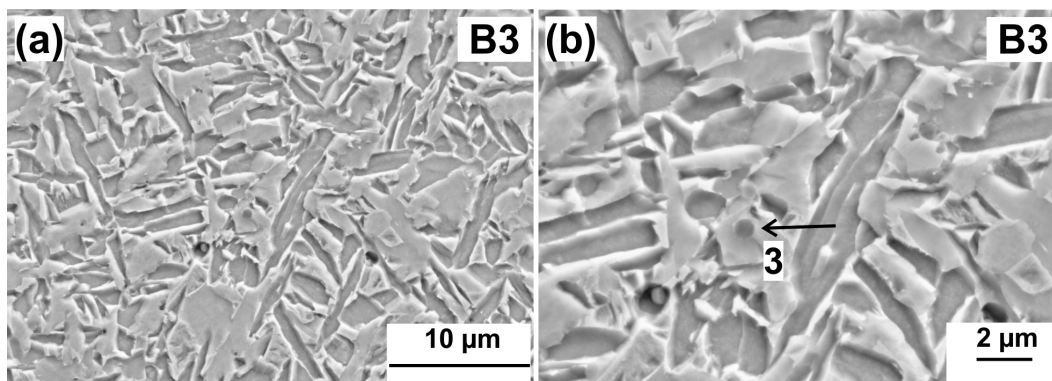


Fig. 6.9: SEM images of weld metal B3 centre [147]

The microstructure in weld metal C shows no significant variation as a function of cooling rate, which primarily consists of acicular ferrite (Fig. 6.10). This observation is similar to the case in weld B. The ferrite morphology does not exhibit any distinguishable differences, compared to Fig. 6.8 and Fig. 6.9. Likewise, the hardness stays at a similar level as well (Fig. 6.3).

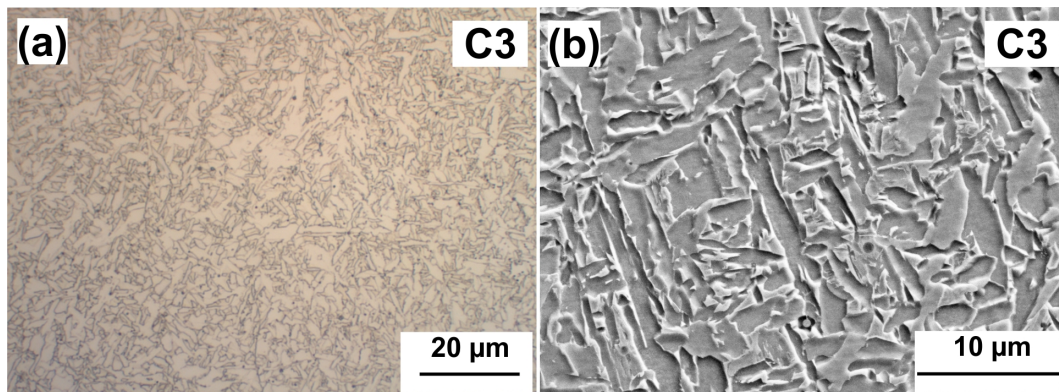


Fig. 6.10: Optical (a) and SEM image (b) of weld metal C3 centre

EDX mapping was carried out to determine the element distribution and atomic percent in the inclusion, indicated by the arrow in Fig. 6.9. The results are shown in Fig. 6.11. The core consists of a mixture of Al, Ti and O with small amounts of Si and Mn, reflecting a very complex deoxidation product. Moreover, a few S could be detected on the surface or edge of the inclusion. This observation is consistent with Kluken and Grong's work [87]. Actually, the inclusions with comparably similar compositions are mostly found in all weld metals. This is expected to occur in all weld metals due to the usage of identical filler metal. A large amount of EDX results performed in weld metal C also shows that the inclusions have similar composition. Hence, the EDX results of weld C are not shown here.

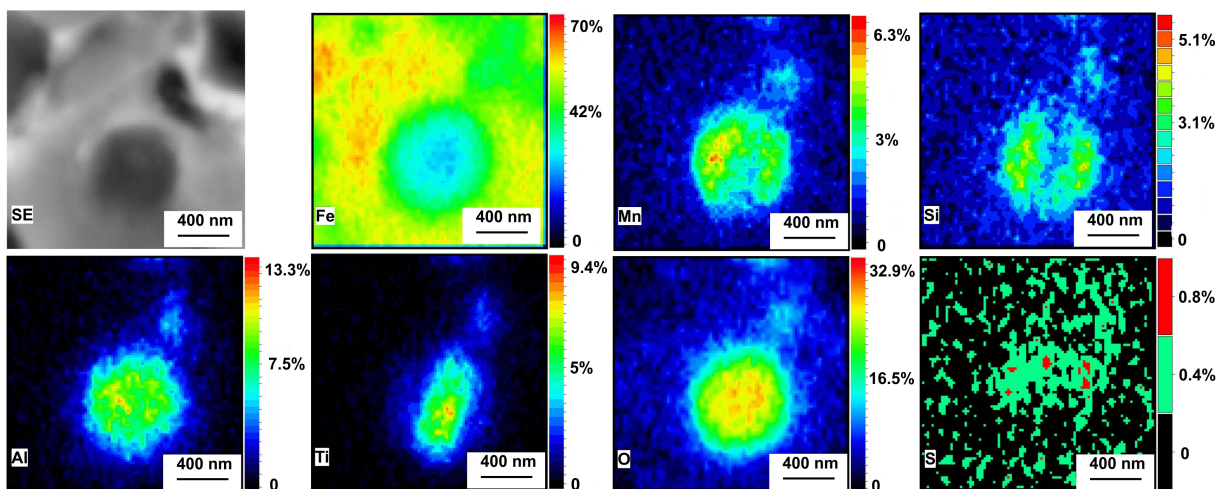


Fig. 6.11: Map the distribution and atomic percent of defined elements in the inclusion from Fig. 6.9

6.3 Toughness results of weld metals

Previous metallographic observations provide insight into the relevance of the microstructure evolution with heat input, weld chemistry and cooling rate. Understanding this microstructural evolution is significant to assess the weld toughness based on the structure-property relationship.

Table 6.1 shows the results of toughness and hardness of the weld metals under varied heat inputs. The CVN values of weld metal A have an abrupt fall under slow cooling, compared to fast cooling. A large fraction of bainite formed under fast cooling does offer an explanation for the low Charpy values. This observation also implies that the toughness value strongly depends on the proportion of AF. Contrary to this, constant high CVN values occur to weld metal B and C under different cooling rates. This is due to no significant variation in the predominant microstructure. Correlating the toughness results

with hardness values (Fig. 6.2), it can be confirmed that lower impact values were obtained at higher hardness. This is consistent with the expectation that high hardness results from hard phases, which could easily develop a brittle fracture mode, causing reduced toughness.

Table 6.1: CVN absorbed energy (J) values of different weld metals [147]

Weld	Cooling rate $t_{8/5}$, s	Hardness, HV10	CVN energy, J (average)	Area distribution, % F, S, R
A1	20.4	267 ± 5	56, 56, 62(58)	8, 66, 26
A2	15.3	298 ± 18	42, 30, 32(35)	4, 38, 58
A3	11.4	339 ± 12	24, 26, 28(26)	4, 21, 75
B1	17.3	256 ± 3	100, 118, 99(106)	9, 67, 24
B2	15	252 ± 1.5	96, 84, 75(85)	6, 69, 25
B3	11.2	254 ± 4	90, 92, 86(89)	12, 64, 24
C1	18.0	252 ± 5	96, 90, 102(96)	8, 54, 38
C2	15.0	256 ± 4	95, 94, 100(96)	6, 65, 29
C3	11.2	267 ± 9	92, 91, 91(91)	7, 59, 34

Note: F fibrous zone, S shear lip zone, R radial zone.

In the Charpy specimen, the fracture surface can usually be divided into three zones: fibrous zone, shear lip zone, and radial zone. At first, a ductile crack is initiated at the centre of the notch root after yielding, subsequently the fibrous zone is formed. As the crack propagates ahead of the notch, it spreads laterally and propagates through the thickness, resulting in the radial zone and the shear lip zone formation at the outer surface. It is noteworthy that the energy absorbed for radial zone and shear lip zone formation account for the major part of the total CVN energy. Fig. 6.12 shows the fracture surfaces of nine representative specimens from the weld metal A, B and C. From the overview, different modes failure in the radial zones are readily distinguishable even under small magnification. A relatively flat appearance in weld metal A is observed, while both weld metal B and C have a tough appearance. The fraction of shear lip zone can reflect its contribution to final absorbed impact energy, because it is characterised by a ductile dimpled mode.

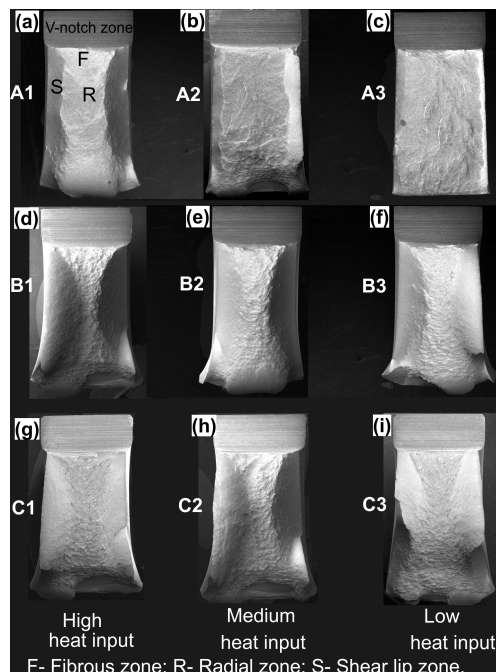


Fig. 6.12: Overview of Charpy specimens of weld A1 – A3 (a – c), B1 – B3 (d – f) and C1 – C3 (g – i) [147]

Further observation on the fibrous zone for weld metal A is displayed in Fig. 6.13. The crack initiation with typical ductile shear mode is visible in front of all the notch tips, as marked by black arrows. Meanwhile, the formation of a shear band with at least 400 μm width is evident. The inclusions acting as microvoid nucleation sites are found inside dimples. Fig. 6.13 (c) – (f) show that an apparent transition zone from ductile dimpled to quasi-cleavage mode exists for medium/fast cooling rate, which indicates that the propagation of crack changes to cleavage mode at radial zone. But there is no transition zone under slow cooling (Fig. 6.13 (a)). Likewise, it should be pointed out that the absence of such a transition zone occurs in all the specimens from weld metals B and C. In terms of the contribution from such fibrous zone to the total absorbed energy, the fibrous zone has limited contribution to the final impact toughness, due to limited widths. Subsequently, observations reveal that the main contribution to the entire absorbed energy is from the radial zone.

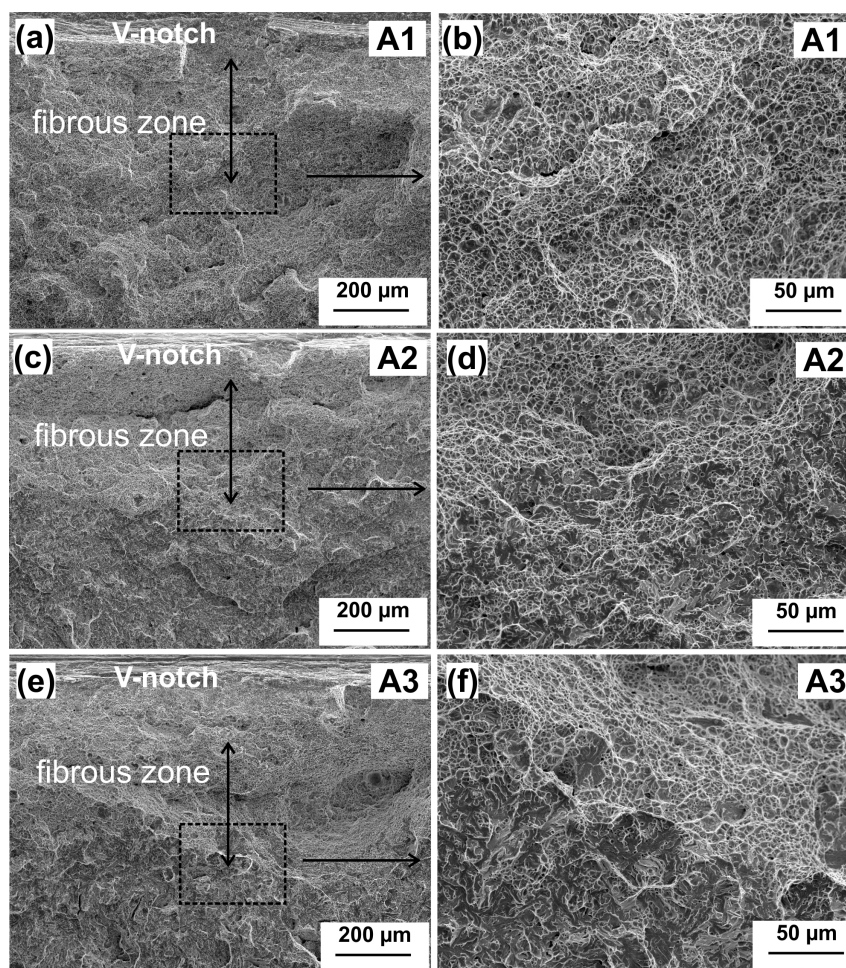


Fig. 6.13: Fractographic examination in the fibrous zone of weld A1 (a, b), A2 (c, d) and A3 (e, f)

It is quite informative to look into the fractographic examination in the radial zone and find out the crack propagation behaviour. One comparison between weld A and B is provided in Fig. 6.14. Fig. 6.14(a) and (b) show that fracture occurs by a mixed ductile and quasi-cleavage mode in weld metal A subjected to slow and medium cooling, whereas it is characterised by a cleavage mode under fast cooling (Fig. 6.14 (c)). Therefore, as the cooling rate increases, cleavage fracture becomes predominant in weld metal A.

Within quasi-cleavage fracture surface, very small facets are found to be connected by tear ridges and

shallow dimples. Relatively large and elongated facets separated by heavy ridges are observed (Fig. 6.14 (c)). Such large cleavage facets also suggest large-sized bainite packet, as shown in Fig. 6.6. It was proposed that bainite packet size corresponded to the fracture facet and large size accounted for the deterioration in the notch toughness [229]. Small inclusions are also observed inside dimples and cleavage facets, but they do not trigger any cleavage fracture.

The fracture features observed in weld metal B (Fig. 6.14 (d), (e) and (f)) are fully ductile under different cooling rates. The microvoid coalescence is the main cause of fracture. Such an observation is the most common fracture feature of acicular ferrite structure. The reason is that the fine interlocked ferrite plates have high angle boundaries and can efficiently prevent brittle fracture and then assist in ductile fracture. The inclusions in microvoids are further identified to have similar chemical composition like those observed in weld metal (Fig. 6.7 and Fig. 6.11). This result needs no further discussion here.

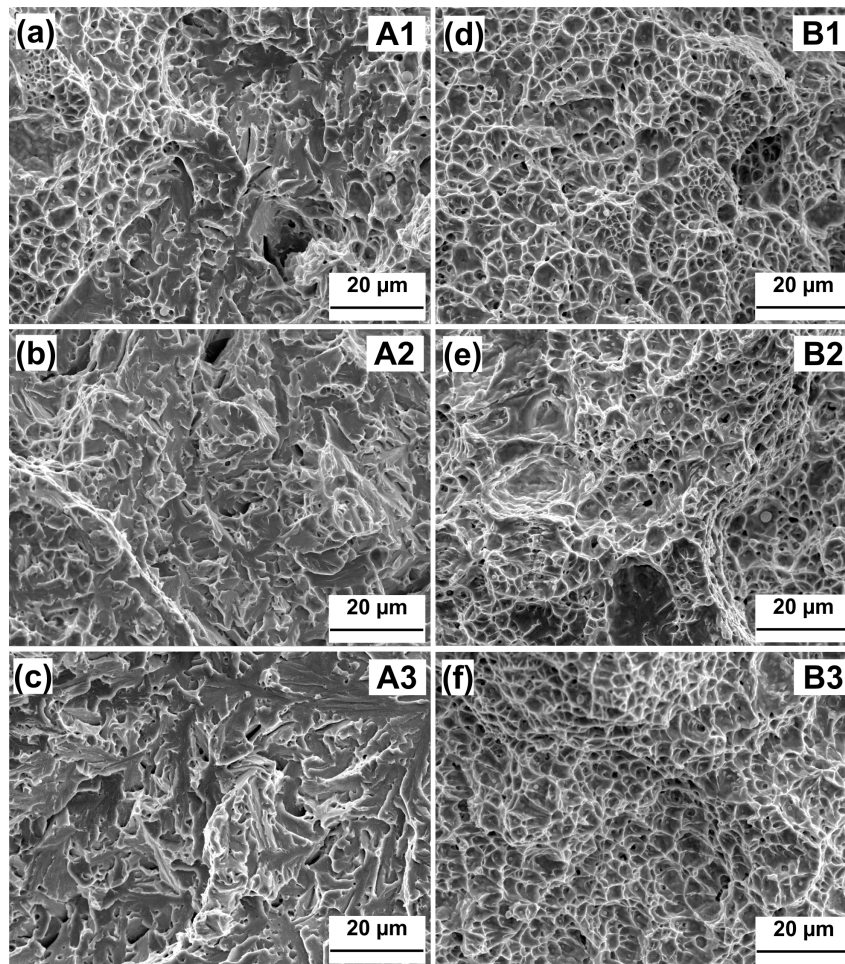


Fig. 6.14: Fractographic examination in the radial zone of weld A (a – c) and B (d – f)

As indicated by a similar main microstructure in both weld B and weld C, the consequent fracture behaviour of weld C is in a ductile manner similar to that in weld B. Hence, the fractographic examinations for weld C are not shown here. Above all, the final toughness is essentially determined by the fracture mode in radial zone combined with the shear lip zone fraction. In the present study, the substitute of acicular ferrite (Fig. 6.4 (a)) by bainite (Fig. 6.4 (c)) results in a reduced toughness. Such a microstructure variation contributes to the fracture mode change from ductile (Fig. 6.14 (a)) to brittle (Fig. 6.14 (c)).

6.4 Discussion

6.4.1 Effect of microstructure on toughness

Inspection of Table 6.1 reflects that welding parameters are observed to be an important variable that influences the toughness, especially for weld metal A. This is achieved through influencing the weld microstructure and hardness. Microstructural variation as a function of heat input is the most important factor to influence the toughness since different transformation products possess different inherent fracture resistances [230]. This has been well proved in weld metal A. The formation of bainite under fast cooling results in decreased toughness and has a low CVN value. Weld metal B has relatively high CVN energy due to acicular ferrite as the predominant structure. Moreover, examination of toughness test specimens shows that the samples with acicular ferrite as predominant microstructure undergo ductile fracture. However, the fracture surfaces in specimens with bainite exhibited cleavage fracture mode. To conclude from these observations, the characteristics (e.g. fine, interlocking and tough ferrite plates) make acicular ferrite as one desirable microstructure due to the excellent toughness as well as high strength.

6.4.2 Transition between acicular ferrite and bainite

According to Bhadeshia and other researchers [64, 70, 97], the competition between acicular ferrite and bainite formation depends on several factors, such as chemical composition, inclusion characteristics, austenite grain size, and cooling rate. In terms of inclusions characteristics, it has been proved that the presence of potent inclusions is of fundamental importance to the nucleation of acicular ferrite [81, 231]. But if the inclusions are ineffective to act as nucleant, acicular ferrite will not be favoured [232]. It is known that Ti-rich oxides combined with Al-rich oxides or MnS are very potent nuclei for acicular ferrite formation [87]. In the present weld metals, complex oxides are often observed, which are rich in Ti, Al, Mn, Si, O or S elements (Fig. 6.7 and Fig. 6.11). Since identical filler metal is used, oxides with similar composition are mostly obtained in all weld metals. It is revealed previously that weld B and C have a close similarity in predominant microstructure. Hence, the inclusion characteristics comparison is carried out only between weld A and weld B. The size, distribution and number density of inclusions are measured from SEM micrographs. Fig. 6.15 shows the size distribution in welds A and B.

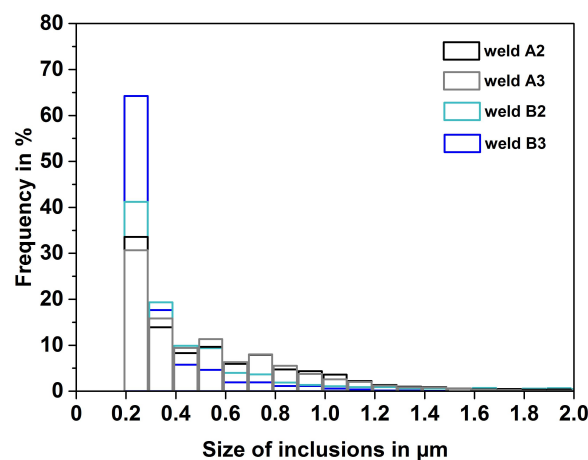


Fig. 6.15: Inclusions size distribution in weld A and B [147]

In a quantitative analysis of the inclusions, very fine ($\leq 0.2 \mu\text{m}$) inclusions are excluded due to the limited resolution of SEM. Fig. 6.15 shows the size distribution from $0.2 \mu\text{m}$ to $2 \mu\text{m}$. Considering the

size distribution suggested in the literature (Fig. 2.19), in the present study inclusion with a size of 0.2 μm to 0.8 μm shows a good potential for nucleant. Zhang and Farrar [231] concluded that sufficient inclusions within appropriate size range are regarded as one main factor to ensure a large fraction of acicular ferrite formation.

Table 6.2 shows that the number density per unit area in weld A and B is at a similar level. The inclusion characteristics suggest that there is no appreciable difference between weld A and B. The beneficial effect of inclusions to promote AF has been well proved in weld metal B. But, even with similar inclusion characteristics, acicular ferrite is absent in the weld metal A, particularly under fast cooling. Hence, the inclusion characteristics are not the primary factor to influence this change in microstructure.

Table 6.2: Inclusion characteristics in weld metal A and B [147]

Weld	Heat input, kJ/cm	Inclusion density, $\times 10^4/mm^2$	Average diameter, μm
A2	10.26	0.78	0.63
A3	8.58	0.94	0.61
B2	9.65	0.77	0.58
B3	7.68	1.04	0.40

Attention should be focused on another major factor that influence phase transformation – the chemical composition. This should correlate not only with the effect of filler metal and metal vaporisation but also with the alloy pick-up from base materials via dilution. Dilution factor can be determined by measuring geometric cross sectional areas of the deposited filler metal and base materials (Fig. 4.2). The modified spray arc welding process used in the present study has deep penetration and high dilution around 50%. This implies a large concentration of alloy pick-up by the weld metal from base metal.

Table 6.3 shows the chemical composition of representative weld metals. It should be pointed out that the elements O, N and S cannot precisely analysed by spark emission spectrometry. Relatively high Mo, Nb and Al are contained in weld metal A due to the high dilution from base metal. The concentrations of Ti, Al, Si, Mn, O and N are closely related to the acicular ferrite formation because the precipitation interaction from these elements can greatly influence the acicular ferrite nucleation.

Table 6.3: Chemical composition in weld metals [147], wt.-%

Weld	Heat input kJ/cm	C	Si	Mn	Mo	Cr	Cu	Ni	Al
A2	10.26	0.14	0.39	1.32	0.36	0.28	0.049	0.72	0.041
A3	8.58	0.14	0.39	1.32	0.35	0.28	0.048	0.70	0.044
B2	9.65	0.14	0.42	1.23	0.19	0.30	0.041	0.92	0.021
B3	7.68	0.14	0.40	1.28	0.21	0.28	0.042	0.62	0.015
C1	12.68	0.12	0.41	1.27	0.34	0.26	0.041	0.74	0.018
C3	8.79	0.13	0.37	1.26	0.31	0.26	0.039	0.64	0.018
		Ti	Nb	V	N	O	P	S	Fe
A2	10.26	0.016	0.014	0.002	0.0071	0.050	0.007	0.008	Bal.
A3	8.58	0.018	0.014	0.002	0.0053	0.039	0.007	0.008	Bal.
B2	9.68	0.022	<0.001	0.002	0.0125	0.054	0.010	0.006	Bal.
B3	7.68	0.022	<0.001	0.002	0.0053	0.049	0.010	0.007	Bal.
C1	12.68	0.023	<0.001	0.006	-	-	0.010	0.005	Bal.
C3	8.79	0.019	<0.001	0.006	-	-	0.010	0.005	Bal.

To address the microstructure transition from acicular ferrite to bainite, with consideration of the fact that inclusion characteristic has no controlling influence on this variation, it is reasonable to assume that combined Mo+Nb effect contributes to this microstructure change under fast cooling. The combined effect of Mo and Nb can be an alternative explanation for promoting bainite formation. Strong evidence can be found from the literature to support this point. The major role of Mo appears to promote bainite formation instead of acicular ferrite. Mo can have a negative effect on toughness, which is closely associated with Mn or Ti contents and cooling rate [63, 142]. Evans and Bailey concluded that addition of 0.25% Mo can promote acicular ferrite and optimised Charpy toughness at 1% Mn concentration, but above 0.5% Mo ferrite with second phase will substitute acicular ferrite [102]. It has been reported that an increase of 0.01% Nb was found to induce upper bainite structure in submerged arc weld deposits [148]. Furthermore, Farrar and Harrison pointed out that the influence of Nb on acicular ferrite formation depended on the overall hardenability, Nb content and cooling rate [149]. The observation from weld A suggests that the synergistic effect of Mo and Nb assists in a large fraction of bainite formation and further results in a degradation of toughness.

As expected in weld C, relatively high Mo and V are contained due to the high dilution. Although the amount of Mo is at the same percentage level as that of weld A, the combined Mo and V shows no tendency to promote bainite formation even under fast cooling. The beneficial effect to enhance acicular ferrite formation is attributed to high V. Evans and Bailey have observed that increased V up to 800 ppm can not only exert a beneficial effect on acicular ferrite formation at the expense of bainite formation but also on refining the structure [102]. The microstructure observation of weld C shows that weld chemistry containing Ti, Al and V addition coupled with high Mo assists in acicular ferrite formation regardless of under fast or slow cooling.

6.5 Summary

This chapter has presented comparison work performed in order to understand the property changes that occur in the weld metal. In summary, a reasonable relationship can be built up between microstructure and toughness.

Although the same strength grade S690QL steels are welded with identical filler metal, various alloy designs from base materials have greatly influenced weld metal composition due to high dilution from modified spray arc welding. In view of microstructural aspects, acicular ferrite acting as predominant structure can safely deliver a good toughness. The replacement of acicular ferrite by bainite results in an abrupt fall of toughness under fast cooling in weld A. The reason for microstructural and toughness variation is attributed to high Mo+Nb level and fast cooling rate. Increased Nb and Mo content in the weld metal is actually picked up from base material. Weld B has additional effect of high Ti picked up from base material, leading to predominant acicular ferrite structure formed in all weld metals. Although high level of Mo is contained in weld C, co-existence of other alloying elements (e.g. Ti, Al and V) have inter-contributed to acicular ferrite formation even under fast cooling.

The above microstructural difference indicates that the final alloying composition in the weld metal can be tailored by the dilution of base metal even in the case of identical filler metal being used. Hence, when modern welding technology with high dilution is applied, it should be noted that the alloy pick-up from base material can occur to the weld metal and appropriate welding parameters must be adjusted to this composition variation.

7 Microstructure evolution and mechanical properties of CGHAZ and FGHAZ

In the CGHAZ and FGHAZ, the initial microstructure of base material undergoes major changes due to a very quick and steep local thermal cycle. The thermal cycle with peak temperature above austenitisation allows austenite grain coarsening. Subsequently, austenite decomposes into low-temperature transformation products that can cause reduced toughness. Hence, metallurgical examination and toughness tests of the HAZ were carried out with particular attention to structural characteristics. Since the evolution of HAZ microstructure depends on several factors (peak temperature, austenite grain, alloy, etc.), physical weld simulation was performed to investigate HAZ microstructure and austenite grain growth behaviour by varying peak temperature.

The microstructure evolution as a result of different weld thermal cycles was observed by optical microscopy and high resolution SEM. The austenite grain growth behaviour is strongly correlated with the type of microalloy precipitates in steels. In order to confirm the presence of fine microalloy precipitates, one representative TEM analysis was carried out. The crystallographic orientation of different structure was also characterised by EBSD analysis.

7.1 Microstructure characterisation

Fig. 7.1 shows optical and SEM images of the CGHAZs from Nb-containing welds A. The Nb-containing CGHAZs exhibit a mixed microstructure containing upper, lower bainite and martensite. In weld A1 with high heat input ($t_{8/5}$ 20.4 s), the time above austenitisation extends, thus grain growth and diffusion process are favoured. The resultant bainitic ferrite products have a comparatively large size. Some coarse carbides precipitate inside and retained austenite films is formed between the laths. As fast cooling is applied (weld A3 with $t_{8/5}$ 11.4 s), limited grain growth occurs and subsequently small bainitic ferrite along with fine precipitates are formed (Fig. 7.1(f)).

The influence of fast cooling on bainitic ferrite refinement can be clearly observed from the SEM images (Fig. 7.1(b), (d) and (f)). The bainitic ferrite lath size decreases as the cooling rate increases. The fine microstructure in the CGHAZ (Fig. 7.1(f)) consists of predominantly lower bainite and martensite, and this structural feature agrees well with the corresponding hardness value. Likewise, FGHAZ microstructure contains lower bainite and martensite but has small austenite grains. Hence, the micrographs are not shown here. Additionally, the hardness values in the FGHAZs show a slight increase due to fine grains and a large fraction of non-tempered martensite, which could be auto-tempered in the CGHAZ.

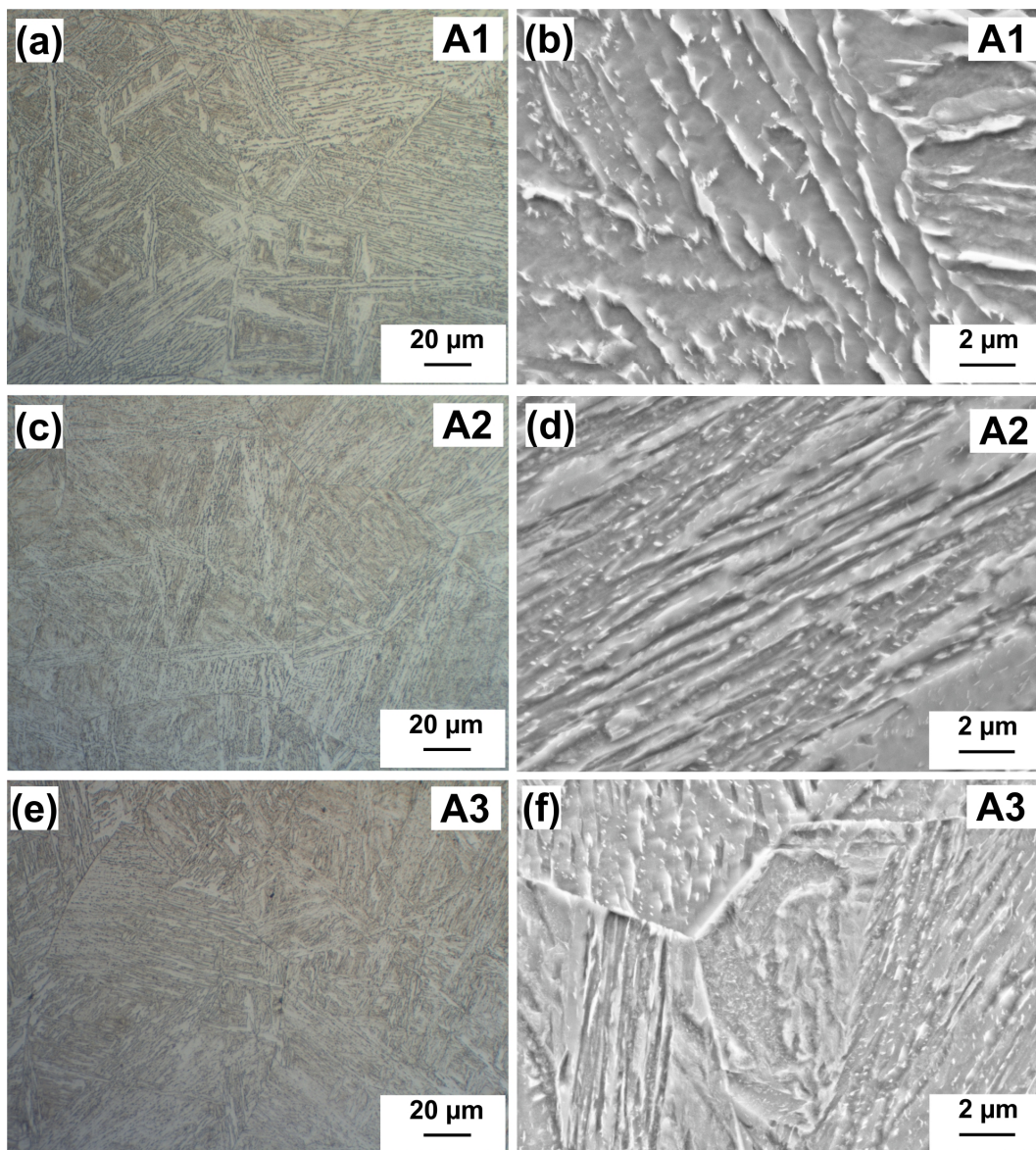


Fig. 7.1: Optical and SEM images of CGHAZ of weld A1 (a, b), A2 (c, d) and A3 (e, f)

Fig. 7.2 shows the microstructure of Ti-containing CGHAZs under different cooling rates. Regardless of slow or fast cooling, the microstructure exhibits a mixture consisting of newly-formed polygonal ferrite, intragranular acicular ferrite (IGF), bainite and martensite. Some retained austenite is also occasionally observed between ferrite plates. Intragranular interlocked ferrite has a chaotic structure, which is well known to be similar to acicular ferrite in the weld metal, as discussed in chapter 6. Another significant microstructural characteristic is the much smaller austenite grains compared with those of the Nb-containing CGHAZ. The austenite grain coarsening behaviour in the three steels is discussed in details in the following section.

An increased cooling contributes to a large fraction of martensite formation (Fig. 7.2 (e) and (f)) and an increased hardness (Fig. 6.2). The FGHAZs contain a mixed microstructure similar to those of the CGHAZs. The small difference in hardness can be attributed to less martensite formation in the FGHAZs.

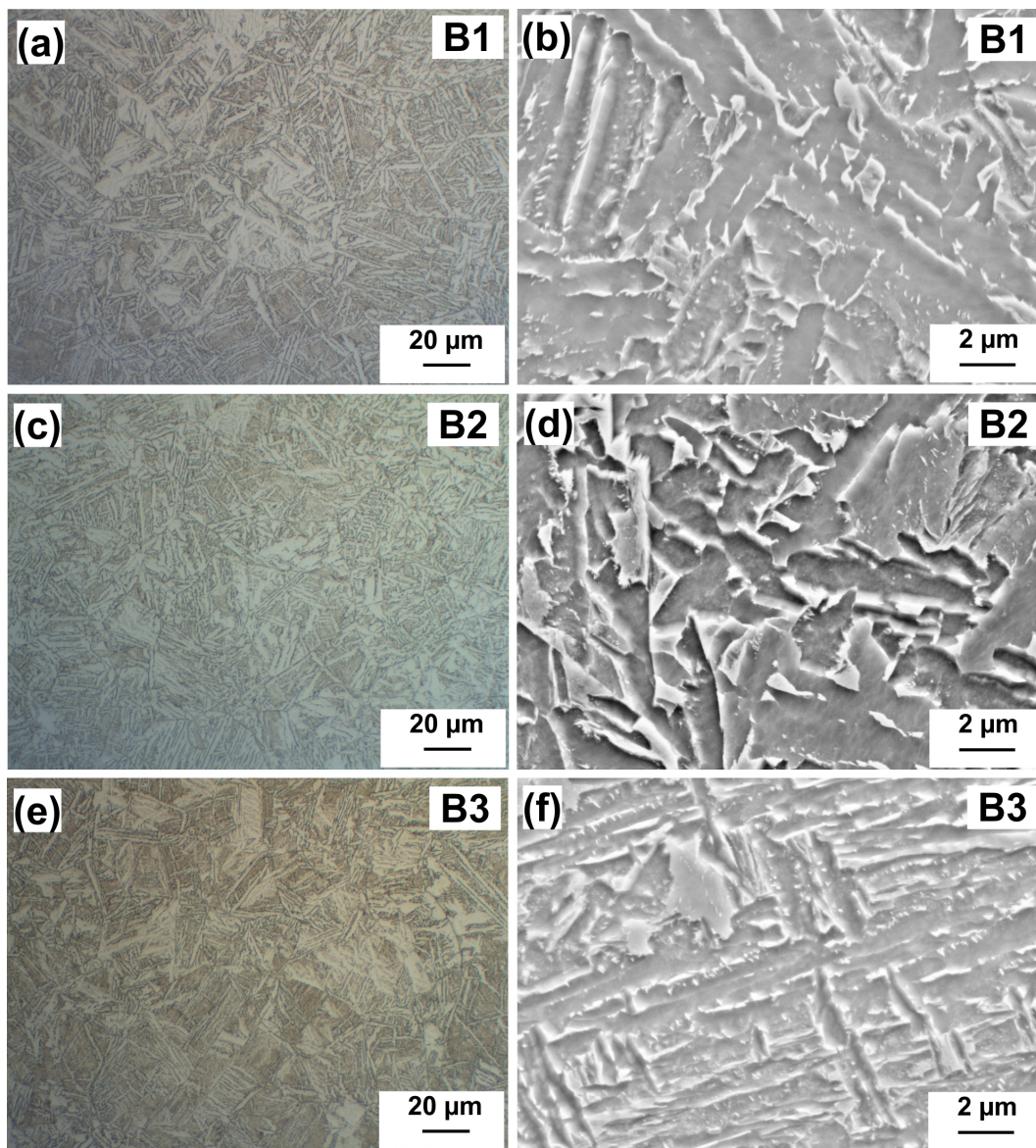


Fig. 7.2: Optical and SEM images of CGHAZ of weld B1 (a, b), B2 (c, d) and B3 (e, f)

The CGHAZ microstructure obtained in the Ti+V-containing welds under different cooling rates is shown in Fig. 7.3. In weld C1 with high heat input, the microstructure is made of IGF, bainite and martensite (Fig. 7.3 (a)). Also, limited retained austenite is formed. A significant grain growth is observed in the CGHAZ compared with Ti-containing CGHAZ. When the cooling rate increases, as a result of decreased heat input, the IGF fraction decreases and bainitic ferrite size becomes small with fine carbides inside. Such a microstructure change, involving bainite and martensite as predominant phases, can explain the corresponding hardness value increase (Fig. 6.3). The hardness in the FGHAZs shows a slight tendency of increase, compared with that in the CGHAZ. This is due to the mixed bainite – martensite microstructure and fine grains.

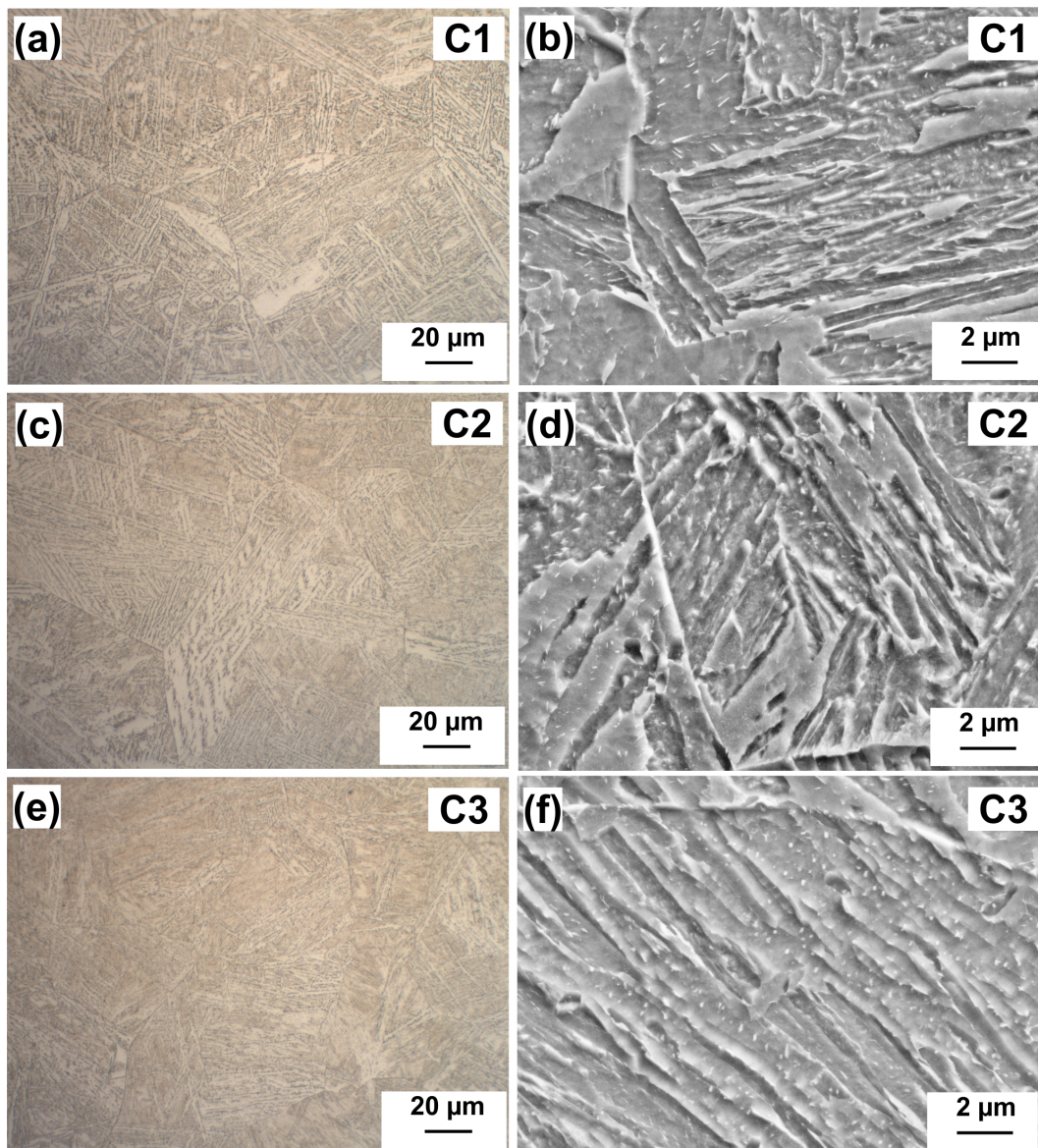


Fig. 7.3: Optical and SEM images of CGHAZ of weld C1 (a, b), C2 (c, d) and C3 (e, f)

7.2 EBSD analysis

The EBSD technique aims to assess the crystallographic features of the two typical microstructure in the CGHAZ that is bainite with second phase between ferrite laths and intragranular acicular ferrite. The presence of the second phase – retained austenite – is strongly linked with the bainite transformation. The chemistry analysis of retained austenite has been performed by EDX mapping to reveal its formation mechanism. The crystallographic misorientation between ferrite plates were analysed to evaluate the resistance of ferrite (with different morphologies) to brittle fracture.

An example of EBSD data obtained with specimen A1 is presented in Fig. 7.4. It shows an image quality map (a), phase map (b) and inverse pole figure IPFX colour maps (c). The image quality map represents the quality of the Kikuchi line for each point measurement. It strongly depends on the specimen preparation condition. If the image quality is low (Fig. 7.4 (a)), the grey-scale level becomes unknown dark point due to the difficulty of obtaining clear Kikuchi-line diffractions in this

region. This occurs very often at grain boundaries (indicated by arrows in Fig. 7.4 (a)) or at retained austenite, where there is many lattice defects. Accordingly, the quality map image (Fig.7.4 (a)) looks like a conventional SEM image. It reveals the typical bainitic structure. Fig. 7.4 (b) illustrates the distribution of different phases, in which red area represents ferrite phase and green represents austenite. Quite limited austenite is identified, as indicated by black arrows. The presence of retained austenite tends to be mostly located at grain boundaries or between bainitic ferrite laths, where unknown black points are often seen. Therefore, this leads to further difficulties in indexing the EBSD patterns. It was confirmed that retained austenite combined with martensite in M – A constituents contains many defects such as dislocations. For this reason, they show especially low image quality, which is often observed in bainite transformation [233]. The colours in Fig. 7.4 (c) correspond to the crystallographic orientation on the transverse direction of observed plane, as indicated by the stereographic triangle. It is evident that the bainitic ferrite have the same crystallographic orientation, corresponding to the prevailing red colour. This indicates that they belong to one crystallographic packet group. Some retained austenite are formed between the ferrite laths. They have also the same crystallographic orientation because they are retained from the same prior austenite.

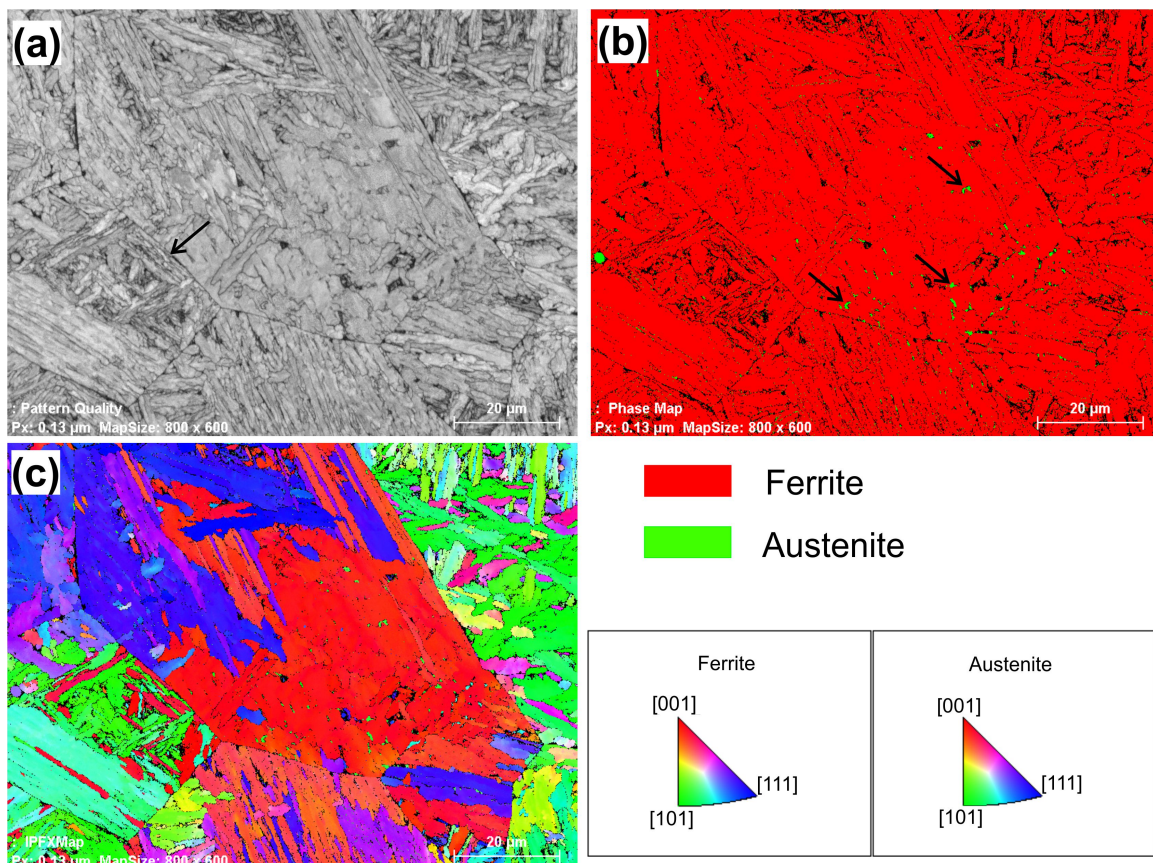


Fig. 7.4: Typical orientation imaging maps obtained from the EBSD measurement. (a) pattern quality, (b) phase map, (c) inverse pole figure (IPF) colour map

Another EBSD measurement was performed around the local retained austenite (Fig. 7.5). A selected region is indicated by red line rectangle in a SEM image (Fig. 7.5 (a)). In the middle of the selected area, a bright white structure is distinguishable from its surrounding matrix. Although this bright structure is of low image quality (Fig. 7.5 (b)), one part of it can still be identified to be retained austenite (indicated by green-coloured phase in Fig. 7.5 (c)). The surrounding matrix is bainitic ferrite

which has a low misorientation angle between the ferrite plates (around 3.5°).

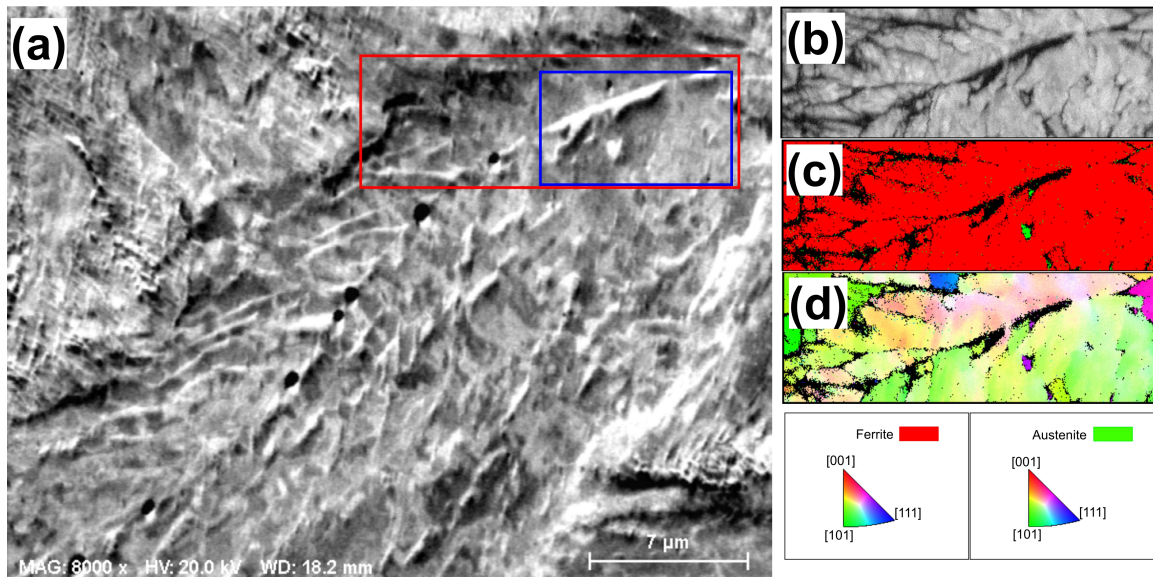


Fig. 7.5: Typical orientation imaging maps obtained from the EBSD measurement. (a) SEM image, (b) pattern quality of the region indicated by red line, (c) the corresponding phase map and (d) IPF colour map

In order to reveal the alloy distribution in the retained austenite, EDX elements mapping is presented in Fig. 7.6. The measured area is indicated by blue rectangle (Fig. 7.5 (a)). Both observed needle-like and blocky-type region has less Fe content compared with the surrounding ferrite matrix (Fig. 7.6 (b)), but they are enriched with high Ni (Fig. 7.6 (c)). Moreover, only an increase of C in needle-like shape region is shown in Fig. 7.6 (d). The elements distributions imply that the alloying elements Ni and C are enriched in retained austenite and stabilise it to room temperature. There is no significant change of Si, Mn and Cr concentration in retained austenite.

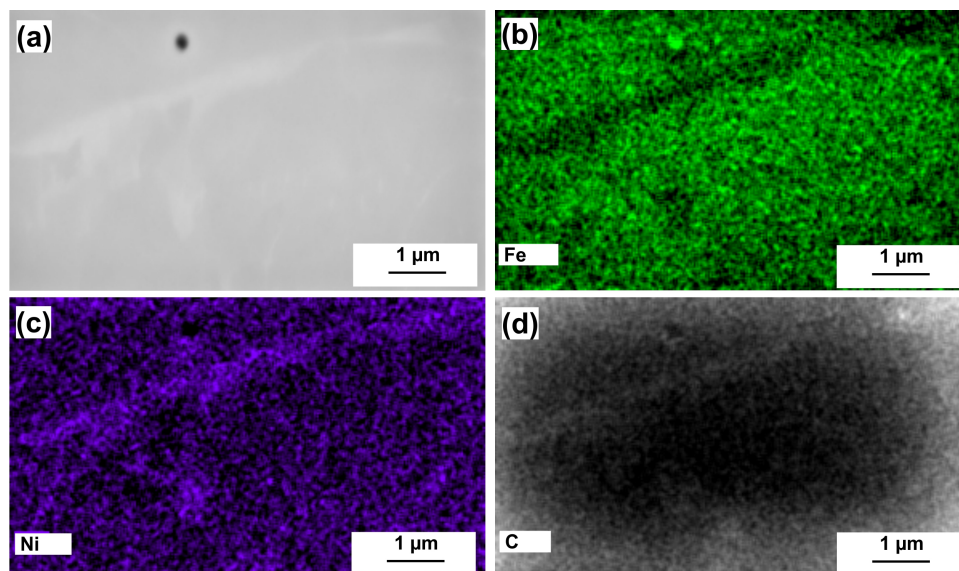


Fig. 7.6: EDX mapping of the region selected by blue line (a) SEM image, (b) Fe, (c) Ni and (d) C

As is the case for the intragranular ferrite microstructure, another EBSD example was obtained with B2 specimen. Fig. 7.7 shows the IPF colour map combined with boundary misorientation distribution and IPF colour map for austenite. The grain boundaries are based on the misorientation between

adjacent points of the EBSD data. Different criteria with varied colours are used to draw the boundary, as shown in Fig. 7.7 (a). The low angle misorientation boundaries are highlighted by red, dark yellow or magenta colours in the bainitic ferrite packet. However, high angle boundaries coloured with blue or violet interrupt the parallel bainite structure. These are grain boundaries between intragranular acicular ferrite and bainite. This point could be deduced based on the morphology characteristics of fine interlocked structure from intragranular ferrite. As discussed in former microstructure analysis, the fine acicular ferrite can grow from the same inclusions but with different crystallographic orientation. Also, some retained austenite is visible in Fig. 7.7 (b), which is accompanied with the formation of intragranular ferrite and bainite.

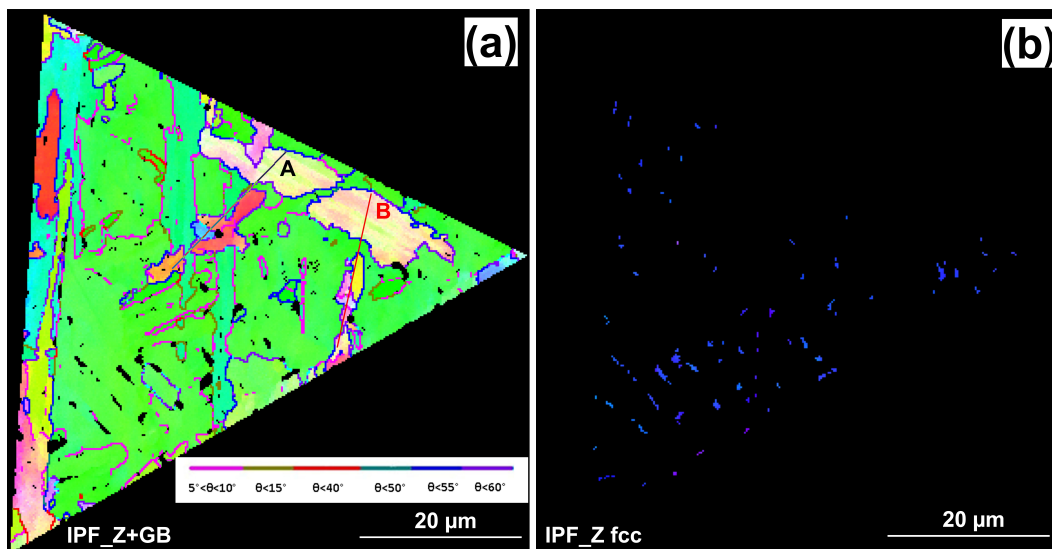


Fig. 7.7: Typical orientation imaging maps obtained from the EBSD measurement. (a) IPF bcc colour map combined with boundary misorientation distribution and (b) IPF fcc colour map for austenite

Further studies on the misorientation were performed in this mixed structure. Fig. 7.8 shows the point to point and point to origin misorientation profile of line A and line B, as indicated in Fig. 7.7 (a). It demonstrates the orientation change between and within the ferrite laths. From Fig. 7.8 (a) and (b), it is evident that nearly all acicular ferrite plates have high angle boundaries with misorientation angle greater than 45° or sometimes with a misorientation of approximately 60° . However, within bainitic ferrite low angle boundaries less than 10° are often found.

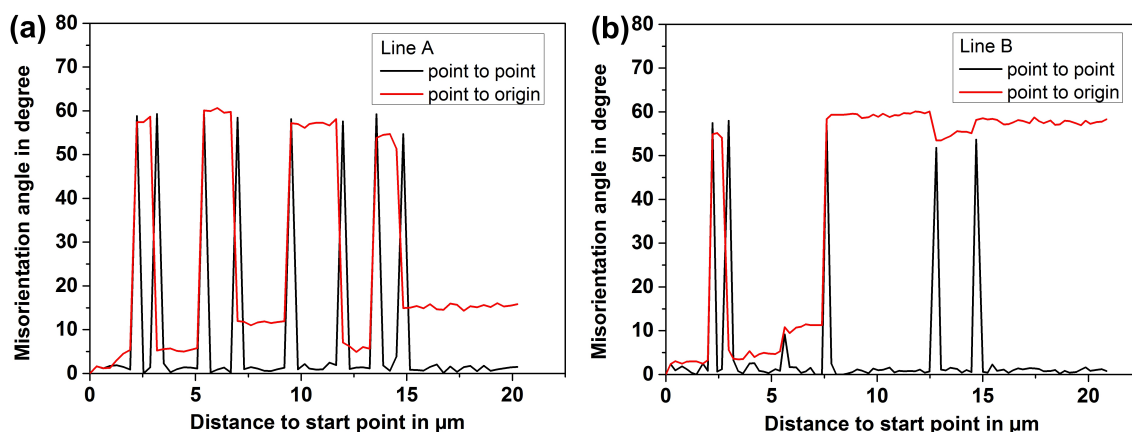


Fig. 7.8: Misorientation along the line A (a) and B (b) including point to point and point to origin misorientation

The characteristic orientation feature is derived from the nature and its formation mechanism of different microstructures. The influence of the misorientation between neighbouring crystallographic ferrite grains is strongly correlated with the ability to resist crack propagation. High angle boundaries are found to induce a noticeable crack deviation and increase the resistance ability, compared with lower misorientation boundaries. Consequently, it is concluded that the intragranular acicular ferrite has high resistance ability to brittle fracture and correspondingly excellent toughness. To summarise, the EBSD results provide useful crystallographic information on the austenite decomposition products such as bainite and intragranular acicular ferrite and this indicates their respective cracking resistance ability. Further discussion on the EBSD results and toughness property is given in the next section.

7.3 Austenite grain growth simulation

As observed in section 7.1, different grain growth behaviours occur to the three microalloyed HAZs. The subsequent transformation products differ considerably as well. Therefore, it is essential to further investigate the austenite grain growth behaviour as well as the effect of the austenite grain size combined with microalloy on further phase transformation. As discussed previously, the austenite grain growth depends on the peak temperature, holding time and the presence of precipitates. Different microalloy precipitates, which have been predicted by Thermo-Calc and confirmed experimentally (section 5.2), are expected to provide restraining effect on austenite coarsening. The present study applies inductive heat-treatment to simulate HAZs by varying the peak temperature (1300°C – 1000°C). The cooling rate $t_{8/5}$ is controlled to be around 15 s. To evaluate the behaviour of microalloy precipitates during thermal cycle, several thermodynamic variables can be used by reference with the calculation results in section 5.2, such as composition of precipitates, dissolution temperature and volume fraction.

7.3.1 Austenite grain growth behaviours

The theory of boundary pinning effect from particles has already been discussed in section 2.4.2. The control of grain growth in the HAZ requires fine precipitates. Moreover, a sufficient amount of precipitates are still stable in the austenite even at elevated temperature. From Table 5.2, different types of microalloy precipitates are formed in the three steels (besides that AlN is contained in the three steels) with varied stabilities and volume fraction. Based on the precipitation characteristics calculated by Thermo-Calc, coupled with grain growth equation involving particle dissolution or coarsening (section 2.4.2), it is expected that such microalloy differences will produce remarkable variation of austenite grain growth. The experimental results are illustrated in Fig. 7.9.

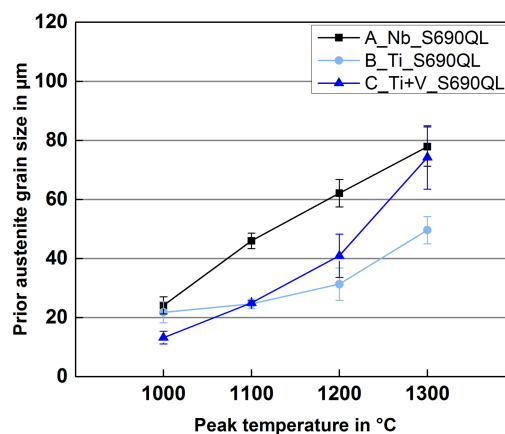


Fig. 7.9: Austenite grain growth as a function of peak temperature of thermal cycle [186]

As expected, the austenite grain size of the three steels increases with increasing T_p . This is caused by the high grain boundary mobility under elevated temperature and less pinning force against grain growth. Such decreased pinning effect is from larger and fewer precipitates as a result of thermal cycle. The response of microalloy precipitates during thermal cycle were observed: dissolution, re-precipitation and Ostwald ripening effect [174]. The behaviour of different precipitates has a significant impact on the grain growth rate and final grain size. Hence, this process strongly depends on the precipitate stability (Table 5.2) and experienced T_p . It should be noted that Cr and Mo carbides are not discussed because they are substantially more soluble in austenite than the other microalloy precipitates.

For the Ti-containing HAZs, the relatively limited grain size change occurs even when the sample is heated up to 1200°C. This suggests that the peak temperature is not high enough to dissolve the Ti-rich carbonitrides. As a result, the strong pinning effect is present and this allows only quite limited grain growth. Thermodynamic calculations by Thermo-Calc indicate that the dissolution temperature of Ti(C,N) is higher than 1450°C. After T_p higher than 1300°C, fine TiN is thermally unstable. Limited dissolution happens due to Ostwald ripening, thus austenite grain grows up to $49.6 \mu\text{m} \pm 4.6 \mu\text{m}$.

In the case of the Nb-bearing steel, as thermal cycle reaches above 1100°C, the austenite grain growth is significant. This is probably attributed to the extensive dissolution of Nb(C,N) and AlN. Furthermore, the grain size obtained after thermal cycle with T_p of 1300°C shows a pronounced increase up to $77.8 \mu\text{m} \pm 6.7 \mu\text{m}$. To compare the growth factor after thermal cycle with T_p of 1300°C from initial austenite, the growth factor for the Nb-containing steel is around 9 whereas 2.5 for the Ti-containing steel. For the Ti+V-containing steel, after thermal cycle with T_p of 1000°C, the austenite exhibits marginal growth compared with initial austenite. As the T_p rises, the austenite grain size increases accordingly. The corresponding growth rate is much faster than that of the Ti-containing steel.

7.3.2 Microstructure of simulated HAZs

Fig. 7.10 displays an overview of optical microstructure in the simulated CGHAZ (T_p 1300 °C) and FGHAZ (T_p 1100°C) for the three steels. Fig. 7.10 (a) and (b) show a similar microstructure between simulated CGHAZ and FGHAZ in the case of Nb-containing steel. It consists of a large fraction of bainite and some martensite. Typical parallel bainitic ferrite is observed, which tends to nucleate along the grain boundaries.

The Ti-containing HAZs shows apparent changes in ferrite morphology (Fig. 7.10 (c) and (d)). The dominant structure contains much finer IGF in weld B. It also contains a small fraction of bainite. However, there is no large bainite packet presence, as the case of weld A. In the FGHAZ, the aspect ratio of IGF is smaller than that in the CGHAZ, moreover, much more polygonal ferrite exists.

The microstructure of the Ti+V-containing CGHAZ is characterised by a mixture of interlocked IGF and plate-like bainite (Fig. 7.10 (e)). But the IGF structure is absent in the FGHAZ. Correspondingly, the main microstructure contains bainite and a small fraction of martensite (Fig. 7.10 (f)). The microstructure feature is further observed by SEM (Fig. 7.11).

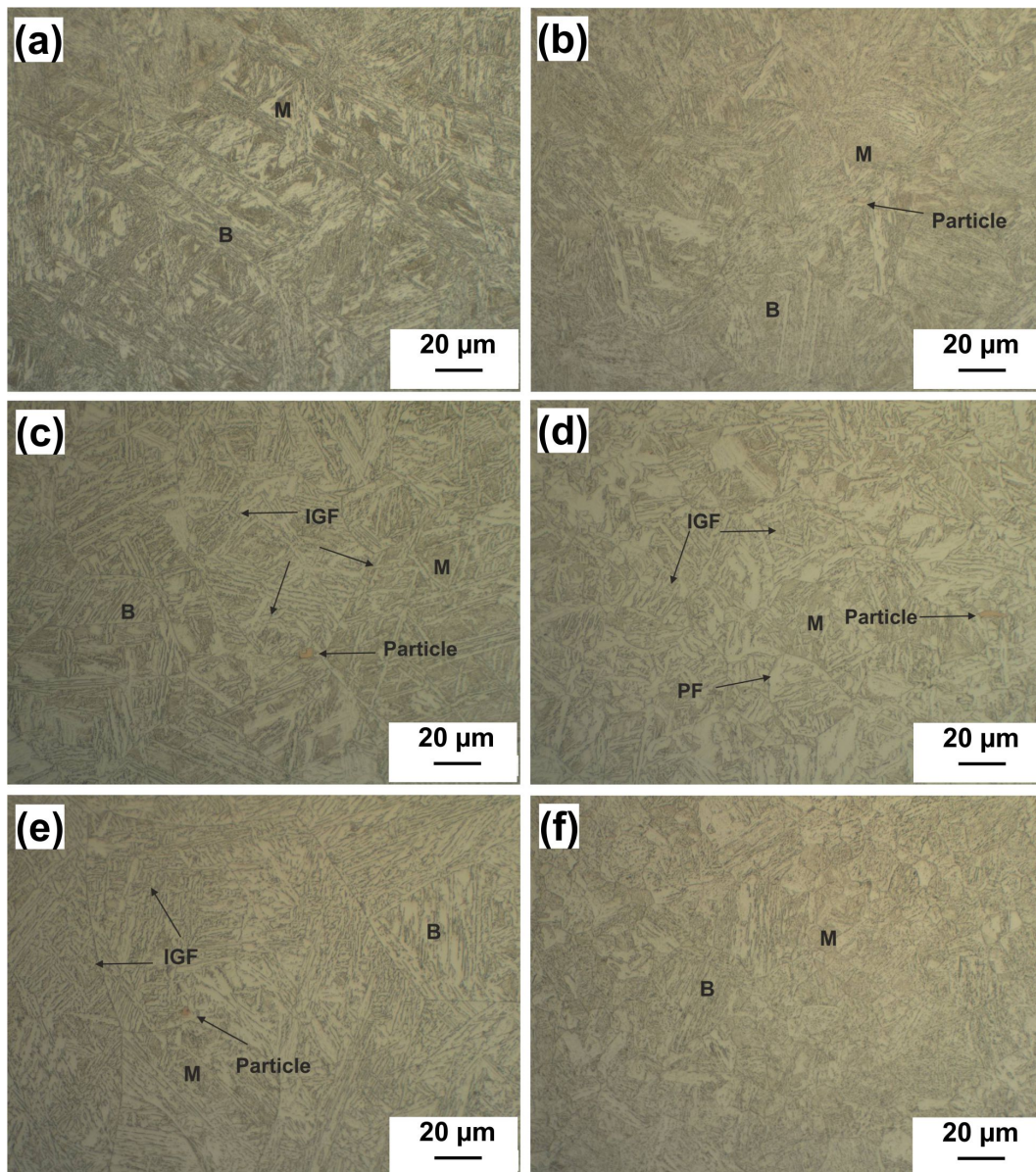


Fig. 7.10: Optical micrographs of simulated CGHAZ and FGHAZ of steel A (a, b), B (c, d) and C (e, f). M, martensite; B, bainite; PF, primary ferrite; IGF, intragranular acicular ferrite [186]

Fig. 7.11 (a) – (d) shows a representative micrograph for the Nb-containing CGHAZ. It has a large amount of needle-like carbides within very fine lath-like bainitic ferrite. This is termed as typical lower bainite microstructure [114]. In Fig. 7.11 (d), parallel elongated carbides within single ferrite lath usually have their longest axis inclined approximately 60° to the growth direction of ferrite. The length of carbides tends to decrease but the density increases as T_p is reduced from 1300°C to 1000°C . Another feature is that small-sized spherical carbides are within the bainitic ferrite laths (Fig. 7.11 (d)). Chun et al. [234] analysed the similar needle-like and spherical carbides in bainite/martensite. They appear to be Fe-rich carbides and multi-microalloyed carbides (Ti, Nb, V and Cr) respectively. In Nb-containing steel, fine spherical carbides are presumed to form multi-alloyed carbides from strong carbide forming elements (Nb, Mo and Cr). Fig. 7.11 (e) shows a micrograph of the tempered martensite. Thin film of retained austenite is sometimes visible.

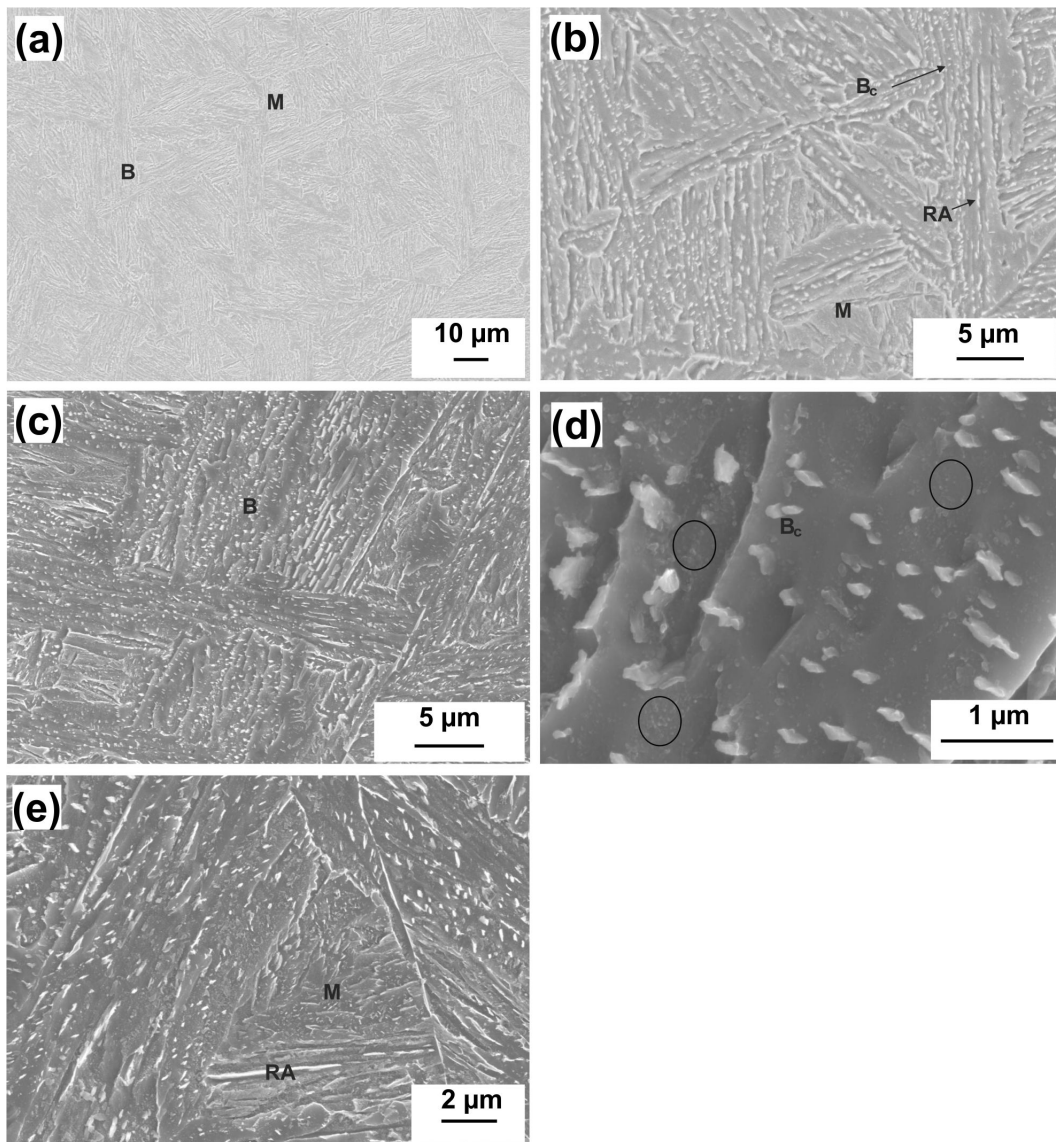


Fig. 7.11: SEM micrographs of simulated Nb-containing HAZs: CGHAZ (a, b) as observed by secondary electrons (VPSE); FGHAZ (c, d) and (e) martensite structure in FGHAZ as observed by secondary electrons (InLens). In black circles much finer spherical precipitates are found within bainitic ferrite. RA, retained austenite; B_c , carbides in bainitic ferrite [186]

In the Ti-containing CGHAZ, interlocked IGF contains small enclosed ferritic plates without parallel second phases (Fig. 7.12 (a) – (c)). Under much higher magnification, cuboidal precipitates in nano-scale can be observed, indicated by arrows (Fig. 7.12 (d)). The smallest side-length is identified around 25 nm. Large-sized precipitates can reach up to above 200 nm. Assumed these cuboidal precipitates are Ti-rich nitrides (which are probably similar to the coloured particles observed in Fig. 7.10), the austenite grain growth behaviour can be explained to be influenced by the pinning effect from these small-sized stable particles. On the other hand, the presence of fine nitrides is closely related to microstructural changes in the HAZs, in particular the presence of IGF. Consequently, the assumption of fine Ti-rich nitride is strongly supported by the grain growth results, microstructural observations and the previous Thermo-Calc simulation results.

Fig. 7.12 (b) and (c) show comparatively more retained austenite around the ferrite plates, which is

observed in bright island or irregular shape. When austenite transforms to IGF and polygonal ferrite, the diffusion of substitutional or carbon atoms across $\gamma \rightarrow \alpha$ interface occurs, invoking carbon or alloying elements enriched in the retained austenite. Also, it is anticipated that in Mo-free steel B, much carbon can partition into austenite but instead of that, carbon is consumed by carbides. After fast cooling this carbon-enriched austenite can be retained or further partially transform into martensite. Fig. 7.12 (e) displays the details of decomposition of retained austenite into martensite. The tempered needle-like carbides is observed within martensite.

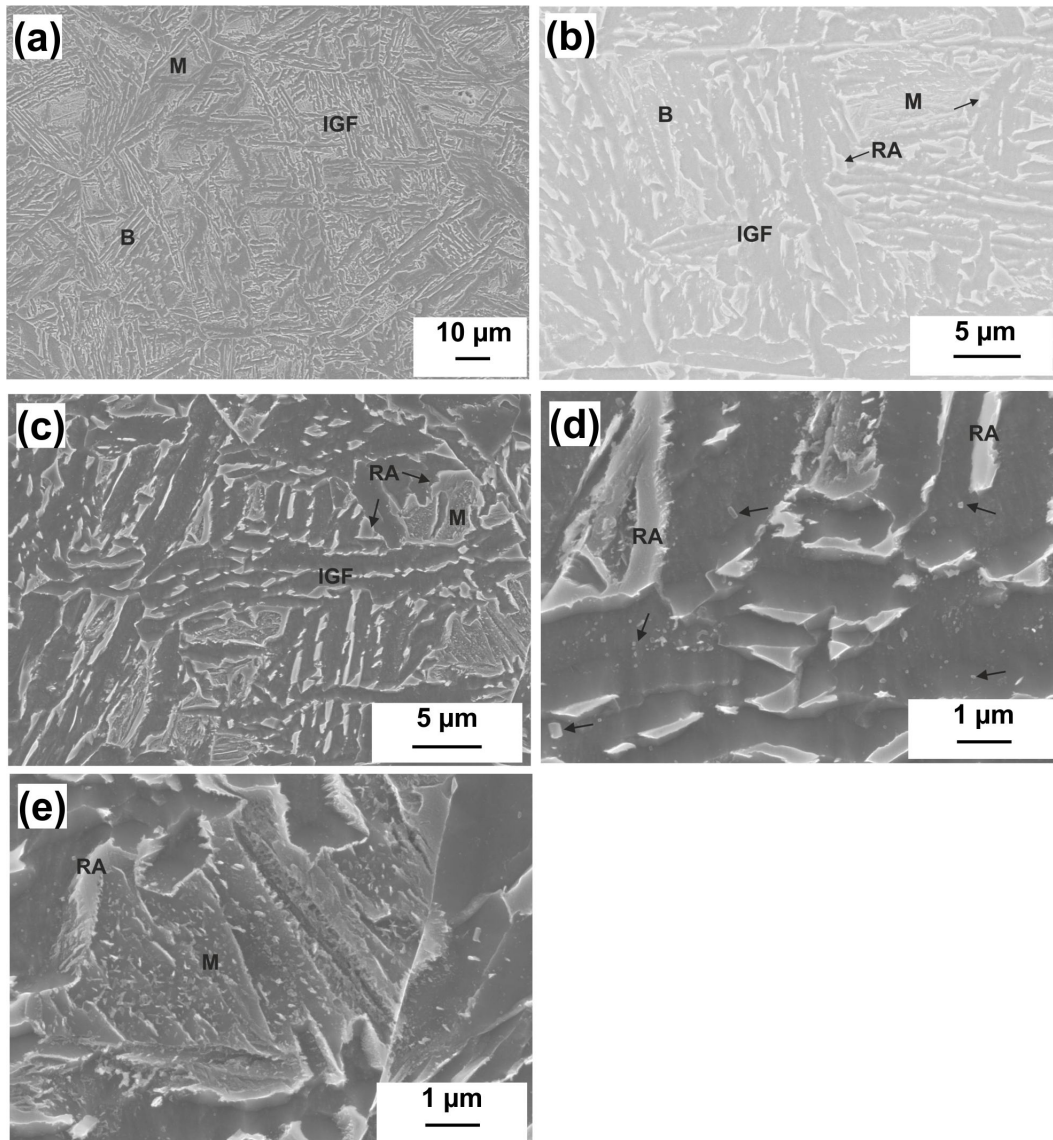


Fig. 7.12: SEM micrographs of simulated Ti-containing HAZs: CGHAZ (a, b) as observed by secondary electrons (VPSE); FGHAZ (c, d) and (e) martensite structure in FGHAZ as observed by secondary electrons (InLens). Black arrows indicate cuboidal shaped precipitates [186]

Fig. 7.13 (a) and (b) illustrate a mixed microstructure of bainite and IGF in the Ti+V-containing CGHAZ. The bainitic ferrite contains a few needle-like carbides. However, in the FGHAZ (Fig. 7.13 (c) and (d)), IGF is almost replaced by bainite. Within bainitic ferrite it contains needle-like carbides with a lower density than that of the Nb-containing steel. Similar fine spherical precipitates and a few cuboidal particles are also found within ferrite laths. Fig. 7.13 (e) and (f) show bainite, martensite

and retained austenite microstructure in the CGHAZ and FGHAZ. Separated martensite island is often formed in the CGHAZ and sometimes surrounded by retained austenite. Also, it is found in island or thin film shape between intragranular acicular ferrite plates or parallel bainitic ferrite.

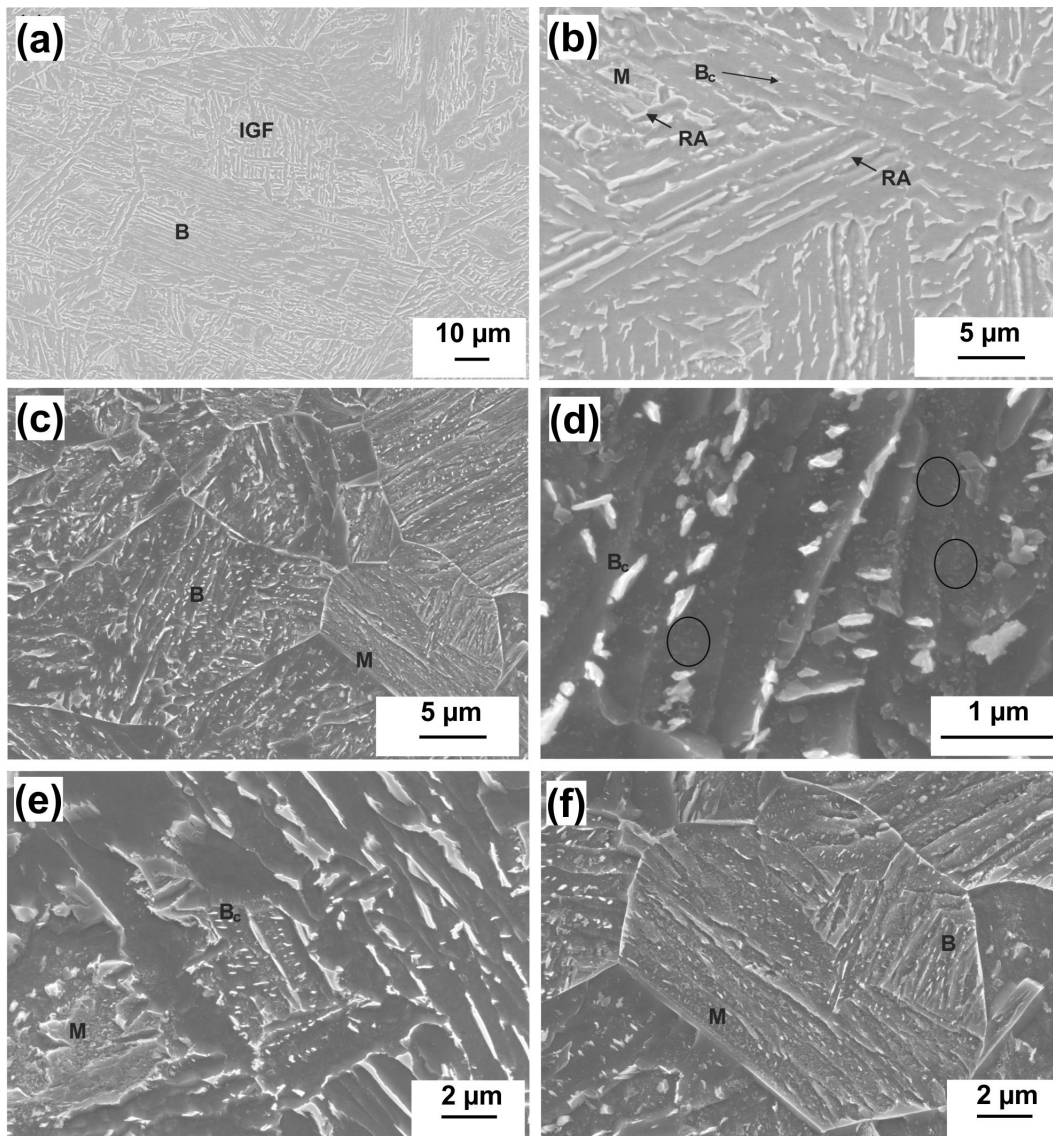


Fig. 7.13: SEM micrographs of simulated Ti+V-containing HAZs: CGHAZ (a, b) as observed by secondary electrons (VPSE); FGHAZ(c, d), bainite (e), and martensite (f) as observed by secondary electrons (InLens). In black circles much finer spherical precipitates are found within bainitic ferrite [186]

7.3.3 Hardness of simulated HAZs

A comparison between the simulated and as-welded HAZs was carried out in order to emphasise the validity of the simulation results. The hardness profiles for the simulated HAZs and as-welded HAZs are plotted in Fig. 7.14. The hardness comparison between the simulation and as-welded specimens shows excellent agreement. The Nb-containing steel has the highest hardness in the all HAZs, around $330 \text{ HV}_{10} \pm 10 \text{ HV}_{10}$. The hardness distribution from CGHAZ to FGHAZ shows a similar increasing tendency in the Ti+V-containing weld. More precisely, the hardness increases from 250 HV_{10} to 290 HV_{10} . The Ti-containing weld has the lowest hardness value, around $260 \text{ HV}_{10} \pm 10 \text{ HV}_{10}$ in the simulated HAZs.

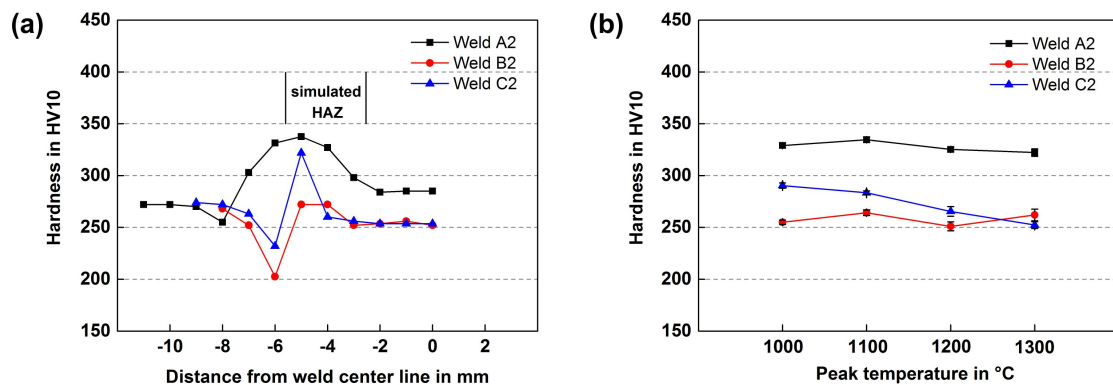


Fig. 7.14: Comparison of hardness results between as-welded (a) and simulated (b) HAZs [186]

Since small temperature gradient exists in the simulated HAZ, grains can grow more rapidly compared with an as-welded HAZ. This can cause slightly different grain boundary strengthening effects. Moreover, the residual stress in the welded joints is not created in the simulated specimens. This can cause limited deformation effect and then influence precipitation behaviour during cooling. As a result, the precipitation hardening effect can be reduced. Both possibilities can cause a small discrepancy in phase transformation process and properties (e.g. hardness) between simulated and as-welded HAZ.

To understand the different trends shown in Fig. 7.14, the hardness values can be interpreted in terms of the specific microstructural characteristics resulting from different alloying elements additions and thermal cycles. The microstructural features depend mainly on the chemical composition, peak temperature and cooling rate. Under the cooling rate ($t_{8/5}$ 15 s), in Nb-containing HAZ, the predominant microstructure is bainitic ferrite with high dense needle-like carbide and fine spherical particles. In the other two steels, the role of Ti and Ti+V addition is to promote intragranular acicular ferrite formation. It is noteworthy to realise that other alloying elements (e.g. Cr, Mo, and Ni) also have strong effects on hardenability and phase transformation. In the present case, the influence of Mo in Nb and Ti+V-containing steel should be considered with regard to bainite formation and precipitation strengthening effect. It was reported that addition of Mo caused much more nucleation sites for (Nb, Mo) carbides and then promoted precipitation hardening [235]. Jang et al. [236] also confirmed that Mo greatly influenced the precipitation and coarsening behaviour of carbide particles in Ti-Nb-Mo steels and retarded the hardness decrease after ageing treatment.

The high hardness value in Nb-containing HAZ, around $330 \text{ HV}_{10} \pm 10 \text{ HV}_{10}$, is due to a mixed bainitic and martensitic structure. The comparatively low hardness of Ti-containing HAZ corresponds well to its large fraction of relatively soft IGF phase. The variable aspect ratio of IGF causes a slight change of hardness. For Ti+V-containing weld C, primary microstructure changes from a mixture of IGF and bainite to bainite. This results in a significant increase in hardness from around 250 HV10 to 290 HV10. The hardness increase in bainitic ferrite is associated with carbides and precipitation strengthening. Hence, for both Nb and Ti+V-containing welds, it is reasonable to consider strong precipitation strengthening effect for the increase in hardness [22]. In contrast, for the Ti-containing weld, it is expected to have coarse particles with a low density and large inter-particle spacing in the final microstructure. This phenomenon can lead to less strengthening in ferrite and is responsible for low precipitation strengthening and a low level of yield strength [237]. The relatively lower hardness of Ti-containing HAZ could imply less precipitation strengthening in the microstructure. But it is unknown

whether a balance between toughness and strength can be obtained due to the refined structure. This needs further investigation with respect to the influence of microstructure on mechanical properties.

7.4 Identification of microalloy precipitates by TEM

To identify microalloy precipitates predicted by Thermo-Calc, one representative TEM analysis on several nano-sized microalloy precipitates has been made with simulated Ti-containing HAZ specimens. The FIB film was selected to be cut close to the grain boundary and AF structure, where there are probably more fine precipitates.

Fig. 7.15 shows the dark field and bright field STEM images. Several cuboidal of precipitates were observed in dark field or bright field. HAADF images reveal the precipitates with high contrast to the matrix structure. One visible particle is located at a grain boundary with a characteristic length of around 80 nm. Fig. 7.16 shows another fine precipitate at grain boundary under high magnification.

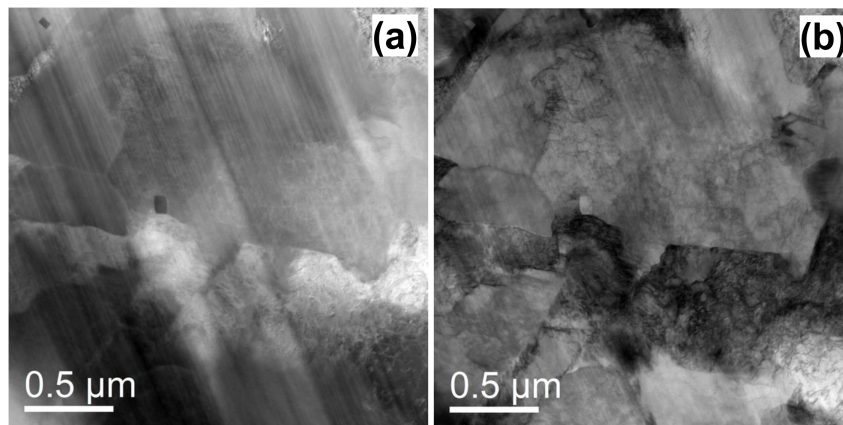


Fig. 7.15: Dark (a) and bright field (b) STEM images

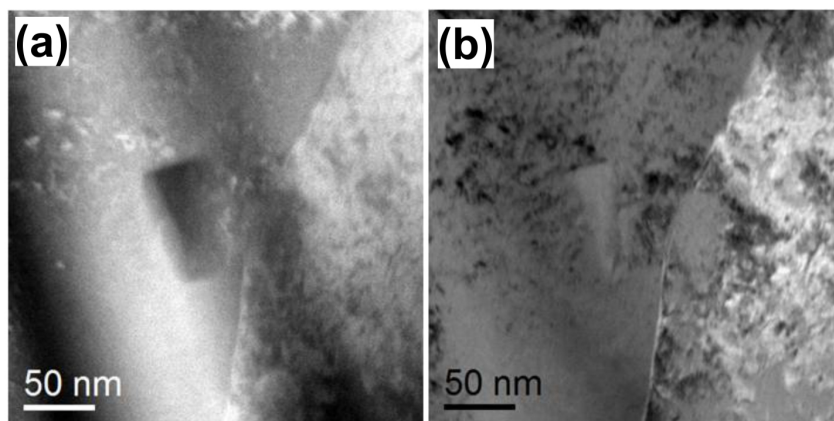


Fig. 7.16: Dark (a) and bright field (b) STEM images for one precipitate at grain boundary

Fig. 7.17 shows the distribution of several precipitates and the corresponding elemental analysis. In Fig. 7.17 (a), some particles are aligned close to grain boundaries. The large one has a characteristic length up to 160 nm, whereas very fine one is only around 30 nm. Fig. 7.17 (c) confirms that they are Ti-rich precipitates. However, Fig. 7.17(d) and (e) show few detectable concentrations of C and N in these precipitates. By EDX point analysis (Fig. 7.18 (c)), the peak of C and N is too weak and difficult to identify (Cu is from the support grid). Further, chemical analysis with EFTEM elements mapping displays Ti, N and C distribution in the precipitate, as shown in Fig. 7.19. Accordingly, in

order to determine particle elemental composition more accurately, characteristic EELS spectra were analysed (Fig. 7.20). The result confirms that the particle is composed of C, N and Ti. This provides additional evidence to identify the particle as Ti-rich carbonitrides.

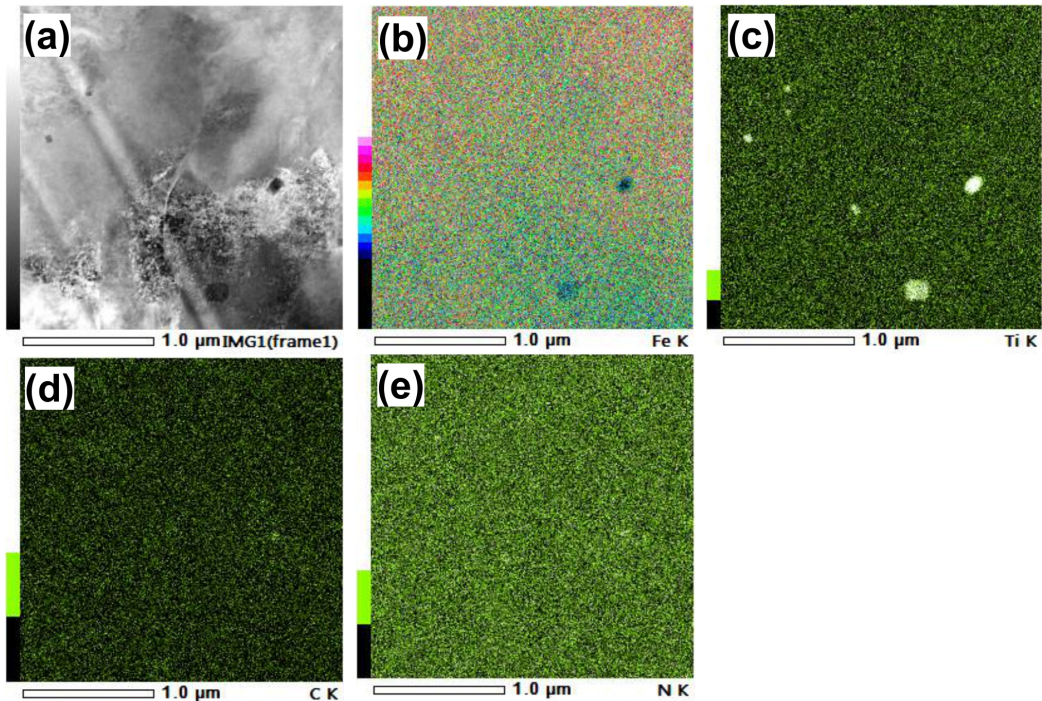


Fig. 7.17: An overview of precipitates distribution (a), elemental mapping of (b) Fe, (c) Ti, (d) C and (e) N

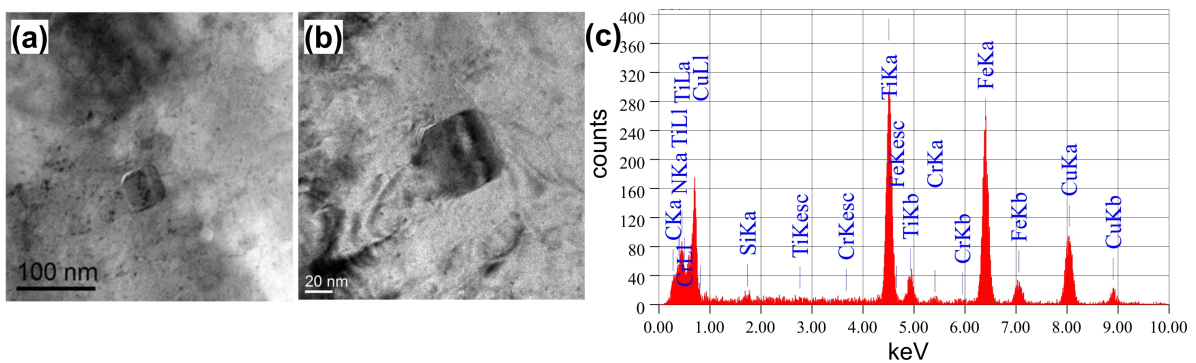


Fig. 7.18: Bright field STEM images of TiN (a), corresponding TEM image (b) and EDX spectra (c)

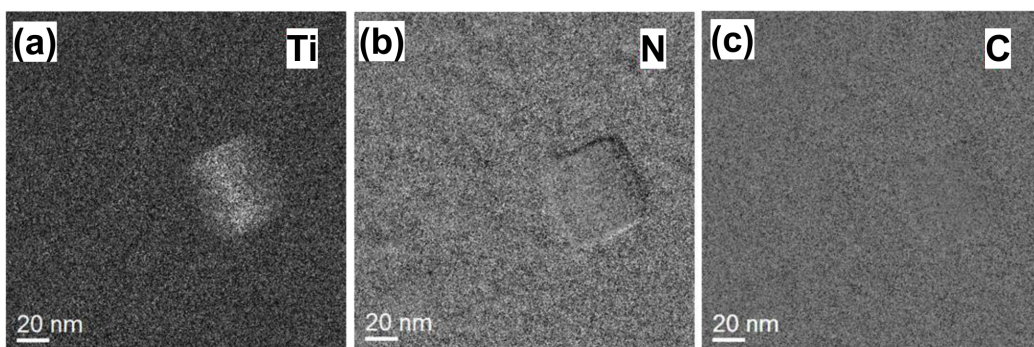


Fig. 7.19: Elements mapping of one precipitate in Fig. 7.18 by EFTEM, (a) Ti, (b) N, (c) C

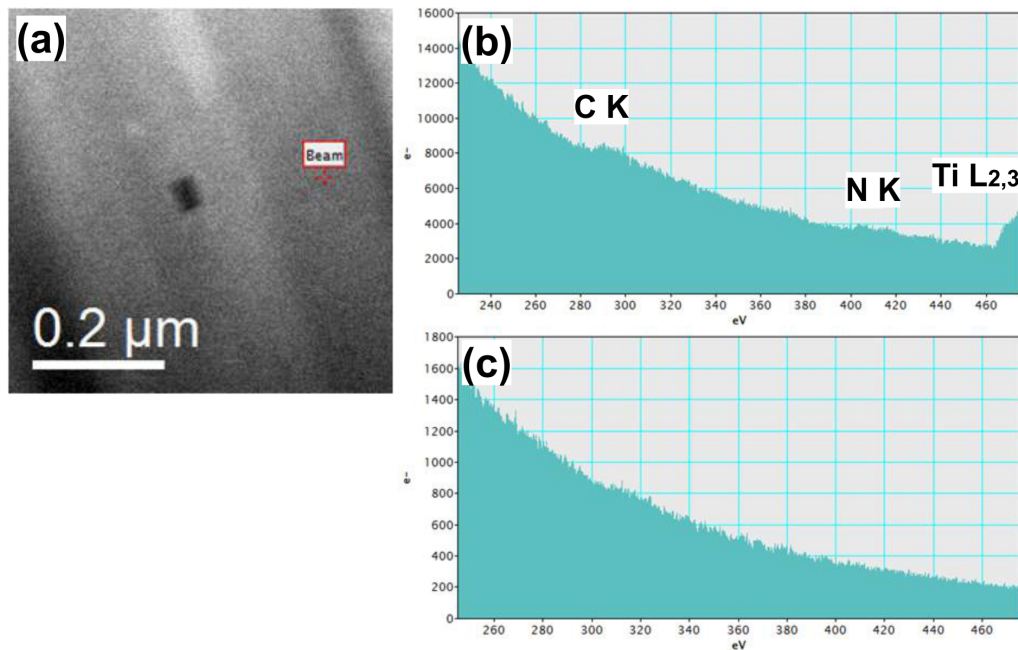


Fig. 7.20: One representative precipitate (a) and elements analysis of precipitate (b) and matrix (c) by EELS

The particles have been referred to as Ti-rich carbonitrides. However, several structural possibilities exist within the titanium-nitrogen/carbon system. In order to identify the crystal structure of particle, observation using high resolution imaging is shown in Fig. 7.21 (a) and (b), where some regions display Moirè fringes patterns. Selected regions were evaluated by means of Fast Fourier Transformation (FFT).

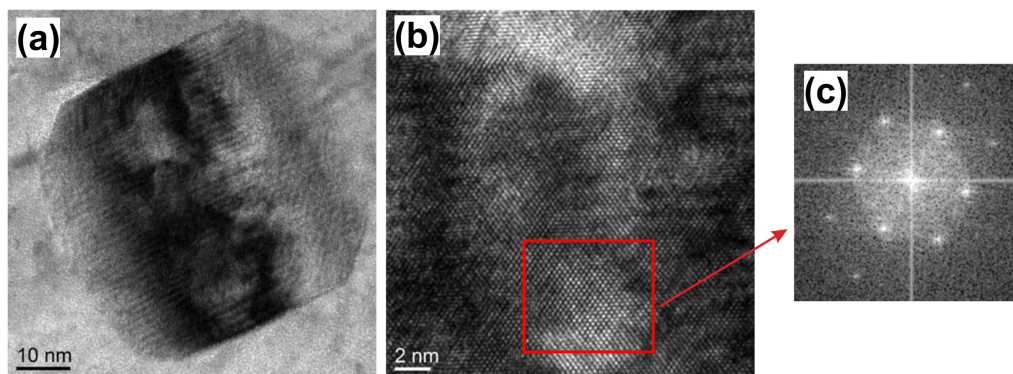


Fig. 7.21: HRTEM image (a, b) of precipitates and the corresponding FFT diagram (c)

The diffraction patterns are shown in Fig. 7.22 (a) and then further analysed using a computer program. The diffraction patterns (Fig. 7.22 (b)) generated from particle can be readily indexed as a [0-11] zone axis pattern for fcc structure (NbCl prototype). Considering the EELS results and previous EDX results on coarse particle of TiN, one conclusion can be made that carbon substitution in nano-sized titanium carbonitride is plausible. Since pure TiC and TiN have similar structure and little difference in lattice parameter ($\text{TiC} = 0.433 \text{ nm}$, $\text{TiN} = 0.424 \text{ nm}$), $\text{Ti}(\text{C},\text{N})$ particle shows a small amount of expansion. In Fig. 7.22 (c), it occasionally reveal faint reflection from cementite (M_3C , M contains Fe and Cr, combined with EDX results from Fig. 7.18), but the volume fraction is too small so that the particles are difficult to be detected amongst the contrast from dislocations and other features within the microstructure. Moreover, it can explain that the observed Moirè fringes arise in the overlap of $\text{Ti}(\text{C},\text{N})$ and M_3C particles.

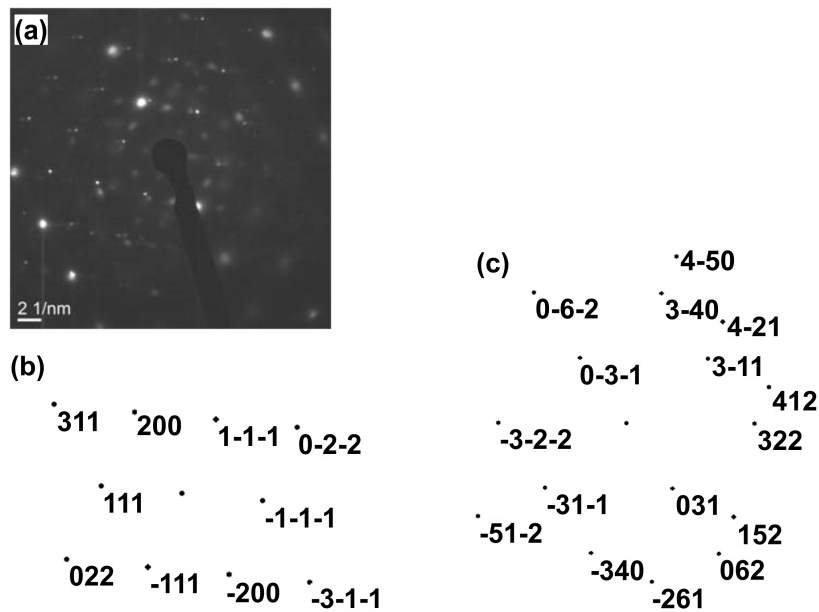


Fig. 7.22: Diffraction patterns (a) of selected region in Fig. 7.18, diffraction pattern solution (b) for $Ti(C,N)$, zone axis $[0-11]$, diffraction pattern solution (c) for cementite M_3C , zone axis $[43-9]$

7.5 HAZ toughness results

The HAZ impact toughness is evaluated on specimens machined from the welded joints. HAZ is a structurally and chemically inhomogeneous. Under this condition, the determination of HAZ toughness characteristics by using selected specimen with standard size is not quite correct, since the obtained toughness result depends greatly on the specimen's location and position of notch but also it is related to the weld geometry and shape.

Table 7.1 summarises the Charpy toughness results from the three HAZs. Note that the observed large toughness value scattering is predetermined by the additional effect of weld shape on toughness values. Such difference in weld shape has already been shown in the previous section. On the other hand, the controlling factors to determine toughness are the hardness and microstructure features which involve the austenite grain size, structure composition and second phases. Contrary to the relationship between hardness and toughness in the weld metal, high HAZ hardness does not always indicate low toughness value, in particular for welds A and C.

Table 7.1: Toughness results of different HAZs

Weld	Cooling rate $t_{8/5}$, s	Hardness, HV10 highest value	CVN impact energy, J Experimental values (average)
A1	20.4	312	14, 16, 11 (14)
A2	15.3	338	12, 14, 16 (14)
A3	11.4	368	18, 36, 38 (31)
B1	17.3	273	52, 64, 47 (54)
B2	15	272	20, 49, 28 (32)
B3	11.2	299	66, 76, 42 (61)
C1	18.0	294	24, 37, 34 (32)
C2	15.0	322	24, 18, 18 (20)
C3	11.2	341	72, 67, 74 (71)

In the case of Nb-containing HAZs, very low impact value occurs under a slow and medium cooling rate, indicating that the cleavage resistance in the HAZs is very poor for these two weld thermal cycles. However, under an increased cooling rate, the impact value exhibits a tendency to increase and meets the standards to a satisfactory level. In comparison with this, Ti-containing HAZs mostly have much higher energy values irrespectively of under a slow or fast cooling. Ti+V-containing steel has a similar toughness variation tendency to Nb-containing steel.

Further fractographic examinations are performed to reveal the fracture behaviour. This explains the toughness property based on the previous metallurgical analysis. The fractographic observations of the radial zone are shown in Fig. 7.23. Fig. 7.23 (a) and (b) illustrate that the fracture of Nb-containing CGHAZ under high heat input is brittle with dominant cleavage. The river lines within the large facet correspond well with the large bainitic ferrite packets. This indicates that the crack can propagate easily without crossing a high angle boundaries that can be understood by the EBSD results. Such an observation confirms that the microstructural coarseness results in a subsequent coarseness of the cleavage facet size. Indeed, it would be desirable to know exactly the initiation factor to get an impression of the brittle fracture mechanism. As suggested in [116, 117, 238], the presence of M – A constituent has a deleterious effect on both crack initiation and propagation. This point could be speculated to cause a reduction in fracture toughness. But the mechanisms for this is beyond the scope of the present work. High Charpy energy obtained in A3 specimens is characterised by small cleavage facet (Fig. 7.23 (c)). This can be explained by the comparatively small austenite grain and fine bainitic ferrite as a result of low heat input.

Fig. 7.23 (d) – (f) refers to the fracture surfaces from Ti-containing HAZs. The three images suggest that the radial zone has a quasi-cleavage fracture mode, corresponding well with the higher impact energy. A close examination of the surfaces was done in order to search for TiN particles and further determine their roles during fracture process. No identifiable TiN is observed to act as the origin of fracture or cause the secondary initiation while no surrounding facets emanate from TiN particles. Therefore, even if potential fracture triggering TiN particles are present in the HAZ, they do not cause any brittle fracture initiation or lower the impact toughness. In addition, reviewing the matrix microstructure, a small austenite grain and bainite packet combined with fine interlocking acicular ferrite have inter-related contribution to excellent toughness and avoid cleavage fracture. Hence, it is confirmed that the possible deleterious influence of TiN particles as crack initiator is deactivated in Ti-containing HAZ by the presence of significantly refined microstructure.

Comparing the fractographic examination of weld C (Fig. 7.23 (g) – (i)) with those in weld A, the fracture with low toughness is similar to that of Nb-containing HAZ, in which the river lines pattern is also visible. This reveals that, due to the potential austenite growth and the subsequent large-sized bainite products, which occurs to both welds, the fracture mode varies in a similar tendency. This also further confirms that toughness is strongly influenced by the grain size and microstructure composition. Note that the comparatively better toughness in weld C than weld A can be explained by the presence of some intragranular ferrite and effective pinning on grain growth. Moreover, the Charpy toughness is significantly improved under fast cooling due to the refined microstructure and the absence of upper bainite.

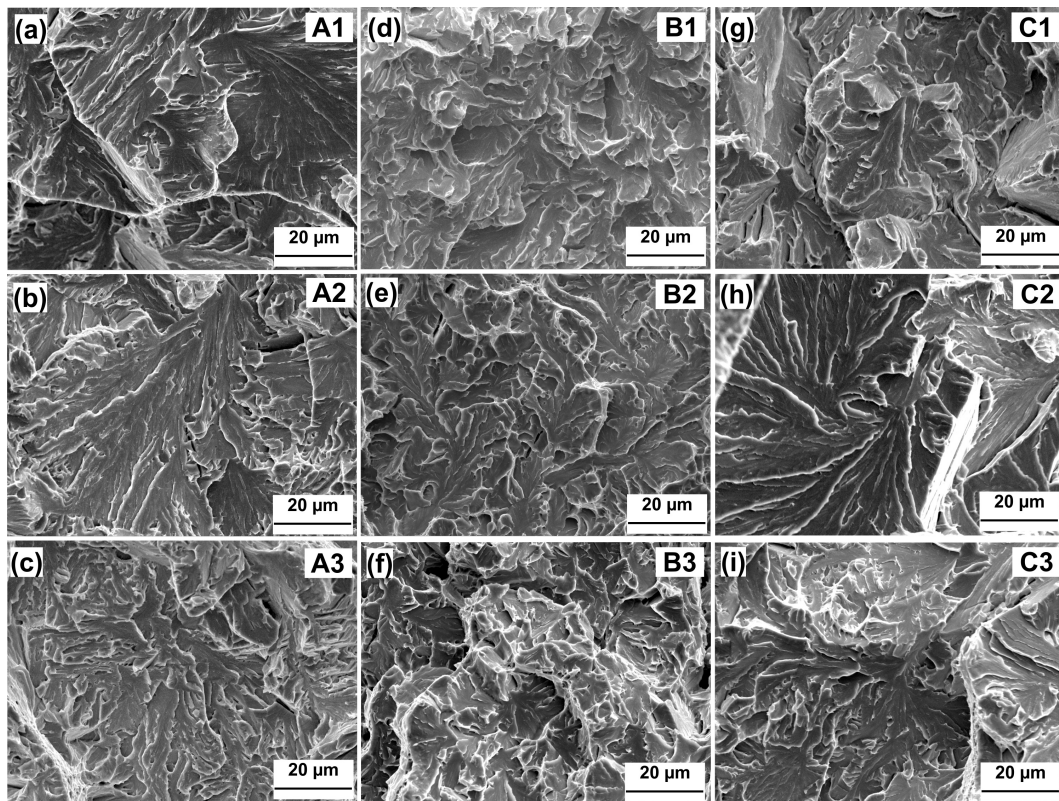


Fig. 7.23: Fractographic examination in weld A1 – A3 (a – c), B1 – B3 (d – f) and C1 – C3 (g – i)

7.6 Discussion

7.6.1 Effect of microalloy precipitates on austenite grain growth

As concluded from austenite grain growth behaviour, equilibrium thermodynamics can be used to make reasonable prediction of microalloy precipitates characteristics. Such characteristic information is closely correlated with the grain coarsening process. The ability of microalloyed steel to resist grain coarsening under elevated temperature follows the order: Ti, Ti+V and Nb-containing steel (or named as steel B, C and A). The difference between Ti and Ti+V-containing HAZ implies that the pinning efficiency from precipitates is comparatively weaker in Ti+V-containing steel than that in Ti-containing steel despite of Ti-rich nitrides present in both steels. This is because a comparison of pinning efficiency cannot be based only upon the type of microalloy precipitates, but also requires the information about chemistry, volume fraction, particle size or even distribution. Such precipitate characteristics in two steels differ from each other, causing the distinguished pinning effect. Although direct evidence by TEM is not performed in the present study, the Thermo-Calc calculation (Table 5.2), shows that the volume fraction in Ti+V-containing steel is assumed to be low. Accordingly, this limited volume can decrease faster during a thermal cycle than that of Ti-containing steel. This is because the pinning force depends dominantly on the particle size and their volume fraction. The similar result is confirmed by the model of Moon et al. [169] and Militzer et al. [141]. If there were not sufficient amount of effective precipitates to interrupt the migration of a grain boundary in Ti+V-containing steel, rapid austenite grain coarsening would take place. Additionally, if the intermixed Ti and V nitride or carbonitride is considered, its relatively enhanced solubility, as compared with that of pure TiN, will make the volume fraction drop progressively with higher peak temperature and thus result in a significant loss of retardation performance from precipitates. Such a behaviour is similar to the

observation in a Ti+V-containing steel, where (Ti,V)N precipitate existed and remarkable dissolution of precipitates occurred during thermal cycle [174, 239].

The above discussion demonstrates that the primary factors to control the grain growth in the HAZs are the microalloy precipitates characteristics and experienced peak temperature. Ti-containing steel with Ti/N ratio of 2 enjoys beneficial influence on grain-refining capability to a larger extent than Ti+V-containing steel. This difference probably results from different precipitates characteristics, especially the volume fraction in the two steels. Another explanation can be made by the dissolution behaviour of varied particles in these two steels, where pure TiN or complex Ti-V carbonitrides are present respectively. However, in comparison with Nb steel, two Ti containing steels exhibit higher grain coarsening temperature.

In fact, an additional attempt of the present simulation is to establish one possible modified equation to predict HAZ austenite grain growth behaviour in microalloyed welds. As suggested by literature, more initial information of the precipitates in base materials, such as particle size, composition, and distribution, combined with calculation work are significant for establishing one reliable prediction equation [240]. Unfortunately, the present study have limited time and budget to carry out extensive experiments (particularly TEM analysis). Therefore, the lack of original characteristics information on precipitates makes it difficult to achieve this ambitious aim. Despite this, the present simulation results are invaluable as an illustration of the austenite grain growth behaviour vs. weld thermal cycle and microalloy precipitates.

7.6.2 Effect of microalloy addition on phase transformation

The present work shows an excellent agreement with other studies that provide convincing evidence to affirm the influence of Nb on assisting in bainite formation [241]. Microalloyed Nb suppresses the transformation start temperature of bainite formation. The width of ferrite plates becomes finer as the cooling rate increases [189]. It is reported that Nb in solution can strongly delay $\gamma \rightarrow \alpha$ transformation. The reason is due to the grain-boundary segregation of Nb, which raises the energy barrier at boundaries and retards the transformation of austenite to grain boundary ferrite or pearlite by solute drag effect [22]. Additionally, Mo also has solute drag effect and can compensate the solute drag loss from fine Nb-rich precipitates, which could happen in the FGHAZ [20, 142]. Hence, the metallurgical result implies that such combined Nb+Mo addition ensures strong delay of $\gamma \rightarrow \alpha$ transformation to obtain bainitic ferrite microstructure in both CGHAZ and FGHAZ.

In Ti-containing HAZs, the limited austenite grain growth is attributed to the fine dispersed TiN precipitates. These fine particles of TiN do not dissolve upon reheating and they can assist in the nucleation of intragranular acicular ferrite. This observation is consistent with [60, 86, 101]. In order to reveal three-dimensional morphology and understand the role of inclusions, Cheng and Wu [242] reconstructed the three-dimensional morphology of IGF by isothermal transformation experiments with serial sectioning. It was concluded that small non-metallic inclusions aided the intragranular nucleation and the feature of IGF changed from equiaxed idiomorphs to laths or plate as undercooling increased. Also, in-situ observation of IGF formation provides direct evidence and kinetic information of IGF nucleation on the small TiO, TiN and MnS particles [86].

One explanation for TiN to act as effective nucleant was its relatively low lattice mismatch with ferrite in certain orientation (3.8%). As discussed previously, this low mismatch ratio is beneficial

to reduce the inclusion – ferrite interfacial energy for ferrite to nucleate. TiN particle having a size of less than 2 μm or even in nanometre-scale are suggested to encourage acicular ferrite to form through the lattice coherency [243, 244]. The effective size of particles on the nucleation potency was calculated by Morikage et al. [243]. It was proposed that the critical size for TiN to effectively facilitate nucleation is 38 nm at 650°C and 160 nm at 750°C. Another possible mechanism is that the formation of a Mn-depleted zone by the precipitation of MnS around TiN contributes to the increase in driving energy for nucleation. But in the present Ti-containing steel, the S content is less than 0.001 wt.-% and thus the contribution from MnS precipitation to the driving force is supposed to be negligible. Consequently, the good lattice coherency between TiN and ferrite becomes one significant factor to assist in nucleation process of IGF. Such a nucleation process will be further discussed in the dilatometer part.

Apart from the mentioned particle TiN, complex particles combined with V, such as VN, V(C, N), (MnS + V(C, N)), and (Ti, V)(C, N) [93, 155, 242, 245], are also suggested to be promising nucleus. VN shows more potential as nucleation site than TiN since the lattice mismatch with ferrite is much lower, only 1.3% [155]. Ishikawa and Capdevila et al. [155, 246] identified the presence of VN precipitates which can develop coherent, low energy interfaces with ferrite as a significant factor controlling the intragranular ferrite nucleation in terms of classical nucleation theory. In addition, the nucleation behaviour on complex (Ti,V)(C,N) precipitates with size of around 250 nm shows that the V-rich cap part forming on the Ti-rich core part increases the nucleation potency, due to the low energy VC – ferrite interface [245]. It was also pointed out by Miyamoto et al. [93] that intragranular ferrite morphology changed from idiomorphs to acicular ferrite as transformation temperature decreased. The presence of intragranular acicular ferrite in Ti+V-containing steels can be correlated with the fast cooling ($t_{8/5}$ 15 s) and steel hardenability. As discussed previously, in the Ti+V-containing CGHAZ with T_p of 1300°C, the precipitate volume fraction is not sufficient for effective pinning, causing austenite coarsening compared with the case in Ti-containing steel. According to Babu [65], one significant factor to form acicular ferrite is the sufficient amount of effective inclusions that can act as nucleus. Therefore, a limited fraction of intragranular ferrite in the CGHAZ can be closely linked to a small quantity of nuclei in the Ti+V-containing steel.

Interestingly, it is observed that microstructure changes from IGF into bainite between the CGHAZ and FGHAZ in the Ti+V-containing weld. This change can be regarded as the competition result between the nucleation processes of IGF and bainite. This competition is known to be influenced by the austenite grain size, potential particles, chemical composition and cooling rate. Generally, small austenite grain is favourable for bainite to form along the grain boundary due to high grain boundaries area per unit volume [65]. Meanwhile, it should be noted that high Mo is expected to effectively promote the bainite formation in the Ti+V-containing steel. Therefore, the replacement of IGF microstructure by bainite in FGHAZ is determined by the combined effect from austenite grain size, potential particles and comparatively high hardenability in the Ti+V-containing steel. Due to a sufficient amount of fine precipitates and the low hardenability of the Ti-containing steel, the IGF microstructure can exist in both CGHAZ and FGHAZ.

Regarding HAZ hardness variations with heat input, in the Nb and Ti+V-containing weld, the progressively increased hardness with increasing cooling rate can be partially explained by both grain refinement strengthening and the interphase strengthening. Furthermore, a structure mixture containing

a large fraction of bainite and some martensite makes additional contribution to the hardness increase. In the Ti-containing welds, a large fraction of acicular ferrite is formed in the HAZs even under fast cooling rate and less strong precipitate strengthening occurs. As a consequence of these factors, the final hardness maintains a constant value in the Ti-containing HAZ.

7.6.3 Effect of crystallographic orientation on fracture toughness

Low misorientation boundaries may be not effective in cleavage crack deviation. The observation within large bainite packet proves that the low-angle misorientation between bainitic ferrite could provide less barrier for crack propagation, leading to a low toughness. Additionally, the presence of M – A constituent or retained austenite is another factor to influence toughness. The area with low image quality, located between ferrite laths, is confirmed to contain partial retained austenite. Literature suggests that it could be M – A constituents that contain many defects such as dislocations, and thus low quality or even less well defined regions are observed [233]. It is accepted that the existence of M – A constituent is due to the incomplete transformation phenomenon and a high concentration of M – A constituent can be obtained, in particular under high heat input [247]. The EDX analysis of alloy concentration in the retained austenite or the M – A constituent shows that Ni and C tend to increase compared with the surrounding matrix. This observation agrees well with the reported work from Okada et al. [248]. They also pointed out that the hardness of M – A constituent and its C content can bear a virtually linear relationship. Although the presence of M – A constituent is strongly correlated with the bainite transformation, its influence on toughness cannot be precisely identified from the metallurgical aspects or this is difficult to be observed in fractographic studies. The influence of M – A constituent on toughness are discussed in next section.

Most acicular ferrite grains are highly misoriented and disordered, as shown in Fig. 7.8. Such characteristics result from its typical nucleation feature and are believed to make the acicular ferrite more resistant to cleavage fracture than bainite. More precisely, the chaotic arrangement of fine ferrite plates and varying crystal structure provides effective obstacles for crack to propagate. They can force the crack to deviate with an increased propagation energy, which gives rise to a high toughness value [67]. Additionally, the fine crystallographic packet size of acicular ferrite corresponds well with the small cleavage crack path. Therefore, the presence of intragranular acicular ferrite is favoured and this point can be explained by its crystallographic characteristics. Its positive effect on improving toughness is confirmed as well in the present study.

7.6.4 Effect of HAZ microstructure on toughness

Following the concept, that the HAZ toughness is directly related to the microstructure evolution, the toughness properties from different microalloyed HAZs can be interpreted. In the case of the Nb-containing steel A, HAZ toughness can be impaired by excessive grain coarsening, large bainitic ferrite packets, or the presence of M – A phase. The relatively large-sized austenite in the HAZ is attributed to the limited pinning effect from Nb-rich carbonitrides and AlN that have comparatively low dissolution temperatures, as discussed in section 7.6.1. As a consequence of large-sized austenite, large-sized bainite packet or bainitic ferrite laths are subsequently formed during austenite decomposition, particularly when welding with high or medium heat input. More precisely, the resultant microstructure consists of a mixture of bainite and micro-constituents in the inter-bainitic regions which contain a combination of austenite, martensite and carbides.

The upper bainite structure is characterised by using EBSD to understand the relevant "grain size" and bainitic packet size which significantly influences the crack propagation. Combining the EBSD analysis with the toughness results, some remarks can be given. The high volume fraction of upper bainite, accompanied with large-sized matrix grain, holds responsible for the loss in toughness. For this reason, the heat input should be controlled to a low level for the Nb-containing welds in order to achieve a high HAZ toughness value. Under a low heat input, limited time is available for austenite grain to grow. Meanwhile, upper bainite is mostly substituted by lower bainite. As a result, a mixture of refined lower bainite and martensite with less retained austenite is formed. Such refined microstructure can further contribute to excellent toughness. The fractographic observations also support this point.

HAZ toughness changes as a function of heat input in Nb containing welds and the combination of Nb/Ti is also suggested to avoid the rapid coarsened austenite [10, 188, 249]. Also, the detrimental effect of higher heat input on the toughness of weld containing niobium has been well documented and explained [188, 249, 250]. The detrimental Nb effect is ascribed to promote the formation of upper bainite and untempered martensite, or granular bainite and M – A constituent. Therefore, it is known that the poor toughness arises primarily from the deleterious effect of the Nb addition, sometimes in combination with Mo or B.

Regarding the cleavage fracture initiator, it is stated that martensite fractures during Charpy impact test due to the inherently brittle nature of high-carbon M – A constituent, or they facilitate the nucleation of fractures on the surface of the interface between ferrite and M – A constituent, and thus the absorbed energy is reduced [116, 117]. Taillard et al. [238] ascribed the reduced CGHAZ toughness to the high volume of retained austenite. However, the combination of austenite and martensite may be beneficial in some steels [115, 118]. Therefore, it can be assumed that the presence of M – A constituent could influence the toughness when considering their co-existence with upper bainite but the exact influence of M – A constituent on fracture process is difficult to determine due to a lack of sufficient information.

Based on the discussion on the Nb-containing HAZ, it can be concluded that several factors, such as large-sized grain, upper bainite or hard second phase, interact to influence the toughness. They can induce the brittle fracture behaviour and impair toughness, particularly under high heat input. But when welding with a low heat input, such a negative effect can diminish. Therefore, a reduced heat input is suggested for weld A. Note that high hardness in the HAZ is obtained under fast cooling, which is often indicative of areas susceptible to hydrogen assisted cracking. But the major concern for welding steels-containing with Nb is not the resistance to cracking but rather the HAZ properties, namely toughness and strength. This was pointed in [10, 188] and is also supported by the present study.

Concerning the austenite growth behaviour in the present Ti-containing weld B, it is found that it is possible to pin the austenite grain boundaries movement and to prevent excessive coarsening by utilising Ti-rich particles as well as by finely-balanced alloy design. Subsequently during further transformation, favourable fine IGF ferrite is formed within refined austenite. In order to confirm that IGF nucleation is related to the presence of Ti-rich particle, the next chapter is to carry out dilatometry experiments to solve this. The EBSD results have confirmed that the high-angle boundaries between IGF plates present high energy barriers for crack propagation and thus contribute to high HAZ toughness. In spite of beneficial effect from Ti-rich particles on IGF formation, another feature about coarse particle of

TiN must be additionally considered. The presence of coarse particles could initiate deterioration on toughness only under certain special conditions. This depends on several other factors, such as matrix structure, grain size, and other second phases [15, 16, 187, 244].

Some researchers [244] claimed a beneficial effect of Ti addition on the toughness. This positive role depends strongly on the overall effects from matrix microstructure, grain size and the TiN precipitate characteristics. It often occurs in steels during solidification that Ti is bonded with nitrogen as coarse particles of TiN, which has been observed in fractographic examinations acting as fracture initiation sites in the case of bainitic structure with large packet size. However, TiN particles are found to be irrelevant for fracture process, not as crack initiator, particularly in the case of fine-grained acicular ferrite as matrix structure [16].

Support of this observation can be found in [251], which points out that the susceptibility to cleavage fracture did not depend on the size of the fracture initiating particle but on the local ferrite grain size. Some suggested that when a fine balance of Ti and N element, where Ti/N weight ratio is close to 2.2, dispersed fine TiN particle have beneficial effect on toughness too [252]. This was proved in the present observation of Ti-containing steel with Ti/N ratio of 2. Therefore, based on the results of Ti-containing welds, indications are that the Ti addition with an acceptable balance with N assists in improved HAZ toughness by the formation of desirable IGF, fine grain size and fine dispersed particles.

To conclude the HAZ toughness behaviour in the Ti+V-containing welds, it is important to highlight that weld C experiences the similar toughness variation tendency as heat input changes compared with that of weld A. The same reasons can be interpreted here by the coarser grain structure than that in the Ti-containing HAZs, combined with upper bainite present in the HAZs when welding under high or medium heat input. It should be noted that the presence of IGF structure in weld C has also positive contribution to toughness. This desirable structure is absent under medium cooling but a large fraction of upper bainite is formed, resulting in decreased toughness. When welding with low heat input, likewise in the other two welds, a satisfactory toughness can be approached due to the refined matrix microstructure of lower bainite and martensite.

7.7 Summary

The HAZ toughness of the three microalloyed welds was compared based upon a comprehensive microstructure characterisation and Charpy impact test analysis. The metallurgical analysis has been made on the basis of light microscopy and high resolution SEM, EBSD testing combined with EDX and TEM.

To assess the HAZ austenite grain growth, the physical simulation was performed with induction equipment. In Nb-containing steel, austenite grain growth is restricted by the presence of Nb-rich carbonitrides, but such a retardation can work effectively only in the FGHAZs with a lower T_p , due to its relatively low dissolution temperature. However, under high heat input, the coarse austenite grain in the CGHAZ transforms into subsequent large-sized products, including upper bainite and M – A constituent. These microstructure features finally result in low impact toughness. Fortunately, low toughness can be avoided by low heat input. The implication of these results is that solute Nb combined with Mo suppresses the ferrite transformation and assists in formation of a mixed refined lower bainite and martensite under fast cooling.

In comparison, the austenite grain growth is significantly retarded by the dispersed fine and stable Ti-rich nitrides even at elevated peak temperature. Meanwhile, the decomposition of austenite into IGF is also attributed to the available fine Ti-rich particles which are directly identified by TEM analysis. As a result of small austenite and refined favourable IGF structure, regardless of a fast or slow cooling, HAZ toughness is greatly improved.

SEM observation reveals that the Charpy specimens fracture is characterised by small facet. This feature can be further interpreted by the crystallographic data of EBSD results, which suggest that intragranular acicular ferrite plates have really high angle boundaries between each others, leaving cracks need more energy to further propagate. However, as for upper bainite in Nb-containing HAZ, large bainitic packet size and low angle misorientation lead to easier cleavage path for crack propagation. It is presumed that the M – A constituent also play a detrimental effect on toughness but the role is not completely understood.

The influence of metallurgical features on the HAZ toughness is further highlighted by the observation in the Ti+V-containing welds. The results confirm that extensive austenite grain growth is not beneficial to toughness. However, the presence of IGF structure can compensate the great reduce of toughness, as suggested by the case under high heat input. Whereas medium heat input is applied, the formation of upper bainite could additionally worsen the toughness. Note that one common point observed in the three welds is that HAZ toughness under low heat input tends to be greatly improved due to the refined matrix microstructure of lower bainite and martensite. Therefore, by taking steps to limit heat input when welding the three microalloyed steels, it can guarantee an improved Charpy HAZ toughness.

In summary, the results presented in this chapter have invaluable implications on HAZ properties for joining the three microalloyed steels. When the heat input is appropriately controlled, the interrelationship between finely balanced elements and weld thermal cycle can contribute to desirable HAZ microstructure composition and excellent toughness.

8 Microstructure evolution and mechanical properties of softened HAZ

In general, the structural integrity of a welded structure is critical and desirable. Tensile test, as one integrity assessment method, is often applied to evaluate the load-deformation behaviour of welded joints containing highly heterogeneous microstructure features. Particularly for QT steels, severe HAZ softening can happen after welding, resulting in a fracture located in the softened HAZ rather than in base metal. In the present study, tensile tests were performed to evaluate the influence of softening on the tensile properties of the three welds under different welding parameters. After identifying the fracture location of tensile specimens, the relationship between softening characteristics and tensile properties is discussed. Further physical simulation is presented for understanding the softening mechanisms by an in-depth study of dilatometry results.

8.1 Tensile properties

Representative load-displacement curves for the three welded joints under different heat inputs are shown in Fig. 8.1. It is evident that a reduced displacement occurs to weld B1 and B2 (Fig. 8.1 (b)). However, ultimate tensile strength of the three welds are comparable to that of the base materials.

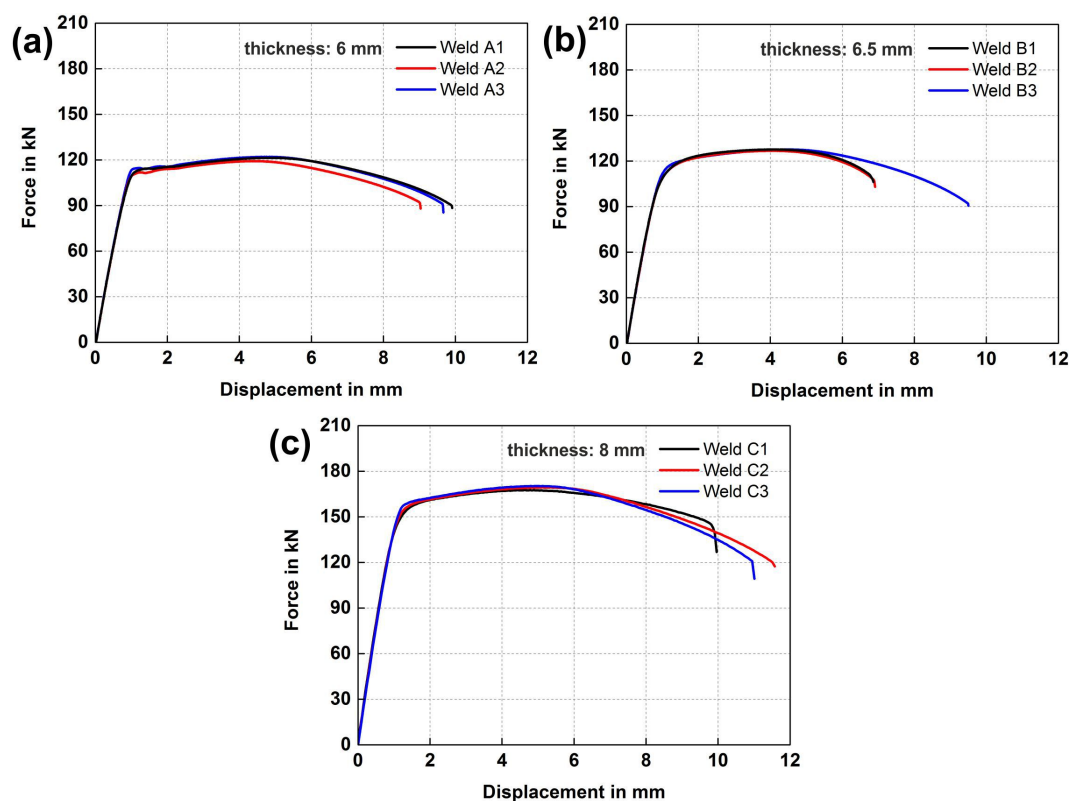


Fig. 8.1: Load-displacement curves of the welded joints: weld A (a), weld B (b) and weld C (c) [193]

The tensile test data and fracture positions are summarised in Table 8.1. All fractured tensile specimens were further observed with regard to their fracture location. Most specimens, except weld B1 and B2, fracture in the base material and no great change in elongation, compared with base material, is observed. For weld B1 and B2, the fracture occurs within HAZ and is characterised by a reduced elongation.

Table 8.1: Summary of the tensile test data and fracture position [193]

Weld	R_m , MPa	A, %	Fracture position
A1	818 ± 5	15.5 ± 0.5	BM
A2	802 ± 5	14.3 ± 0.3	BM
A3	812 ± 4	17.8 ± 1.2	BM
B1	787 ± 7	12.3 ± 0.4	HAZ
B2	788 ± 3	13.9 ± 1.0	HAZ
B3	800 ± 14	17.9 ± 2.4	BM
C1	819 ± 1	16.1 ± 1.2	BM,WM
C2	830 ± 2	19.3 ± 0.9	BM
C3	833 ± 3	18.1 ± 1.0	BM

A representative image of HAZ fracture is presented in Fig. 8.2 (a). The fracture position is not in the CGHAZ or close to fusion line. Comparing Fig. 8.2 (a) with hardness mapping (Fig. 6.1), such a position is confirmed to be located exactly within the softened HAZ which is more than 3 mm off the fusion line. Thus it is evident that the softened HAZ is the preferred fracture site rather than base metal. Moreover, the reduced displacement, in Fig. 8.1 (b), is related to the profound softening as a consequence of high and medium heat input. Fig. 8.2 (a) also depicts the local necking effect in the other softened HAZ of the welds.

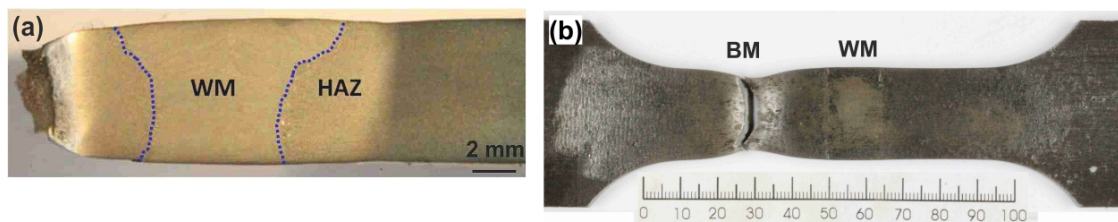


Fig. 8.2: Tensile specimen of weld B2 failed in the HAZ (a) and weld A1 failed in base metal (b) [193]

Fig. 8.2 (b) shows one representative tensile specimen of weld A1 which fractures in base metal. In fact, most welds A and C fracture in base metal rather than in the HAZ. Meanwhile, this result indicates that although there is quite limited HAZ softening in welds A and C (Fig. 6.1), the fracture during tensile test can occur in the base metal. One exception is identified for weld C1 but the weld does not show any loss of tensile properties compared with the other welds. Compared with welds A and C, welds B have a lower extent of hardening but a higher extent of softening in the HAZ. Even though limited hardening exists in weld B, no significant tensile strength reduction of welded joints is observed under high or medium heat input. This is due to the expected constraint effect from surrounding high yield strength regions on the softened HAZ. Overall, the softening effect in steel A and C does not greatly change the tensile properties under different welding conditions, whereas a maximum heat input should be recommended to steel B for avoiding severe HAZ softening.

8.2 HAZ softening in the welded joints

The softening characteristics, such as softened width, minimum hardness, and microstructure, were analysed in order to establish a relationship between HAZ softening and welding parameters for the investigated welds. Fig. 8.3 shows the variations of the softened zone width and softening ratio as a function of heat input. The softened width increases continuously with an increase in heat input for the three welds. Welds B have more profound softening than the other two welds. Also, the widest softened zone can reach to approximately 1.8 mm under high heat input, which is almost two times

larger than the other welds. Moreover, the corresponding maximum relative thickness ratio is around 0.28, whereas the maximum value for the other two welds is only approximately 0.13. In the case of the relative thickness ratio for steel B above 0.18, the fracture during tensile test occurs in the softened zone. This indicates that the critical relative thickness for steel B is a little lower compared with the literature [18, 194]. Referring to Fig. 8.3(b), welds B exhibit the largest extent of hardness decrease in the softened zone, followed by welds C. Welds A exhibit the lowest extent of softening.

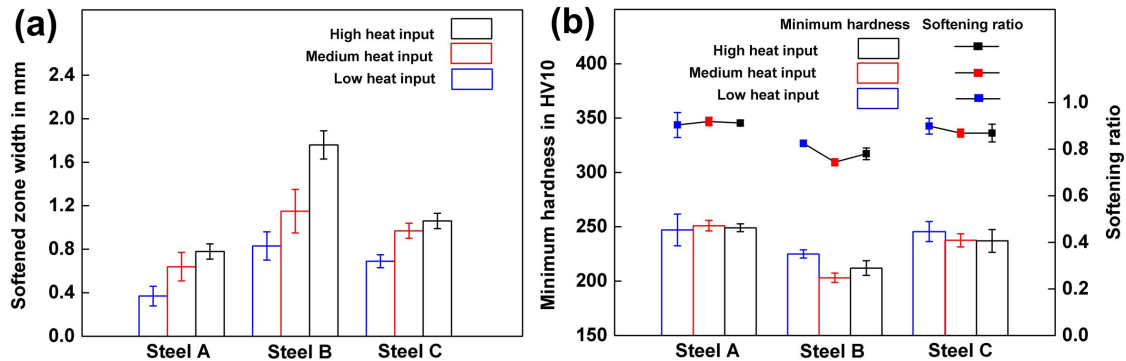


Fig. 8.3: Softened zone width (a), minimum hardness and softening ratio (b) as a function of heat input [193]

In the case of weld B, the minimum hardness is reduced to around 203 HV10. This is about 70 HV10 less than that of base material and the corresponding softening ratio is around 0.74. For welds C, the hardness in the softened zone is approximately 237 HV10 with a softening ratio of 0.87. This comparison indicates that multi-microalloyed steels has stronger resistance to softening than single-microalloyed welds B. However, in welds A, the hardness drop of 20 HV10 is observed and the corresponding softening ratio is over 0.9.

The width of softened zone changes with the heat input. Ti-containing steel suffers pronounced softening, particularly under high heat input and this makes the eventual fracture of tensile test occur in the softened HAZ. However, the tensile fracture location shifts from the softened HAZ to the base metal when the softened width decreases as a result of low heat input. Hence, several important factors (e.g. steel type, alloying composition, and welding parameters) should be considered in order to control or minimise the softening extent. Further analysis is made on the microstructural features of different steels after welding. The observed microstructure is located close to the corresponding hardness points (as indicated by dashed circles in Fig. 8.4). The hardness drop in softened zone is displayed as well. The corresponding optical micrographs are shown in Fig. 8.5.

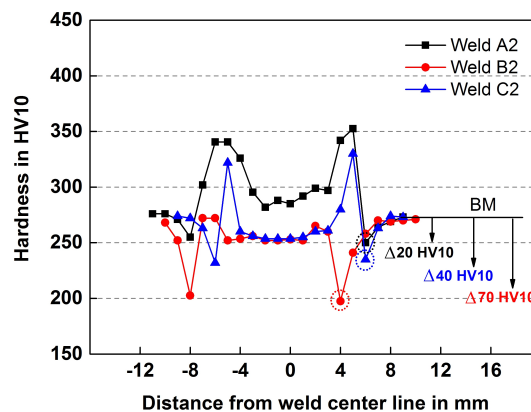


Fig. 8.4: Hardness decrease in the softened zone of the three welds [193]

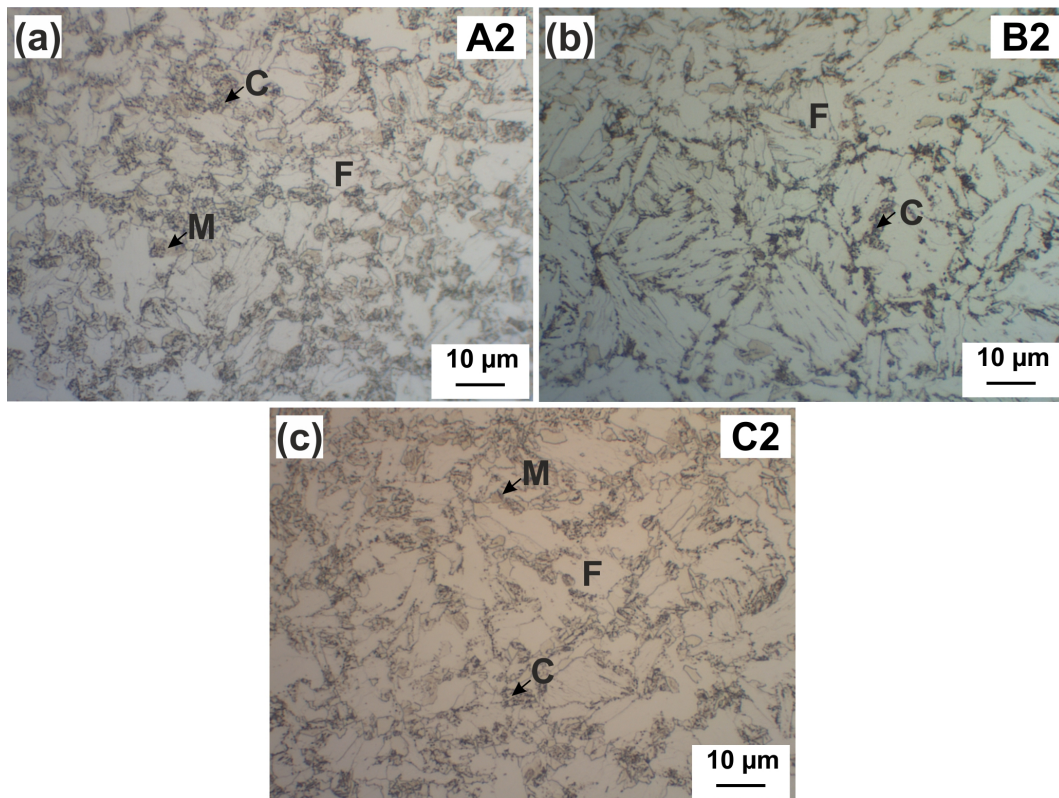


Fig. 8.5: Optical micrographs of softened HAZs in weld A2 (a), B2 (b) and C2 (c). C, carbides [193]

An overview of microstructure composition indicates that partial phase transformation happens in the subcritical HAZs of the three welds, but the transformation products differ markedly among them. The white area is ferrite matrix. The fraction of ferrite is the largest in Ti-containing weld B, followed by Ti+V-containing welds. Nb-containing weld has a limited fraction of ferrite. Additionally, the ferrite grain size in Ti-containing welds appears much larger than that in the other welds. This can be attributed to the comparatively large prior austenite grain of base metal. Such large-sized ferrite as predominant structure combined with apparent carbide clusters along the grain boundary results in much lower hardness observed in the Ti-containing softened zone. However, martensite (grey area) and uniformly distributed carbide-rich phases (black area) is observed in Fig. 8.5 (a). Due to such a structural characteristic, Nb-containing HAZ shows strong resistance to softening and no significant decrease in hardness. In Fig. 8.5 (c), Ti+V steel exhibits structural characteristic similar to the Nb-containing steel. It consists of ferrite, martensite, carbides and a small fraction of retained austenite.

Representative SEM micrographs (Fig. 8.6) shows the details of ferrite matrix, martensite and carbides-rich phase in the softened HAZ. The partially-tempered martensite blocks have broken lath with the presence of refined needle-shaped particles (Fig. 8.6 (b) and (f)). Occasional presence of retained austenite is observed near the blocky martensite island. In the weld A2, fine spherical particles within the ferrite are labeled as bainite structure. However, compared with the weld B, most carbides appear coarser and are aligned along the grain boundaries. Some large needle-shaped carbides are indicated by arrows in Fig. 8.6. As often reported, this precipitated carbide could probably be cementite [132, 133]. Also, it has been proposed that the extent of softening follows the increase tendency of cementite size during tempering process. The carbides precipitated in the weld A and C are more evenly distributed than those in the weld B. This can explain the enhanced softening resistance in the welds A and C.

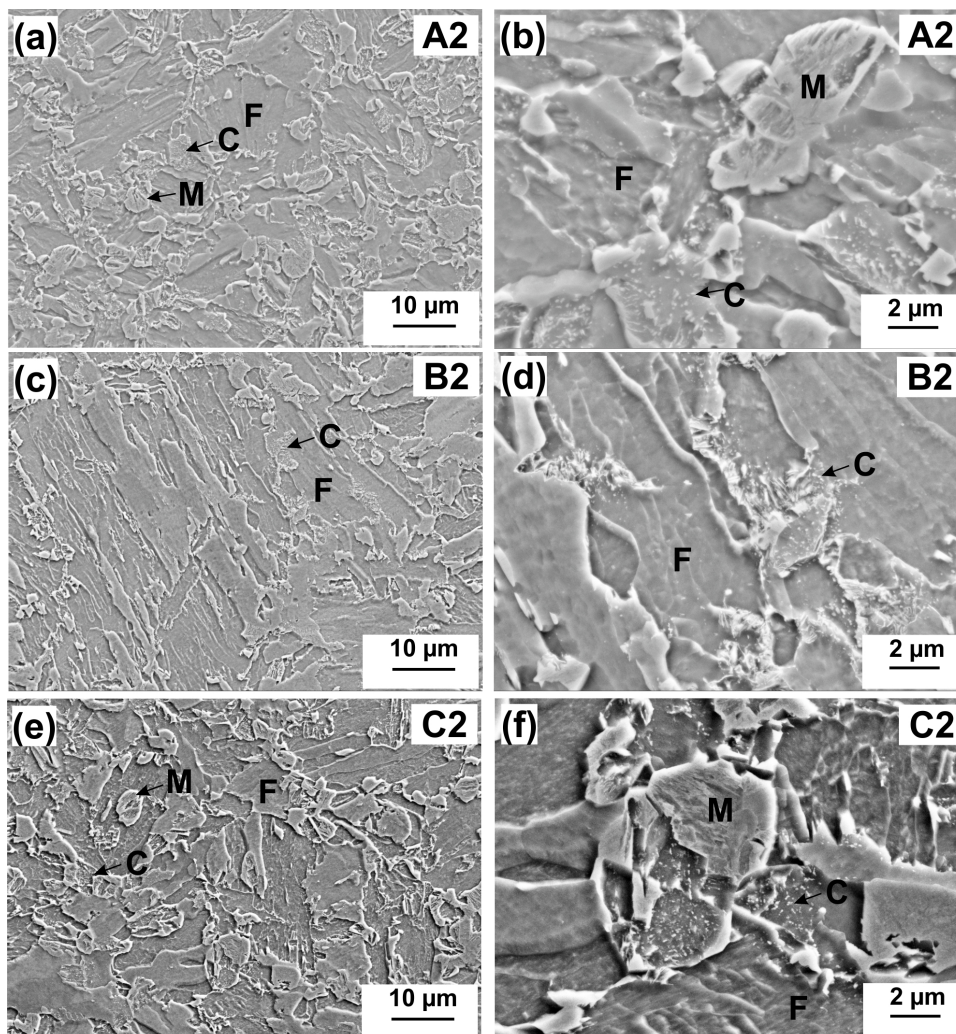


Fig. 8.6: SEM images of softened HAZs in weld A2 (a, b), weld B2 (c, d) and weld C2 (e, f) [193]

Combing the observation from Fig. 8.6 and hardness results from Fig. 8.4, it can be concluded that the microstructural feature is closely related to the hardness and the corresponding softening extent. Concerning phase transformation in the softened zone, several aspects should be considered: peak temperature, cooling rate, steel's alloy chemistry, and prior austenite grain size. The peak temperature in the softened HAZ determines whether partial austenitisation and further phase transformation occurs or only tempering reaction happens. The observed microstructure (Fig. 8.6) is from the intercritical zone but the tempering reaction in the subcritical zone can also contribute to the hardness decrease. There is no doubt that this point needs further research. Due to the difficulty to separate tempering microstructure from base metal only by electron microscopy, further dilatometry experiments are carried out. The aim is to reveal the softening mechanism in the three microalloyed steels.

8.3 Dilatometry

Dilatometry is applied to observe the phase transformation and precipitation behaviour during different thermal cycles. The investigated thermal cycles can represent the subcritical and intercritical HAZ. In order to clarify the softening mechanism in the HAZ, the evolution of austenite decomposition products and hardness is of particular interest.

8.3.1 Hardness of softened HAZs

The hardness of the simulated HAZs specimens is found to vary as a function of both the position in HAZ (as defined by the peak temperature) and the steel chemistry condition (as defined by the microalloy design type), as shown in Fig. 8.7.

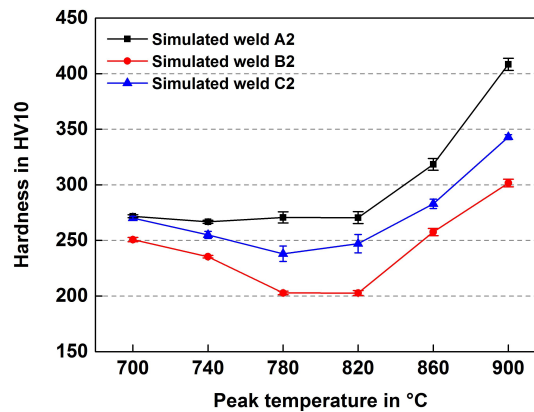


Fig. 8.7: Hardness of simulated HAZs

A comparison of hardness variations in the three steels (Fig. 8.7) suggests that Ti-containing HAZ softens the most, followed by Ti+V-containing HAZ and finally Nb-containing HAZ. More precisely, the simulated HAZs of weld B exhibit the most pronounced softening, in particular after a thermal cycle with T_p of 780°C and 820°C. In both cases, the hardness drops abruptly to around 200 HV10, indicating a loss of 70 HV10 relative to the base metal. However, after even the same thermal cycles, simulated HAZs of weld C experience moderate softening, whereas simulated HAZs of weld A show almost hardly softening. The hardness results of simulated HAZs (Fig. 8.7) agree well with those of the softened HAZs in welded joints (Fig. 8.4). This confirms that the physical simulation by a dilatometer can be one good alternative to represent the welded HAZs. It is also one valuable tool to analyse the microstructural variation in different HAZ regions. The hardness data can be further interpreted in terms of the microstructural changes resulted from different thermal cycles.

8.3.2 Phase transformation analysis

Fig. 8.8 represents an overview of dilatation curves for simulated HAZs with T_p of 900°C, 820°C and 740°C. In general, linear expansion is observed during heating until austenitisation starts. Nearly constant linear change is shown in case of no phase transformation during thermal cycle, as shown in Fig. 8.8 (c) with T_p lower than A_{c1} . However, for Fig. 8.8 (a) and (b) the transition temperature from ferromagnetic to paramagnetic state is firstly found around 760°C, which is also called Curie temperature. Since Curie temperature is much closer to the onset of austenite formation, it influences the precise definition of the A_{c1} temperature.

During cooling, fresh formed austenite decomposes to different ferrite products or partially retain to ambient temperature. Upon completion of phase transformation, linear expansion resumes. From Fig. 8.8 (a) and (b), the S type dilatation curves suggest that most austenite transforms to different ferrite at different start temperatures. Additionally, the heating and cooling curves do not superimpose. However, the cooling curve lies below the heating curve, indicating that a negative displacement is left after thermal cycle. The specimen has contracted as a result of microstructural changes during thermal cycle. This may also be related to a small fraction of austenite retained at room temperature.

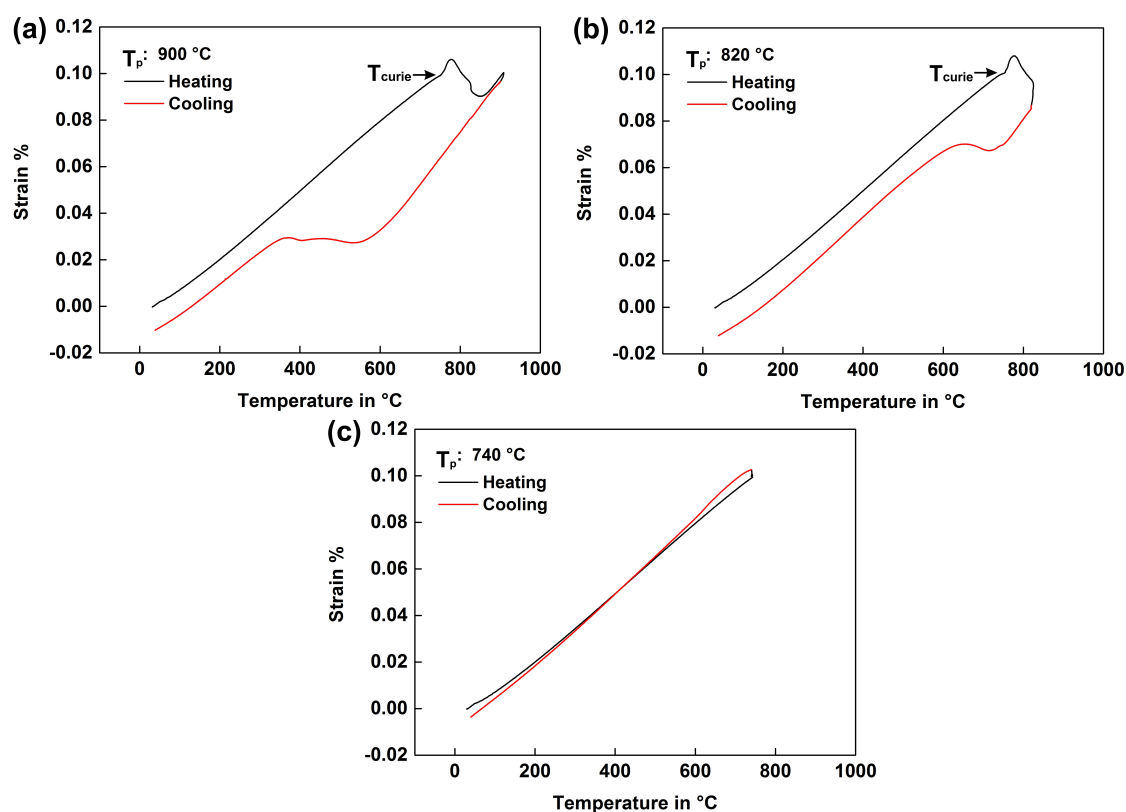


Fig. 8.8: Representative dilatation curves from simulated HAZs with T_p of (a) 900°C , (b) 820°C and (c) 740°C

The measured A_{c1} and A_{c3} temperatures of the three steels are summarised in Table 8.2. The values are somewhat higher than those calculated by Thermo-Calc software (Table 5.1), but this difference is reasonable to occur in para-equilibrium condition since the phase transformation start temperature increases with increasing heating rate of thermal cycle. More precisely, increased heating rates offer less time for alloying elements to diffuse, which leads to a concomitant delay in the start of phase transformation [183].

Table 8.2: Measured A_{c1} and A_{c3} temperatures

Steel	$A_{c1}, ^\circ\text{C}$	$A_{c3}, ^\circ\text{C}$
A	780	876
B	771	871
C	782	878

Fig. 8.9 depicts the cooling parts of dilatation curves with different peak temperatures in the three steels. If the curve shows consistent linear contraction (T_p of 700°C and 740°C), it indicates that there is no phase transformation from austenite to ferrite during thermal cycle. As a result, only tempering reaction occurs in the simulated HAZs. Thus, the specimens with T_p of 700°C and 740°C are representative of the subcritical HAZ, which can also be understood by the T_p lower than A_{c1} temperature. Other curves are observed to contain non-linear changes during cooling, indicating the occurrence of phase transformation. Based on the curve characteristics combined with measured A_{c1} and A_{c3} temperature, it can be concluded that thermal cycles with T_p of 780°C , 820°C and 860°C are representative of the intercritical HAZ and those with T_p of 900°C are for the FGHAZ. When full or partial austenitisation occurs, the transformation start temperatures are defined as a temperature, at which the measured dilatation curve deviates from the austenite thermal contraction line.

The dilatometric data during cooling can further be post-processed to calculate the volume fraction of austenite decomposed as a function of temperature. This analysis should be based on a boundary condition that the austenite has to fully transform into ferrite products during cooling. However, it should be noted that there is still some retained austenite left in the simulated HAZ, with an amount of 1.9% – 4.8%. This amount is detected in all specimens, which experience full or partial austenitisation, by phase determination method with X-ray diffraction technique. Therefore, the austenite formed during heating is presumed to fully decompose into ferrite during cooling. The lever rule method used for this analysis has been introduced in the experimental parts (section 4.6.2).

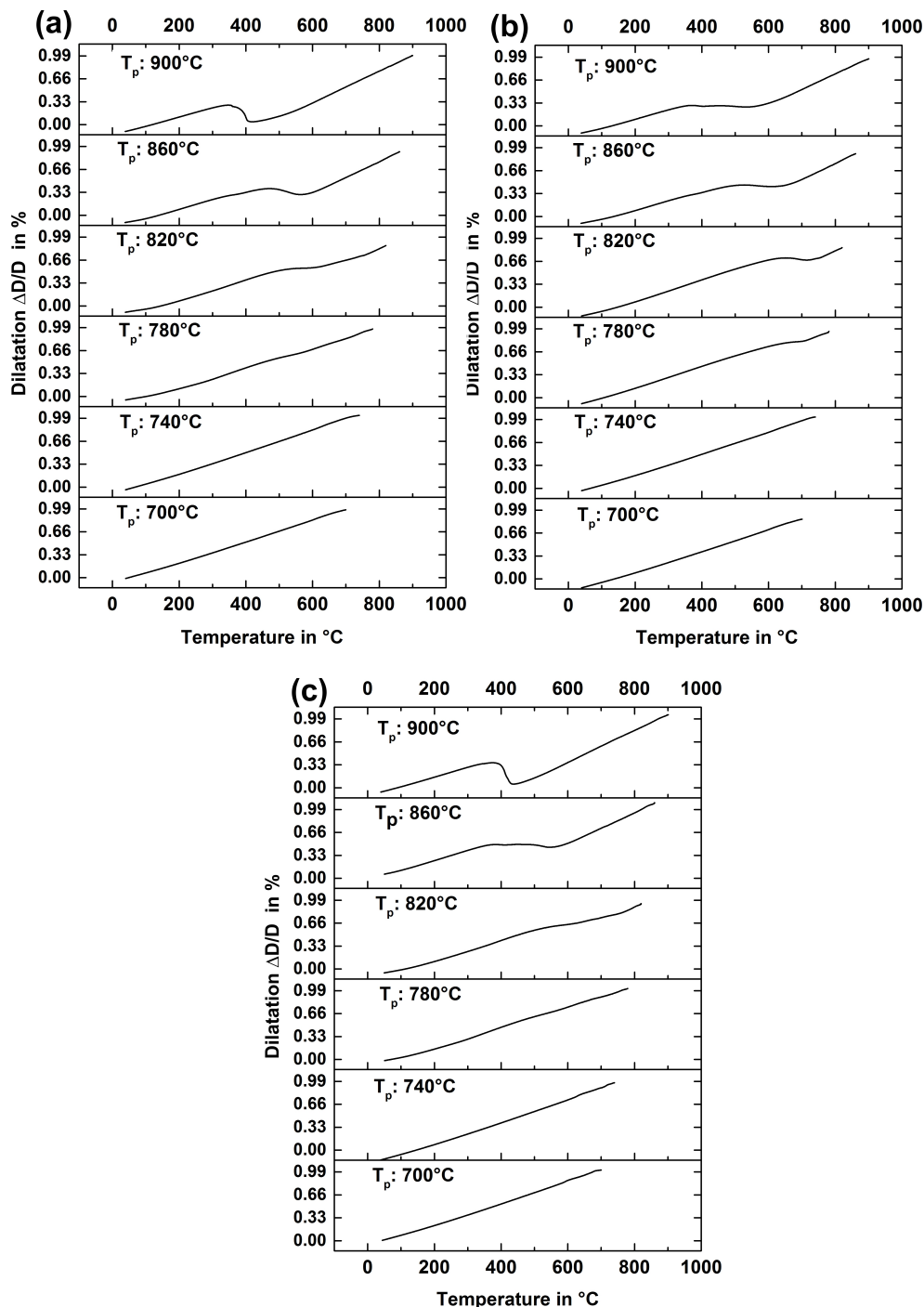


Fig. 8.9: Cooling parts of dilatation curves from steel A (a), B (b) and C (c)

Plots of the fraction of austenite decomposed during cooling are presented in Fig. 8.10. The T_p lower than A_{c1} , corresponding to the tempered region of HAZ, are not shown since there is no austenitisation in this case. Likewise, the curve with T_p of 780°C is absent because not enough detectable fresh austenite is formed to allow for a reliable quantitative analysis. Comparing the Fig. 8.10 (a), (b) and (c), it is observed that the phase transformation kinetics during cooling differs substantially between Ti-containing steel B and the other two steels.

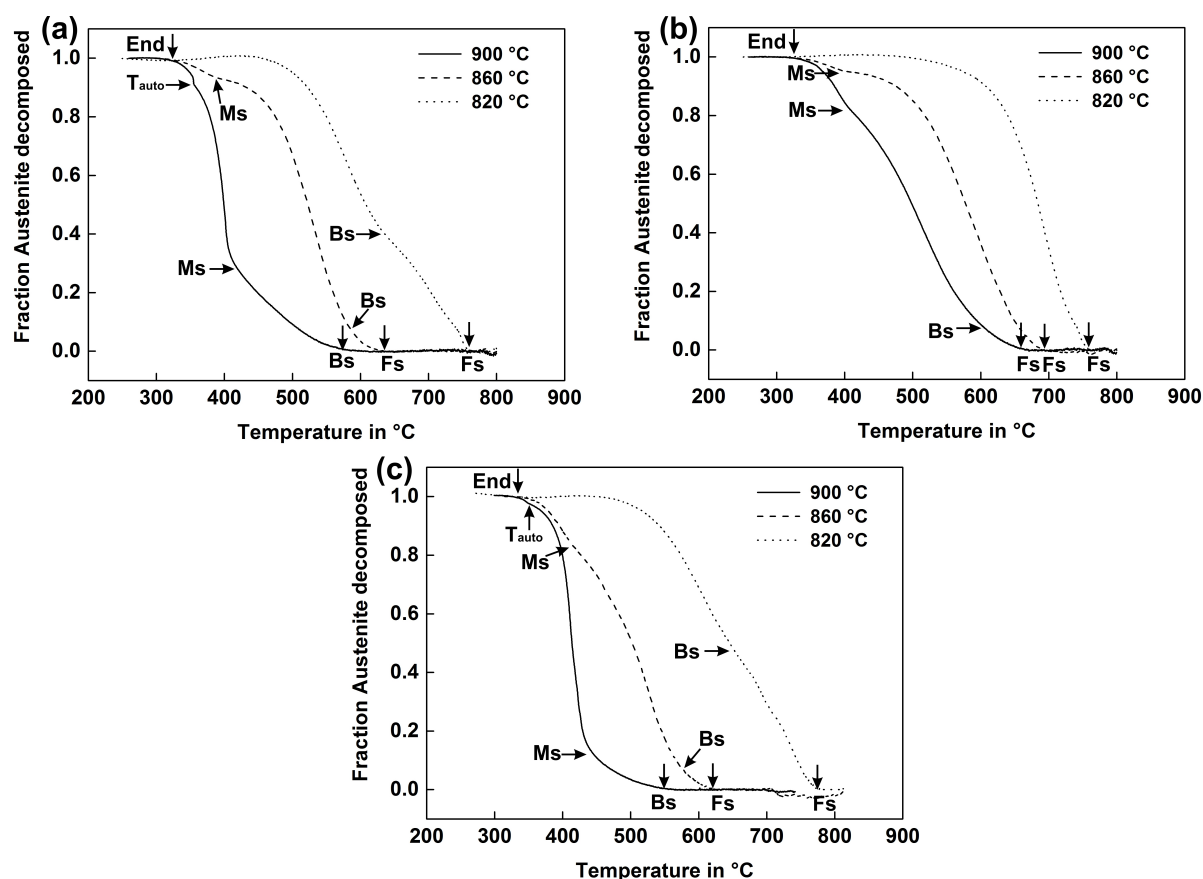


Fig. 8.10: The fraction of austenite decomposed as a function of temperature decrease. The curves correspond to varied peak temperatures for weld A (a), weld B (b) and weld C (c). F_s , ferrite start temperature; B_s , bainite start temperature; M_s , martensite start temperature; T_{auto} , martensite automatically tempered temperature

Fig. 8.10 (a) illustrates the austenite decomposition in the simulated Nb-containing HAZs. The thermal cycle with T_p of 900°C is representative of the FGHAZ. The corresponding curve indicates that the onset of austenite decomposition begins around 573°C. When the temperature decreases until 412°C, only a small fraction of austenite transforms into bainite and then the martensite transformation prevails. Also, a deflection is visible around 357°C, which suggests newly-formed martensite automatically tempers. Accordingly, in the simulated FGHAZ, a distinct bainitic reaction occurs, followed by a dominant martensitic transformation. The specimen, performed under thermal cycle with T_p of 860°C, experiences nearly full austenitisation during heating. During cooling, the austenite begins to decompose until approximately 626°C and then bainite transformation takes place around 582°C. As a further drop in temperature, the martensite formation occurs around 393°C. The curve for simulated HAZ with T_p of 820°C demonstrates that the phase transformation starts much earlier at a high temperature of around 775°C. The transformation product is firstly ferrite, followed by bainite. Bainite formation occurs at 635°C when less than 40% austenite is decomposed.

Comparing with Fig. 8.10 (a), the simulated Ti-containing HAZs in Fig. 8.10 (b), experience transformation with higher start temperature. In the simulated FGHAZ, the onset temperature begins around 665°C and ferrite is firstly formed. In the present case, such high-transformation-temperature products include intragranular acicular ferrite and equiaxed ferrite, which often refers to polygonal ferrite. As temperature further decreases, bainite transformation starts around 603°C. Below 415°C martensite is formed in a small amount. Hence, in the simulated Ti-containing FGHAZs, a large amount of ferrite combined with bainite is firstly formed, followed by martensite formation. In partially austenitised HAZ with T_p of 860°C, the beginning of phase transformation is detected around 697°C. Only a small amount of austenite transforms into martensite as the temperature is below 401°C. As T_p further reduces to 820°C, only ferrite transformation occurs which starts around 772°C. As a result, the final microstructure contains a large fraction of ferrite.

Fig. 8.10 (c) shows the austenite transformation behaviour in the simulated Ti+V-containing HAZs. The three curves are similar to those of Nb-containing HAZs. In the simulated FGHAZs with T_p of 900°C, the onset temperature of austenite decomposition into bainite is around 562°C. Below 426°C, austenite transforms into martensite. The freshly-formed martensite then further experiences auto-tempering process around 353°C. Upon transformation with partial austenitisation (T_p of 860°C), the start temperature of transformation is advanced to around 631°C and ferrite is firstly formed. Bainite and martensite transformation begin around 573°C and 423°C, respectively. A similar trend with high transformation-start-temperature is observed in simulated HAZs with T_p of 820°C, where austenite transforms into ferrite at around 776°C and into bainite around 651°C.

To conclude the austenite transformation behaviour, discussed previously from Fig. 8.10, the remarkable difference is found in simulated Ti-containing HAZs. The simulated HAZs of weld B always have higher transformation-start-temperature and contain less low-temperature transformation product, compared with other two types of simulated HAZs (Table 8.3). However, one similarity is that the onset temperature of phase transformation increases as peak temperature decreases in all simulated HAZs. Although there are only three curves presented in Fig. 8.10, being representative of full or partial austenitisation, another partial austenitisation case with T_p of 780°C can be assumed to follow the same trend with a high transformation-start-temperature.

Table 8.3: The start temperature of different ferrite products during austenite decomposition

HAZs	T_p 900°C				T_p 860°C			T_p 820°C		
	F_s , °C	B_s , °C	M_s , °C	T_{auto} , °C	F_s , °C	B_s , °C	M_s , °C	F_s , °C	B_s , °C	M_s , °C
Steel A	-	573	412	357	626	582	393	775	635	-
Steel B	665	603	415	-	697	-	401	772	-	-
Steel C	-	562	426	353	631	573	423	776	651	-

In the case of HAZs tempered with T_p of 740°C and 700°C, a close observation on the strain curves of the heating part shows that different slope changes occur over three temperature ranges: 60°C to 200°C, 200°C to 400°C and 600°C to T_p 700°C or 740°C. According to Jung et al. [253], the two lower temperature ranges correspond to tempering stage 1 and stage 3. The higher temperature range is related to the dissolution and coarsening behaviour of M_7C_3 and cementite. Although there is a lack of further TEM analysis on the precipitates, some behaviours of precipitate (dissolution, coarsening and other strengthening effect) can be qualitatively understood in the tempered HAZ. Considering the comparison between strain curve features, the Thermo-Calc calculation and hardness results, it is reasonable to expect that the tempering reaction plays an important role in influencing the softening

effect. Further discussion is made in the next part.

8.3.3 Microstructure of the softened HAZs

To understand the microstructural evolutions in the simulated HAZs, microstructure characterisations are performed by optical microscopy and SEM. The microstructural features from Nb and Ti-containing HAZs are discussed firstly due to their single-microalloyed chemistry design but a great contrast in softening phenomenon. Fig. 8.11 shows optical micrographs that correspond to each dilatometry specimen from simulated Nb ((a) – (d), 900°C to 780°C) and Ti ((e) – (h), 900°C to 780°C)-containing HAZs. The corresponding high resolution SEM images are shown in Fig. 8.12.

Fig. 8.11 (a) shows the microstructure of the simulated Nb-containing FGHAZ. It contains a refined mixture of a large fraction of freshly-formed martensite (partially auto-tempered) and some bainite. Such a structure contributes to the high hardness value (Fig. 8.7) and agrees well with the previous dilatometry data (Fig. 8.10 (a)). The refined structure is closely associated with limited austenite coarsening which is due to the retardation effect of the Nb-rich carbonitrides. Since the austenite grain size of base metal is around 8.6 μm , the transformation products, martensite and bainite, are small in size as well (Fig. 8.12 (a)).

In the simulated HAZ cooled from T_p 860°C, the sample undergoes nearly full austenitisation. The microstructure in Fig. 8.11 (b) looks partially different from the homogeneously dark-coloured mixture of bainite and martensite in Fig. 8.11 (a). In addition to a similar mixture of bainite and martensite, there are also regions with bright contrast and in large size. In these regions, the microstructure is apparently transformed firstly into austenite during heating and then decomposed into ferrite during cooling.

In the corresponding SEM images (Fig. 8.12 (b)), the freshly formed ferrite, newly-transformed martensite and bainite are clearly visible. Meanwhile the heavily tempered martensite-plus-bainite structure is resolvable which is characterised by fine decoration of sub-micron particle (white) in interlath regions. Occasional presence of chunky retained austenite islands (white) are observed as the second phase. Considering the observed different phase fractions and hardness values, it can be concluded that a large amount of fresh ferrite along with less martensite contributes to the reduced hardness.

Another simulated intercritical HAZ with T_p of 820°C, following the above mentioned trend, shows even more ferrite as final transformation product. A high volume fraction of bright colour phase can be observed in Fig. 8.11 (c). Of particular interest is the presence of banding, as the light bands running horizontally across the micrograph. This banding is indicative of segregation of substitutional elements such as Mn and Ni in as-received steel. It is known that these high solute contents generally stabilise the austenite phase and increase hardenability. As a result, regions with high alloying elements can prefer martensite formation. In addition, such a similar phenomenon can be more remarkable in Fig. 8.11 (d), from simulated specimen with T_p of 780°C. Hence, in the simulated intercritical HAZs, the ferrite phase becomes the predominant structure. The corresponding SEM images Fig. 8.12 (c) and Fig. 8.12 (d) present the white carbide feature with a high resolution. No abundant clusters or overwhelmed coarsening occurs.

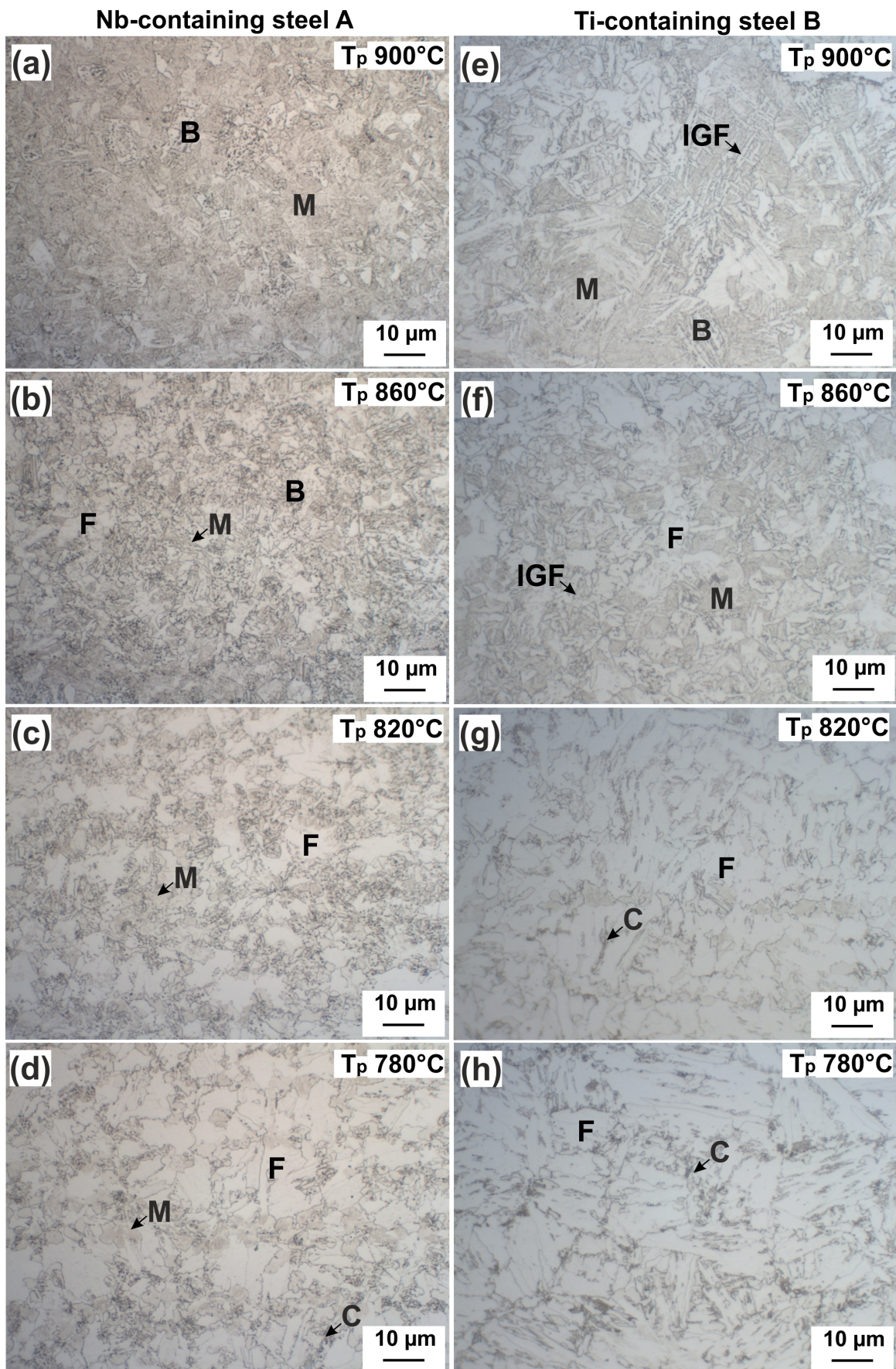


Fig. 8.11: Optical micrographs of simulated HAZs of steel A (a – d) and B (e – h)

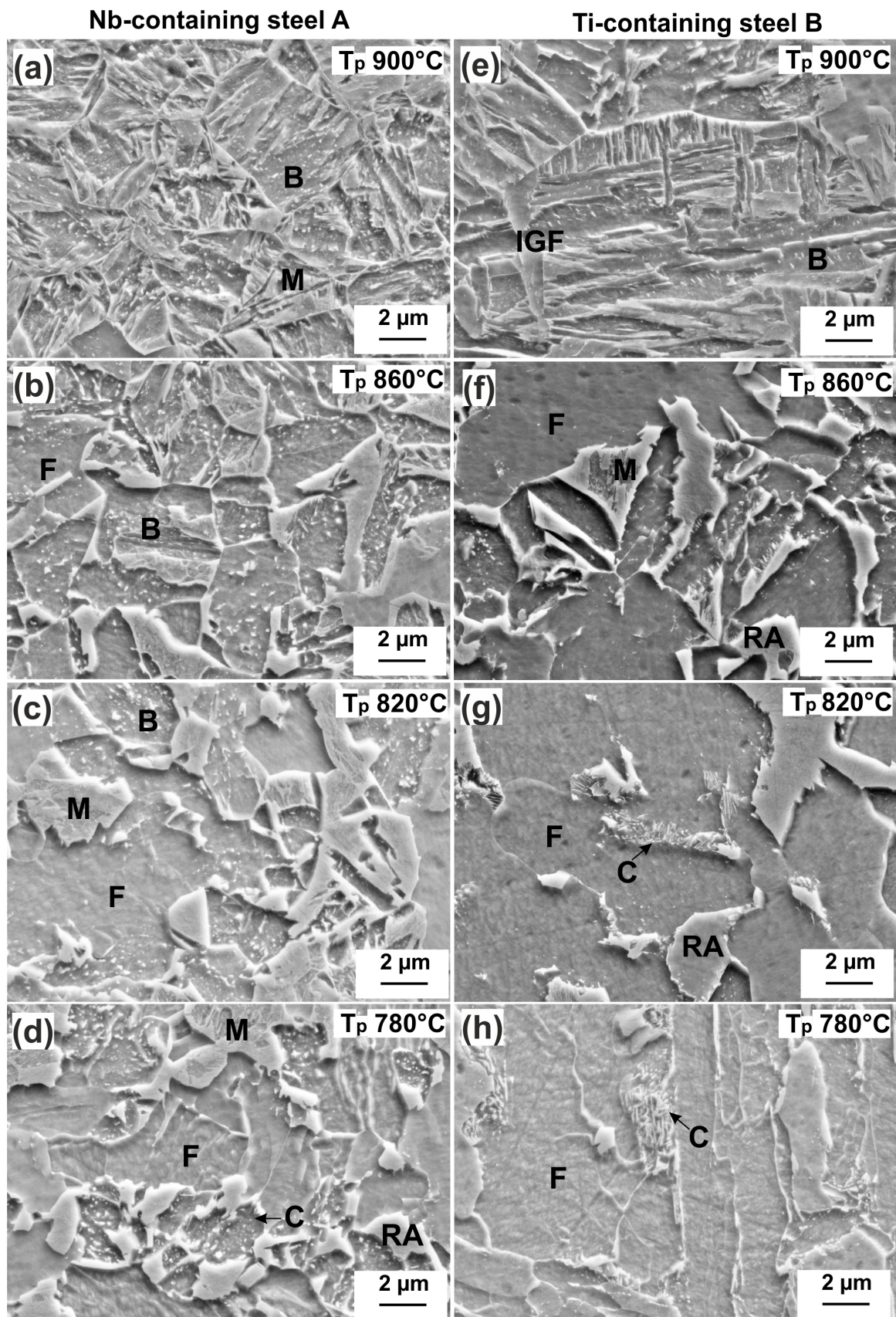


Fig. 8.12: SEM images of simulated HAZs of steel A (a – d) and B (e – h)

In the case of the simulated Ti-containing HAZs (Fig. 8.11 (e) – (h)), the microstructure of each simulation differs significantly from those of weld A (Fig. 8.11 (a) – (d)). The previous dilatometry data (Fig. 8.10(b)) reveals that the phase transformation in Ti-containing HAZs cooled from T_p 900°C and 860°C produce high-temperature transformation product in a large proportion. This results in relatively low hardness (Fig. 8.7), when compared with those in Nb-containing HAZs containing mainly low-temperature transformation product. Fig. 8.11 (e) and (f) shows the presence of ferrite and intragranular acicular ferrite under the optical level of resolution. Although bainite and martensite are also visible, especially in SEM images (Fig. 8.12 (e)), the bainite and martensite packet size is much larger, compared to those in Fig. 8.12 (a). This point is associated with the larger austenite grain in steel B than that in steel A. The apparent similarity in limited austenite coarsening behaviour in steel A and B can explain the resultant different-sized transformation product. Due to the strong pinning effect from the stable Ti- and Nb-rich carbonitrides, no significant austenite coarsening occurs in all dilatometry specimens.

Both Fig. 8.11 (g) and (h), corresponding to the intercritical HAZs, has ferrite as predominant structure. Some precipitates are often observed to be clustered on lath boundaries or grain boundaries. Moreover, some coarsened precipitates are formed in a long rod-like shape, as shown in Fig. 8.12 (g) and (h). Also, ferrite regions show comparatively low precipitation densities compared to the bainitic structure. These microstructural features with coarse ferrite as matrix and precipitates on boundaries are the significant reasons for the low hardness in the two intercritical HAZs, which also represent the typical softening region. Furthermore, to compare the difference in the intercritical HAZs between Nb and Ti-containing HAZs (from weld A and B), a special focus should be given to the ferrite size and the precipitates characteristics including size and distribution. Due to the comparatively large austenite grain, the subsequent ferrite formed in Ti-containing intercritical HAZs exhibits larger than those in Nb-containing HAZs. Meanwhile, the precipitates coarsening or coalescence is quite limited in Nb-containing intercritical HAZs. Therefore, it can be concluded that the severe softening in the intercritical HAZs is due to the synergistic effect between ferrite matrix and the precipitate features. The fine-grained ferrite combined with uniformly-distributed fine precipitates contribute to the enhanced resistance to softening.

The moderate softening behaviour in the Ti+V-containing HAZs lies between Ti- and Nb-containing HAZs, as confirmed by the hardness values in Fig. 8.7. The explanation for this can be understood by the aforementioned dilatometry data and the microstructure characterisation (Fig. 8.13). Comparing with Nb and Ti-containing HAZs (weld A and B), simulated Ti+V-containing HAZs shows a similarity in the microstructure changes as a function of T_p to the Nb-containing steel. This point is proved by the dilatometry curve analysis (Fig. 8.10 (a) and (c)). In addition, the similarity in microstructure composition is found in Fig. 8.13. Nevertheless, there is still some differences in the hardness value, especially in the intercritical HAZs, which is ascribed to the varied fractions of ferrite and its size.

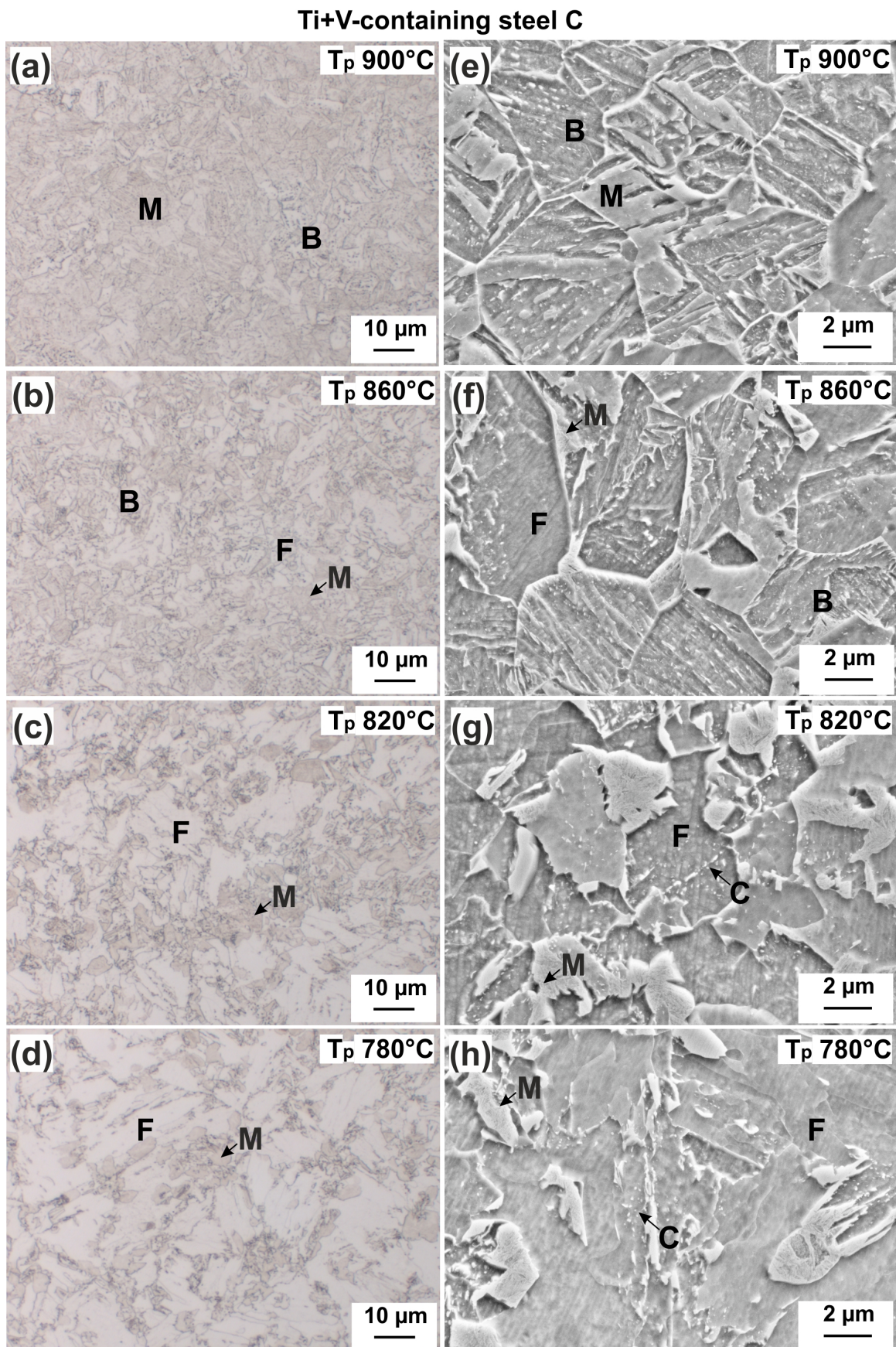


Fig. 8.13: Optical (a – d) and SEM images (e – h) of simulated Ti+V-containing HAZs

The above discussion has attempted to explain the softened HAZ from the aspect of considering phase transformation after full or partial austenitisation. The hardness drop in specimens with T_p below A_{c1} temperature (Fig. 8.7) can be explained by a tempering process. As indicated by the aforementioned dilatometry data, the specimens with T_p of 740°C and 700°C experience only tempering reaction. The hardness result (Fig. 8.7) shows that the three steels have different tempering resistance, among which the microstructure with Ti addition softens to the greatest extent. In support of this point, further metallurgical observation was done (Fig. 8.14). Even observed by high resolution SEM (Fig. 8.14), the tempered regions have substantially the same microstructure as the base metal (Fig. 5.2), except for the coarsened precipitates formed in some favourable locations (e.g. lath or grain boundaries indicated by arrows).

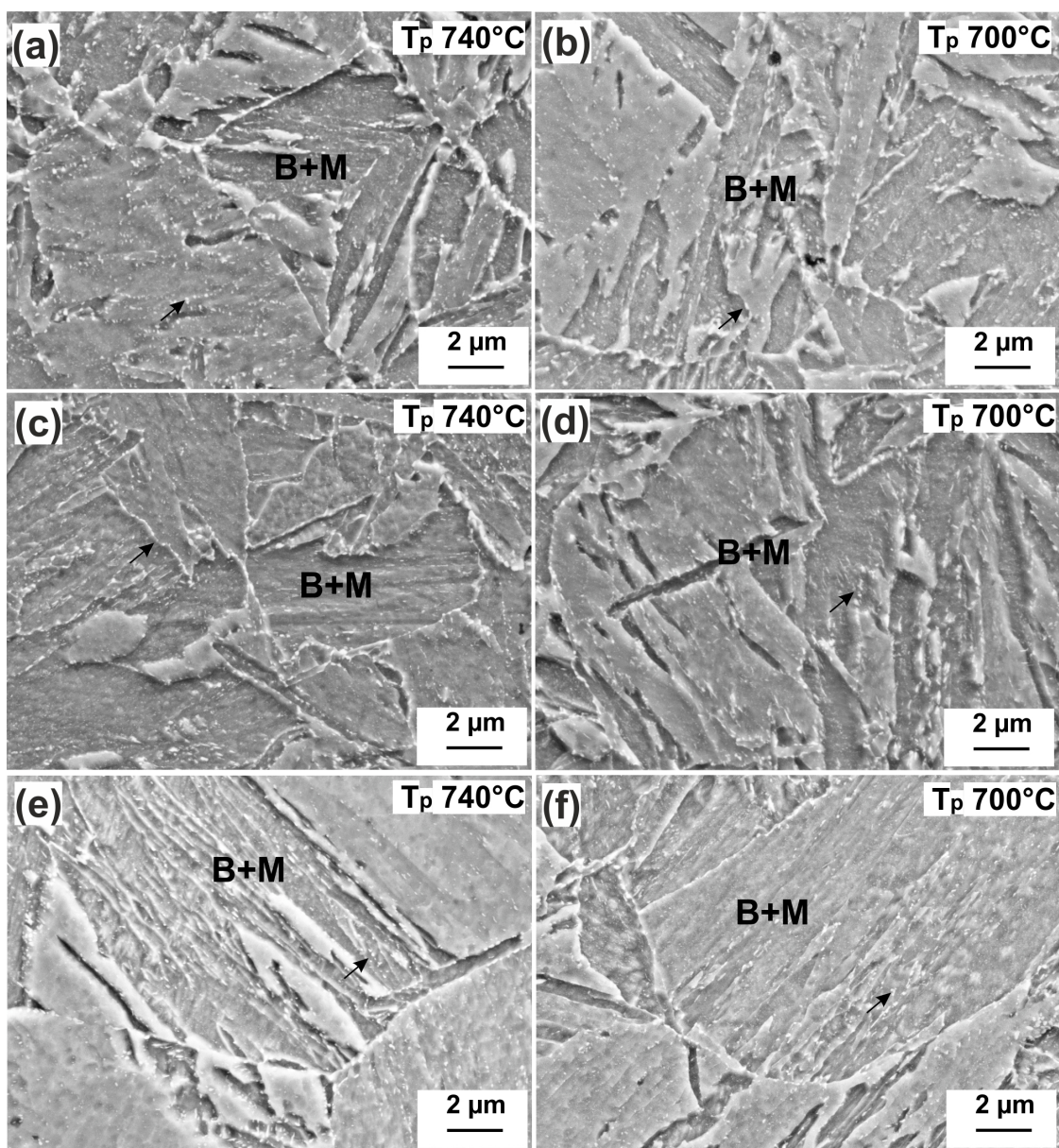


Fig. 8.14: SEM images of tempered HAZs of steel A (a, b), steel B (c, d) and steel C (e, f)

As a result of thermal exposure, carbide precipitates and coarsens preferably at grain boundaries and internal structural defects, since the excess carbon is suggested to be positioned at defects within the ferrite plates [254]. Also, these carbides agglomerate progressively as tempering temperature increases. The quantity of tempered carbide depends on the amount of carbon in solution, alloying elements, peak temperature and cooling time. It is found that the tempered carbide is larger at grain boundaries than that within the grains. This can be ascribed to the faster growth rate at grain boundaries, as a result, large particles grow at the expense of small particles that act as a source of carbon. Likewise, in the HAZs exposed to T_p of 740°C, the coarsening of precipitates occurs to a larger extent than to 700°C (Fig. 8.14), due to a long dwell time for coarsening.

Tempering reaction is the supplementary contribution to the decrease in hardness. It would be anticipated to know more qualitative and quantitative information on precipitates, but this is not possible achieved only by SEM analysis. Further extensive TEM analysis or simulation work should be additionally performed but this is beyond the scope of the present study. From the previous calculation by Thermo-Calc and literature review [133], it is assumed that cementite coarsening occurs along some of prior austenite grain and/or ferrite packet boundaries. Besides the main contribution from the precipitation or coarsening of carbides, both annihilation of dislocation and relieving lattice stresses is also responsible for tempering softening.

8.4 Discussion

8.4.1 Effect of softening on tensile properties

The tensile test results indicate that varied tensile properties can be one major issue in microalloyed S690QL steel welds, since after weld thermal cycle a hardness drop in the HAZ can be developed to different extents. Such a soft zone can have a negative effect on the strength and elongation of the weld if the width of soft zone exceeds a critical value and the corresponding hardness is extremely low. Data acquired from Ti-containing welds reveals that under high heat input the fracture location shifts from base metal to the softened HAZ, due to the pronounced softening, whereas under low heat input limited softening is obtained and this does not compromise integrity of the welded joint during tensile test. In the case of the Nb-containing welds, there is no remarkable softening under different cooling rates and limited HAZ softening shows only minor influence on the tensile properties. The Ti+V-containing welds always exhibit moderate HAZ softening that lies between Ti and Nb-containing welds. Meanwhile, the hardness in the Ti+V-containing softened HAZ is higher than that of Ti-containing steel, indicating that it shows a characteristic of hardness variation close to the Nb-containing welds. Accordingly, special concern for welding Ti-containing steel is to avoid high heat input because the potential formation of excessive softened HAZ could deteriorate the tensile properties of welded joints.

From the load vs. displacement curves (Fig. 8.1), it is found that HAZ softening is more related to ultimate tensile strength and elongation than with the yield strength. The tensile properties do not greatly change if limited softening exists because it is still possible to achieve similar level of elongation to that of the base metal. However, once a pronounced softening occurs under high heat input, the reduced elongation is observed from the decrease in strain hardening process after approaching the yield point. To analyse the strain evolution during tensile test, Farren [183] applied digital image correlation measurement. The observation showed that prior to fracture, the locally softened HAZ region underwent the greatest strain, while the fusion zone underwent the least strain. Compared

with [183], it is reasonable to accept that the locally softened HAZ underwent the concentrated highest strain in the present welded joints. After extensive deformation, the eventual failure occurs in the softened HAZ.

8.4.2 Softening mechanisms

The different resistance to softening in the three steels results in varied influences on tensile properties. Such a difference in softening behaviour can be understood by the metallurgical analysis on the as-welded HAZ and simulated HAZ. In dilatometry experiments, all simulated peak temperatures are not high enough to dissolve microalloy precipitates and then no significant grain coarsening occurs after thermal cycling. As suggested by grain size measurement, Ti-containing steel has the largest austenite grain size, followed by Ti+V-containing steel and finally Nb-containing steel. This is the same trend in dilatometry specimens even after thermal cycle. As a general rule, coarse austenite grain tends to produce coarse ferritic structure. Hence, the austenite grain size is one significant factor to determine the subsequent ferrite size after phase transformation.

In the simulated FGHAZ, the sample is austenitised at T_p of 900°C with a holding time 2 s, longer than the actual welding process. This heat treatment process somewhat enhances the dissolution of existing precipitates in comparison to the case in the as-welded HAZs. High temperature probably causes more Mo and Nb in solution. This further increases the hardenability, which enhances low-temperature transformation [189]. The dilatometry experiments also prove the strong retarding effect of solute alloy on the austenite decomposition kinetics. It is claimed that solute Mo and Nb substantially delay the decomposition of austenite [145]. The positive role of Mo addition on bainite transformation is widely accepted. One suggested explanation for the effect of solute Nb is due to Nb atoms segregation on austenite grain boundaries and this can reduce carbon diffusivity [255]. Moreover, Nb can raise the energy barrier and influence the nucleation of austenite transformation product. Besides this segregation behaviour of Nb, other explanations correlated the influence of Nb on phase transformation with the solute drag effect on the motion of ferrite/austenite interface [20, 142, 256]. But the exact mechanism to understand the effect of Nb on hardenability and phase transformation is still controversial. The observed retardation effect of combined Nb and Mo, in particular with elevated T_p of 900°C, is consistent with the results of [145, 189, 257]. Fossaert et al. [145] found that bainite formation is retarded by Nb in solid solution and accelerated by Nb carbide precipitates. The observation in sample with a low T_p (e.g. 860°C) shows that bainite transformation starts much earlier as compared to that with T_p of 900°C. Therefore, in the case with a low T_p , it shows a tendency to diminish the retardation effect of combined Nb and Mo. This is due to less Nb and Mo in solute form but more in precipitates state as compared to the case in specimen with T_p of 900°C.

As T_p is further reduced to 820°C (partial austenitisation occurs), ferrite formation begins at much higher temperature, indicating a tendency of hardness decrease. Nevertheless, a certain fraction of untempered martensite is freshly formed and this contributes to a complementary increase in hardness. During ferrite transformation, due to the carbon rejection into the retaining austenite, the resultant newly-formed martensite having a high carbon content would be anticipated to enhance the hardness increase. In the non-transformed regions, heavily-tempered martensite and high density of dispersed precipitates exist, which is presumed to consist of cementite and carbide phases from strong carbide-forming (Nb, Cr, Mo) elements [258]. In the case with T_p of 780°C, where a small fraction of re-austenitisation occurs, the phase transformation is essentially similar to the case in the sample

simulated with 820°C. Also, both simulated HAZs have almost the same level of hardness. Therefore, in the Nb-containing intercritical HAZs, the resistance to softening is significantly influenced by the combined Nb and Mo effect.

In the simulated Nb-containing HAZs, with T_p lower than A_{c1} , the tempering reaction causes a marginal reduce in hardness, even accompanied with precipitation and coarsening or recovery. This suggests that Nb-containing HAZ does not suffer severe softening. To consider the tempering behaviour of bainite, it is accepted that bainite shows greater stability to tempering than martensite. Bainite reaction is a process of auto-tempering and less sensitive to additional tempering heat treatment [70]. In terms of low temperature martensite tempering, extensive researches were carried out on its reaction in different steels or under different welding processes [132, 133, 259]. Generally, in martensite containing steel, it is claimed that the resistance to softening is proportional to the martensite volume fraction. Thus, it is correlated with the extent of martensite decomposition and its kinetics depends on the C content and carbide forming elements [133, 259]. It is known that the final martensite decomposition product is often cementite (sometimes in M_3C type, $M = Fe, Cr, Mn$), corresponding to the last stage of tempering [132]. Precipitation of cementite is proposed to be governed by carbon diffusion into lattice defects, whereas the coarsening mechanism is dislocation diffusion controlled. A large fraction of carbide forming elements (such as Cr and Mo) is affirmed to increase the resistance to softening by reducing the driving force of tempering [132, 133]. This indicates the positive effect of Mo and Cr element on stabilising martensite and retarding tempering reaction. In addition, fine cementite with plate-like morphology delays the recovery process greatly and in tempering it can inhibit the climb of dislocation by pinning effect [132].

Besides cementite precipitation or coarsening, tempering reaction may contain the evolution of other types of alloy carbides. Considering tempering temperature above 400°C up to 740°C and the high content of strong carbides forming elements (Nb, Cr, Mo), it would not rule out the possibility of alloy precipitates formation during tempering process. It is known that the coarsening of alloy precipitate depends on the long range diffusion of carbide forming elements that is more sluggish process than C and Fe atoms. Meanwhile, the freshly-precipitated particles cannot coarsen easily within a very limited tempering time. As a consequence, once a dispersion of fine alloy precipitates exists, this would contribute to an increase in hardness and tends to reduce coalescence of carbides during tempering. Although this assumption has to be confirmed by performing TEM analysis, the similar influence of carbides forming elements on softening resistance can be well understood from other steels containing alloying elements that have a strong affinity for carbon, such as creep-resistant steel with Cr, Mo and V [200]. Furthermore, Kojima et al. [12] attributed the HAZ softening of high Cr ferritic steel to the lack of fine Nb and V carbonitrides coherent with the matrix. Another effect of Nb is to delay recovery of dislocations, leading to a dispersion of exceptionally fine secondary carbides formed during tempering reaction [20, 142, 256]. The influence of alloy carbides on the tempering resistance is still not fully understood. But one assumption is that a form of short range order or segregation may exist in the ferrite, which would be anticipated to impede dislocation movement.

The presented references and obtained results suggest that Nb-containing HAZs does not experience remarkable softening in both intercritical and subcritical HAZs. The combined Nb and Mo effect is one significant factor to promote the enhanced resistance to softening by promoting low-temperature transformation products and to retard tempering reaction. Such highly alloyed Nb+Mo-containing

steel A has a strong resistance to softening, which is also supported by other studies [132, 133].

In the Ti-containing HAZs, the most pronounced softening occurs, which is ascribed to the ferrite formation and severe tempering reaction after weld thermal cycle. Upon austenite decomposition from 900°C, the dilatometry results show that the transformation starts much earlier as compared to Nb-containing HAZ. The micrographs (Fig. 8.11) confirm that ferrite with a different morphology from typical bainite is formed in the simulated Ti-containing FGHAZs. In particular, the intragranular acicular ferrite, which is formed in the CGHAZs, is also found in FGHAZ. A large fraction of intragranular acicular ferrite and limited bainite and martensite contributes to a lower hardness value compared with Nb-containing FGHAZs. It is known that the acicular ferrite nucleates intragranularly on heterogeneous nucleation sites, e.g. TiN in the present case [60, 86, 101]. The formation of acicular ferrite can be also promoted by the large austenite grain [65]. To confirm this characteristic, the nucleation of intragranular ferrite was studied by additional dilatometry experiments, which are in details described in the previous experimental section. The plots of decomposed austenite fraction vs. temperature are shown in Fig. 8.15. The corresponding micrographs are shown in Fig. 8.16.

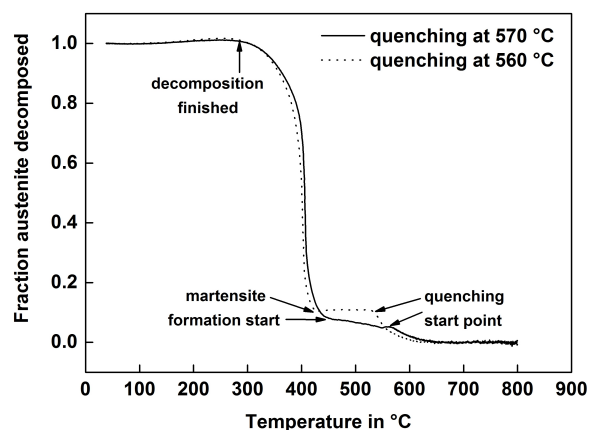


Fig. 8.15: The fraction austenite decomposed as a function of temperature in fast quenched specimens

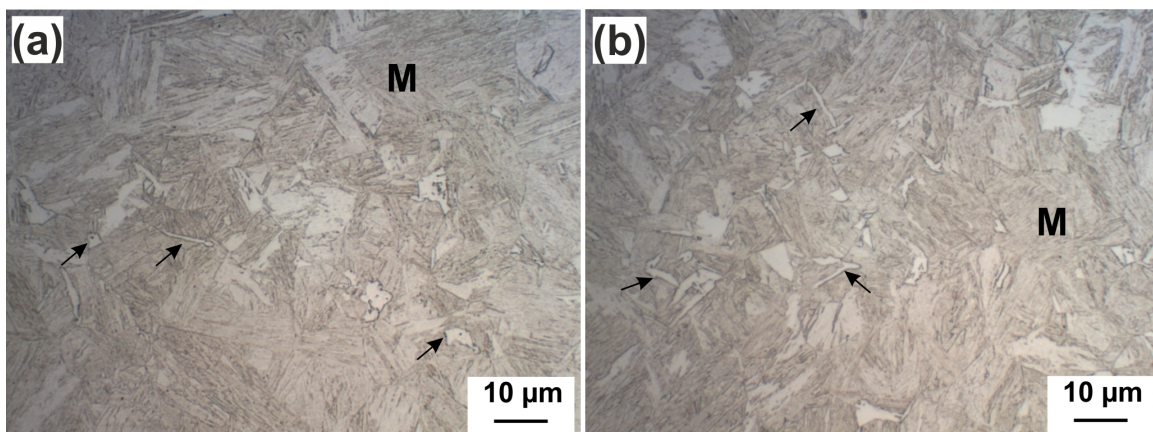


Fig. 8.16: Optical micrographs of quenched specimens with T_p of 570°C (a) and 560°C (b)

Fig. 8.15 shows that austenite starts to decompose into ferrite shortly after 600°C. Once quenching gas is applied at 570°C or 560°C, the ferrite transformation is suddenly interrupted. Then, the austenite fraction remains roughly constant for a limited time. As temperature decreases to martensite start temperature (M_s), the retained austenite is further transformed into martensite. While the nucleation

or growth process of ferrite is interrupted by the fast quenching gas, consequently, the newly-formed ferrite can be easily found among the martensite matrix (indicated by arrows in Fig. 8.16).

During the very beginning of transformation, the polygonal ferrite is mostly formed close to grain boundaries (Fig. 8.16(a)) and meanwhile the intragranular acicular ferrite formation starts. The typical shape characteristic is illustrated in Fig. 8.16 (b). Several needle-shaped ferrite plates (bright colour under light microscopy) are nucleated at the same centre within grain or some are auto-catalytically nucleated on the existing ferrite plates. Such an observation is consistent with [81, 85, 86]. As a result, the beneficial effect of Ti addition on promoting intragranular acicular ferrite can be directly confirmed by the dilatometer results.

Indeed, in the simulated Ti-containing FGHAZ with T_p of 900°C and 860°C, the mixture of intragranular ferrite along with bainite and small fraction of martensite contributes to no decrease in hardness. This microstructure composition implies that no softening happens in this simulated FGHAZ, whereas a reduced hardness occurs in the intercritical HAZs (Fig. 8.7).

In specimens with T_p of 820°C, the austenite starts to decompose into ferrite at very high temperature and subsequently less bainite and martensite is formed. The corresponding abrupt drop of hardness is closely related to the ferrite as predominant phase and less low-temperature transformation product. Additionally, the size of ferrite appears coarser than that of Nb-containing HAZ with the same T_p (due to the large initial austenite grain). Another feature is that a dense coalescence of carbides is formed along the lath or grain boundaries. Therefore, the low hardness value is reached if Ti-containing HAZ is subjected to thermal cycle with T_p of 820°C and 780°C. This can be attributed to a change in ferrite size coupled with a dense cluster of coarse carbides.

The austenite decomposition behaviour in simulated Ti-containing HAZs is quite different from that of Nb-containing HAZs. This can be explained by the varied alloy designs and austenite grain size in the two steels. As previously discussed, the combined Nb and Mo effect is the main reason for the high resistance to softening from the point of phase transformation and tempering retardation. Nevertheless, the austenite grain size plays also a significant role in the aforementioned reactions. Ti-containing steel has less alloy addition (especially Mo), lower hardenability but large austenite grains. These characteristics combine to favour the ferrite phase formation after the thermal cycling. Also, certain concentration of carbides forming elements may not be sufficient to retard the coalescence of cementite. Hence, the pronounced softening observed in the Ti-containing intercritical HAZs is driven by the coarse carbides and large-sized ferrite.

Additional contribution to softening can be understood by the tempering process due to the lack of strong carbide forming elements that can stabilise martensite. Although Ti is added, Ti-rich nitrides are precipitated at very high temperature and can easily coarsen during thermal cycle. Anyway, the alloy design of Ti-containing steel shows limited resistance to tempering-induced softening. Furthermore, when heat input increases (cooling time $t_{8/5}$ longer than 15 s), it allows cementite and other particles to precipitate or coarsen more seriously. As a result, severe tempering-induced softening occurs in the weld. If the heat input is above a critical value, extremely wide softening zone exist due to both phase transformation and tempering effect. This softened zone can experience locally concentrated deformation during tensile test and cause a failure in softened HAZ, accompanied with a reduced elongation. This issue becomes one critical factor to determine the integrity of Ti-containing welded

joints. In practice, the extent of softening should be carefully controlled by appropriate welding variables to avoid any negative influence on tensile properties.

In the case of the Ti+V-containing HAZs, the simulated samples suggest that the softening resistance behaviour lies between Ti and Nb-containing HAZs. More precisely, it is much closer to Nb-containing HAZs. In support of this point, the dilatometry curves and metallurgical observations provide sufficient evidence. The presence of Mo and V elements in the Ti+V-containing HAZs increase steel hardenability. Combined effect of the two alloying elements plays a positive role in enhancing low-temperature transformation product, thus increasing the resistance to softening. Also, during tempering process, V also acts as strong carbide former like Mo and Cr. This has a significant retardation effect on hardness loss during tempering. Such a beneficial effect of V addition has been often reported [128, 130, 154]. In the Ti+V-containing steel, the limited V (0.01%) together with other alloying shows relatively lower resistance to softening compared with Nb-containing steel. This indicates that both alloy types and concentration are important factors to determine the softening resistance.

8.5 Summary

The tensile test results show that the failure of welded joints is located in base metal in most cases except the Ti-containing welds under medium or high level heat input, in which the eventual failure is in the HAZ. More precisely, the location is not directly close to fusion line but in the softened zone. Such a narrow layer with reduced hardness probably experiences intensively local deformation during tensile tests. As a result, this can cause the eventual failure by reduced elongation.

The softening behaviour strongly depends on the welding parameter and the steel type. Increased heat input extends the softening zone width and reinforces the negative effects of softening. Among the three steels, Ti-containing weld exhibits the most pronounced softening, followed by Ti+V-containing welds and finally Nb-containing welds. A close microstructure observation shows that the softening is closely correlated with different phase compositions and morphologies. In order to explain these difference and understand softening mechanisms, the physical simulation of softened HAZ were performed by the dilatometry experiments.

The dilatometry results quantitatively characterise the hardness variation in HAZ regions with respect to different peak temperatures achieved during thermal cycling. This hardness information can be used to assess the varied contribution from a given HAZ region to the entire softening. Combining the hardness results with the dilatometry analysis, it can be concluded that the HAZ softening depends on several factors such as the steel alloy design, austenite grain size, weld thermal cycle and kinetics of phase transformation. Although the present simulation has been performed under one given cooling rate ($t_{8/5}$ 15 s), it is expected that the extent of softening increases with increasing heat input. Most importantly, the steel chemistry can greatly influence the softening behaviour.

A comparison of two steels (one containing Nb with strong carbide former Mo and the other containing Ti without Mo) has been firstly investigated. In Ti-containing HAZ, the phase transformation products after partial austenitisation, particularly with large-size ferrite and coarse carbides coalescence, provide considerable contribution to softening. Also, tempering process results in additional softening effect. This is attributed to insufficient carbides formers formed in the Ti-containing steel. However, in the Nb-containing HAZ, the combined Nb and Mo effect can promote low-temperature transformation product

and retard the carbide coalescence, thus causing no significant hardness decrease. Additionally, the small initial austenite grain size favours fine transformation products formation. All these interacted factors enhance the resistance of Nb-containing HAZ to softening. Ti+V-containing HAZs exhibits a softening behaviour similar to Nb-containing HAZs, which is ascribed to the presence of Mo and V. Nevertheless, due to the comparatively low concentration of these carbide forming elements, Ti+V-containing HAZ shows lower resistance to softening than Nb-containing HAZ.

In summary, the microalloyed steel with small austenite grains and sufficient carbide forming alloys (Mo, Cr, V, Nb) can withstand excessive HAZ softening, as in the case of Nb-containing HAZs. Another implication of the simulated FGHAZ is that the synergistic interaction of Nb and Mo assists in low-temperature transformation product. In addition, the dilatometry experiments also provide one compelling evidence that fine Ti-rich carbonitrides act as heterogeneous nucleation sites and promote the intragranular acicular ferrite formation.

The results establish a deep understanding of the microstructure evolution in softened HAZ with respect to the influence of microalloy addition. This work also provides some references for welding engineers to ensure a balance between microstructure and properties. More precisely, appropriate welding parameters should be adjusted with a consideration of steel alloy design, in order to achieve welded joints that can produce reliable properties for service, in particular with acceptable strength and/or ductility.

9 General conclusions and future works

This thesis contains an account of the special concerns that reinforce the primary goal of understanding the joining of microalloyed steel by modern welding technologies. A major part of the research was focused on examining metallurgical aspects and mechanical properties, with emphasis on strength and toughness, as a response to various welding parameters. The results reveal how the finely balanced alloy design influences the mechanical behaviour in different regions of the welded joints. This generates key experimental evidence for suggestions and guidelines with respect to welding modern microalloyed steels. In addition, useful strategies for improving weldment properties are provided.

1. Detailed characterisation of three microalloyed S690QL steels (Nb, Ti and Ti+V containing) shows that a similar mixture of tempered bainite and martensite predominates the parent microstructure but different coarse microalloy precipitates are visible even under light microscopy. The addition of microalloy elements are responsible for the presence of microalloy precipitates and further thermodynamic calculation data confirms this point. Also, cementite and other alloy precipitates may be present. Another discrepancy among the three steels is the austenite grain size. This may be able to explain the varied yielding phenomena in the obtained strain vs. stress curves.
2. One typical advantage of applying modern welding technologies is the high efficiency, deep penetration and low cost. Along with deep penetration and high dilution aspects, this indicates that a large amount of alloy pick-up from the base metal occurs to the weld metal. This alloy pick-up combined with weld deposits from identical filler metal determines the final alloy composition in the weld metal.
3. The differences in alloy design of the base metal has been further inherited by the weld metal. This tends to promote considerable transformation changes under different cooling rates. Particularly in Nb-containing welds, a large amount of Mo coupled with Nb that was picked up, has made the weld metal sensitive to the cooling rate. More precisely, this means that under fast cooling, the transformation products change into bainite with a lower toughness value, whereas under slow cooling, acicular ferrite forms which is more desirable.
4. Such variation of austenite decomposition was deeply studied from the aspects of the transition between acicular ferrite and bainite. The main reason for this transition is the alloy variation of the weld metal due to microalloy pick-up. This observation will become one of special concern as modern welding technology with high dilution is used.
5. HAZ toughness is of particular interest. In inductively heat-treated samples, the austenite grain growth behaviour of the CGHAZ and FGHAZ is well demonstrated. The results indicate that the Nb-containing HAZ (even with the smallest original austenite grain) experiences significant coarsening process due to relatively weaker pinning effect from the dissolution of Nb-rich precipitates. However, Ti-containing HAZ exhibits a limited grain growth even at elevated temperature, due to the fine stable Ti-rich particles. The austenite coarsening behaviour of Ti+V-containing HAZ lies between the other two steels, which is explained by the insufficient precipitates that are available for the retardation effect.
6. The simulation data revealed the different austenite growth behaviours are due to presence

of microalloy precipitates. The microstructure and hardness values of the actual welded HAZ supports this observation.

7. It is confirmed that solute Nb coupled with Mo contributes to bainite formation and significant HAZ hardening, whereas the addition of Ti enhances intragranular acicular ferrite formation. This remarkable difference in the HAZ microstructure determines the varied HAZ toughness. This can be interpreted by the different characteristics of crystallographic misorientation between coarse upper bainite packets and intragranular acicular ferrite.
8. In previous literature, coarse precipitates of TiN in the base material have negative influence on cleavage fracture. However, the results from HAZ toughness do not imply that the TiN initiates any microcracks or deteriorates the crack propagation despite being large in size.
9. The toughness of the Ti-containing HAZ is much higher than that of the Nb-containing HAZ under similar slow cooling conditions. The high angle boundaries of fine acicular ferrite provide the strong barriers for the propagation of cracks in Ti-containing HAZ. Alternately, the high concentration of upper bainite influences brittle cleavage fracture in Nb-containing HAZ. Under fast cooling conditions in Nb-containing HAZ, upper bainite formation is suppressed and the resultant refined microstructure has improved toughness. Faster cooling conditions provide no great change to the Ti-containing HAZ. This indicates the beneficial role of acicular ferrite and limited upper bainite formation on the toughness of the HAZ.
10. The toughness characteristic in the case of Ti+V-containing HAZ can be understood by the combined influences of upper bainite formation and acicular ferrite influencing fracture mechanisms, as stated previously.
11. Influence from welding parameters affects the HAZ, potentially causing a softening zone. The narrow layer with reduced hardness experiences intensively local deformation during tensile tests and causes the eventual failure in the softened HAZ. Increased heat input extends the softening zone width and reinforces the negative effects of softening. Among the three steels, Ti-containing welds exhibit the most pronounced softening, followed by Ti+V-containing welds and finally Nb-containing welds displaying the least pronounced softening. The HAZ softening zones are further divided into two areas of interest, the subcritical zone and the intercritical zone.
12. The HAZ softening behaviour is governed by two significant factors, the transformation products and tempering resistance. The phase transformation products after partial austenitisation, particularly with large-size ferrite and coarse carbides coalescence, provide considerable contribution to the softening in the Ti-containing HAZ.
13. In the Ti-containing HAZ, the low tempering resistance in the subcritical HAZ has additional contributions to the softening behaviour. The reason for this is low concentrations of carbide forming elements present in the Ti-containing steel. In comparison to this, Nb-containing steels are able to resist tempering reaction and also obtain refined ferrite matrix along with dispersed carbides in the intercritical HAZ, causing only marginal softening.
14. The softening behaviour of Ti+V-containing steels falls in between the other two steels; it shows a similarity to the Nb-containing welds.

15. A solution to alleviate HAZ softening is to limit austenite grain growth by microalloy addition and increase strong carbides formers content. In addition, excessive softening can be offset by an decrease of heat input.

In summary, it is noteworthy that each region of welded joints (weld metal and all HAZs regions) must have acceptable properties when considering the weldment integrity. With respect to the HAZ properties, the final strength or mechanical properties is a balancing act between HAZ hardening and softening. The negative aspects which include low toughness or severe softening, can be offset by appropriate selection of welding parameters. Specifically, low heat input with cooling time $t_{8/5}$ around 11 s is suggested for the investigated steels. For application of advanced welding technology (modified spray arc welding), the weld metal properties should be focused on the choice of filler metal and the high dilution of base materials; alloy pick-up becomes the significant factor in understanding the microstructure evolution in the weld metal. In conclusion, to gain a reliable weldment of modern microalloyed steels, special focus needs to be placed on steel alloy design as well as applied welding process.

9.1 Future works

The research summarised in this thesis contributes to an in-depth understanding to the microstructure and property evolution in three different S690QL microalloyed steel welds. The results have significant implications for joining microalloyed steels by modern welding technology and can be applied to improve the design of microalloyed steels and filler metal. However, much work still needs to be done in order to further understand the complex interaction of alloying elements and then for these results to have a direct impact to industrial operations. Several points are outlined below:

1. It would be valuable to further investigate the influence of fine alloy carbides contributing to precipitation strengthening effects and then investigate their respective coarsening behaviour during welding. High resolution SEM images would reveal the presence of alloy carbides, but the challenge would be the specific identification of each. The thermodynamic calculation along with hardness results have also indirectly supported the presence of alloy carbides, but this needs to be verified experimentally by extensive TEM work combined with EDX analysis. Information about fine precipitates will allow for a deeper understanding of the role of alloying elements.
2. It would be useful to develop a model to interpret or predict the tempering process using thermodynamic and kinetic calculation along with experimental analysis on cementite or alloy precipitates. To verify these simulation results, more dilatometry experiments will have to be performed. As a result, the carbides growth kinetics during tempering will be well understood, particularly in the aspect of the role of substitutional alloying elements such as Cr and Mo.
3. This work only deals with single pass welding of microalloyed steels, but further research on multi-pass welding for thick-plate microalloyed steels needs to be studied. These results would provide useful information and references for carrying out multi-pass welding with respect to: suitable welding parameters, filler metal, and adequate pre/post heat treatments. The research on single pass welds contained in this document will also provide invaluable knowledge when applied to multi-pass welding.

References

- [1] J. Raoul and H.-P. Günther, *Use and application of high-performance steels for steel structures*, vol. 8. Iabse, 2005.
- [2] H. Bhadeshia and R. Honeycombe, *Steels: microstructure and properties: microstructure and properties*. Butterworth-Heinemann, 2011.
- [3] DIN EN 10025-6:2011-04, "Warmgewalzte Erzeugnisse aus Baustählen - Teil 6: Technische Lieferbedingungen für Flacherzeugnisse aus Stählen mit höherer Streckgrenze im vergüteten Zustand."
- [4] J. Billingham, J. Sharp, J. Spurrier, and P. Kilgallon, "Review of the performance of high strength steels used offshore," tech. rep., 2003.
- [5] P. Wongpanya, *Effects of heat treatment procedures on the cold cracking behaviour of high strength steel welds*. Bundesanstalt für Materialforschung und-prüfung (BAM), 2008.
- [6] J. M. Gray, "Weldability of niobium containing high strength low alloy steel," tech. rep., 1976.
- [7] C. D. Lundin, T. Gill, C. Qiao, Y. Wang, and K. Khan, "Carbon equivalence and weldability of microalloyed steels," tech. rep., DTIC Document, 1989.
- [8] M. Shome, D. Sarma, O. Gupta, and O. Mohanty, "Precipitate dissolution and grain growth in the heat affected zone of HSLA-100 steel," *ISIJ international*, vol. 43, no. 9, pp. 1431–1437, 2003.
- [9] M. Maalekian, R. Radis, M. Militzer, A. Moreau, and W. J. Poole, "In situ measurement and modelling of austenite grain growth in a Ti/Nb microalloyed steel," *Acta Materialia*, vol. 60, no. 3, pp. 1015–1026, 2012.
- [10] R. B. Lazor, A. G. Glover, and R. D. McDonald, *Properties of welds in thick section Nb-containing steels*, pp. 1–9. Pergamon, 1984.
- [11] P. Mitchell, P. Hart, and W. Morrison, "The effect of microalloying on HAZ toughness," in *Microalloying 95 Conf. Proc.*, pp. 149–162, 1995.
- [12] T. Kojima, K. Hayashi, and Y. Kajita, "HAZ softening and creep rupture strength of high Cr ferritic steel weldments," *ISIJ International*, vol. 35, no. 10, pp. 1284–1290, 1995.
- [13] R. Ito, C. Shiga, Y. Kawaguchi, T. Nakamura, K. Hiraoka, T. Hayashi, and S. Torizuka, "Controlling of the softened region in weld heat affected zone of ultra fine grained steels," *ISIJ International*, vol. 40, no. Suppl, pp. S29–S33, 2000.
- [14] D. P. Fairchild, D. G. Howden, and W. A. T. Clark, "The mechanism of brittle fracture in a microalloyed steel: Part I. Inclusion-induced cleavage," *Metallurgical and Materials Transactions A*, vol. 31, no. 3, pp. 641–652, 2000.
- [15] L. P. Zhang, C. L. Davis, and M. Strangwood, "Dependency of fracture toughness on the inhomogeneity of coarse tin particle distribution in a low alloy steel," *Metallurgical and Materials Transactions A*, vol. 32, no. 5, pp. 1147–1155, 2001.
- [16] A. Echeverria and J. M. Rodriguez-Ibabe, "The role of grain size in brittle particle induced fracture of steels," *Materials Science and Engineering: A*, vol. 346, no. 1-2, pp. 149–158, 2003.
- [17] H. G. Pisarski and R. E. Dolby, "The significance of softened HAZs in high strength structural steels," *Welding in the World*, vol. 47, no. 5-6, pp. 32–40, 2003.
- [18] F. Hochhauser, W. Ernst, R. Rauch, R. Vallant, and N. Enzinger, "Influence of the soft zone on the strength of welded modern HSLA steels," *Welding in the World*, vol. 56, no. 5-6, pp. 77–85, 2012.
- [19] A. Marian and M. Gizejowski, *Progress in Steel, Composite and Aluminium Structures: Pro-*

- ceedings of the XI Int Conf on Metal Structures (Icms 2006), Rzeszow, Poland, 21-23 June 200.* Taylor & Francis, 2006.
- [20] H. Mohrbacher, "Mo and Nb alloying in plate steels for high performance applications," in *The International Symposium on the Recent Developments in Plates Steels*, pp. 169–179, 2011.
- [21] E. Gogou, "Use of high strength steel grades for economical bridge design," Master's thesis, TU Delft, Delft University of Technology, 2012.
- [22] T. Gladman, *The physical metallurgy of microalloyed steels*. Institute of Materials, London, 1997.
- [23] E. Orowan, *Internal Stress in Metals and Alloys*. The Institute of Metals, London, 1948.
- [24] M. Gáspár and A. Balogh, "GMAW experiments for advanced (Q+T) high strength steels," *Journal of Production Processes and System*, vol. 6, no. 1, pp. 9–24, 2013.
- [25] ASTM A514, "Standard specification for high-yield-strength, quenched and tempered alloy steel plate, suitable for welding."
- [26] ISO 630-4:2012, "Structural steels – Part 4: Technical delivery conditions for high-yield-strength quenched and tempered structural steel plates."
- [27] J. E. Bringas, *Handbook of comparative world steel standards*. ASTM International, West Conshohocken, PA., 3th. ed., 2004.
- [28] P. Dainelli and F. Maltrud, "Management of welding operations with high strength steels," *Soudage et techniques connexes*, vol. 66, no. 7-8, pp. 33–38, 2012.
- [29] DIN EN 10025-4:2011-04, "Warmgewalzte Erzeugnisse aus Baustählen - Teil 4: Technische Lieferbedingungen für thermomechanisch gewalzte schweißgeeignete Feinkornbaustähle."
- [30] DIN EN 10149-2:2013-12, "Warmgewalzte Flacherzeugnisse aus Stählen mit hoher Streckgrenze zum Kaltumformen - Teil 2: Technische Lieferbedingungen für thermomechanisch gewalzte Stähle."
- [31] P. Hatto, "Standards and standardisation: A practical guide for researchers," 2011.
- [32] C. W. Wegst, *Stahlschlüssel*. Verlag Stahlschlüssel Wegst, 2013.
- [33] H.-G. Hillenbrand and C. Kalwa, "Production and service behaviour of high-strength large-diameter pipe," *Pipes and pipelines international*, vol. 47, no. 6, pp. 20–28, 2002.
- [34] World Steel Association, "Crude steel production." Available from <https://www.worldsteel.org/statistics/statistics-archive/steel-archive.html>, May 2015.
- [35] N. J. Bristow, "Setting the scene - from steel to raw materials." OECD Workshop on Steelmaking Raw Materials, December 2011.
- [36] C. Farrar, *The alloy tree: a guide to low-alloy steels, stainless steels and nickel-base alloys*. Elsevier, 2004.
- [37] M. Korchynsky, "A new role for microalloyed steels-adding economic value," in *Proceedings of the 9th International Ferro Alloy Conference Infacon*, vol. 9, p. 11, 2001.
- [38] InfoMine, "Commodity and metal prices." Available from <http://www.infomine.com/investment/metal-prices/>, May 2015.
- [39] N. Yurioka, "Physical metallurgy of steel weldability," *ISIJ International*, vol. 41, no. 6, pp. 566–570, 2001.
- [40] J. Dearden and H. O'Neill, "A guide to the selection and welding of low alloy structural steels," *Transactions of the Institute of welding*, vol. 3, pp. 203–214, 1940.
- [41] Y. Ito and K. Bessyo, *Weldability formula of high strength steels: related to Heat-affected Zone cracking*. IIW, Doc IX-576-68, 1968.
- [42] DIN-Fachbericht CEN ISO/TR 17844:2004-11, "Welding - Comparison of standardised methods

- for the avoidance of cold cracks (ISO/TR 17844:2004); German translation of CEN ISO/TR 17844:2004.”
- [43] N. Yurioka, S. Ohshita, and H. Tamehiro, “Study on carbon equivalents to assess cold cracking tendency and hardness in steel welding,” in *AWRA Symposium Pipeline Welding in the 80's*, pp. 1–5, 1981.
- [44] H. Suzuki and H. Tamura, “Weldability of high strength steels evaluated by synthetic haz ductility test,” *Transactions of national research institute for metals*, vol. 3, no. 1, pp. 47–59, 1961.
- [45] N. Hannerz, *The influence of silicon on the weldability of mild and high tensile structural steel*. IIW, Doc IX-1169-80, 1980.
- [46] DIN EN 1011-2:2001-05, “Schweißen—Empfehlungen zum Schweißen metallischer Werkstoffe; Teil 2: Lichtbogenschweißen von ferritischen Stählen.”
- [47] C. Düren, “Equations for the prediction of cold cracking in field-welding large diameter pipes,” pp. 434–439, 3R International, 3R International, 1985.
- [48] B. Graville, “Cold cracking in welds in HSLA steels,” *Welding of HSLA(Microalloyed) Structural Steels*, pp. 85–101, 1976.
- [49] N. Yurioka, H. Suzuki, and S. Oshita, “Determination of necessary preheating temperature in steel welding,” *Welding Journal*, vol. 62, no. 6, pp. 147s–153s, 1983.
- [50] P. H. M. Hart and P. L. Harrison, “Compositional parameters for HAZ cracking and hardening in C-Mn steels,” *Welding Journal Research Supplement*, vol. 66, no. 10, pp. 310s–322s, 1987.
- [51] K. Easterling, *Introduction to the physical metallurgy of welding*. Butterworths, 1983.
- [52] N. Yurioka and H. Suzuki, “Hydrogen assisted cracking in C-Mn and low alloy steel weldments,” *International Materials Reviews*, vol. 35, no. 1, pp. 217–249, 1990.
- [53] P. Hansson, *Control of weldability: Research leading to the development of two new quenched and tempered tool steels*. PhD thesis, Royal Institute of Technology, Stockholm, 2004.
- [54] M. S. Węglowski, “Modern toughened steels—their properties and advantages,” *Biuletyn Instytutu Spawalnictwa*, no. 02, pp. 25–36, 2012.
- [55] P. Kah, H. Latifi, R. Suoranta, J. Martikainen, and M. Pirinen, “Usability of arc types in industrial welding,” *International Journal of Mechanical and Materials Engineering*, vol. 9, no. 1, pp. 1–12, 2014.
- [56] D. Iordachescu and L. Quintino, “Steps toward a new classification of metal transfer in gas metal arc welding,” *Journal of Materials Processing Technology*, vol. 202, no. 1–3, pp. 391–397, 2008.
- [57] H. Cramer, L. Baum, and S. Pommer, “Überblick zu modernen Lichtbogenprozessen und deren Werkstoffübergängen beim MSG-Schweißen,” *DVS-Berichte*, no. 275, pp. 232–237, 2011.
- [58] B. Budig, “EWM-forceArc - ein kraftvolles Werkzeug zum MIG-/MAG-Schweißen,” *Erstveröffentlichung DVS-Jahrbuch*, 2005.
- [59] M. de Dompablo, “New solutions in coldArc and forceArc welding technology,” *Welding International*, vol. 27, no. 1, pp. 24–29, 2013.
- [60] Y. Ito and M. Nakanishi, “Study on charpy impact properties of welds (report 2) : Relationship between charpy impact properties and control of micro structures of weld metals,” *Journal of the Japan welding society*, vol. 44, no. 10, pp. 815–821, 1975.
- [61] Y. Ito and M. Nakanishi, “Study on charpy impact properties of weld metal with submerged arc welding,” *Sumitomo Search*, no. 15, pp. 42–62, 1976.
- [62] Ø. Grong and D. K. Matlock, “Microstructural development in mild and low-alloy steel weld metals,” *International Metals Reviews*, vol. 31, no. 1, pp. 27–48, 1986.
- [63] D. J. Abson and R. J. Pargeter, “Factors influencing as-deposited strength, microstructure, and

- toughness of manual metal arc welds suitable for C-Mn steel fabrications," *International Metals Reviews*, vol. 31, no. 1, pp. 141–196, 1986.
- [64] S. S. Babu and H. K. D. H. Bhadeshia, "Mechanism of the transition from bainite to acicular ferrite," *Materials Transactions Jim*, vol. 32, no. 8, pp. 679–688, 1991.
- [65] S. S. Babu, "The mechanism of acicular ferrite in weld deposits," *Current Opinion in Solid State and Materials Science*, vol. 8, no. 3–4, pp. 267–278, 2004.
- [66] S. S. Babu and S. A. David, "Inclusion formation and microstructure evolution in low alloy steel welds," *ISIJ International*, vol. 42, no. 12, pp. 1344–1353, 2002.
- [67] A. F. Gourgues, H. M. Flower, and T. C. Lindley, "Electron backscattering diffraction study of acicular ferrite, bainite, and martensite steel microstructures," *Materials Science and Technology*, vol. 16, no. 1, pp. 26–40, 2000.
- [68] M. Díaz-Fuentes, A. Iza-Mendia, and I. Gutiérrez, "Analysis of different acicular ferrite microstructures in low-carbon steels by electron backscattered diffraction. study of their toughness behavior," *Metallurgical and Materials Transactions A*, vol. 34, no. 11, pp. 2505–2516, 2003.
- [69] C. van der Eijk, G. Ø., and J. Walmsley, "Mechanisms of inclusion formation in low alloy steels deoxidised with titanium," *Materials Science and Technology*, vol. 16, no. 1, pp. 55–64, 2000.
- [70] H. K. D. H. Bhadeshia, *Bainite in steels*. Institute of Materials, London, U.K., 2001.
- [71] J. Yang and H. Bhadeshia, "Acicular ferrite transformation in alloy-steel weld metals," *Journal of Materials Science*, vol. 26, no. 3, pp. 839–845, 1991.
- [72] R. A. Ricks, P. R. Howell, and G. S. Barritte, "The nature of acicular ferrite in HSLA steel weld metals," *Journal of Materials Science*, vol. 17, no. 3, pp. 732–740, 1982.
- [73] A. Borgenstam, M. Hillert, and J. Ågren, "Metallographic evidence of carbon diffusion in the growth of bainite," *Acta Materialia*, vol. 57, no. 11, pp. 3242 – 3252, 2009.
- [74] H. Bhadeshia, "The lower bainite transformation and the significance of carbide precipitation," *Acta Metallurgica*, vol. 28, no. 8, pp. 1103 – 1114, 1980.
- [75] G. Thewlis, "Materials perspective - classification and quantification of microstructures in steels," *Materials Science and Technology*, vol. 20, no. 2, pp. 143–160, 2004.
- [76] A. R. Mills, G. Thewlis, and J. A. Whiteman, "Nature of inclusions in steel weld metals and their influence on formation of acicular ferrite," *Materials Science and Technology*, vol. 3, no. 12, pp. 1051–1061, 1987.
- [77] S. St-Laurent and G. L'Espérance, "Effects of chemistry, density and size distribution of inclusions on the nucleation of acicular ferrite of C-Mn steel shielded-metal-arc-welding weldments," *Materials Science and Engineering: A*, vol. 149, no. 2, pp. 203–216, 1992.
- [78] S. Zhang, N. Hattori, M. Enomoto, and T. Tarui, "Ferrite nucleation at ceramic/austenite interfaces," *ISIJ International*, vol. 36, no. 10, pp. 1301–1309, 1996.
- [79] E. Pagounis and V. K. Lindroos, "The role of internal stresses on the phase transformation of iron alloys," *Scripta Materialia*, vol. 37, no. 1, pp. 65–69, 1997.
- [80] I. Madariaga and I. Gutierrez, "Role of the particle–matrix interface on the nucleation of acicular ferrite in a medium carbon microalloyed steel," *Acta materialia*, vol. 47, no. 3, pp. 951–960, 1999.
- [81] T.-K. Lee, H. J. Kim, B. Y. Kang, and S. K. Hwang, "Effect of inclusion size on the nucleation of acicular ferrite in welds," *ISIJ International*, vol. 40, no. 12, pp. 1260–1268, 2000.
- [82] J. H. Shim, Y. J. Oh, J. Y. Suh, Y. W. Cho, J. D. Shim, J. S. Byun, and D. N. Lee, "Ferrite nucleation potency of non-metallic inclusions in medium carbon steels," *Acta Materialia*, vol. 49, no. 12, pp. 2115–2122, 2001.

- [83] J. S. Byun, J. H. Shim, Y. W. Cho, and D. N. Lee, "Non-metallic inclusion and intragranular nucleation of ferrite in Ti-killed C-Mn steel," *Acta Materialia*, vol. 51, no. 6, pp. 1593–1606, 2003.
- [84] J. Zachrisson, J. Börjesson, and L. Karlsson, "Role of inclusions in formation of high strength steel weld metal microstructures," *Science and Technology of Welding and Joining*, vol. 18, no. 7, pp. 603–609, 2013.
- [85] Y. Komizo and H. Terasaki, "Optical observation of real materials using laser scanning confocal microscopy part 2-direct observation of ferrite nucleation sites in weld metal and heat affected zone," *Science and Technology of Welding and Joining*, vol. 16, no. 1, pp. 61–67, 2011.
- [86] D. Zhang, H. Terasaki, and Y. Komizo, "In situ observation of the formation of intragranular acicular ferrite at non-metallic inclusions in C-Mn steel," *Acta Materialia*, vol. 58, no. 4, pp. 1369–1378, 2010.
- [87] A. Klucken, A. and Ø. Grong, "Mechanisms of inclusion formation in Al- Ti- Si- Mn deoxidized steel weld metals," *Metallurgical Transactions A*, vol. 20, no. 8, pp. 1335–1349, 1989.
- [88] N. Mori, H. Homma, S. Okita, and M. Wakabayashi, "Mechanism of notch toughness improvement in weld metals containing Ti and B," *Journal Of the Japan Welding Society*, vol. 50, no. 2, pp. 174–181, 1981.
- [89] G. Thewlis, "Transformation kinetics of ferrous weld metals," *Materials Science and Technology*, vol. 10, no. 2, pp. 110–125, 1994.
- [90] K. Yamamoto, T. Hasegawa, and J.-i. Takamura, "Effect of boron on intra-granular ferrite formation in Ti-oxide bearing steels," *ISIJ International*, vol. 36, no. 1, pp. 80–86, 1996.
- [91] H. Mabuchi, R. Uemori, and M. Fujioka, "The role of Mn depletion in intra-granular ferrite transformation in the heat affected zone of welded joints with large heat input in structural steels," *ISIJ International*, vol. 36, no. 11, pp. 1406–1412, 1996.
- [92] J. M. Gregg and H. K. D. H. Bhadeshia, "Bainite nucleation from mineral surfaces," *Acta metallurgica et materialia*, vol. 42, no. 10, pp. 3321–3330, 1994.
- [93] G. Miyamoto, T. Shinyoshi, J. Yamaguchi, T. Furuhashi, T. Maki, and R. Uemori, "Crystallography of intragranular ferrite formed on (MnS + V(C, N)) complex precipitate in austenite," *Scripta Materialia*, vol. 48, no. 4, pp. 371–377, 2003.
- [94] F. Barbaro, P. Krauklis, and K. Easterling, "Formation of acicular ferrite at oxide particles in steels," *Materials science and technology*, vol. 5, no. 11, pp. 1057–1068, 1989.
- [95] B. Kim, S. Uhm, C. Lee, J. Lee, and Y. An, "Effects of inclusions and microstructures on impact energy of high heat-input submerged-arc-weld metals," *Journal of Engineering Materials and Technology*, vol. 127, no. 2, pp. 204–213, 2005.
- [96] A. Takada, H. Terasaki, and Y. Komizo, "Effect of aluminium content on acicular ferrite formation in low carbon steel weld metals," *Science and Technology of Welding and Joining*, vol. 18, no. 2, pp. 91–97, 2013.
- [97] D. S. Sarma, A. V. Karasev, and P. G. Jonsson, "On the role of non-metallic inclusions in the nucleation of acicular ferrite in steels," *ISIJ International*, vol. 49, no. 7, pp. 1063–1074, 2009.
- [98] J. Byun, J. H. Shim, and Y. W. Cho, "Influence of Mn on microstructural evolution in Ti-killed C-Mn steel," *Scripta Materialia*, vol. 48, no. 4, pp. 449–454, 2003.
- [99] S. K. Liu and J. Zhang, "The influence of the Si and Mn concentrations on the kinetics of the bainite transformation in Fe-C-Si-Mn alloys," *Metallurgical Transactions A*, vol. 21, no. 6, pp. 1517–1525, 1990.
- [100] Y. Peng, W. Chen, and Z. Xu, "Study of high toughness ferrite wire for submerged arc welding

- of pipeline steel," *Materials characterization*, vol. 47, no. 1, pp. 67–73, 2001.
- [101] S. Ohkita and Y. Horii, "Recent development in controlling the microstructure and properties of low alloy steel weld metals," *ISIJ International*, vol. 35, no. 10, pp. 1170–1182, 1995.
- [102] G. M. Evans and N. Bailey, *Metallurgy of basic weld metal*. Woodhead Publishing, 1997.
- [103] M. Takahashi, "Recent progress: kinetics of the bainite transformation in steels," *Current Opinion in Solid State and Materials Science*, vol. 8, no. 3-4, pp. 213–217, 2004.
- [104] G. Shiflet and R. Hackenberg, "Partitioning and the growth of bainite," *Scripta Materialia*, vol. 47, no. 3, pp. 163–167, 2002.
- [105] D. Quidort and Y. Bréchet, "The role of carbon on the kinetics of bainite transformation in steels," *Scripta Materialia*, vol. 47, no. 3, pp. 151–156, 2002.
- [106] O. Ko and S. A. Cottrell, "The formation of bainite," *Journal of the Iron and Steel Institute*, no. 172, pp. 307–313, 1952.
- [107] M. Takahashi and H. K. D. H. Bhadeshia, "Model for transition from upper to lower bainite," *Materials Science and Technology*, vol. 6, no. 7, pp. 592–603, 1990.
- [108] E. Swallow and H. Bhadeshia, "High resolution observations of displacements caused by bainitic transformation," *Materials Science and Technology*, vol. 12, no. 2, pp. 121–125, 1996.
- [109] F. G. Caballero, M. K. Miller, C. Garcia-Mateo, and J. Cornide, "New experimental evidence of the diffusionless transformation nature of bainite," *Journal of Alloys and Compounds*, vol. 577, pp. S626–S630, 2013.
- [110] H. J. Stone, M. J. Peet, H. K. D. H. Bhadeshia, P. J. Withers, S. S. Babu, and E. D. Specht, "Synchrotron x-ray studies of austenite and bainitic ferrite," *Proceedings of the Royal Society a-Mathematical Physical and Engineering Sciences*, vol. 464, no. 2092, pp. 1009–1027, 2008.
- [111] D. Quidort and Y. J. M. Brechet, "Isothermal growth kinetics of bainite in 0.5% C steels," *Acta Materialia*, vol. 49, no. 20, pp. 4161–4170, 2001.
- [112] F. G. Caballero and H. K. D. H. Bhadeshia, "Very strong bainite," *Current Opinion in Solid State and Materials Science*, vol. 8, no. 3-4, pp. 251–257, 2004.
- [113] M. Y. Sherif, C. G. Mateo, T. Sourmail, and H. K. D. H. Bhadeshia, "Stability of retained austenite in TRIP-assisted steels," *Materials Science and Technology*, vol. 20, no. 3, pp. 319–322, 2004.
- [114] S. Zajac, V. Schwinn, and K. Tacke, "Characterisation and quantification of complex bainitic microstructures in high and ultra-high strength linepipe steels," in *Materials Science Forum*, vol. 500, pp. 387–394, 2005.
- [115] H. K. Bhadeshia, "Local brittle zones and the role of niobium," in *Materials Science Forum*, vol. 783, pp. 2129–2135, Trans Tech Publ, 2014.
- [116] A. Lambert-Perlade, A. F. Gourgues, J. Besson, T. Sturel, and A. Pineau, "Mechanisms and modeling of cleavage fracture in simulated heat-affected zone microstructures of a high-strength low alloy steel," *Metallurgical and Materials Transactions A*, vol. 35, no. 13, pp. 1039–1053, 2004.
- [117] B. C. Kim, S. Lee, N. J. Kim, and D. Y. Lee, "Microstructure and local brittle zone phenomena in high-strength low-alloy steel welds," *Metallurgical Transactions A*, vol. 22, no. 1, pp. 139–149, 1991.
- [118] B. C. De Cooman, "Structure-properties relationship in TRIP steels containing carbide-free bainite," *Current Opinion in Solid State and Materials Science*, vol. 8, no. 3-4, pp. 285–303, 2004.
- [119] S. Morito, H. Yoshida, T. Maki, and X. Huang, "Effect of block size on the strength of lath

- martensite in low carbon steels," *Materials Science and Engineering: A*, vol. 438, pp. 237–240, 2006.
- [120] P. Payson and C. H. Savage, "Martensite reactions in alloy steels," *Trans. ASM*, vol. 33, pp. 261–280, 1944.
- [121] R. Grange and H. Stewart, "The temperature range of martensite formation," *Trans. AIME*, vol. 167, pp. 467–501, 1946.
- [122] W. Steven and A. Haynes, "The temperature of formation of martensite and bainite in low-alloy steels," *Journal of the Iron and Steel Institute*, vol. 183, no. 8, pp. 349–359, 1956.
- [123] K. W. Andrews, "Empirical formulae for the calculation of some transformation temperatures," *J.I.S.I.*, no. 203, pp. 721–727, 1965.
- [124] C. Capdevila, F. Garc Caballero, and C. Garc de Andrs, "Analysis of effect of alloying elements on martensite start temperature of steels," *Materials Science and Technology*, vol. 586, pp. 581–586, 2003.
- [125] S.-J. Lee and K.-S. Park, "Prediction of martensite start temperature in alloy steels with different grain sizes," *Metallurgical and Materials Transactions A*, vol. 44, no. 8, pp. 3423–3427, 2013.
- [126] C. H. Young and H. K. D. H. Bhadeshia, "Strength of mixtures of bainite and martensite," *Materials Science and Technology*, vol. 10, no. 3, pp. 209–214, 1994.
- [127] R. C. Thomson and M. K. Miller, "Carbide precipitation in martensite during the early stages of tempering Cr- and Mo-containing low alloy steels," *Acta Materialia*, vol. 46, no. 6, pp. 2203–2213, 1998.
- [128] R. A. Grange, C. R. Hribal, and L. F. Porter, "Hardness of tempered martensite in carbon and low-alloy steels," *Metallurgical Transactions A*, vol. 8, no. 11, pp. 1775–1785, 1977.
- [129] S. I. Kwun and R. A. Fournelle, "Low cycle fatigue behavior of a quenched and tempered niobium bearing HSLA steel," *Metallurgical Transactions A*, vol. 11, no. 8, pp. 1429–1437, 1980.
- [130] I. Robertson, "Temper resistance of pressure hull steel microalloyed with niobium, titanium, and vanadium," *Materials Science and Technology*, vol. 9, no. 11, pp. 1031–1036, 1993.
- [131] S. K. Dhua, D. Mukerjee, and D. S. Sarma, "Influence of tempering on the microstructure and mechanical properties of HSLA-100 steel plates," *Metallurgical and Materials Transactions A*, vol. 32, no. 9, pp. 2259–2270, 2001.
- [132] V. H. Baltazar Hernandez, S. S. Nayak, and Y. Zhou, "Tempering of martensite in dual-phase steels and its effects on softening behavior," *Metallurgical and Materials Transactions A*, vol. 42, no. 10, pp. 3115–3129, 2011.
- [133] E. Biro, J. R. McDermid, J. D. Embury, and Y. Zhou, "Softening kinetics in the subcritical heat-affected zone of dual-phase steel welds," *Metallurgical and Materials Transactions A*, vol. 41A, no. 9, pp. 2348–2356, 2010.
- [134] A. C. Hunt, A. O. Kluken, and G. R. Edwards, "Heat input and dilution effects in microalloyed steel weld metals," *Welding Journal*, vol. 73, no. 1, pp. S9–S15, 1994.
- [135] F. G. Caballero, J. Chao, J. Cornide, C. Garcia-Mateo, M. J. Santofimia, and C. Capdevila, "Toughness deterioration in advanced high strength bainitic steels," *Materials Science and Engineering: A*, vol. 525, no. 1-2, pp. 87–95, 2009.
- [136] Ø. Grong, T. A. Siewert, G. P. Martins, and D. L. Olson, "A model for the silicon-manganese deoxidation of steel weld metals," *Metallurgical and Materials Transactions A*, vol. 17, no. 10, pp. 1797–1807, 1986.
- [137] S. Liu and D. Olson, "The influence of inclusion chemical composition on weld metal microstructure," *Journal of Materials engineering*, vol. 9, no. 3, pp. 237–251, 1987.

- [138] S. H. Kim, C. Y. Kang, and K. S. Bang, "Weld metal impact toughness of electron beam welded 9% Ni steel," *Journal of Materials Science*, vol. 36, no. 5, pp. 1197–1200, 2001.
- [139] Z. Zhang and R. A. Farrar, "Influence of Mn and Ni on the microstructure and toughness of C-Mn-Ni weld metals," *Welding Journal*, vol. 76, no. 5, p. 183, 1997.
- [140] E. Keehan, L. Karlsson, and H. O. Andrén, "Influence of carbon, manganese and nickel on microstructure and properties of strong steel weld metals: Part 1 effect of nickel content," *Science and Technology of Welding and Joining*, vol. 11, no. 1, pp. 1–8, 2006.
- [141] K. Banerjee, M. Militzer, M. Perez, and X. Wang, "Nonisothermal austenite grain growth kinetics in a microalloyed X80 linepipe steel," *Metallurgical and Materials Transactions A*, vol. 41A, no. 12, pp. 3161–3172, 2010.
- [142] H. Mohrbacher, "Principal effects of Mo in HSLA steels and cross effects with microalloying elements," *Central Iron and Steel Research Institute (CISRI)*, pp. 75–96, 2010.
- [143] E. A. Metzbower, J. J. DeLoach, S. H. Lalam, and H. K. D. H. Bhadeshia, "Analysis of toughness of welding alloys for high strength low alloy shipbuilding steels," *Science and Technology of Welding and Joining*, vol. 6, no. 6, pp. 368–374, 2001.
- [144] A. DeArdo, J. Gray, and L. Meyer, "Fundamental metallurgy of niobium in steel," *Niobium*, pp. 685–759, 1981.
- [145] C. Fossaert, G. Rees, T. Maurickx, and H. K. D. H. Bhadeshia, "The effect of niobium on the hardenability of microalloyed austenite," *Metallurgical and Materials Transactions A*, vol. 26, no. 1, pp. 21–30, 1995.
- [146] H. L. Andrade, M. G. Akben, and J. J. Jonas, "Effect of molybdenum, niobium, and vanadium on static recovery and recrystallization and on solute strengthening in microalloyed steels," *Metallurgical Transactions A*, vol. 14, no. 10, pp. 1967–1977, 1983.
- [147] L. Zhang, A. Pittner, T. Michael, M. Rhode, and T. Kannengiesser, "Effect of cooling rate on microstructure and properties of microalloyed HSLA steel weld metals," *Science and Technology of Welding and Joining*, vol. 20, no. 5, pp. 371–377, 2015.
- [148] M. M. Watson, P. L. Harrison, and R. A. Farrar, "How niobium influence SA mild steel weld metals part 1: microstructure, mechanical properties," *Welding and Metal Fabrication*, vol. 39, no. 3, pp. 101–108, 1981.
- [149] R. Farrar and P. Harrison, "Acicular ferrite in carbon-manganese weld metals: an overview," *Journal of Materials Science*, vol. 22, no. 11, pp. 3812–3820, 1987.
- [150] B. Beidokhti, A. H. Koukabi, and A. Dolati, "Effect of titanium addition on the microstructure and inclusion formation in submerged arc welded HSLA pipeline steel," *Journal of Materials Processing Technology*, vol. 209, no. 8, pp. 4027–4035, 2009.
- [151] B. Beidokhti, A. H. Koukabi, and A. Dolati, "Influences of titanium and manganese on high strength low alloy SAW weld metal properties," *Materials Characterization*, vol. 60, no. 3, pp. 225–233, 2009.
- [152] Z. X. Zhu, L. Kuzmikova, M. Marimuthu, H. J. Li, and F. Barbaro, "Role of Ti and N in line pipe steel welds," *Science and Technology of Welding and Joining*, vol. 18, no. 1, pp. 1–10, 2013.
- [153] H. H. Jin, J. H. Shim, Y. W. Cho, and H. C. Lee, "Formation of intragranular acicular ferrite grains in a Ti-containing low carbon steel," *ISIJ International*, vol. 43, no. 7, pp. 1111–1113, 2003.
- [154] S. Zajac, "Precipitation and grain refinement in vanadium-containing steels," in *Proceedings International Symposium 2001 on Vanadium Application Technology*, pp. 62–82, 2001.
- [155] F. Ishikawa, T. Takahashi, and T. Ochi, "Intragranular ferrite nucleation in medium-carbon

- vanadium steels," *Metallurgical and Materials Transactions A*, vol. 25, no. 5, pp. 929–936, 1994.
- [156] K. He and D. V. Edmonds, "Formation of acicular ferrite and influence of vanadium alloying," *Materials Science and Technology*, vol. 18, no. 3, pp. 289–296, 2002.
- [157] R. Willms, "High strength steel for steel constructions," *Nordic Steel*, 2009.
- [158] A. Ohta, N. Suzuki, Y. Maeda, K. Hiraoka, and T. Nakamura, "Superior fatigue crack growth properties in newly developed weld metal," *International Journal of Fatigue*, vol. 21, pp. S113–S118, 1999.
- [159] S. Zenitani, N. Hayakawa, J. Yamamoto, K. Hiraoka, Y. Morikage, T. Kubo, K. Yasuda, and K. Amano, "Development of new low transformation temperature welding consumable to prevent cold cracking in high strength steel welds," *Science and Technology of Welding and Joining*, vol. 12, no. 6, pp. 516–522, 2007.
- [160] A. Kromm, T. Kannengiesser, and J. Gibmeier, "In situ studies of phase transformation and residual stresses in LTT alloys during welding using synchrotron radiation," in *In-situ Studies with Photons, Neutrons and Electrons Scattering*, pp. 13–26, Springer, 2010.
- [161] O. Akselsen, Ø. Grong, N. Ryum, and N. Christensen, "HAZ grain growth mechanisms in welding of low carbon microalloyed steels," *Acta Metallurgica*, vol. 34, no. 9, pp. 1807–1815, 1986.
- [162] M. Ashby and K. E. Easterling, "A first report on diagrams for grain growth in welds," *Acta metallurgica*, vol. 30, no. 11, pp. 1969–1978, 1982.
- [163] J. C. Ion, K. E. Easterling, and M. F. Ashby, "A second report on diagrams of microstructure and hardness for heat-affected zones in welds," *Acta Metallurgica*, vol. 32, no. 11, pp. 1949–1962, 1984.
- [164] S. Mishra and T. DebRoy, "Non-isothermal grain growth in metals and alloys," *Materials science and technology*, vol. 22, no. 3, pp. 253–278, 2006.
- [165] M. Shome, O. P. Gupta, and O. N. Mohanty, "A modified analytical approach for modelling grain growth in the coarse grain HAZ of HSLA steels," *Scripta Materialia*, vol. 50, no. 7, pp. 1007–1010, 2004.
- [166] J. W. Cahn, "The impurity-drag effect in grain boundary motion," *Acta Metallurgica*, vol. 10, no. 9, pp. 789–798, 1962.
- [167] H. Hu and B. B. Rath, "On the time exponent in isothermal grain growth," *Metallurgical Transactions*, vol. 1, no. 11, pp. 3181–3184, 1970.
- [168] I. Andersen and Ø. Grong, "Analytical modelling of grain growth in metals and alloys in the presence of growing and dissolving precipitates i. normal grain growth," *Acta metallurgica et materialia*, vol. 43, no. 7, pp. 2673–2688, 1995.
- [169] J. Moon, J. Lee, and C. Lee, "Prediction for the austenite grain size in the presence of growing particles in the weld HAZ of Ti-microalloyed steel," *Materials Science and Engineering: A*, vol. 459, no. 1-2, pp. 40–46, 2007.
- [170] P. R. Rios, "Overview no. 62: A theory for grain boundary pinning by particles," *Acta Metallurgica*, vol. 35, no. 12, pp. 2805–2814, 1987.
- [171] S. Uhm, J. Moon, C. Lee, J. Yoon, and B. Lee, "Prediction model for the austenite grain size in the coarse grained heat affected zone of Fe-C-Mn steels: considering the effect of initial grain size on isothermal growth behavior," *ISIJ International*, vol. 44, no. 7, pp. 1230–1237, 2004.
- [172] J. Strid and K. E. Easterling, "On the chemistry and stability of complex carbides and nitrides in microalloyed steels," *Acta Metallurgica*, vol. 33, no. 11, pp. 2057–2074, 1985.
- [173] E. T. Turkdogan, "Causes and effects of nitride and carbonitride precipitation during continuous casting," *Iron and Steelmaker*, vol. 16, no. 5, pp. 61–75, 1989.

- [174] G. R. Wang, T. W. Lau, G. C. Weatherly, and T. H. North, "Weld thermal cycles and precipitation effects in Ti-V-containing HSLA steels," *Metallurgical Transactions A*, vol. 20, no. 10, pp. 2093–2100, 1989.
- [175] J. Speer, J. Michael, and S. Hansen, "Carbonitride precipitation in niobium/vanadium microalloyed steels," *Metallurgical Transactions A*, vol. 18, no. 2, pp. 211–222, 1987.
- [176] B. Loberg, A. Nordgren, J. Strid, and K. E. Easterling, "The role of alloy composition on the stability of nitrides in Ti-microalloyed steels during weld thermal cycles," *Metallurgical Transactions A*, vol. 15, no. 1, pp. 33–41, 1984.
- [177] R. M. Poths, R. L. Higginson, and E. J. Palmiere, "Complex precipitation behaviour in a microalloyed plate steel," *Scripta Materialia*, vol. 44, no. 1, pp. 147–151, 2001.
- [178] A. J. Craven, K. He, L. A. J. Garvie, and T. N. Baker, "Complex heterogeneous precipitation in titanium-niobium microalloyed Al-killed HSLA steels- (Ti,Nb)(C,N) particles," *Acta Materialia*, vol. 48, no. 15, pp. 3857–3868, 2000.
- [179] K. Poorhaydari and D. Ivey, "Precipitate alterations in the heat-affected zone of a grade 100 microalloyed steel," *Journal of Materials Science*, vol. 46, no. 14, pp. 4953–4963, 2011.
- [180] J. Agren, "Kinetics of carbide dissolution," *Scand. J. Metall.*, vol. 19, no. 1, pp. 2–8, 1990.
- [181] M. G. Burke, L. J. Cuddy, J. Piller, and M. K. Miller, "Combined APFIM–TEM study of Nb(CN) precipitation in HSLA steel," *Materials Science and Technology*, vol. 4, no. 2, pp. 113–116, 1988.
- [182] J. Lu, O. Omotoso, J. B. Wiskel, D. Ivey, and H. Henein, "Strengthening mechanisms and their relative contributions to the yield strength of microalloyed steels," *Metallurgical and Materials Transactions A*, vol. 43, no. 9, pp. 3043–3061, 2012.
- [183] J. D. Farren, *Microstructural Evolution and Mechanical Properties of Fusion Welds and Simulated Heat-Affected Zones in an Iron-Copper Based Multi-Component Steel*. PhD thesis, Lehigh University, 2012.
- [184] R. E. Dolby, "HAZ toughness of structural and pressure vessel steels - improvement and prediction," *Welding Journal Research Supplement*, pp. 225–238, August 1979.
- [185] S. F. Medina, M. Chapa, P. Valles, A. Quispe, and M. I. Vega, "Influence of Ti and N contents on austenite grain control and precipitate size in structural steels," *ISIJ International*, vol. 39, no. 9, pp. 930–936, 1999.
- [186] L. Zhang and T. Kannengiesser, "Austenite grain growth and microstructure control in simulated heat affected zones of microalloyed HSLA steel," *Materials Science and Engineering: A*, vol. 613, pp. 326 – 335, 2014.
- [187] J. Du, "Examination of the effect of TiN particles and grain size on the charpy impact transition temperature in steels," Master's thesis, University of Birmingham, July 2012.
- [188] R. J. Hattingh and G. Pienaar, "Weld HAZ embrittlement of Nb containing C-Mn steels," *International Journal of Pressure Vessels and Piping*, vol. 75, no. 9, pp. 661–677, 1998.
- [189] J. Yang, C. Huang, and C. Chiou, "Microstructures of heat-affected zone in niobium containing steels," *Materials Transactions, JIM(Japan)*, vol. 40, no. 3, pp. 199–208, 1999.
- [190] Y. Li, D. Crowther, M. Green, P. Mitchell, and T. Baker, "The effect of vanadium and niobium on the properties and microstructure of the intercritically reheated coarse grained heat affected zone in low carbon microalloyed steels," *ISIJ International*, vol. 41, no. 1, pp. 46–55, 2001.
- [191] B. Hanhold, S. S. Babu, and G. Cola, "Investigation of heat affected zone softening in armour steels part 1 - phase transformation kinetics," *Science and Technology of Welding and Joining*, vol. 18, no. 3, pp. 247–252, 2013.

- [192] K. Satoh and M. Toyoda, "Static strength of welded plates including soft interlayer under tension across a weld line," *Transactions of the Japan Welding Society*, vol. 1, no. 2, pp. 10–17, 1970.
- [193] L. Zhang and T. Kannengiesser, "HAZ softening in Nb-, Ti- and Ti+ V-bearing quenched and tempered steel welds," *Welding in the World*, vol. 60, no. 2, pp. 177–184, 2016.
- [194] D. M. Rodrigues, L. F. Menezes, A. Loureiro, and J. V. Fernandes, "Numerical study of the plastic behaviour in tension of welds in high strength steels," *International Journal of Plasticity*, vol. 20, no. 1, pp. 1–18, 2004.
- [195] K. Bang and W. Kim, "Estimation and prediction of HAZ softening in thermomechanically controlled-rolled and accelerated-cooled steel," *Welding Journal (New York)*, vol. 81, no. 8, pp. 174–S, 2002.
- [196] J. Bassett, "Laser welding of high hardness armour steel," *Science and Technology of Welding and Joining*, vol. 3, no. 5, pp. 244–248, 1998.
- [197] J. Koo, M. Luton, N. Bangaru, R. Petkovic, D. Fairchild, C. Petersen, H. Asahi, T. Hara, Y. Terada, M. Sugiyama, *et al.*, "Metallurgical design of ultra-high strength steels for gas pipelines," in *The Thirteenth International Offshore and Polar Engineering Conference*, pp. 10–18, International Society of Offshore and Polar Engineers, 2003.
- [198] T. Mohandas, G. Madhusudan Reddy, and B. Satish Kumar, "Heat-affected zone softening in high-strength low-alloy steels," *Journal of Materials Processing Technology*, vol. 88, no. 1, pp. 284–294, 1999.
- [199] W. Maurer, W. Ernst, R. Rauch, S. Kapl, A. Pohl, T. Krüssel, R. Vallant, and N. Enzinger, "Electron beam welding of a TMCP steel with 700 MPa yield strength," *Welding in the World*, vol. 56, no. 9-10, pp. 85–94, 2012.
- [200] J. R. Davis *et al.*, *ASM specialty handbook: heat-resistant materials*. ASM International, 1997.
- [201] M. Shome, O. Gupta, and O. Mohanty, "Effect of simulated thermal cycles on the microstructure of the heat-affected zone in HSLA-80 and HSLA-100 steel plates," *Metallurgical and Materials Transactions A*, vol. 35, no. 3, pp. 985–996, 2004.
- [202] R. Ito, K. Hiraoka, and C. Shiga, "Softening characteristics in ultra-narrow gap GMA welded joints of ultra-fine grained steel," *Science and Technology of Welding and Joining*, vol. 10, no. 4, pp. 468–474, 2005.
- [203] A. A. Syed, A. Pittner, M. Rethmeier, and A. De, "Modeling of gas metal arc welding process using an analytically determined volumetric heat source," *ISIJ International*, vol. 53, no. 4, pp. 698–703, 2013.
- [204] DIN EN ISO 17636-1:2013, "Non-destructive testing of welds - radiographic testing - part 1: X- and gamma-ray techniques with film (ISO 17636-1:2013)," 2013.
- [205] DIN EN ISO 643, "Steels - Micrographic determination of the apparent grain size (ISO 643:2012); German version EN ISO 643:2012."
- [206] G. E. Lloyd, "Atomic number and crystallographic contrast images with the sem: a review of backscattered electron techniques," *Mineralogical Magazine*, vol. 51, no. 359, pp. 3–19, 1987.
- [207] P. J. Goodhew, J. Humphreys, and B. R., *Electron microscopy and analysis*. CRC Press, 2000.
- [208] S. I. Wright, M. M. Nowell, R. de Kloe, P. Camus, and T. Rampton, "Electron imaging with an EBSD detector," *Ultramicroscopy*, vol. 148, pp. 132 – 145, 2015.
- [209] D. B. Williams and C. B. Carter, *The transmission electron microscope*. Springer, 1996.
- [210] O. L. Krivanek, M. K. Kundmann, and K. Kimoto, "Spatial resolution in EFTEM elemental maps," *Journal of Microscopy*, vol. 180, no. 3, pp. 277–287, 1995.
- [211] P. Warbichler, F. Hofer, P. Hofer, and E. Letofsky, "On the application of energy-filtering TEM

- in materials science: III. Precipitates in steel," *Micron*, vol. 29, no. 1, pp. 63 – 72, 1998.
- [212] I. Yoichi, S. Genichi, S. Masaaki, and S. Daisuke, "Visualization of fine precipitates TiN in low-alloy steel by using energy-filtered transmission electron microscopy," *Tetsu-to-Hagane*, vol. 93, no. 2, pp. 163–168, 2007.
- [213] N. D. Browning, D. J. Wallis, P. D. Nellist, and S. J. Pennycook, "EELS in the STEM: Determination of materials properties on the atomic scale," *Micron*, vol. 28, no. 5, pp. 333–348, 1997.
- [214] DIN EN ISO 9015-1:2011-05, "Zerstörende Prüfung von Schweißverbindungen an metallischen Werkstoffen - Härteprüfung - Teil 1: Härteprüfung für Lichtbogenschweißverbindungen (ISO 9015-1:2001); Deutsche Fassung EN ISO 9015-1:2011."
- [215] DIN EN ISO 6892-1:2009-12, "Metallische Werkstoffe - Zugversuch - Teil 1: Prüfverfahren bei Raumtemperatur (ISO 6892-1:2009); Deutsche Fassung EN ISO 6892-1:2009."
- [216] DIN EN ISO 4136:2013-02, "Zerstörende Prüfung von Schweißverbindungen an metallischen Werkstoffen - Querzugversuch (ISO 4136:2012); Deutsche Fassung EN ISO 4136:2012."
- [217] DIN EN ISO 148-1:2011, "Metallic materials - Charpy pendulum impact test - Part 1: Test method (ISO 148-1:2009); German version EN ISO 148-1:2010," 2011.
- [218] DIN EN ISO 9016:2013-02, "Zerstörende Prüfung von Schweißverbindungen an metallischen Werkstoffen - Kerbschlagbiegeversuch - Probenlage, Kerbrichtung und Beurteilung (ISO 9016:2012); Deutsche Fassung EN ISO 9016:2012."
- [219] J. O. Andersson, T. Helander, L. Höglund, P. Shi, and B. Sundman, "Thermo-Calc & DICTRA, computational tools for materials science," *Calphad*, vol. 26, no. 2, pp. 273 – 312, 2002.
- [220] W. G. Johnston and J. J. Gilman, "Dislocation velocities, dislocation densities, and plastic flow in lithium fluoride crystals," *Journal of Applied Physics*, vol. 30, no. 2, pp. 129–144, 1959.
- [221] S. Vervynckt, P. Thibaux, and K. Verbeken, "Effect of niobium on the microstructure and mechanical properties of hot rolled microalloyed steels after recrystallization-controlled rolling," *Metals and Materials International*, vol. 18, no. 1, pp. 37–46, 2012.
- [222] S. Rešković and I. Jandrić, "Influence of niobium on the beginning of the plastic flow of material during cold deformation," *The Scientific World Journal*, vol. 2013, 2013.
- [223] C. Yu, P. Kao, and C. Chang, "Transition of tensile deformation behaviors in ultrafine-grained aluminum," *Acta Materialia*, vol. 53, no. 15, pp. 4019 – 4028, 2005.
- [224] A. Ghosh, A. Ray, D. Chakrabarti, and C. L. Davis, "Cleavage initiation in steel: Competition between large grains and large particles," *Materials Science and Engineering: A*, vol. 561, pp. 126–135, 2013.
- [225] A. H. Cottrell and B. A. Bilby, "Dislocation theory of yielding and strain ageing of iron," *Proceedings of the Physical Society. Section A*, vol. 62, no. 1, p. 49, 1949.
- [226] K. Tomimura, H. Nagamori, S. Takaki, and Y. Tokunaga, "Tensile deformation behavior in metastable austenitic stainless steel having ultra fine grain structure," *Journal of the Japan Institute of Metals*, vol. 55, no. 4, pp. 376–382, 1991.
- [227] R. B. Punch, *Toughness enhancement of high strength low alloy strip steels*. PhD thesis, University of Birmingham, July 2014.
- [228] M. Joo, D.-W. Suh, J. Bae, and H. Bhadeshia, "Role of delamination and crystallography on anisotropy of charpy toughness in api-x80 steel," *Materials Science and Engineering: A*, vol. 546, pp. 314–322, 2012.
- [229] J. A. Gianetto, N. J. Smith, J. T. Mcgrath, and J. T. Bowker, "Effect of composition and energy input on structure and properties of high-strength weld metals," *Welding Journal*, vol. 71, no. 11,

- pp. S407–S419, 1992.
- [230] G. L. F. Powell and G. Herfurth, “Charpy V-notch properties and microstructures of narrow gap ferritic welds of a quenched and tempered steel plate,” *Metallurgical and Materials Transactions A*, vol. 29, no. 11, pp. 2775–2784, 1998.
- [231] Z. Zhang and R. A. Farrar, “Role of non-metallic inclusions in formation of acicular ferrite in low alloy weld metals,” *Materials Science and Technology*, vol. 12, no. 3, pp. 237–260, 1996.
- [232] T. Koseki and G. Thewlis, “Overview inclusion assisted microstructure control in C-Mn and low alloy steel welds,” *Materials Science and Technology*, vol. 21, no. 8, pp. 867–879, 2005.
- [233] H. Terasaki and Y.-i. Komizo, “Morphology and crystallography of bainite transformation in a single prior-austenite grain of low-carbon steel,” *Metallurgical and Materials Transactions A*, vol. 44, no. 6, pp. 2683–2689, 2013.
- [234] E. Joon Chun, H. Do, S. Kim, D.-G. Nam, Y.-H. Park, and N. Kang, “Effect of nanocarbides and interphase hardness deviation on stretch-flangeability in 998 MPa hot-rolled steels,” *Materials Chemistry and Physics*, vol. 140, no. 1, pp. 307–315, 2013.
- [235] W. B. Lee, S. G. Hong, C. G. Park, K. H. Kim, and S. H. Park, “Influence of Mo on precipitation hardening in hot rolled HSLA steels containing Nb,” *Scripta Materialia*, vol. 43, no. 4, pp. 319–324, 2000.
- [236] J. Jang, Y. Heo, C. Lee, H. Bhadeshia, and D.-W. Suh, “Interphase precipitation in Ti-Nb and Ti-Nb-Mo bearing steel,” *Materials Science and Technology*, vol. 29, no. 3, pp. 309–313, 2013.
- [237] Y. Li, J. A. Wilson, D. N. Crowther, P. S. Mitchell, A. J. Craven, and T. N. Baker, “The effects of vanadium, niobium, titanium and zirconium on the microstructure and mechanical properties of thin slab cast steels,” *ISIJ International*, vol. 44, no. 6, pp. 1093–1102, 2004.
- [238] R. Taillard, P. Verrier, T. Maurickx, and J. Foct, “Effect of silicon on CGHAZ toughness and microstructure of microalloyed steels,” *Metallurgical and Materials Transactions A*, vol. 26, no. 2, pp. 447–457, 1995.
- [239] R. Varughese and A. Pense, “Microstructural development in the coarse-grained, heat-affected zone in titanium-vanadium microalloyed HSLA steels,” *Materials Characterization*, vol. 30, no. 1, pp. 35–43, 1993.
- [240] S.-F. Tao, F.-M. Wang, G.-L. Sun, Z.-B. Yang, and C.-R. Li, “DICTRA simulation of holding time dependence of NbC size and experimental study of effect of NbC on austenite grain growth,” *Metallurgical and Materials Transactions A*, vol. 46, no. 8, pp. 3670–3678, 2015.
- [241] T. Furuhashi, T. Yamaguchi, G. Miyamoto, and T. Maki, “Incomplete transformation of upper bainite in Nb bearing low carbon steels,” *Materials Science and Technology*, vol. 26, no. 4, pp. 392–397, 2010.
- [242] L. Cheng and K. M. Wu, “New insights into intragranular ferrite in a low-carbon low-alloy steel,” *Acta Materialia*, vol. 57, no. 13, pp. 3754–3762, 2009.
- [243] Y. Morikage, K. Oi, F. Kawabata, and K. Amano, “Effect of TiN size on ferrite nucleation on TiN in low-C steel,” *Tetsu- to- Hagane*, vol. 84, no. 7, pp. 510–515, 1998.
- [244] Y. Tomita, N. Saito, T. Tsuzuki, Y. Tokunaga, and K. Okamoto, “Improvement in HAZ toughness of steel by TiN-MnS addition,” *ISIJ International*, vol. 34, no. 10, pp. 829–835, 1994.
- [245] J. Hu, L. X. Du, and J. J. Wang, “Effect of V on intragranular ferrite nucleation of high Ti bearing steel,” *Scripta Materialia*, vol. 68, no. 12, pp. 953–956, 2013.
- [246] C. Capdevila, F. G. Caballero, C. Garcia-Mateo, and C. G. de Andres, “The role of inclusions and austenite grain size on intragranular nucleation of ferrite in medium carbon microalloyed steels,” *Materials Transactions*, vol. 45, no. 8, pp. 2678–2685, 2004.

- [247] A. Lambert-Perlade, A. F. Gourgues, and A. Pineau, "Austenite to bainite phase transformation in the heat-affected zone of a high strength low alloy steelokada," *Acta Materialia*, vol. 52, no. 8, pp. 2337–2348, 2004.
- [248] H. Okada, K. Ikeuchi, F. Matsuda, I. Hrivnak, and Z. Li, "Metallographic investigation of M-A constituent deterioration and improvement of HAZ toughness in 780 and 980 MPa class HSLA steels welded with high heat inputs (2nd report)," *Welding International*, vol. 8, no. 11, pp. 886–892, 1994.
- [249] Y.-q. Zhang, H.-q. Zhang, J.-f. Li, and W.-m. Liu, "Effect of heat input on microstructure and toughness of coarse grain heat affected zone in Nb microalloyed HSLA steels," *Journal of Iron and Steel Research, International*, vol. 16, no. 5, pp. 73–80, 2009.
- [250] G. Wang, T. North, and K. Leewis, "Microalloying additions and HAZ fracture toughness in HSLA steels," *Welding Journal*, vol. 69, no. 1, pp. 14–22, 1990.
- [251] N. J. Petch, "The influence of grain boundary carbide and grain size on the cleavage strength and impact transition temperature of steel," *Acta Metallurgica*, vol. 34, no. 7, pp. 1387–1393, 1986.
- [252] I. Rak, V. Gliha, and M. Koçak, "Weldability and toughness assessment of Ti-microalloyed offshore steel," *Metallurgical and Materials Transactions A*, vol. 28, no. 1, pp. 199–206, 1997.
- [253] M. Jung, S.-J. Lee, and Y.-K. Lee, "Microstructural and dilatational changes during tempering and tempering kinetics in martensitic medium-carbon steel," *Metallurgical and Materials Transactions A*, vol. 40, no. 3, pp. 551–559, 2009.
- [254] C. Garcia-Mateo, M. Peet, F. Caballero, and H. Bhadeshia, "Tempering of hard mixture of bainitic ferrite and austenite," *Materials Science and Technology*, vol. 20, no. 7, pp. 814–818, 2004.
- [255] M. A. Miodownik, J. W. Martin, and E. A. Little, "Grain boundary segregation in an oxide-dispersion-strengthened ferritic steel," *Journal of Materials Science Letters*, vol. 12, no. 11, pp. 834–835, 1993.
- [256] T. Jia and M. Militzer, "The effect of solute Nb on the austenite-to-ferrite transformation," *Metallurgical and Materials Transactions A*, vol. 46, no. 2, pp. 614–621, 2015.
- [257] G. I. Rees, J. Perdrix, T. Maurickx, and H. K. D. H. Bhadeshia, "The effect of niobium in solid solution on the transformation kinetics of bainite," *Materials Science and Engineering: A*, vol. 194, no. 2, pp. 179–186, 1995.
- [258] G. Spanos, R. W. Fonda, R. A. Vandermeer, and A. Matuszeski, "Microstructural changes in HSLA-100 steel thermally cycled to simulate the heat-affected zone during welding," *Metallurgical and Materials Transactions A*, vol. 26, no. 12, pp. 3277–3293, 1995.
- [259] M. Xia, E. Biro, Z. Tian, and Y. N. Zhou, "Effects of heat input and martensite on HAZ softening in laser welding of dual phase steels," *ISIJ international*, vol. 48, no. 6, pp. 809–814, 2008.

List of Tables

2.1	International standards for structural steels with a minimum yield strength 690 MPa [3, 25–27]	8
2.2	Mechanical properties of structural steels with thickness of less than 50 mm [3, 25–27]	8
2.3	Some European standards specifications [3, 29, 30]	9
2.4	Chemical composition of the same strength steel according to different standards in wt.-% [3, 25, 26, 32]	9
2.5	Chemical composition of X100 steels produced by different approaches [33]	10
2.6	Mechanical properties of X100 steels produced by different approaches [33]	10
2.7	Comparison of alloy designs on different steel grade 350, 450 and 690 (in wt.-%) [4]	11
2.8	Specified alloy contents ranges applied to different carbon equivalents [42]	14
2.9	Carbon equivalents calculation from different researchers	15
2.10	Impact of development of metallurgical processes on the levels of impurities in steel [54]	16
2.11	Comparison of welding parameters between modified and standard spray arc welding [58]	18
2.12	Misfit values between different inclusions and ferrite [76, 88]	23
2.13	Chemical composition and carbon equivalent values of two S690QL steels	37
2.14	Solubility products of precipitates defined based on equation 2.15 [172] [173]	42
4.1	Chemical composition and carbon equivalent value of the investigated steels	57
4.2	Mechanical properties of the investigated steels	57
4.3	Chemical composition of filler metal, wt.-%	57
4.4	Welding Parameters, cooling rate and dilution for each weld	59
5.1	Calculated equilibrium phase transformation temperatures using Thermo-Calc	69
5.2	Calculated T_{diss} , °C and volume fraction f of microalloy precipitates in the three steels	72
5.3	Summary of the mechanical properties of the three steels	74
6.1	CVN absorbed energy (J) values of different weld metals [147]	85
6.2	Inclusion characteristics in weld metal A and B [147]	89
6.3	Chemical composition in weld metals [147], wt.-%	89
7.1	Toughness results of different HAZs	108
8.1	Summary of the tensile test data and fracture position [193]	118
8.2	Measured A_{c1} and A_{c3} temperatures	123
8.3	The start temperature of different ferrite products during austenite decomposition	126

List of Figures

2.1	Historical development of production processes for rolled steel products [1]	3
2.2	Material and welding cost of higher strength steels relative to S355 [20]	4
2.3	Solid solute strengthening coefficients shown as a function of the lattice dilation due to the solute additions. Both strengthening and lattice dilation are expressed in terms of the weight percentage of solute [22]	5
2.4	The increase in yield strength of steels compared to the predictions of the Ashby-Orowan equation [22]	6
2.5	Strengthening effects in HSLA steel [20]	7
2.6	Production process of QT high-strength steel [24]	7
2.7	Different approaches to achieve X100 by varying steel composition and cooling parameters [33]	10
2.8	Worldwide crude steel production (Data source: World Steel Association [34])	12
2.9	Approximate cost of major alloying elements relative to iron [36]	12
2.10	Price of alloying elements since 2005 (Data source: InfoMine.com) [38]	13
2.11	Arc types and main properties [55, 57]	17
2.12	Comparison of joint design for modified (left) and standard (right) spray arc welding [58]	18
2.13	Schematic of the sub-zone in the HAZ and relation to the equilibrium Fe – C phase diagram [51]	18
2.14	Schematic of the phase transformation sequences that occur in the weld metal during cooling [66]	20
2.15	Optical micrograph of samples mainly containing (a) bainitic ferrite and (b) acicular ferrite [66]	21
2.16	Schematic of different crack propagation paths for (a) ferrite with side plates and (b) acicular ferrite [69]	21
2.17	Schematic illustration of different mechanisms for nucleation of acicular ferrite on inclusions [65]	23
2.18	Schematic illustration of a Mn-depletion zone [90]	24
2.19	Effect of inclusion size on the probability of ferrite nucleation [81]	25
2.20	Schematic illustration of different mechanisms by which bainite formation can be suppressed to form AF: (a) austenite grain size, (b) poisoned austenite grain boundary, (c) presence of potent inclusions [65]	26
2.21	Schematic illustration of the bainite formation in steels [107]	27
2.22	Bainite classification according to Zajac [114]	28
2.23	Plot of toughness vs. strength for a variety of microstructure in ultra high-strength steels [70]	30
2.24	Preheating temperature T_0 predicted by carbon equivalent CE and CET methods	36
2.25	Typical working ranges of steels (S355J2, 80 mm; S500M, 50 mm; S690QL, 30 mm) [157]	37
2.26	The general effects of microalloy additions on the grain coarsening temperature of austenite [22]	38
2.27	Comparison of the solubility products of microalloy carbides and nitrides [22]	42
2.28	TEM micrographs showing the particle morphology in the base metal (a) and welded sample (b) [172]	45

2.29	Particle size distribution in as-received steel (dash line) and after weld thermal cycle (solid line) [163]	46
2.30	Austenite grain size influenced by ratio of Ti/N at 1100°C, 1300°C for 10 min [185]	47
2.31	SEM fractographs of TiN at initiation site (a) and TiN particle not as initiator (b) [14,16]	48
2.32	Vickers hardness profile of welded joints from QT steel and TMCP steel [18]	50
2.33	Schematic illustration showing substructure changes of martensite phase in DP steel subjected to non-isothermal tempering [132]	52
4.1	Schematic of welded plates and specimen positions for mechanical tests	58
4.2	Schematic view of different parts of cross section considered in a graphical measurement	58
4.3	Schematic illustration of the interaction volumes and the emitted signals [206,207]	60
4.4	Images of (a) Nb-rich and (b) Ti-rich particles in the QBSD mode	61
4.5	TEM sample preparation using FIB imaging in secondary ion (a) and secondary electron (b) mode	63
4.6	Hardness measurement on a cross-section sample	64
4.7	Geometry (in mm) (a) and image (b) of the tensile specimen	64
4.8	Geometry of the Charpy V-notch specimen, in mm	65
4.9	Thermal cycle (a) used in dilatometry experiment and the analysis on dilatation curve (b)	66
5.1	Optical micrographs of steel A (a), steel B (b) and steel C (c)	67
5.2	SEM images of steel A (a, b), steel B (c, d), and steel C (e, f)	68
5.3	Phase diagrams calculated for steel A (a), steel B (b) and steel C (c)	70
5.4	Nb(C,N) composition as functions of temperature	71
5.5	Ti(C,N) composition as functions of temperature	71
5.6	Ti(C,N) and complex Nb,Ti,V(C,N) composition as functions of temperature	72
5.7	Volume fraction of AlN (a) and microalloy precipitates (b) as functions of temperature	73
5.8	Optical micrographs of coarse precipitates in steel A (a), steel B (b) and steel C (c)	73
5.9	EDX spectra of precipitate in steel A (a), steel B (b) and steel C (c)	74
5.10	Strain-stress curves of steel A (a), steel B (b) and steel C (c)	74
5.11	Charpy specimens of steel A (a, b), steel B (c, d), steel C (e, f). a, c and e are longitudinally orientated and b, d, f are transversely orientated	75
5.12	SEM images of delaminations crack propagation (a) and the head of delaminations crack (b) in steel B	75
5.13	TiN in ductile voids (a) and the corresponding EDX spectrum (b)	76
6.1	UCI hardness maps of weld A1 – A3 (a – c), B1 – B3 (d – f) and C1 – C3 (g – i)	79
6.2	Hardness profiles of weld A (a) and B (b) under different cooling rates	80
6.3	Hardness profiles of weld C (a) and comparison of average hardness from all weld metals (b)	80
6.4	Optical micrographs of weld metal A1 (a), A2 (b) and A3 (c) [147]	81
6.5	SEM images of weld metal A1 (a, b) and A2 in weld centre (c) [147]	81
6.6	SEM images of weld metal A3 in weld centre (a, b) and near FZ (c, d) [147]	82
6.7	EDX spectra of inclusions in weld metal A1 (Fig.6.5 (b)) and A3 (Fig.6.6 (b))	82
6.8	Optical micrographs of weld metal B1 (a), B2 (b) and B3 (c) [147]	83
6.9	SEM images of weld metal B3 centre [147]	83
6.10	Optical (a) and SEM image (b) of weld metal C3 centre	84

6.11 Map the distribution and atomic percent of defined elements in the inclusion from Fig. 6.9	84
6.12 Overview of Charpy specimens of weld A1 – A3 (a – c), B1 – B3 (d – f) and C1 – C3 (g – i) [147]	85
6.13 Fractographic examination in the fibrous zone of weld A1 (a, b), A2 (c, d) and A3 (e, f)	86
6.14 Fractographic examination in the radial zone of weld A (a – c) and B (d – f)	87
6.15 Inclusions size distribution in weld A and B [147]	88
7.1 Optical and SEM images of CGHAZ of weld A1 (a, b), A2 (c, d) and A3 (e, f)	92
7.2 Optical and SEM images of CGHAZ of weld B1 (a, b), B2 (c, d) and B3 (e, f)	93
7.3 Optical and SEM images of CGHAZ of weld C1 (a, b), C2 (c, d) and C3 (e, f)	94
7.4 Typical orientation imaging maps obtained from the EBSD measurement. (a) pattern quality, (b) phase map, (c) inverse pole figure (IPF) colour map	95
7.5 Typical orientation imaging maps obtained from the EBSD measurement. (a) SEM image, (b) pattern quality of the region indicated by red line, (c) the corresponding phase map and (d) IPF colour map	96
7.6 EDX mapping of the region selected by blue line (a) SEM image, (b) Fe, (c) Ni and (d) C	96
7.7 Typical orientation imaging maps obtained from the EBSD measurement. (a) IPF bcc colour map combined with boundary misorientation distribution and (b) IPF fcc colour map for austenite	97
7.8 Misorientation along the line A (a) and B (b) including point to point and point to origin misorientation	97
7.9 Austenite grain growth as a function of peak temperature of thermal cycle [186]	98
7.10 Optical micrographs of simulated CGHAZ and FGHAZ of steel A (a, b), B (c, d) and C (e, f). M, martensite; B, bainite; PF, primary ferrite; IGF, intragranular acicular ferrite [186]	100
7.11 SEM micrographs of simulated Nb-containing HAZs: CGHAZ (a, b) as observed by secondary electrons (VPSE); FGHAZ (c, d) and (e) martensite structure in FGHAZ as observed by secondary electrons (InLens). In black circles much finer spherical precipitates are found within bainitic ferrite. RA, retained austenite; B _c , carbides in bainitic ferrite [186]	101
7.12 SEM micrographs of simulated Ti-containing HAZs: CGHAZ (a, b) as observed by secondary electrons (VPSE); FGHAZ (c, d) and (e) martensite structure in FGHAZ as observed by secondary electrons (InLens). Black arrows indicate cuboidal shaped precipitates [186]	102
7.13 SEM micrographs of simulated Ti+V-containing HAZs: CGHAZ (a, b) as observed by secondary electrons (VPSE); FGHAZ(c, d), bainite (e), and martensite (f) as observed by secondary electrons (InLens). In black circles much finer spherical precipitates are found within bainitic ferrite [186]	103
7.14 Comparison of hardness results between as-welded (a) and simulated (b) HAZs [186] .	104
7.15 Dark (a) and bright field (b) STEM images	105
7.16 Dark (a) and bright field (b) STEM images for one precipitate at grain boundary . . .	105
7.17 An overview of precipitates distribution (a), elemental mapping of (b) Fe, (c) Ti, (d) C and (e) N	106
7.18 Bright field STEM images of TiN (a), corresponding TEM image (b) and EDX spectra (c)	106

7.19	Elements mapping of one precipitate in Fig. 7.18 by EFTEM, (a) Ti, (b) N, (c) C . . .	106
7.20	One representative precipitate (a) and elements analysis of precipitate (b) and matrix (c) by EELS	107
7.21	HRTEM image (a, b) of precipitates and the corresponding FFT diagram (c)	107
7.22	Diffraction patterns (a) of selected region in Fig. 7.18, diffraction pattern solution (b) for Ti(C,N), zone axis [0-11], diffraction pattern solution (c) for cementite M_3C , zone axis [43-9]	108
7.23	Fractographic examination in weld A1 – A3 (a – c), B1 – B3 (d – f) and C1 – C3 (g – i)	110
8.1	Load-displacement curves of the welded joints: weld A (a), weld B (b) and weld C (c) [193]	117
8.2	Tensile specimen of weld B2 failed in the HAZ (a) and weld A1 failed in base metal (b) [193]	118
8.3	Softened zone width (a), minimum hardness and softening ratio (b) as a function of heat input [193]	119
8.4	Hardness decrease in the softened zone of the three welds [193]	119
8.5	Optical micrographs of softened HAZs in weld A2 (a), B2 (b) and C2 (c). C, carbides [193]	120
8.6	SEM images of softened HAZs in weld A2 (a, b), weld B2 (c, d) and weld C2 (e, f) [193]	121
8.7	Hardness of simulated HAZs	122
8.8	Representative dilatation curves from simulated HAZs with T_p of (a) 900°C, (b) 820°C and (c) 740°C	123
8.9	Cooling parts of dilatation curves from steel A (a), B (b) and C (c)	124
8.10	The fraction of austenite decomposed as a function of temperature decrease. The curves correspond to varied peak temperatures for weld A (a), weld B (b) and weld C (c). F_s , ferrite start temperature; B_s , bainite start temperature; M_s , martensite start temperature; T_{auto} , martensite automatically tempered temperature	125
8.11	Optical micrographs of simulated HAZs of steel A (a – d) and B (e – h)	128
8.12	SEM images of simulated HAZs of steel A (a – d) and B (e – h)	129
8.13	Optical (a – d) and SEM images (e – h) of simulated Ti+V-containing HAZs	131
8.14	SEM images of tempered HAZs of steel A (a, b), steel B (c, d) and steel C (e, f) . . .	132
8.15	The fraction austenite decomposed as a function of temperature in fast quenched specimens	136
8.16	Optical micrographs of quenched specimens with T_p of 570°C (a) and 560°C (b) . . .	136

Nomenclature

Abbreviations

Abbreviation Meaning

ACC	Accelerated cooling
AF	Acicular ferrite
AS	Standards Australia
ASTM	American society for testing and materials
B	Bainite
BCC	Body centred cubic
BCT	Body centred tetragonal
BF	Bright field
BM	Base metal
C	Carbides
CBED	Convergent beam electron diffraction
CCT	Continuous cooling transformation
CE	Carbon equivalent
CEN	European Committee for Standardisation
CGHAZ	Coarse grained heat affected zone
CSA	Canadian Standards Association
CTOD	Crack tip opening displacement
CVN	Charpy V-notch
DF	Dark field
DP	Dual phase
EBSD	Electron backscatter diffraction
EBW	Electron beam welding
EDS/EDX	Energy dispersive X-ray spectroscopy system
EELS	Electron energy loss spectroscopy
EFTEM	Energy filtered transmission electron microscopy
F	Ferrite
FCC	Face centred cubic
FEG-SEM	Field emission gun scanning electron microscopy

FFT	Fast Fourier transformation
FGHAZ	Fine grained heat affected zone
FIB	Focused ion beam
FZ	Fusion zone
GMAW	Gas metal arc welding
GTAW	Gas tungsten arc welding
HAADF	High-angle annular dark field
HAZ	Heat affected zone
HRTEM	High resolution transmission electron microscopy
HSLA	High strength low alloy
IC GC HAZ	Intercritically reheated coarse grained heat affected zone
IGF	Intragranular acicular ferrite
ISO	International organisation for standardisation
JIS	Japanese Standards Association
LOM	Light optical microscopy
M	Martensite
M-A	Martensite-austenite constituent
MDZ	Mn depleted zone
NBD	Nano-beam diffraction
PF	Polygonal ferrite
QBSD	Quadrant backscatter detector
QST	Quenched and self-tempered
QT	Quenched and tempered
RA	Retained austenite
SAW	Submerged arc welding
SE	Secondary electron
SEM	Scanning electron microscopy
SMAW	Shield metal arc welding
STEM	Scanning transmission electron microscopy
TEM	Transmission electron microscopy
TMCP	Thermo-mechanically controlled processing

TRIP	Transformation induced plasticity
TTT	Time – Temperature – Transformation
UCI	Ultrasonic contact impedance
WM	Weld metal
XRD	X-ray diffraction

Greek characters

α	Alpha-Ferrite	-
δ	Delta-ferrite	-
γ	Austenite	-
γ	Grain boundary surface free energy	J/m^2

Latin characters

ΔP	Net driving pressure on the boundary	$\text{J}/\mu\text{m}^3$
A	Elongation after fracture	%
A_{BF}	Area of base metal fusion	mm^2
A_{c1}	Temperature of the onset of austenite formation on heating	$^{\circ}\text{C}$
A_{c3}	Temperature of the completion of austenite formation on heating	$^{\circ}\text{C}$
A_{e1}	Temperature when austenite begins to form under equilibrium	$^{\circ}\text{C}$
A_{e3}	Temperature when austenisation is complete under equilibrium	$^{\circ}\text{C}$
A_{e4}	Temperature of the onset of delta ferrite formation under equilibrium	$^{\circ}\text{C}$
A_{RG}	Area of weld root gap	mm^2
A_{RR}	Area of root reinforcement	mm^2
A_{TR}	Area of top reinforcement	mm^2
A_{WD}	Area of total weld deposit	mm^2
B_s	Bainite start temperature	$^{\circ}\text{C}$
C	Molar fraction of interstitial element	%
c_3	A dimensionless geometric coefficient	-
c_4	A dimensionless Zener coefficient	-
c_i	Concentration of the solute	$\text{wt}\%$
C_m	Solute concentration in the matrix	-
C_p	Concentration of solute in the particle	-
D	Mean austenite grain diameter	μm

Nomenclature

d	Grain diameter	mm
D_0	Initial austenite grain diameter	μm
D_m	Element bulk diffusivity	-
dD/dt	Growth rate of grain boundary	$\mu\text{m}/\text{s}$
E_0	Primary electron	-
f	Volume fraction of particles	-
f_0	Initial volume fraction of particles	-
F_s	Ferrite start temperature	$^{\circ}\text{C}$
k	Pinning efficiency of the precipitate	-
$K_{1,2}$	Kinetic constant	-
k_i	Strengthening coefficient of the solute	MPa/wt%
k_s	Solubility product	-
k_y	Strengthening coefficient of grain size	MPa $\cdot\text{mm}^{1/2}$
M	Molar fraction of microalloying element	%
M_0	Pre-exponential mobility factor	$\mu\text{m}^4/\text{J} \cdot \text{s}$
M_s	Martensite start temperature	$^{\circ}\text{C}$
n	Time exponent	-
p	Maximum pinning force exerted by a particle on grain boundary	nm
P_{DL}	Dilution percentage	%
P_d	Driving pressure for grain growth	$\text{J}/\mu\text{m}^3$
P_p	Summarised pinning force from multiple precipitates	$\text{J}/\mu\text{m}^3$
P_z	Pinning force per unit volume of the grain boundary	$\text{J}/\mu\text{m}^3$
Q_{app}	Apparent activation energy of grain boundary motion	kJ/mol
Q_s	Activation energy of the coarsening process	kJ/mol
R	Gas constant	J/mol \cdot K
r	Radius of particle	nm
R_{eH}	Upper yield strength	MPa
R_{eL}	Lower yield strength	MPa
R_e	Yield strength	MPa
R_m	Tensile strength	MPa
$R_{p0.2}$	0.2% proof strength	MPa

t	Time	s
T_0	Preheating temperature	°C
$t_{8/5}$	Cooling time from 800°C to 500°C	°C
T_{auto}	Martensite automatically tempered temperature	°C
T_{curie}	Curie temperature	°C
T_{diss}	Dissolution temperature of precipitate	°C
T_p	Peak temperature	°C
X	True three dimensional diameter of particles	nm
x	Average diameter of particles in the plane of intersection	nm
Z	Reduction of area	%
Z	Atomic number	-